Design and testing of hybrid InP/Si photonic integrated components/circuits for LIDAR applications

Martin Peyrou

THÈSE

Pour obtenir le grade de

DOCTEUR DE L'UNIVERSITÉ GRENOBLE ALPES

École doctorale : EEATS - Electronique, Electrotechnique, Automatique, Traitement du Signal (EEATS)
Spécialité : Optique et Radiofréquences
Unité de recherche : Grenoble Images Parole Signal Automatique

Conception et test de composants/circuits photoniques intégrés hybrides InP/Si pour applications LIDAR

Design and testing of hybrid InP/Si photonic integrated components/circuits for LIDAR applications

Présentée par :

Martin PEYROU

Direction de thèse :

Yannis LE GUENNEC MAITRE DE CONFERENCES, Université Grenoble Alpes	Directeur de thèse
Sylvie MENEZO	Co-encadrante de thèse

Rapporteurs :

Christelle AUPETIT-BERTHELEMOT
PROFESSEUR DES UNIVERSITES, UNIVERSITE DE LIMOGES
Christophe PEUCHERET
PROFESSEUR DES UNIVERSITES, UNIVERSITE DE RENNES

Thèse soutenue publiquement le **23 mars 2023**, devant le jury composé de :

Yannis LE GUENNEC MAITRE DE CONFERENCES HDR, GRENOBLE INP	Directeur de thèse
Christelle AUPETIT-BERTHELEMOT PROFESSEUR DES UNIVERSITES, UNIVERSITE DE LIMOGES	Rapporteure
Christophe PEUCHERET PROFESSEUR DES UNIVERSITES, UNIVERSITE DE RENNES	Rapporteur
Frédéric GRILLOT PROFESSEUR DES UNIVERSITES, INSTITUT POLYTECHNIQUE DE PARIS	Examinateur
Patrick FENEYROU INGENIEUR DOCTEUR, THALES RESEARCH & TECHNOLOGY	Examinateur
Florence PODEVIN PROFESSEUR DES UNIVERSITES, GRENOBLE INP	Présidente

Invités :

Sylvie MENEZO
INGENIEUR DOCTEUR, SCINTIL Photonics

Abstract

The development of intelligent systems for automotive applications requires high-precision sensors to capture dynamic environments. The race to fully autonomous vehicles has already started, and multi-sensor fusion is foreseen as the ultimate solution for high performance environment perception. Light Detection And Ranging (LIDAR) produces high-resolution 3D point clouds that complement and overcome the limitations of cameras and RADAR systems. Frequency-Modulated Continuous Wave (FMCW) LIDAR offers several advantages over other LIDAR architectures, including velocity information of the object, higher sensitivity, and background immunity due to coherent detection. Nevertheless, today's commercial LIDARs are bulky and prone to mechanical failure, preventing their mass deployment in embedded systems where high level of parallelism is needed. Hence, the integration of LIDAR on mass producible photonic chip is highly desirable. Interestingly, the data communication industry has pursued the same objective over the past decades. By leveraging the mature CMOS supply chain, optical fibered components have been shrunk down to produce silicon photonics integrated transceivers. However, LIDAR and transceiver architectures require laser sources and amplifiers, but silicon is not an efficient gain medium. On the contrary, III-V compound materials are known for producing very efficient laser sources and semiconductor optical amplifiers (SOA). The objectives of this work are to investigate the benefits and challenges related to the integration of a FMCW LIDAR system on III-V/Si chip.

The approach is based on three phases: FMCW LIDAR system modelization, design/layout of components and circuits, and performance verification through characterization.

First, I present an overview of LIDAR architectures, performance metrics and scanning methods with a comparison between Optical Phased Array (OPA) and Focal Plane Switch Array (FPSA). I also describe the chip-scale integration of FMCW LIDAR systems to improve the footprint and the power consumption. This part highlights the interest of FMCW LIDAR for automotive LIDAR applications and the key differentiator of the III-V/Si integration platform. A set of automotive LIDAR specifications is finally presented. Based on these considerations, a numerical model is provided to link the FMCW LIDAR system performances with the silicon photonic component specifications. I also show through simulations that the range and velocity estimation algorithm can be modified to detect targets beyond the laser coherence length with a good precision. Then, a set of FMCW LIDAR building blocks (balanced photodiodes, 90° optical hybrid, tunable laser, DBR laser, SOA, IQ modulator and thermo-optic switching element) were prototyped and characterized. I also present the realization of a single transmitter/receiver FMCW LIDAR tile comprising a coherent receiver and a III-V/Si SOA operating in a temperature range between 20-60 °C. Besides, the FMCW LIDAR source was investigated through linewidth and chirp linearity measurements. Then, a small-scale FPSA beam scanning unit was realized to assess the switch performances. Finally, I share the perspectives to build an integrated FMCW LIDAR demonstrator for automotive applications.

Keywords: FMCW LIDAR, III-V/Si, silicon photonics, linewidth, coherent receiver, beam-scanning, semiconductor optical amplifier, tunable laser, photodiodes, frequency modulation, linearity, IQ modulator.

Résumé

Le développement de systèmes intelligents pour les applications automobiles nécessite des capteurs de haute précision pour détecter des environnements dynamiques. La course aux véhicules autonomes a déjà commencé, et la fusion de données multicapteurs est considérée comme la solution ultime pour une perception performante de l'environnement. Le LIDAR (Light Detection And Ranging) produit des nuages de points 3D à haute résolution qui complètent et surmontent les limites auxquelles les caméras et les systèmes RADAR font face. Le LIDAR FMCW offre plusieurs avantages par rapport aux autres architectures LIDAR, dont des informations sur la vitesse de l'objet, une plus grande sensibilité et une immunité au bruit de fond grâce à une détection cohérente. Néanmoins, les LIDAR commerciaux actuels sont encombrants et sujets à des défaillances mécaniques, ce qui empêche leur déploiement massif dans les systèmes embarqués où un haut niveau de parallélisme est nécessaire. Par conséquent, l'intégration du LIDAR sur une puce photonique pouvant être produite en masse est hautement souhaitable. Il est intéressant de noter que l'industrie des communications de données a poursuivi le même objectif au cours des dernières décennies. En tirant parti d'une industrie CMOS mature, les composants à fibres optiques ont été réduits en taille pour produire des circuits optiques intégrés en photonique sur silicium. Cependant, les architectures LIDAR et les circuits optiques nécessitent des sources laser et des amplificateurs, mais le silicium n'est pas un milieu à gain favorable. A l'inverse, les matériaux III-V sont connus pour produire des sources laser et des amplificateurs optiques à semi-conducteurs (SOA) très efficaces. Les objectifs de ce travail sont d'étudier les bénéfices et les défis liés à l'intégration d'un système LIDAR FMCW sur une puce III-V/Si.

L'approche suivie est basée sur trois phases : la modélisation du système LIDAR FMCW, la conception/layout des composants et circuits, et la vérification des performances par la caractérisation.

Tout d'abord, nous présentons une vue d'ensemble des architectures LIDAR, des mesures de performance et des méthodes de balayage avec une comparaison entre le réseau optique à commande de phase (OPA) et le réseau à commutation situé dans le plan focal (FPSA). L'intégration sur puce des systèmes LIDAR FMCW est ensuite présentée, dans le but d'améliorer leur encombrement et leur consommation énergétique. Cette partie souligne l'intérêt du LIDAR FMCW pour les applications LIDAR automobiles ainsi que le différentiateur clé de la plateforme d'intégration III-V/Si. Un ensemble de spécifications pour un LIDAR automobile est finalement présenté. Sur la base de ces considérations, un modèle numérique a été réalisé afin de relier les performances du système LIDAR FMCW aux spécifications des composants photoniques en silicium. Il est ensuite démontré par des simulations que l'algorithme d'estimation de distance et vitesse peut être modifié pour détecter des cibles au-delà de la longueur de cohérence avec une bonne précision. Par la suite, un ensemble de blocs consitutifs du LIDAR FMCW (photodiodes équilibrées, hybride optique 90°, laser accordable, laser DBR, SOA, modulateur IQ et élément de commutation thermo-optique) ont été prototypés sur la plateforme III-V/Si puis caractérisés. Ainsi, nous avons réalisé une tuile LIDAR FMCW à émetteur/récepteur unique comprenant un récepteur cohérent et une SOA III-V/Si fonctionnant dans une plage de température comprise entre 20 et 60 °C. Par ailleurs, après une étude de la source LIDAR FMCW, des mesures de largeur de raie et de linéarité du chirp sont présentées. Une unité de balayage de faisceau FPSA a également été réalisée

pour évaluer les performances du commutateur. Enfin, les perspectives pour construire un démonstrateur LIDAR FMCW intégré pour des applications automobiles sont partagées.

Mots-clés: LIDAR FMCW, III-V/Si, photonique silicium, largeur de raie, récepteur cohérent, balayage de faisceau, amplificateur optique à semiconducteurs, laser accordable, photodiodes, modulation de fréquence, linéarité, modulateur IQ.

Résumé substantiel

Le développement de systèmes intelligents pour les applications automobiles nécessite des capteurs de haute précision pour capter des environnements dynamiques. La course aux véhicules entièrement autonomes a déjà commencé, et la fusion de données multicapteurs est considérée comme la solution ultime pour une perception performante de l'environnement. Le LIDAR (Light Detection And Ranging) est un système d'imagerie 3D produisant des nuages de points à haute résolution. Le système LIDAR complète et surmonte les limites auxquelles les caméras et les systèmes RADAR font face. Parmi les architectures LIDAR, le LIDAR à onde continue modulée en fréquence (FMCW) offre plusieurs avantages incluant la mesure de la vitesse de l'objet, une plus grande sensibilité et une immunité au bruit ambient grâce à une détection cohérente. Néanmoins, les LIDAR commerciaux actuels sont encombrants et sujets à des défaillances mécaniques, ce qui empêche leur déploiement massif dans les systèmes embarqués où un haut niveau d'intégration est nécessaire. Par conséquent, l'intégration du LIDAR sur une puce photonique pouvant être produite en masse est hautement souhaitable. Il est intéressant de noter que l'industrie des communications de données a poursuivi le même objectif au cours des dernières décennies. En tirant parti d'une industrie CMOS mature, les composants à fibres optiques ont été réduits en taille pour produire des circuits optiques intégrés en photonique sur silicium (Si). Cependant, les architectures LIDAR et les circuits optiques nécessitent des sources laser et des amplificateurs, mais le silicium n'est pas un milieu à gain favorable. A l'inverse, les matériaux III-V sont connus pour produire des sources laser et des amplificateurs optiques à semi-conducteurs (SOA) très efficaces. Cette dissertation de thèse étudie les défis liés à l'intégration d'un système LIDAR FMCW sur une puce III-V/Si. Notre approche pour répondre à ce problème est basée sur trois phases : la modélisation du système LIDAR FMCW, la conception/layout des composants et circuits et la vérification des performances par la caractérisation.

Dans un premier temps, nous présentons le principe de fonctionnement ainsi qu'une vue d'ensemble des architectures LIDAR. Nous montrons en particulier l'intérêt de l'approche LIDAR FMCW par rapport aux LIDAR à temps de vol direct ou indirect, dans le contexte des applications automobiles. L'architecture LIDAR FMCW est prometteuse pour les applications de détection 3D de haute précision. Elle fournit une estimation de la vitesse, l'immunité face au bruit de fond et une sensibilité élevée, ce qui la rend adaptée à la détection à longue distance. Par la suite, nous présentons des métriques de performance pour un système LIDAR, telles que la résolution, la précision, le champ de vue, le nombre d'images par seconde capturées par le LIDAR et la distance d'opération. Nous discutons le choix de la longueur d'onde d'émission et des conséquences sur la sécurité pour l'œil humain. Suite à cela, les différentes méthodes d'illumination sont présentées, en différentiant les techniques comprenant ou non un balayage de faisceau. Le balayage de faisceau permet d'atteindre une plus longue portée de cible car la puissance optique est concentrée sur un point. Les solutions de balayage de faisceaux intégrées sur puce sont préférées aux solutions mécaniques en raison de leur faible consommation d'énergie, de leur faible encombrement et de leur bonne fiablilité. Nous comparons de manière quantitative deux solutions intégrées, à savoir le réseau optique à commande de phase (OPA) et le réseau à commutation situé dans le plan focal (FPSA). Notre

choix d'investiguer le FPSA est basé sur des observations en termes de consommation d'énergie, de diaphonie et de complexité. Enfin, nous discutons de l'intégration à l'échelle de la puce des systèmes LIDAR FMCW afin d'améliorer l'encombrement, le poids et la consommation d'énergie. La plateforme d'intégration "Backside on Box" developpée par Scintil Photonics est présentée et son procédé de fabrication est décrit. L'intégration de matériaux III-V sur Si avec le silicium (Si), le nitrure de silicium (SiN) et le germanium (Ge) est un facteur de différenciation qui permet la fabrication de composants et de circuits à la pointe de la technologie sur une même puce.

Cette partie souligne l'intérêt du LIDAR FMCW pour les applications LIDAR automobiles et met en avant les avantages de la plateforme d'intégration III-V/Si. Un ensemble de spécifications à l'échelle d'un système LIDAR FMCW pour l'automobile est finalement présenté. La partie suivante consiste à modéliser le système LIDAR FMCW pour en déduire des spécifications pour les composants photoniques correspondants.

Sur la base de ces considérations, nous décrivons ensuite les blocs constitutifs d'un LIDAR FMCW. Ce dernier est composé :
• d'une source émettant un signal modulé en rampe de fréquence dans l'infrarouge
• d'un module d'illumination pour transmettre le signal et de collection pour recevoir le signal réfléchi
• d'un récepteur cohérent pour démoduler le signal reçu (RX) par mélange avec un oscillateur local (LO) de référence
• d'un module électronique pour réaliser le contrôle et le traitement des signaux.

Du point de vue du système, chacun de ces éléments est responsable des pertes et/ou contribue au bruit total. Ainsi, nous proposons dans cette partie de construire un modèle de bruit et d'effectuer un budget de puissance afin de quantifier les métriques de performances et d'identifier les limitations d'un système LIDAR FMCW. Pour débuter, la théorie décrivant le récepteur cohérent est présentée. Ce type de récepteur est constitué d'un mélangeur suivi de photodiodes. Le mélangeur peut être réalisée avec un coupleur 3 dB ou avec un hybride 90° aussi appelé démodulateur IQ. Cette deuxième option permet d'extraire les composantes en phase (I) et en quadrature (Q) du signal et de résoudre l'ambiguïté de détection de cibles fantômes. Pour la photodétéction, deux photodiodes connectées en série sont utilisées afin de former un photodétecteur équilibré. Sous le même éclairage, si les photodiodes sont identiques, les photocourants produits sont égaux et le photodétecteur balancé permet d'annuler la composante continue provenant de la détection du signal et d'annuler aussi la contribution en bruit d'intensité provenant de la source. Par la suite, les formes d'onde utilisées pour moduler la source d'un LIDAR FMCW sont présentées. Deux options sont possibles : les formes d'onde en dents de scie ou en triangle. La première option permet l'estimation de la distance à la cible. La modulation triangulaire permet d'estimer la distance ainsi que la vitesse de la cible via l'effet Doppler. Pour les deux méthodes, la distance à la cible (et sa vitesse pour une modulation triangulaire) est extraite à partir de la valeur de la fréquence du signal produit par la détection cohérente entre les signaux LO et RX. Une transformée de Fourier est donc appliquée à ce signal temporel en sortie

de la photodiode. La fréquence de ce signal est ensuite estimée à partir du spectre fréquentiel et la distance de la cible (et sa vitesse) est obtenue. Ce principe est illustré sur la Fig. 1. La bande passante électrique du récepteur est dimensionnée de sorte à détecter les fréquences qui correspondent aux distances et vitesse maximales de cibles déterminées par les spécifications.

Nous fournissons ensuite un modèle numérique permettant de relier les performances du système LIDAR FMCW aux spécifications des composants photoniques sur silicium. Pour ce modèle, nous avons considéré une brique élémentaire LIDAR FMCW composée d'un seul transmetteur (TX) et d'un seul récepteur (RX).

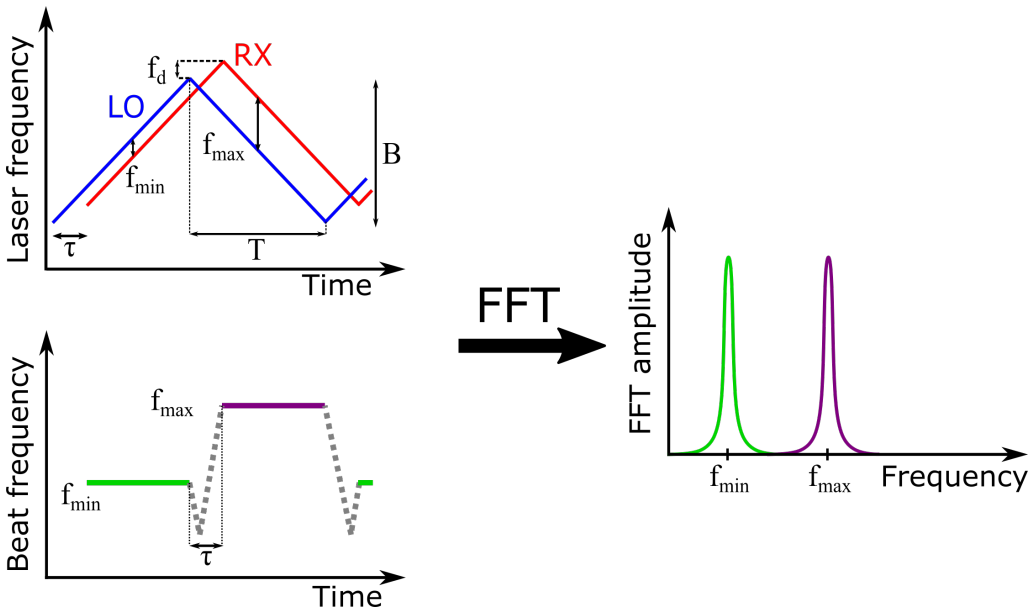

Figure 1: Principe du LIDAR FMCW utilisant une forme d'onde triangulaire. FFT : transformée de Fourier rapide.

Afin d'établir le budget de puissance de cette architecture LIDAR FMCW, les pertes en espace libre sont exprimées en utilisant une forme simplifiée de l'équation LIDAR. La plus grande contribution à ces pertes est liée à la propagation dans l'air entre un LIDAR intégré ayant une ouverture de quelques cm^2 et une cible située à plusieurs centaines de mètres. Pour assurer une puissance transmise suffisante, nous proposons d'ajouter un amplificateur optique à semiconducteur dans le chemin de transmission du LIDAR FMCW, comme décrit sur la Fig. 2.

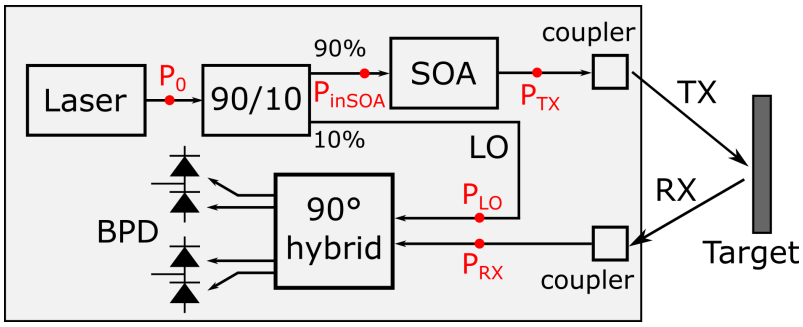

Figure 2: Architectures LIDAR FMCW avec un amplificateur optique à semi-conducteurs (SOA). 90/10 : diviseur 90%-10% ; BPD : photodiodes équilibrées.

Les contributions en bruit du système sont le bruit de grenaille, le bruit de phase du laser, le bruit d'amplification, le RIN, le bruit thermique, le bruit de quantification de l'ADC et la puissance équivalente de bruit (NEP) du TIA. Après avoir décrit et validé le modèle de bruit de phase du laser par simulations de Monte Carlo, nous avons évalué l'influence du bruit de phase du laser sur le photocourant détecté. Pour les cibles situées au-delà de la longueur de cohérence, le signal de l'oscillateur local (LO) et le signal reçu (RX) sont fortement décorrélés. Le spectre du photocourant est alors modifié et passe d'une allure en sinus cardinal pour des cibles situées avant la longueur de cohérence, à une allure Lorentzienne pour des cibles au-delà de la longueur de cohérence. Nous avons ensuite simulé le rapport signal sur bruit (RSB) incluant toutes ces sources de bruits pour différentes distances de cible et en fonction de la largeur de raie du laser, de la période de mesure, du diamètre d'ouverture du récepteur ainsi que pour différentes conditions environnementales. Nous montrons également par des simulations Monte Carlo sur le bruit de fréquence, que l'algorithme d'estimation de distance et vitesse peut être modifié pour détecter des cibles au-delà de la longueur de cohérence avec une bonne précision.

Nous concluons cette partie par un ensemble de spécifications sur les composants photoniques en lien avec les simulations effectuées. Ces spécifications de composants sont utilisées dans le chapitre suivant, où nous décrivons la réalisation et la caractérisation des composants et circuits LIDAR FMCW basés sur la technologie Scintil en photonique silicium.

Par la suite, nous introduisons les différentes étapes nécessaires à la réalisation de puces photoniques. Durant cette thèse, j'ai principalement été investi dans les étapes de conception de masques de fabrication de composants et circuits, et de caractérisation à l'échelle de puces/plaques ou boitier.

Le Tab. 1 donne un aperçu des modules LIDAR FMCW qui ont été réalisés.

Blocs LIDAR	Nom	Composants testés	Boitier or plaque/puce
Récepteur cohérent et SOA	brique LIDAR FMCW	GC; MMI; hybride 90°; PD; SOA	plaque/puce
Source et modulateur	Laser accordable	Anneaux résonants ; GC	boitier
	Laser DBR	GC; Laser DBR	plaque/puce
	Modulateur IQ avec SOA	SOA; Modulateur IQ; GC	boitier
Balayage	FPSA à 4 émetteurs	déphaseur thermo-optique ; GC	plaque/puce

Table 1: Aperçu des éléments constitutifs du LIDAR FMCW. GC : coupleur surfacique de réseau ; MMI : coupleur d'interférence multimode ; PD : photodiode ; SOA : amplificateur optique à semiconducteurs ; DBR : réseau de Bragg distribué.

Nous présentons d'abord la structure et la caractérisation d'une brique LIDAR FMCW à émetteur/récepteur unique comprenant un récepteur cohérent et un SOA en III-V/Si. La mesure des coupleurs surfaciques, des coupleurs/diviseurs MMI et de l'hybride optique 90° est effectué sur plusieurs puces afin d'obtenir des résultats statistiques sur ces composants à l'échelle d'une plaque de Silicium. Les photodiodes Ge sont également caractérisées en termes de responsivité et de courant d'obscurité pour différentes tensions d'alimentation de la photodiode. Les résultats de mesure du récepteur cohérent répondent aux spécifications de la norme IC-TROSA et sont en accord avec l'état de l'art. Nous présentons ensuite les mesures sur l'amplificateur optique à semiconducteur (SOA) en III-V/Si. Celui-ci fournit une amplification sur puce dans la bande C et peut fonctionner à des températures comprises entre 20°C et 60°C. Une figure de bruit (NF) de 13 dB est mesurée pour ce SOA. Nous décrivons ensuite une campagne de mesures sur un laser accordable pouvant être utilisé comme source pour le LIDAR FMCW. Ce laser est constitué d'un SOA et d'une cavité formée par deux anneaux accordables en longueurs d'onde. Une première caractérisation de l'accordabilité des anneaux permet de quantifier la consommation électrique des sections d'accord en longueurs d'onde des anneaux, ainsi que la forme spectrale des filtres optiques constitués par les anneaux résonnants. Nous démontrons ensuite une accordabilité sur l'ensemble de la bande C avec un rapport de suppression du mode latéral (Side Mode Suppression Ratio) supérieur à 35 dB. Enfin, nous décrivons la mesure de largeur de raie du laser accordable en utilisant la technique d'interférométrie auto-hétérodyne retardée. Une largeur de raie intrinsèque de 184 kHz est mesurée. Cependant, la raie laser observée à l'analyseur de spectre optique montre la présence de pics latéraux polluant le pic principal. Cela peut s'expliquer par la présence d'auto-injection dans la cavité laser en raison de réflexions à l'intérieur de la cavité.

Une seconde option de laser a été évaluée : un laser DBR. Nous présentons la caractérisation électro-optique du laser. Cependant, un comportement multimode est observé lorsque le courant d'injection augmente.

Concernant la modulation de fréquence, nous avons réalisé une mesure de linéarité des rampes de fréquences générées par un modulateur IQ suivi d'un SOA en III-V/Si.

La non-linéarité des rampes de modulation a pour effet d'élargir le spectre du signal détecté, ce qui dégrade le rapport signal/bruit et la résolution du LIDAR. Nous mesurons une distorsion liée à la non-linéarité de 1.8% en considérant la portion 5-95% de la période de modulation. Sur la base de cette modulation, des mesures de distance de fibres (2 to 18 m) ont également été effectuées, permettant de confirmer la linéarité suffisante des rampes de fréquences optiques générées par le modulateur IQ.

Ensuite, une unité de balayage de faisceau (FPSA) a été réalisée pour évaluer les performances du commutateur. Celle-ci comprend 3 commutateurs basés sur des interféromètres de Mach-Zehnder (MZI) thermo-optiques permettant d'adresser 4 émetteurs. Des sorties optiques et des photodiodes Ge intégrées sur la puce permettent de contrôler l'évolution du signal optique lors de sa propagation dans le circuit. Nous présentons d'abord la caractérisation électrique des déphaseurs thermo-optiques ainsi que les pertes optiques induites par un commutateur. Par la suite, la mesure de diaphonie, de stabilité en puissance et de temps de réponse du commutateur sont réalisées. D'après nos mesures, le commutateur présente une faible perte d'insertion (<0.6dB). En termes de puissance électrique consommée, 27 mW sont nécessaires pour commuter le signal optique dans l'une des deux sorties. La diaphonie entre les émetteurs est inférieure à -15 dB et peut être améliorée en ajoutant des SOA sur chaque sortie optique. En revanche, ces commutateurs sont limités à des vitesses de montée/descente de l'ordre de 62.5 kHz, ce qui pourrait être limitant pour atteindre les vitesses de balayage requises par un LIDAR automobile.

L'intégration des matériaux III-V avec le Si, le SiN et le Ge est bénéfique pour la réalisation d'un LIDAR FMCW sur puce. En effet, les sources laser intégrées présentant une faible largeur de raie peuvent être modulées en rampe linéaire de fréquence en utilisant un modulateur IQ en Si. Un SOA en III-V/Si peut être utilisé pour compenser les pertes du circuit, assurant une puissance élevée du signal transmis. Enfin, le récepteur cohérent peut être intégré sur puce. Celui-ci inclut un hybride optique 90° et des photodiodes Ge permettant de générer le signal contenant les informations de distance et de vitesse de la cible.

Enfin, nous concluons ce travail en apportant une réponse à la problématique d'intégration du système LIDAR FMCW. L'intégration des éléments constitutifs d'un LIDAR FMCW sur puce III-V/Si apporte de nombreux avantages en termes de réduction de la consommation d'énergie, de l'encombrement, des pertes de couplage, et des risque de défaillance mécanique. Nous partageons également des perspectives pour compléter ce travail en vue de construire un démonstrateur LIDAR FMCW intégré pour des applications automobiles.

Acknowledgements

First, I would like to thank my thesis supervisor Sylvie Menezo, CEO and CTO of Scintil Photonics, and my thesis director Yannis Le Guennec, associate Professor at GIPSA-lab, Grenoble INP-Phelma. Thank you for your dedication and the time you spent to transmit me your knowledge. Thank you Sylvie for welcoming me at Scintil Photonics, which is to me a very stimulating place for doing science and conduct ambitious projects. Yannis, thank you for introducing me to the academic world and for presenting me the variety of projects conducted within GISPA-lab GAIA team. I really appreciated working with you and learn from two different point of view. It has been three extremely rewarding years between research and industry. I consider myself very lucky to be part of this journey and to be one of your colleagues.

I also want to thank the jury members for accepting the invitation to my thesis. I am grateful to Professor Christelle Aupetit-Berthelemot from XLIM/ENSIL and Professor Christophe Peucheret from FOTON/ENSSAT for reviewing my PhD dissertation. Thank you also to Professor Emil Novakov for chairing my thesis oral presentation. I also want to thank the examiners Professor Frédéric Grillot from Télécom ParisTech and Doctor Patrick Feneyrou from Thales TRT.

Thanks also to the whole Scintil Photonics team in Grenoble and Toronto : Florian Denis-Le-Coarer, Kevin Froberger, Marylise Marchenay, Jason Mak, Frédéric Mazur, Laurent Milord, Zheng Yong, Torrey Thiessen, Yannick Paillard, Jean-Marc Gillet, Olivier Girard, Marion Lormeau and Pascal Langlois. From component design to micro fabrication, characterization, packaging and costumer meetings, I learned a lot from all of you. We have great challenges in sight for the next few years.

I also want to thank Philippe Grosse, Karen Ribaud and André Myko from CEA Leti test team, for introducing me to the automatic probe tester and for the interesting characterization discussions.

I would like to express my gratitude to Frédéric Grillot, Heming Huang and Shihao Ding for hosting me in Telecom ParisTech. I learned a lot from your expertise on laser phase noise.

Thank you to Gabriel Vasile and Frédéric Grillot for being part of my individual thesis committee and for the interesting discussions we had over these three years.

I want to thank my friends in Grenoble for sharing these 3 challenging years. I am looking forward to share great moments with you in the coming years. For the ones leaving in postdocs abroad I wish you the best. I particularly want to thank Félix, Tamara, Martin, Laetitia, Victor, Rémy, Justine, Stenzel, Clara and Adrian.

Thank you also to Sandrine, Benoit, Noa, Olivia and Sarah for considering me as part of your family.

I want to express my thanks to my family for their love and their continuous interest in my research: my parents, Rosa and Dominique, my sister Clara and my brother Thomas. I am very lucky to have such a tight-knit family. Finally, I would like to thank my wife Suzy for all the moments she encouraged and motivated me during these three years. She turned difficult moments into pleasant ones.

Contents

List of Figures **17**

List of Tables **22**

List of acronyms **24**

1 Introduction **27**

2 Fundamentals of Light Detection And Ranging **32**
2.1 Principle of LIDAR . . . 32
2.2 LIDAR architectures . . . 32
2.2.1 DToF . . . 33
2.2.2 iToF or AMCW . . . 34
2.2.3 FMCW LIDAR . . . 34
2.3 Performance metrics . . . 35
2.3.1 Resolution . . . 35
2.3.2 Range Precision . . . 36
2.3.3 Field-of-View . . . 37
2.3.4 Frame rate . . . 37
2.3.5 Operating range . . . 37
2.3.6 Immunity to parasitic background . . . 38
2.3.7 SNR comparison between DToF and FMCW LIDARs . . . 38
2.3.8 LIDAR output information . . . 38
2.4 Wavelength . . . 39
2.5 Eye safety . . . 40
2.6 Long-range automotive LIDAR . . . 41
2.7 Illumination . . . 42
2.7.1 Flash and scanning techniques . . . 42
2.7.2 Optical Phased Arrays (OPA) . . . 45
2.7.3 Focal plane switch array (FPSA) . . . 52
2.7.4 1D OPA vs 1D FPSA comparison . . . 57
2.8 Towards integration of LIDAR systems . . . 60
2.8.1 Silicon photonics for FMCW LIDAR . . . 60
2.8.2 III-V on Si integration . . . 61
2.8.3 State of the art FMCW LIDAR . . . 64
2.9 Chapter conclusion . . . 66

3 FMCW LIDAR model 67
3.1 Overview of the FMCW LIDAR system . . . 67
3.2 Pre-requisite on coherent detection . . . 68
3.2.1 With 3 dB coupler . . . 68
3.2.2 With 90 degree hybrid . . . 69
3.2.3 Balanced photodetection . . . 71
3.3 FMCW LIDAR waveforms . . . 72
3.3.1 Sawtooth FMCW waveform . . . 72
3.3.2 Triangular FMCW waveform . . . 75
3.4 Electrical bandwidth . . . 76
3.5 Model description . . . 78
3.6 Free space loss . . . 78
3.7 Attenuation due to polarization . . . 80
3.8 Laser chirp nonlinearity . . . 81
3.9 FMCW LIDAR link budget and noise study . . . 82
3.9.1 FMCW LIDAR signal . . . 82
3.9.2 Shot noise and receiver sensitivity . . . 83
3.9.3 SOA noise . . . 84
3.9.4 Thermal noise . . . 86
3.9.5 NEP noise for PD with TIA . . . 86
3.9.6 Quantization noise . . . 86
3.9.7 Relative intensity noise (RIN) . . . 87
3.9.8 Phase noise . . . 87
3.10 Laser phase noise model . . . 88
3.11 Impact of phase noise on the photocurrent . . . 89
3.12 Signal-to-noise ratio (SNR) . . . 91
3.12.1 SNR against linewidth $\Delta\nu$ . . . 92
3.12.2 SNR against measurement period T . . . 93
3.12.3 SNR against receiver aperture D_{rx} . . . 94
3.12.4 SNR against environment alpha and target reflectivity . . . 95
3.13 Target detection beyond the laser coherence length . . . 95
3.14 Chapter Conclusion . . . 99

4 Realization of a silicon photonic FMCW LIDAR 101
4.1 Layout and characterization overview . . . 101
4.2 FMCW LIDAR circuit overview . . . 104
4.3 Grating couplers . . . 105
4.4 MMI . . . 107
4.5 90° optical hybrid . . . 108
4.5.1 Insertion loss . . . 108
4.5.2 Imbalance . . . 109
4.5.3 CMRR . . . 109
4.5.4 Phase errors . . . 110
4.5.5 90° hybrid summary . . . 112
4.6 Photodiodes . . . 112
4.6.1 Ge photodiode . . . 112
4.6.2 III-V photodiodes . . . 115
4.7 The semiconductor optical amplifier . . . 116

4.7.1 SOA gain . . . 116
4.7.2 SOA noise figure . . . 118
4.8 Low linewidth tunable laser . . . 120
4.8.1 The tunable laser structure . . . 120
4.8.2 Grating coupler measurement . . . 122
4.8.3 Ring filter characterization . . . 124
4.8.4 Tunability measurement . . . 126
4.8.5 Linewidth measurement . . . 127
4.8.6 Results and discussion . . . 128
4.9 DBR laser . . . 130
4.10 Frequency chirp with IQ modulator . . . 134
4.11 Beam scanning unit . . . 141
4.11.1 The structure . . . 142
4.11.2 Characterization overview . . . 143
4.11.3 Grating coupler measurement . . . 143
4.11.4 Heater characterization . . . 144
4.11.5 Switch insertion loss . . . 145
4.11.6 Heater electrical power consumption . . . 146
4.11.7 Crosstalk . . . 146
4.11.8 Power stability . . . 147
4.11.9 AC characterization . . . 147
4.12 Chapter conclusion . . . 150

5 Conclusion and perspectives **151**
5.1 Conclusion . . . 151

Bibliography **154**

List of publications **168**

List of Figures

1 Principe du LIDAR FMCW utilisant une forme d'onde triangulaire. FFT : transformée de Fourier rapide. 8
2 Architectures LIDAR FMCW avec un amplificateur optique à semiconducteurs (SOA). 90/10 : diviseur 90%-10% ; BPD : photodiodes équilibrées. 9

1.1 Levels of driving automation from the Society of Automotive Engineers (SAE) [6]. 28
1.2 Projected growth of the LIDAR market (from [8]). 29
1.3 Types of sensors in ADAS (Nidec Corporation). 29

2.1 DToF principle. 33
2.2 AMCW principle. 34
2.3 FMCW principle. 35
2.4 Range resolution. 36
2.5 Field of View. 37
2.6 Atmospheric extinction coefficient calculated for 905 nm and 1550 nm wavelengths and typical atmospheric conditions [37]. 40
2.7 Maximum Permissible Exposure (MPE) for the human eye as a function of wavelength and for different pulse durations [10]. 40
2.8 Illustration of an autonomous vehicle consisting of multiple sensors. . 41
2.9 Illumination techniques classification. MEMS: Microelectromechanical systems; OPA: Optical Phased Array; FPSA: Focal Plane Switch Array; LC: Liquid Crystal. 43
2.10 Schematic of a) a flash LIDAR and b) a scanning LIDAR. 43
2.11 Schematic of a 1D Linear Uniform OPA. 45
2.12 Simulated OPA radiation pattern for several values of β, $N = 32$ and $d = \lambda/2 = 775$ nm. 46
2.13 Simulated angular resolution for several channel count N, $\beta = 0°$ and $d = \lambda/2$. SLSR: Side Lobe Suppression Ratio. 47
2.14 Schematics and simulated normalized radiation patterns for an OPA with a channel spacing a) $d = \lambda/2$ and b) $d = 3\lambda/2$. The channel count is $N = 32$ in both plots. GC: grating coupler. 48
2.15 OPA tradeoff taken from [58]. 50
2.16 Schematic of a 8-emitter FPSA. 52
2.17 Simulation of angular resolution and FoV of a 1024-emitter 1D FPSA with d=20μm, as a function of focal length. 53
2.18 Gaussian beam approximation. 53
2.19 Comparison between a) FPSA and b) OPA implementations. 58

2.20 III-V material integration with silicon photonics wafer using a) photonic package assembly [92] b) flip chip bonding of processed III-V dies [93], c) micro-transfer printing [94], d) Hetero-epitaxial growth [95] and e) III-V/Si wafer or die bonding. 62
2.21 Scintil 'Backside on Box' fabrication process [102]. 64

3.1 Schematic of the FMCW building blocks. 67
3.2 Coherent receiver using 3 dB coupler. BPD: balanced photodiodes. . 68
3.3 Coherent receiver using a 90° optical hybrid. BPD: balanced photodiodes. 70
3.4 Representation of a sawtooth linear frequency chirp a) in time domain and b) in the Fourier domain. 73
3.5 FMCW LIDAR principle using sawtooth waveform. FFT: fast Fourier transform. 74
3.6 FMCW LIDAR principle using sawtooth waveform in the presence of Doppler effect. 75
3.7 FMCW LIDAR principle using triangular waveform. FFT: fast Fourier transform. 76
3.8 Schematic of a simple transimpedance amplifier (TIA) circuit connected to a photodiode (PD) under illumination. Op amp: operational amplifier. 77
3.9 Chirp resolution comparison. 78
3.10 a) Example of automotive LIDAR environment specifications and b) contributions to the free space loss. 80
3.11 Attenuation due to polarization. 80
3.12 Polarization diverse coherent receiver. PBS: polarization beam splitter. 81
3.13 Illustration of nonlinear distortion on the beat signal. 81
3.14 Schematic of the FMCW LIDAR tile. 90/10: 90%-10% splitter; BPD: balanced photodiodes. 82
3.15 FMCW LIDAR architectures with a booster semiconductor optical amplifier (SOA) added at the TX. 90/10: 90%-10% splitter; BPD: balanced photodiodes. 84
3.16 Monte Carlo simulations to validate the Lorentzian shape of the phase noise considering a laser white frequency noise model with N=10 and N=1000 iterations for averaging, and a laser linewidth $\Delta\nu$ of 1 MHz. 89
3.17 Simulation of FMCW LIDAR photodetected current spectra for different target ranges, considering a laser linewidth of 1 MHz, corresponding to a laser coherence length of 95m (47.5 m single-trip, 95 m round-trip). 90
3.18 SNR against laser linewidth for several target ranges. 93
3.19 SNR against target range for several measurement periods T. 93
3.20 SNR against target range for several receiver apertures D_{rx}. 94
3.21 SNR against target range for several a) environmental conditions and b) target reflectivities ρ. 95
3.22 Monte Carlo model building blocks. PER: periodogram; LLSE: Lorentzian least squares estimation; iter: iteration. 96
3.23 PER for coherent and incoherent regimes based on 100 Monte Carlo simulations, 1 MHz laser linewidth. 97

3.24 Range precision as a function of target range and laser linewidth and for a target velocity v_r = 60 km/h= 16.7 m/s. 98
3.25 Velocity precision as a function of target range and laser linewidth and for a target velocity v_r = 60 km/h= 16.7 m/s. 98

4.1 Steps for the elaboration of the demonstrators. 101
4.2 Example of a layout consisting in two components made of 4 different layers. 102
4.3 Schematic of wafer level characterization setup. FA: fiber array. . . . 102
4.4 Picture of the automatic probe tester with a fiber array (FA) and two DC probes. 103
4.5 Schematic of the FMCW LIDAR core circuit architecture with III-V/Si booster SOA, SiN 2x2 MMI coupler and Ge photodiodes. 105
4.6 Schematic of a grating coupler. 106
4.7 Measured transmission response of one SiN grating coupler over 10 dies. 106
4.8 Wafer level characterization of SiN grating couplers on 10 dies showing a) the peak wavelength and b) the insertion loss at the average peak wavelength. 107
4.9 Measured transmission of a 2x2 SiN MMI. IL: insertion loss. 107
4.10 Test structure for measuring the 90° hybrid insertion loss, imbalance and CMRR. 108
4.11 Measured insertion loss of the SiN 90° hybrid over 10 dies. 108
4.12 Measured imbalance of the SiN 90° hybrid at 1564 nm and over 10 dies. 109
4.13 Measured CMRR of the SiN 90° hybrid at 1564 nm and over 10 dies. 110
4.14 Test structure for measuring the 90° hybrid phase error. DLI: delay line interferometer. 110
4.15 Spectral response of the four hybrid outputs using the error test structure. 111
4.16 Histogram of a) E1-E4 and b) E2-E3 phase errors. 111
4.17 Optical microscope view of two vertical PIN Ge photodiodes in balanced configuration. P and N contacts are also indicated. 113
4.18 Ge photodiode responsivity as a function of wavelength for several reverse bias. 114
4.19 Measured I-V curve of the Ge photodiode. 114
4.20 Measured CMRR of the Ge balanced photodiodes at 1510 nm wavelength for several PD biases. 115
4.21 Microscope image of the fabricated III-V/Si balanced photodiodes. . . 116
4.22 Dedicated test structure for the measurement of SOA gain. OSA: Optical Spectrum Analyzer, PM: Power meter. 116
4.23 Measured transmission loss of the “reference path” from (“GC in” to “GC out1”) at several chip temperatures. 117
4.24 SOA VI curves at 20°C, 40°C and 60°C. 117
4.25 SOA gain against chip temperature at 1510, 1530 and 1550 nm for 80 mA, 100 mA and 120 mA SOA currents. The SOA input power is set to -2 dBm (top) and -20 dBm (bottom). 118
4.26 Measurement of P_{ASE} and G for noise figure extraction. 119
4.27 Schematic of the tunable laser. 121

4.28 a) 3D view of the packaged tunable laser using vertical fiber coupling and b) microscope image of the ring resonators. 122
4.29 Through port transmissions of ring 1 and ring 2. 123
4.30 a) Transmission between 3 and 5. Light path includes two grating couplers, through port of ring 2 and through port of ring 1. The superposed spectra correspond to a voltage sweep on ring 1 b) Insertion loss of one grating coupler based on cubic interpolation of the measured envelope in a). 123
4.31 Drop port measurements of a) ring 1 for several ring 1 voltages and b) ring 2 for several ring 2 voltages. 124
4.32 Individual measurement response of ring 1 (blue) in out 5, ring 2 (green) in out 2 and computed filter response ring 1 + ring 2 (red). . 124
4.33 Measurement of the filter response on output 3 with a) a voltage sweep on ring 1 and b) a voltage sweep on ring 2. 125
4.34 Ring heaters electrical power consumption. 126
4.35 Superposition of spectra measured at the output 3 by tuning the wavelength across the C band (1530 nm-1565 nm) SMSR greater than 35 dB. 126
4.36 Linewidth measurement setup based on the Delayed Self Heterodyne Interferometer technique. EDFA: Erbium- Doped Fiber Amplifier; PC: Polarization Controller; AOM: Acousto-Optic Modulator; ESA: Electrical Spectrum Analyzer. 127
4.37 Linewidth measurement of a reference DFB laser (Alcatel 1905 LMI). 128
4.38 Linewidth measurement of the tunable laser fitted with pseudo-Voigt function. 129
4.39 Spectra measured at the OSA for several TEC temperatures and at 82 mA SOA current. 130
4.40 DBR laser measurement setup. 131
4.41 Microscope image of the fabricated III-V/Si DBR laser. 131
4.42 Insertion loss (IL) of one SiN GC over 7 dies. 132
4.43 LIV curve of the DBR laser measured at “GC 1” over 7 dies. 132
4.44 Measured a) wide wavelength span spectrum and b) narrow wavelength span spectrum for the DBR laser in die 6. 133
4.45 Measured spectra at 150 mA of the DBR laser over the 7 dies. 133
4.46 Picture of the PIC package with its motherboard. 135
4.47 Schematic of our FMCW LIDAR frequency synthesis scheme. The I and Q RF signals generation are applied to the PIC composed of an IQ modulator and III-V/Si SOA. 136
4.48 Measurement setup to evaluate the chirp linearity from the IQ modulator. PC: polarization controller; SOA: semiconductor optical amplifier; DL: delay line; PD: photodiode; TIA: transimpedance amplifier; DSO: digital storage oscilloscope. 137
4.49 Measured a) VCO command signal, $V_{tuneVCO}$(t) and b) time domain beat signal, s_{beat}(t) on the DSO. 139
4.50 a) Retrieved instantaneous frequency profile over 5%-95% of the up-ramp period T. b) Chirp nonlinearity obtained by subtracting the instantaneous frequency profile with a linear fit. 140
4.51 Measured FFT spectra for several fiber lengths. 140

4.52 Beat frequency against fiber length showing high linear dependency (R^2=0.999). 141
4.53 Schematic of the 4-emitter focal plane switch array circuit. GC: grating coupler; S1: switch 1; S2: switch 2; S3: switch 3; PD: photodiode; tap: 10%/90% tap. 142
4.54 Microscope view of the fabricated 4-emitter FPSA circuit. GC: grating coupler; PD: photodiode; S: switch. 143
4.55 Measured transmission of one SiN grating coupler. 144
4.56 Measured IV curves of the three of thermo-optic phase shifters. . . . 144
4.57 Measured optical power at the output of switch 1 "GC G" against the electrical power of heater 1. $P_{2\pi}$ is the required heater electrical power to produce a 2π phase shift. 145
4.58 a) Link budget to compute the IL of switch 1 and b) table of corresponding powers and IL. 145
4.59 a) Measured photocurrent at the output of the internal photodiode PD_{2L} (in log scale) and b) produced phase shift as a function of electrical power consumed by the switch 2 heater. 146
4.60 Evolution of heater 1 electrical power consumption over a 10 minute time period. 147
4.61 AC measurement setup to assess the switch 2 temporal response. . . . 148
4.62 Measured temporal square voltage input waveform and output voltage response. 148
4.63 Measurement of the response measurement of switch 2 showing 26 μs rise time. 149

List of Tables

1 Aperçu des éléments constitutifs du LIDAR FMCW. GC : coupleur surfacique de réseau ; MMI : coupleur d'interférence multimode ; PD : photodiode ; SOA : amplificateur optique à semiconducteurs ; DBR : réseau de Bragg distribué. 10

2.1 Specifications for an automotive FMCW LIDAR. 42
2.2 State of the art OPA demonstrations. (NA: not available). 51
2.3 State of the art FPSA demonstrations. NA: not available; SiPh: Silicon Photonics 56
2.4 Summary table of the key formulas for OPA and FPSA and the specifications. 57
2.5 Table of the computed parameters for the comparison between 1D OPA and 1D FPSA described in Table 2.4. 59
2.6 Summary table of state of the art FMCW LIDAR demonstrations. wo : without. 65

3.1 Summarize of our model inputs and outputs. 78
3.2 Table of air attenuation factor values from [38] 79
3.3 Link budget of the FMCW LIDAR system. 82
3.4 Link budget of the FMCW LIDAR system using a booster SOA. . . . 84
3.5 Table of coherence length values L_c for several laser linewidths $\Delta\nu$. . 88
3.6 Summary of formulas for SNR computation at the beat frequency. . . 91
3.7 Summary of parameters for SNR simulation against linewidth. 92
3.8 System specifications. 97
3.9 Table of SiPh component specifications for an automotive FMCW LIDAR. 100

4.1 Overview of the FMCW LIDAR building blocks. GC: grating coupler; MMI: MultiMode Interference coupler; PD: photodiode; SOA: semiconductor optical amplifier; DBR: Distributed Bragg Grating. . . 104
4.2 Comparative table summarizing the performances of our 90° hybrid with IC-TROSA specifications and a reference publication [137]. . . . 112
4.3 Materials used as photodiodes with their bandgap and typical wavelengths of operation. 113
4.4 Summary table of the SOA gain and noise figure measured for -2 dBm and -20 dBm SOA input powers, at λ=1510 nm and with a SOA current of 120 mA. The temperature is 20 °C. 119
4.5 Computed optical power budget of the chirp linearity measurement setup. 138
4.6 Measured crosstalk on the four emitter FPSA circuit. 147

List of acronyms

AC Alternating Current.

ADAS Advanced Driver Assistance Systems.

AMCW Amplitude-Modulated Continuous-Wave.

AOM Acousto Optic Modulator.

BPD Balanced PhotoDiode.

CMRR Common Mode Rejection Ratio.

CRLB Cramer-Rao Lower Bound.

DBR Distributed Bragg Reflector.

DC Direct Current.

DToF Direct Time-of-Flight.

EDFA Erbium-Doped Fiber Amplifier.

ESA Electrical Spectrum Analyzer.

FA Fiber Array.

FFT Fast Fourier Transform.

FMCW Frequency-Modulated Continuous-Wave.

FoV Field of View.

FPSA Focal Plane Switch Array.

FR Frame Rate.

FWHM Full Width at Half Maximum.

GC Grating coupler.

I/O Input/Output.

ICTROSA Integrated Coherent Transmitter-Receiver Optical Subassembly.

IL Insertion Loss.

IToF Indirect Time-of-Flight.

LC Liquid Crystal.

LIDAR Light Detection And Ranging.

LLSE Lorentzian Least Squares Estimation.

LO Local Oscillator.

MEMS Micro Electro Mechanical Systems.

MMI Multi Mode Interference.

MPE Maximum Permissible Exposure.

MPW Multi Project Wafer.

MZI Mach-Zehnder Interferometer.

NEP Noise Equivalent Power.

NF Noise Figure.

OPA Optical Phased Array.

OSA Optical Spectrum Analyzer.

PBS Polarization Beam Splitter.

PD PhotoDiode.

PER Periodogram.

PIC Photonic Integrated Circuit.

PLL Phase-Locked Loop.

RADAR Radio Detection And Ranging.

RIN Relative Intensity Noise.

RX Received.

SAE Society of Automotive Engineers.

SMSR Side Mode Suppression Ratio.

SNR Signal-to-Noise Ratio.

SOA Semiconductor Optical Amplifier.

SOI Silicon On Insulator.

SONAR Sound Detection And Ranging.

TIA TransImpedance Amplifier.

TX Transmitted.

Chapter 1

Introduction

Motivated by the increasing demand for intelligent and autonomous systems, perceiving the environment with high precision has become a necessity. Researchers have been working for years on technologies that reproduce and enhance the five human senses to get rid of alienating labour and mitigate human risks. For instance, the democratization of imaging systems is an excellent substitute to the human sight in many applications. The automotive industry has been massively investing in advanced driver assistance systems (ADAS) to mitigate the risk of human error in vehicles and improve traffic jams in urban areas. In 2019, the National Highway Traffic Safety Administration (NHTSA) reported 36,096 american deaths due to automotive accident with 94% due to human error [1]. Today, recent cars are equipped with ADAS systems such as blind spot sensors, rearview cameras, lane departure warning systems, adaptive cruise control or automatic parking systems. To quantify the degree of human intervention in the driving task, the Society of Automotive Engineers (SAE) has edited 6 levels of driving automation as shown in Fig. 1.1.

Level 5 is the ultimate objective, as the vehicle would be completely autonomous under all conditions without any driver intervention. The race to level 5 full automation is ongoing and the development of high precision sensors will be a key enabler to reach this goal. A fully autonomous vehicle should detect and identify targets in real-time in order to predict their actions. To do so, the XYZ spatial data of surrounding targets are essential. Depth perception (Z) has been mastered with stereo vision cameras or detection and ranging systems [2]. Stereo vision is based on the human binocular vision, as it makes use of two cameras that takes the same image from different positions. The depth information (Z) is computed by comparing the location of the two images, resulting in a disparity map [3][4]. Stereo vision camera is a low cost solution but it has some limitations such as long computation time, poor resolution at long distances and can be blinded by sun glare, rain, fog and snow conditions. On the other hand, SOund Navigation And Ranging (SONAR), Radio Detection And Ranging (RADAR) and Light Detection And Ranging (LIDAR) emit acoustic-waves, micro-waves and light-waves, respectively, to measure the depth information [5]. By collecting the echo signal that is reflected on the target, these systems can measure the target range and velocity. SONAR is widely used in water for tracking targets, as the sound travels farther and faster than in air. On the contrary, RADAR uses shorter wavelength that are quickly absorbed in water but propagates over long distances in air.

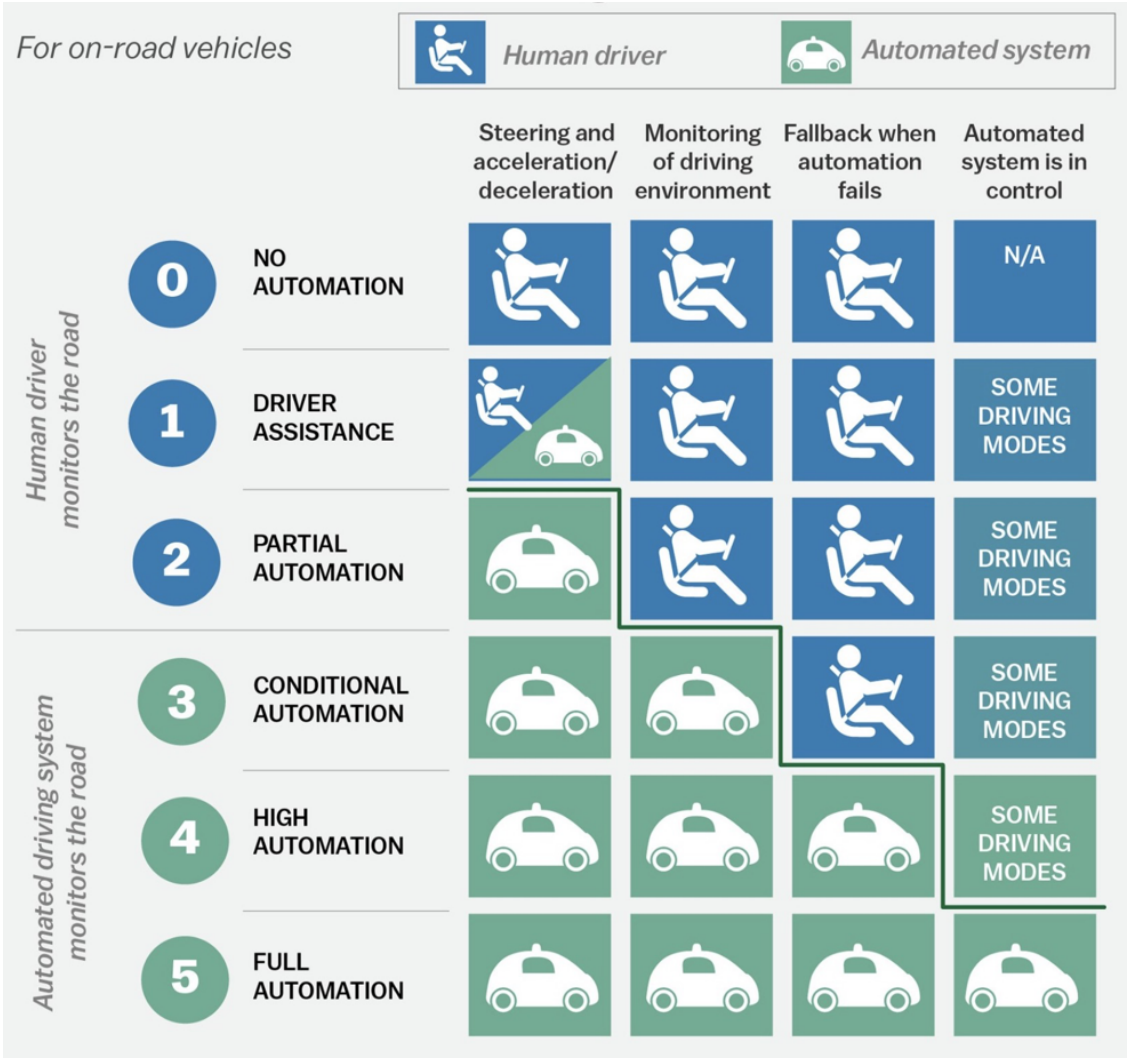

Figure 1.1: Levels of driving automation from the Society of Automotive Engineers (SAE) [6].

LIDAR has drawn a lot of attention over the past few years for its ability to provide high precision and high resolution 3D point clouds. LIDAR provides superior resolution compared to RADAR owing to the wavelength of operation. This enables to discriminate very closely spaced elements. As mentioned, camera can be blinded under harsh weather and cannot detect targets at hundreds of meters compared to LIDAR. Therefore, LIDAR is of great interest for a broad range of applications such as unmanned vehicles, robotics, topography, space observation or anemometry [7].

Recently, massive investments on LIDAR technology have been made by automotive players (Volvo, General Motors, Audi, Volkswagen, BMW...). The Fig. 1.2 shows the projected growth of the automotive LIDAR market from 2019 to 2030 and expected SAE levels of automation. The objective of these investments is to decrease the cost of LIDAR, which could lead to a massive use of this type of sensors and provide new types of data that could help reaching higher levels of automation.

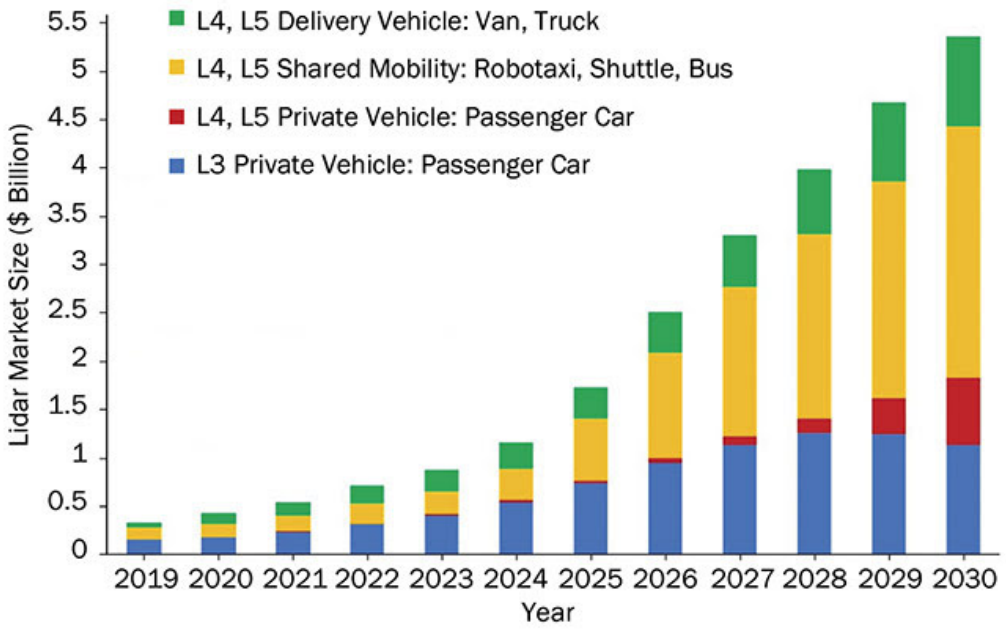

Figure 1.2: Projected growth of the LIDAR market (from [8]).

Cameras, RADAR, LIDAR and other sensors all have strengths and limitations, and there is a consensus on the fact that automation is possible with data fusion, i.e. by combining data from multiple sensors to increase redundancy as shown in Fig. 1.3.

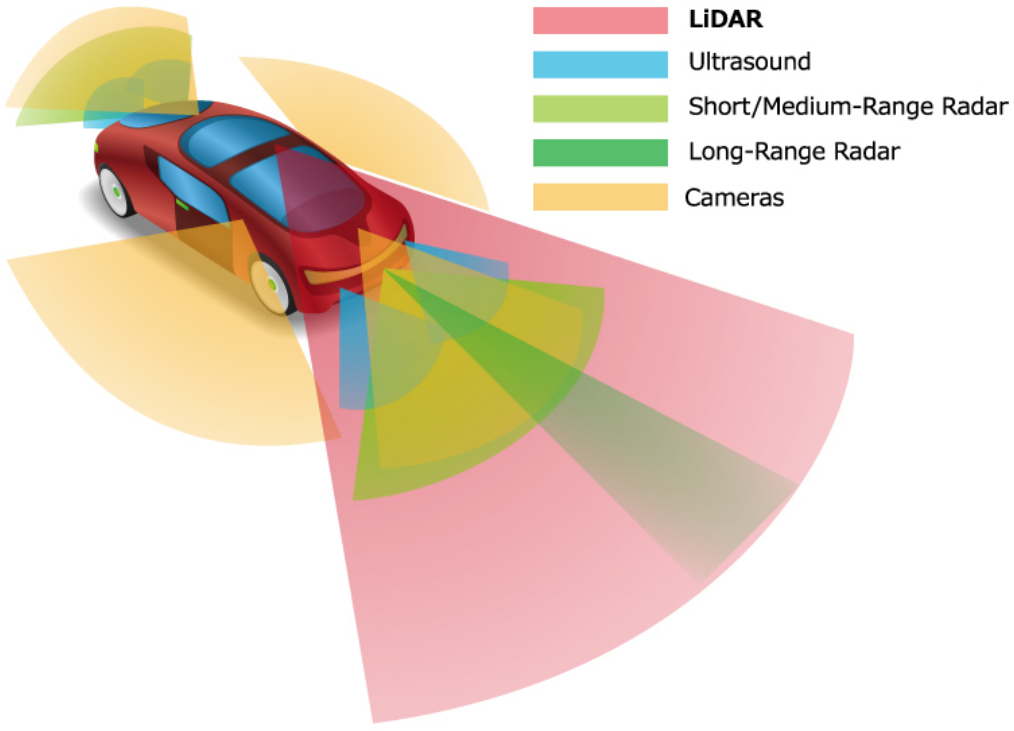

Figure 1.3: Types of sensors in ADAS (Nidec Corporation).

There are several types of LIDAR systems such as Direct Time-of-Flight (DToF), Amplitude-Modulated Continuous Wave (AMCW) or Frequency-Modulated Continuous Wave (FMCW) LIDAR. Compared to the DToF and AMCW, FMCW LIDAR provides high-resolution distance and velocity measurements without requiring fast electronics. While today, DToF is the most popular automotive LIDAR architecture, it is likely to evolve to FMCW LIDAR due to the benefits of coherent detection such as immunity to interferences, extra gain due to coherent detection and lower photoreceiver electrical bandwidth. Hence, the focus of this thesis is FMCW LIDAR systems for automotive applications.

In 1971, a decade after the invention of the laser by Maiman, NASA Apollo 15 mission revealed the first high resolution image of the moon surface using a LIDAR. Nowadays, the development of semiconductor lasers and optical integrated circuits has offered new perspectives for LIDAR use. Self-driving cars, robotics, consumer or medical applications require compactness, low power consumption, robustness to thermal variations and vibrations and reasonable cost. As a consequence, the integration of LIDAR becomes necessary.

However, the chip-scale integration of LIDAR is challenging. The technology platform should combine efficient laser sources, optical amplifiers, modulators, routing functions and receivers. In addition, an illumination module should direct the LIDAR signal towards the region of interest and collect the echo signal being reflected on a target. Mechanical scanners are mainly used in present LIDAR systems but they have limitations compared to emerging integrated approaches. Indeed, on-chip beam scanning solutions can offer lower power consumption, compact footprint, less failure due to mechanical fatigue and much higher scanning speeds. In addition, very large arrays of emitters and receivers can be fabricated enabling high resolution imaging and wide field-of-view.

Over the past 50 years, the development of the microelectronics industry has enabled the fabrication of lithographic feature size of few tens of atoms. It is legitimate to wonder if such cutting edge tools and processes can be adapted for the fabrication of silicon-based photonic chip. This is the ultimate goal of silicon photonics, which aims at combining the best of photonics in a CMOS compatible process [9]. Indeed, photonics is gradually taking hold in foundries with the aim of guiding, modulating, emitting and detecting light onto silicon wafers. Leveraging the mature CMOS industry, Photonic Integrated Circuits (PIC) can be fabricated with high level of integration, in high volumes and low cost with high yield.

Motivated by the increasing data traffic of our connected societies, the rise of silicon photonics over the past decades has been motivated by the realization of optical transceivers for data communication at 1310 nm and 1550 nm wavelengths. Today, foundries integrate CMOS compatible materials such as silicon nitride (SiN) or germanium (Ge) onto silicon on insulator (SOI) wafer to realize various optical functions. The major challenge has been to integrate III-V materials on silicon to build efficient and low-cost lasers and optical amplifiers. Among the proposed solutions to overcome this obstacle, heterogeneous integration of III-V materials onto silicon was pioneered by UCSB and CEA-Leti, IMEC and III-V lab. Based on CEA-Leti III-V/Si bonding technology, Scintil Photonics developped a technology called Back-Side-on-BOX laser integration that enables the monolithic integration

of III-V/Si lasers and amplifiers, germanium waveguide-photodiodes, silicon active and silicon nitride passive devices on the same photonic integrated circuit (PIC). This integration platform enables a high level of integration and parallelism and can sustain high volumes demand.

In this thesis, we evaluate the feasibility and the challenges related to the integration of FMCW LIDAR components and circuits on our III-V/Si integration platform.

In chapter 2, we introduce the general principle of LIDAR. Then, we present an overview of the main LIDAR architectures and their performance metrics. We also examine the different illumination module families based on their mechanism and their level of integration. In addition, a quantitative comparison between two major chip-scale beam scanning solutions is given. Based on this, we conclude this chapter on the benefits and challenges related to the integration of LIDAR systems on chip. By considering a realistic automotive scenario, we deliver a set of LIDAR system specifications.

In chapter 3, we introduce the theory behind coherent receivers to understand the detection principle of FMCW LIDAR. We then describe the main modulation waveforms applied to FMCW LIDAR sources and the associated target range and velocity extraction method. The sizing of receiver bandwidth is also discussed. Then, we present a model to derive the link budget and signal-to-noise ratio (SNR) of the FMCW LIDAR system. While we discuss all the noise contributions in the system, we emphasize the importance of the laser phase noise and its influence on the received LIDAR signal. Based on this model, we connect the LIDAR system specifications to photonic component specifications.

Chapter 4 reports on the realization of a FMCW LIDAR photonic chip fabricated on Scintil Photonics III-V/Si technology platform. First, we present the characterization environment enabling wafer level testing. Then, we describe the structure of a packaged tunable laser emitting in the C band, and we report on the linewidth measurement. We also present our measurements on linear frequency chirps generation using an on-chip IQ modulator followed by a III-V/Si SOA. Afterwards, the SOA is characterized and the gain curve is obtained at different temperatures and laser operating wavelengths. Besides, we tested a coherent receiver made of SiN 90° hybrid and Ge balanced photodiodes. Finally, we demonstrate the switching function on a 4 emitter Focal Plane Switch Array (FPSA) circuit.

Finally, we conclude and share some perspectives for this work in chapter 5.

Chapter 2

Fundamentals of Light Detection And Ranging

2.1 Principle of LIDAR

Light Detection And Ranging (LIDAR) is a 3D sensing technology that recovers the depth information from reflections on objects. While its counterparts RADAR and SONAR employ radio waves and acoustic waves, LIDAR uses a laser as the emitter. Transmit and receive optics can be used to direct the LIDAR beam towards the targets and maximize the collection efficiency, respectively. A LIDAR system is also composed of a receiver that detects the reflected signal. Electronic processing converts the received signal into depth information.

LIDAR development was enabled by the invention of laser by Maiman in 1960 on a ruby crystal. Initially, military and observation (ground, atmosphere, ocean and space) LIDARs were developped using CO2 and Nd:YAG lasers at $10.6\mu m$ and $1.064\mu m$ respectively [10]. For instance, in 1971, NASA Apollo 15 mission revealed the first high resolution LIDAR images of the moon surface.

With the advances in the semiconductor industry, LIDAR has evolved in terms of compactness, power consumption, robustness, and cost. It is gaining interest for self-driving cars, robotics, consumer and medical applications [7]. In this chapter, we will focus on automotive applications with the aim of detecting targets at several hundreds of meters.

2.2 LIDAR architectures

In this section, we focus on the 3 main integrated LIDAR architectures which are Direct Time-of-Flight (DToF), Indirect Time-of-Flight (IToF) or Amplitude Modulated Continuous Wave (AMCW), and Frequency Modulated Continuous Wave (FMCW) LIDAR. In DToF, the LIDAR emits short pulses and collects the echo signal coming from reflection on targets. This type of LIDAR uses direct detection receiver which converts the incoming optical power into intensity. In the AMCW and FMCW, the LIDAR continuously emits and receives a modulated waveform. AMCW uses a phase detector to compare the transmitted and received signals. FMCW uses coherent detection where the received signal is mixed with a reference

signal to produce a beat tone. Coherent detection is beneficial for a Signal-to-Noise Ratio (SNR) point of view [11].

Another promising architecture is called chaotic LIDAR (CLIDAR). It makes use of the nonlinear dynamics of semiconductor lasers to produce chaotic light as the LIDAR source [12]. The detection of targets is obtained by correlating the echo signal being reflected on the object, with a reference signal. CLIDAR systems have been proposed in [13][14] with the aim of improving the isolation against the background light and enhance the system sensitivity. Although CLIDAR is promising over several aspects, this thesis will focus on the 3 above-mentioned architectures.

2.2.1 DToF

In Direct Time of Flight (DToF) LIDAR, short pulses of light (few ns duration) are transmitted (Tx) and collected (Rx) after reflection on a target Fig. 2.1. The round-trip time, τ between the Tx pulse and Rx pulse is proportional to the target range R through:

$$\tau = \frac{2R}{c} \tag{2.1}$$

where c is the speed of light.

DToF LIDAR relies on direct detection. The baseband electrical signal produced by the photodiode is proportional to the input optical power which contains external perturbations (sun, background lights) and $1/f$ low frequency noise. Filters can be used to clear the frequency spectrum from such noises. As seen on Fig. 2.1, at the receiver, a Time to Digital Converter (TDC) converts the pulse time of arrival into a digital signal. The LIDAR range resolution therefore depends on the time counting resolution.

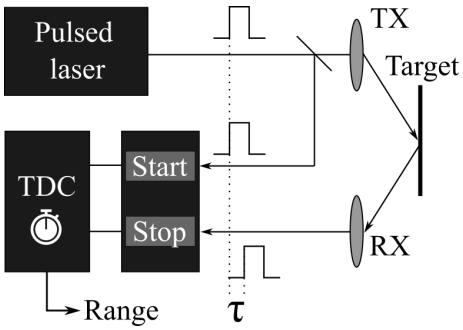

Figure 2.1: DToF principle.

DToF LIDARs operating up to several hundreds of meters have been reported [15] [16]. However, due to the laser energy spread after reflection on diffusive targets, high power pulse in combination with high sensitivity receiver are needed to ensure a certain detection probability. As a consequence, DToF LIDAR requires high performance receivers such as Avalanche PhotoDiodes (APDs), Single Photon Avalanche Diodes (SPADs) or Silicon PhotoMultiplier (SiPM) that ensure single photon sensitivity and picosecond timing resolution [16]. Hence, DToF LIDAR relies on high speed electronics. Timing jitter which corresponds to the statistical variation of the temporal response of the devices must also be minimized for precise

range estimation. Indeed, any uncertainty in the detector impulse response will lead to a variation of the time of flight and alter the image. In [17], a timing jitter predictive model is proposed in order to improve the temporal response of the SPAD devices.

2.2.2 iToF or AMCW

In indirect Time of Flight (iToF) or Amplitude Modulated Continuous Wave (AMCW) LIDAR, a continuous, amplitude modulated laser signal (typically with a modulation frequency of a tenth of MHz) is sent to the target. As shown in Fig. 2.2, a phase shifted signal is detected at the receiver using direct detection. There are also AMCW LIDAR using heterodyne detection. When direct intensity modulation of a laser source is realized, the bandwidth is limited to a few GHz and high speed photodiode is necessary at detection. The target range, R is retrieved from the phase difference ($\Delta\Phi$) between Tx and Rx AMCW signals using [18][19]:

$$R = \frac{c}{2}\frac{\Delta\Phi}{2\pi f_m} \tag{2.2}$$

where f_m is the amplitude modulation frequency.

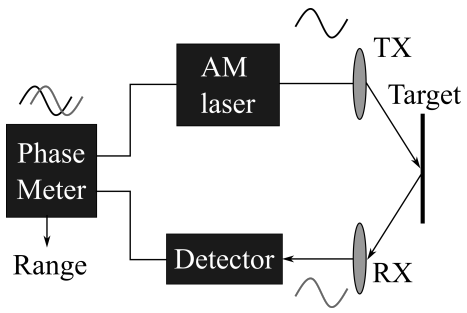

Figure 2.2: AMCW principle.

AMCW LIDAR is a mature technology which is already commercialized [20] [21] [22] [23]. More details on the power budget derivation and the main figure of merits of AMCW LIDAR can be found in [24].

However, AMCW LIDAR suffers from phase wrapping, i.e. the signal phase is constrained between 0 and 2π to prevent from any ambiguous range estimation. From Eq. (2.2), it can be seen that the modulation frequency, f_m sets the distance for the emitted wave to complete a full phase cycle. In addition, the modulation frequency, f_m also determines the range resolution. The larger the modulation frequency, f_m, the better the resolution but the shorter the unambiguous range measurement. Therefore, the AMCW LIDAR architecture presents a trade-off between maximum unambiguous range detection and range resolution. As a consequence, AMCW LIDAR is usually used in short range indoor applications with tens of MHz modulation frequencies.

2.2.3 FMCW LIDAR

The architecture of a FMCW LIDAR is shown on Fig. 2.3. It consists of a frequency modulated (FM) or chirped laser and a coherent receiver. During each modulation

period, T the laser frequency is linearly chirped, starting from a frequency f_0 to a frequency f_1. The frequency excursion B is defined as $|f_1 - f_0|$ and the chirp rate s is defined as B/T. The FMCW signal hits a target and the reflected signal (Rx) is mixed with the FM laser used as a Local Oscillator (LO) onto the coherent receiver. The produced beat signal has a frequency f_b proportional to the target range R [25]:

$$f_b = s\frac{2R}{c} \tag{2.3}$$

where s is the slope of the frequency modulation.

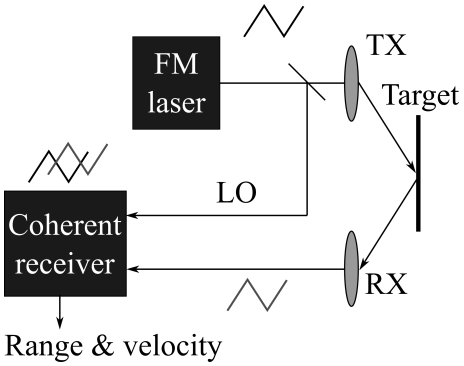

Figure 2.3: FMCW principle.

If the target is moving, two beat signals with distinct frequencies are produced during the up and down ramps. In this case, the radial velocity can also be obtained thanks to Doppler effect.

In FMCW LIDAR, coherent detection provides strong selectivity against background light and high sensitivity, making it suitable for long-range detection [26]. Moreover, coherent detection induces optical mixing during the detection process, which lowers the frequency of the detected electronic signal (i.e. the beat frequency), compared to DToF LIDAR and AMCW LIDAR. As a consequence, electronics circuits used in FMCW LIDAR receiver work at lower speed.

2.3 Performance metrics

2.3.1 Resolution

Resolution characterizes the ability of a LIDAR to distinguish closely spaced targets. There are two types of resolution:

1. Range resolution ΔR corresponds to the minimum resolvable distance between two targets in the same line of sight.

   It is given by [26]:

   $$\Delta R = \frac{c}{2B}, \tag{2.4}$$

   where B is the optical frequency excursion.

   The range resolution ΔR is related to the Full Width at Half Maximum (FWHM) of the received signal as depicted on Fig. 2.4.

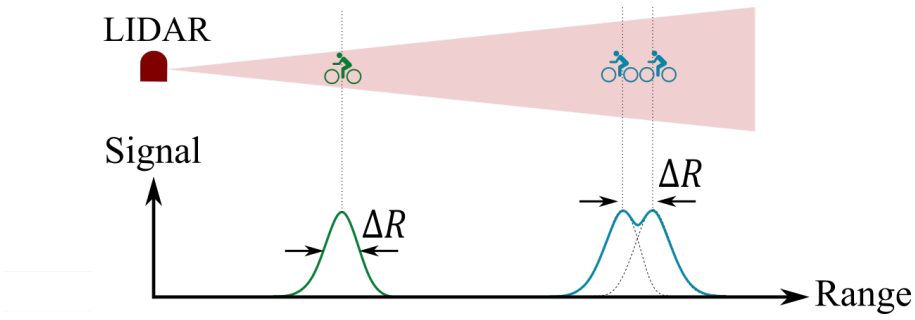

Figure 2.4: Range resolution.

2. Lateral or angular resolution θ is the ability of the LIDAR to separate two adjacent points:

   It is given by the Airy disk resulting from the diffraction by a circular aperture:

   $$\theta = 1.22\frac{\lambda}{d}, \tag{2.5}$$

   where λ is the wavelength and d is the aperture diameter.

   The Eq. (2.5) highlights the angular resolution improvement of LIDAR compared to RADAR systems. Optical waves with micrometer wavelength can achieve lateral resolutions of 0.1° with aperture sizes of only a few hundred micrometers that easily fits on a single chip. In RADAR, millimeter waves require aperture size of few meters in order to obtain the same angular resolution which is a limiting factor in many applications. CMOS cameras working in the visible spectrum region (380-750 nm), have excellent angular resolution (<0.1°) as long as lighting, air quality and contrast conditions are satisfied. Indeed, LIDAR are working in the μm wavelength region and can easily reach 0.1° angular resolution with aperture diameter d of few millimeters.

   Angular resolution can be converted into a image width, x for a target located at a distance R as :

   $$x = 2R\tan(\frac{\theta}{2}) \tag{2.6}$$

   A 0.1° angular resolution corresponds to 35 cm pixel size for a target range R of 200 m.

2.3.2 Range Precision

Range precision σ_R corresponds to the standard deviation of a series of repeated range measurements on the same target. It is related to the range resolution ΔR and the system Signal-to-Noise Ratio (SNR) [26] through:

$$\sigma_R = \frac{\Delta R}{\sqrt{SNR}} \tag{2.7}$$

High SNR enables to measure target ranges at precision much below the range resolution.

The Cramér-Rao lower bound (CRLB) obtained with Maximum Likelihood (ML) frequency estimation gives the best achievable range precision in the presence of white Gaussian noise [27] [28] :

$$CRLB_R = \frac{c}{4\pi B}\sqrt{\frac{3}{SNR}} \tag{2.8}$$

The $CRLB_R$ indicates that the theoretical precision limit of FMCW LIDAR ranging measurements is determined by the optical frequency excursion B and the SNR.

2.3.3 Field-of-View

Field of View (FoV) is used to describe the region of the environment that will be used for LIDAR detection as depicted on Fig. 2.5. FoV is given as a set of two angles corresponding to the horizontal (HFoV) and vertical (VFoV) angular spans. In automotive LIDAR, a typical FoV is 120° (HFoV) and 30° (VFoV).

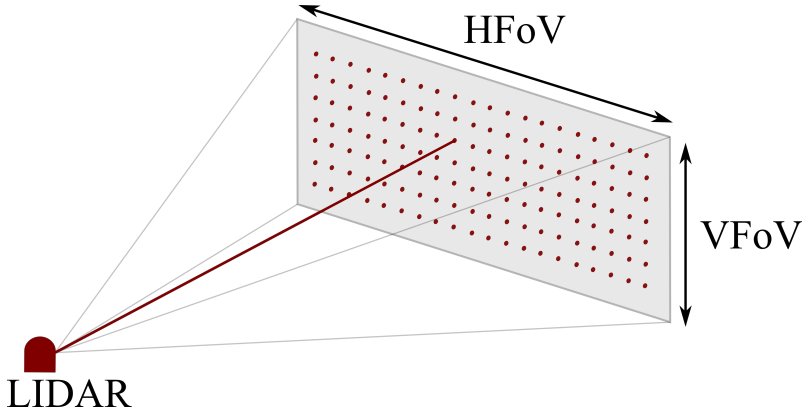

Figure 2.5: Field of View.

Considering the same angular resolution θ of 0.1° for the horizontal and vertical directions, the number of points P across the automotive LIDAR FoV is given by:

$$P = \frac{HFoV \times VFoV}{\theta^2} = 360,000 \tag{2.9}$$

2.3.4 Frame rate

The Frame Rate (FR) corresponds to the number of 3D pointcloud images (frames), with size defined by the number of point P, that can be produced by the LIDAR in one second. Typical automotive LIDAR frame rate is comparable to video frame rates i.e. 20-30Hz to avoid motion blur. Considering the automotive LIDAR case, this corresponds to 7.2-10.8 million pixels to adress in one second. Achieving such FR is challenging as it limits the time allocated to each point across the FoV which in turns reduces the SNR [29].

2.3.5 Operating range

The operating range refers to the maximum distance where a target with specified reflectivity can be detected.

The upper limit of the operating range is determined by unambiguous detection. Indeed, to avoid ambiguity between detected signals, one modulation period must be sent and received before transmitting the next one. The measurement time, T should therefore be larger than the maximum round trip time to the target τ_{max}. This sets a limitation on the operating range R_{max} to avoid ambiguity :

$$R_{max} = \frac{cT}{2} \tag{2.10}$$

where c is the speed of light.

Practically, the measurement time is chosen 5-10 times larger than the maximum round-trip delay τ_{max}.

2.3.6 Immunity to parasitic background

LIDAR detected signal can be affected by the background noise from the sun or other light sources. DToF are particularly sensitive to this parasitic signal as it relies on direct detection over a large bandwidth. Camera can be blinded due to sun glare making LIDAR essential to complement this technology.

While coherent LIDAR strongly reduces background noise, it is shown in [30] that solar radiation may also affect the LIDAR signal integrity through additive shot noise, beat noise with Local Oscillator (LO) and self mixing effects at the receiver. Interference with signals from other surrounding LIDARs may also be detrimental for detecting target. Therefore, depending on the application, a LIDAR should be able to operate under various ambient light conditions and other users scenario.

2.3.7 SNR comparison between DToF and FMCW LIDARs

For shot noise limited systems, the SNR in DToF and FMCW LIDARs are given by [11]:

$$SNR_{DToF} = \frac{RP_{RX}}{2q\Delta f} \tag{2.11}$$

$$SNR_{FMCW} = \frac{RP_{RX}}{q\Delta f} \tag{2.12}$$

where η is the photodiode responsivity, P_{RX} is the signal received on the photodiode, q is the electronic charge and Δf is the noise equivalent bandwidth of the detector.

Therefore, coherent detection offers a 3dB SNR gain compared to direct detection. This improvement is independant on the local oscillator power P_{LO} as long as the system reaches shot noise limited operation.

2.3.8 LIDAR output information

Most LIDAR systems provide a 3D pointcloud information of their environment i.e. the XYZ space informations. In some cases, additional informations can be extracted from LIDAR data such as the target radial velocity measured from the

Doppler effect, the calibrated target reflectivity or the polarization information for target material classification [31].

In the following, we discuss the importance of the LIDAR operating wavelength and eye-safety regulations.

2.4 Wavelength

Most integrated LIDAR systems operate in the Near InfraRed (NIR) region of the electromagnetic spectrum (0.78-2.5 μm). In this way, the LIDAR systems does not interfere with other sensors such as cameras in the visible spectrum or RADAR and is invisible to human eye. Within the NIR wavelength region, LIDAR systems mainly operates in two windows : 905 nm and 1550 nm.

At 905 nm, low-cost silicon photodetectors are used as this wavelength corresponds to their maximum sensitivity. Low cost pulsed laser diode are also available at this wavelength.

At 1550 nm, silicon is transparent and is replaced by III-V or Germanium photodiode. The sources are also made out of III-V materials such as InP, InGaAs, GaAs. The use of such materials increases the overall cost of the LIDAR system compared to 905 nm. Hopefully, the data communication C band (1530–1565 nm) that corresponds to the minimum transmission loss in optical fiber has been studied for decades, enabling the development of sources, detectors, passive components for integrating transceivers on silicon wafers [32].

For atmospheric, clouds and wind measurements, LIDAR using the Nd:Cr:YAG laser at 1064 nm and 532 nm by frequency doubling, have been extensively used [33]. For inter-satellite communications, wavelength within the 830-1550 nm window have been used. 1550nm wavelength enables higher data rates communications (>10 Gbps) thanks to the increase of SNR using Erbium-Doped Fiber Amplifier (EDFA).

Another important region for LIDAR is mid-IR (3-50 μm) as it corresponds to the vibrational resonance of important molecules such as water, methane, CO2 and polymers. Mid-IR LIDAR systems are used in spectroscopy, e.g. for gaz monitoring [34]. The mid-IR also contains two atmospheric transmission windows (3-5 μm and 8-12 μm) so that lasers at this wavelength can propagate over large distances. For instance, Quantum Cascade Lasers (QCLs), that rely on intersubband transitions in a semiconductor, can emit over the entire mid-IR wavelength range by engineering of the bandgap structure [35]. Significant improvements of QCLs performances in terms of peak power, wall-plug efficiency and integration with silicon [36] are beneficial for the development of mid-IR LIDAR.

Snow, rain, haze and fog strongly impact the LIDAR performances by attenuating the received signal. The two involved phenomena are water absorption and scattering. Absorption is proportional to the water density in the air while scattering depends on size of droplets. The interaction between LIDAR optical signal and water molecules is wavelength dependent. A detailed comparison of 905 nm and 1550 nm LIDAR performances under various environmental conditions can be

found in [37], and a comparative table is shown in Fig. 2.6. Under the same environmental conditions, the atmosphere extinction coefficient is two times larger at 905 nm wavelength than at 1550 nm. In [38], the same comparison is made between 785nm and 1550nm LIDARs.

Atmospheric extinction coefficient γ (km^{-1}), Rel. Humid. 50%					
Visibility (km)	1	5	10	15	23
$\lambda = 905$ nm	2.333	0.463	0.229	0.151	0.096
$\lambda = 1550$ nm	1.146	0.227	0.112	0.073	0.047

Figure 2.6: Atmospheric extinction coefficient calculated for 905 nm and 1550 nm wavelengths and typical atmospheric conditions [37].

In general, 905 nm wavelength is less absorbed by water than 1550 nm. However, at 1550 nm the solar irradiance is three times smaller than at 905 nm, which reduces interferences and improves the Signal to Noise Ratio (SNR) [30].

2.5 Eye safety

Eye safety regulations limit the maximum transmitted power for LIDAR applications. The Maximum Permisible Exposure (MPE) corresponds to the the highest power [W/m^2] or energy [J/m^2] density of light that can be delivered without causing damage to the human eye and skin. According to IEC 60825-1, Fig. 2.7 shows the MPE against the operating wavelength for several laser pulse durations.

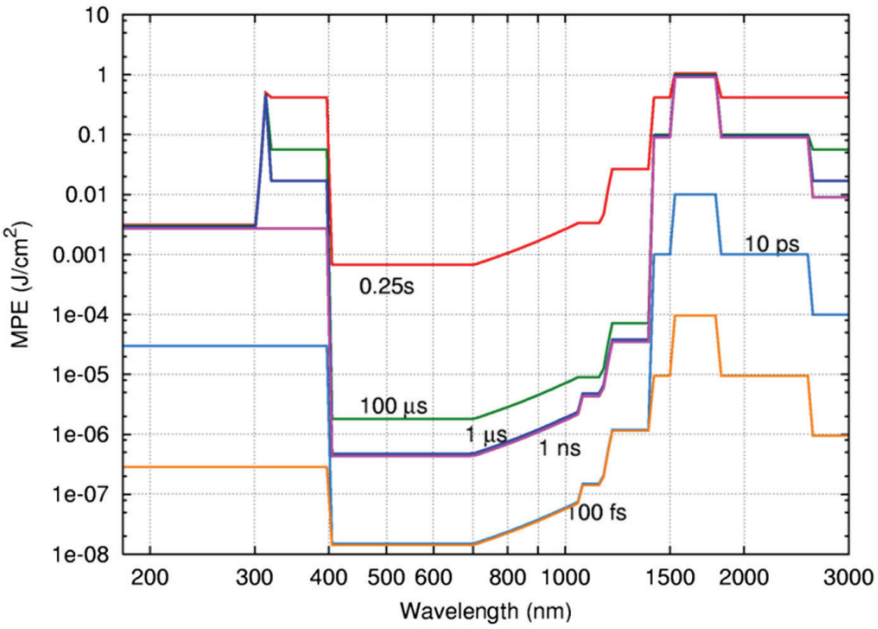

Figure 2.7: Maximum Permissible Exposure (MPE) for the human eye as a function of wavelength and for different pulse durations [10].

Moving from 905 nm to 1550 nm relaxes the MPE by few orders of magnitude

thanks to the human eye filtering by the crystalline lens (1300–1400 nm) and vitreous body (1400–1600 nm) [39].

According to IEC 60825-1, for $\lambda = 1550$ nm and an exposure time between 1 ns and 10 s, the $MPE = 10^4 J/m^2$.

Considering that the human eye is a disk with an aperture diameter $D_{eye} = 4$ mm, its surface is given by :

$$S_{humaneye} = \pi(D_{eye}/2)^2 \tag{2.13}$$

Then, the maximum allowed laser power is given by :

$$P_{max} = \frac{MPE \times S_{humaneye}}{T} \tag{2.14}$$

When considering an exposure time T of 10 s, the maximum allowed laser power P_{max} is 12.6 mW using Eq. (2.14). Now, if the LIDAR beam is scanned with an exposure time T of 10 μs, the laser power is no more limited by eye safety (its upper limit P_{max} is several kW).

2.6 Long-range automotive LIDAR

Optical sensing is essential for reaching high levels of automation in automotive. Indeed, optical sensors such as LIDARs provide accurate information on the environment in a short period of time. Along with the information measured from other sensors (Fig. 2.8), the detected targets can be classified for real time monitoring of the environment. Long-range LIDAR is intended to detect targets at 200m to provide emergency braking and avoid collisions.

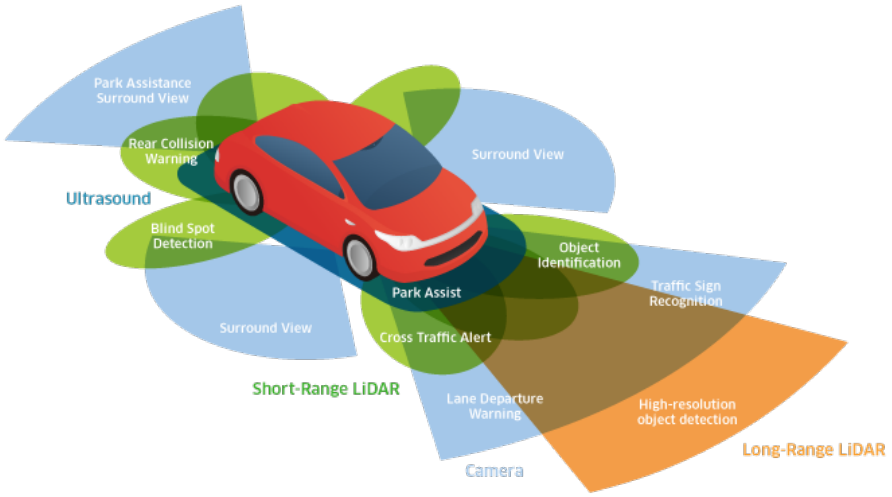

Figure 2.8: Illustration of an autonomous vehicle consisting of multiple sensors.

The Table 2.1 summarizes a set of specifications according to [40],[41],[42],[43].

Property	Value	Units
Max target range (10% reflectivity)	200	m
Range resolution	$\sim$ 10	cm
Range precision	$\sim$ 1	cm
Horizontal Field of View	120	°
Vertical Field of View	30	°
Angular resolution	0.1	°
Laser classification	CLASS 1 : IEC60825-1	-
Dimensions	15x15x15	cm
Overall power consumption	$\sim$ 15	W
Operating temperature	-40 to 80	°C
Frame rate	20-30	Hz
Outputs	XYZ, radial velocity, reflectivity	-

Table 2.1: Specifications for an automotive FMCW LIDAR.

2.7 Illumination

2.7.1 Flash and scanning techniques

In order to sense its environment, a LIDAR must be able to measure spatially separated points. The most demanding applications in terms of Field-of-View (FoV) and resolution (e.g. automotive) specify the measurement of hundreds of thousands of resolved points, in combination with a measurement frame rate of 25 Hz. Typical FoV for automotive LIDAR is 120° in the horizontal direction and 30° in the vertical direction with 0.1° angular resolution in both directions corresponding to 360,000 points to address in 40ms. In addition, detecting targets at 200m is very challenging in terms of power budget. Such requirements put tough constraints on the illumination module. As shown in Fig. 2.9, illumination techniques can be divided into scanning and non scanning techniques. Non scanning approach is also referred to flash.

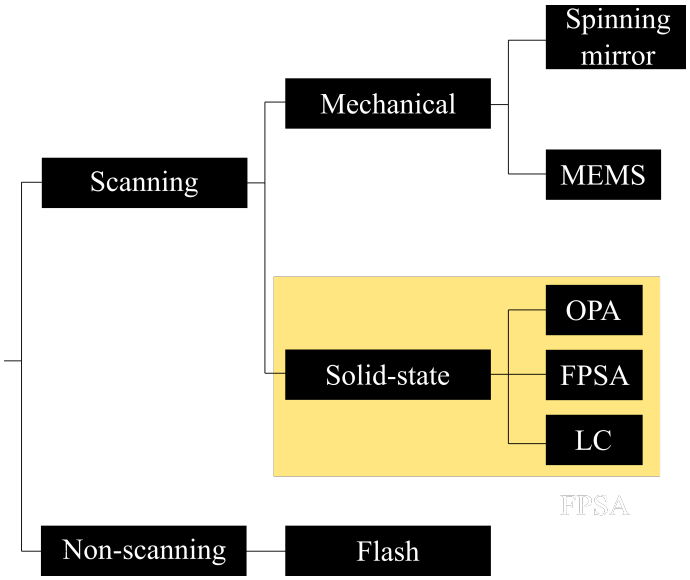

Figure 2.9: Illumination techniques classification. MEMS: Microelectromechanical systems; OPA: Optical Phased Array; FPSA: Focal Plane Switch Array; LC: Liquid Crystal.

In flash LIDAR, a highly divergent laser beam illuminates the entire field of view. The use of flash LIDAR is very relevant when the scene is moving quickly as the whole FoV is observed at the same time. Therefore, the scene can be imaged with fast frame rates (> 30 Hz). A high transmitted power pulse is used in order to collect enough power from the echo signals. Such high pulse can damage human eye, therefore limitiong the operating range of flash LIDARs to < 50 m. The receiver is generally composed of a 2D array of detectors that receives the reflected signals at once and build a 3D pointcloud of the scene.

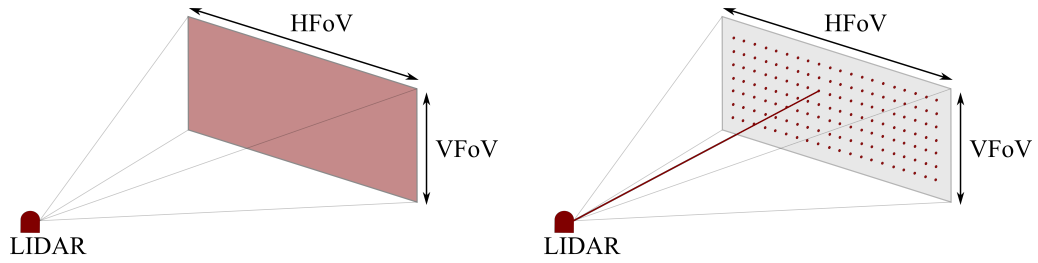

Figure 2.10: Schematic of a) a flash LIDAR and b) a scanning LIDAR.

In the scanning approach, light is steered across the FoV. The laser beam is collimated and illuminates each point sequentially. Scanning techniques can be divided into mechanical and solid state approaches.

Mechanical beam steering techniques include :

- spinning where the TX and RX parts are mounted on a rotating head to perform 2D scanning

- MEMS mirrors that deflect the incoming laser beam to the desired location in the far field

For instance, the HDL-64E spinning LIDAR [44] uses 64 lasers and 64 detectors to cover 1,300,000 points per second. However, it is heavy (12.7 kg), power hungry (60 W) and expensive (> 50 k$). Such LIDAR using spinning beam scanners are generally unwanted because they are more exposed to mechanical failures, are slower and often have large footprint and power consumption.

MEMS mirrors deflection can be used to steer the LIDAR beam. In [45], MEMS scanners have been classified according to 1) their deflection principle (refractive mirror or lens, diffraction grating) 2) their actuation principle (electrostatic, piezoelectric, electromagnetic and electrothermal) and 3) their fabrication process. Electrostatic effect is based on the principle that two conductive plates with opposite charges undergo Coulomb attraction. This type of actuation can provide fast scanning rate with low power consumption. Piezoelectric actuation consists in applying an electrical voltage to a piezoelectric material to produce mechanical stress. Piezoelectric actuation can provide fast scanning rate with low power consumption. However, hysteresis appears in the displacement-voltage characteristic of the actuator, which affects the accuracy of the mirror position [46]. Electromagnetic actuators are based on the Lorentz force being created when an electrical current flows in a conductive element placed in a static magnetic field. It generally requires high power consumption [47]. Electrothermal actuation uses resistive heating to produce thermal expansion and therefore deflection of the mirror. It can provide large FoV but is limited in scanning rate and has a high power consumption.

MEMS still faces some challenges. The larger the mirror size, the larger the receiver aperture and therefore the larger the operating range. However, this also lowers the MEMS resonant frequency which means lower scanning speed.

Hence, mechanical scanning has some limitations. Solid state scanning solutions that are integrated on chip and do not comprise any mechanical part, can offer better performances with lower power consumption, compact footprint, less failure due to mechanical fatigue, low manufacturing cost and high scanning speeds. The integration of the beam scannner also offers the possibility to design large arrays of emitters and receiver to achieve excellent resolution and wide FoV. Therefore solid-state scanning techniques are promising for embedded applications.

Liquid Crystals (LC) are also part of solid-state beam scanning solutions that can be used to steer the LIDAR beam. In the presence of an electric or magnetic field, liquid crystal molecules show preferential orientations which results in effective index variations. Therefore, modulating the effective index is possible to produce beam steering. One drawback of this technique is the long recovery time of liquid crystal molecules that limits the scanning speed. The other drawback is that liquid crystals are not CMOS compatible which limits its integration with Scintil Photonics process flow. In [48], a 16° steering angle is achieved with a 1D liquid crystal array. Future works will include the modification of the fabrication process to be CMOS compatible on 200mm wafers.

In the following, we focus on two promising solid-state beam scanning approaches:

Optical Phased Array (OPA) and Focal Plane Switch Array (FPSA).

2.7.2 Optical Phased Arrays (OPA)

Optical Phased Arrays (OPA) is the photonic counterpart of electronic phased array that is widely used in RADAR systems [49]. For radio waves, the spacing between antennas can be chosen smaller than half wavelength, enabling 180° steering range without grating lobes. However, additional challenges appear when working at $1.55\mu m$ where the components size is larger or comparable to the wavelength. An OPA steers the LIDAR beam in different directions by changing the phase and amplitude at each antenna of the array. In the following, we consider a 1D linear uniform OPA as shown in Fig. 2.11, and we refer to antenna or channel equivalently. We define d as the channel spacing, N as the channel count (number of radiating elements), θ as the scanning angle and $\Psi = kdcos(\theta)+\beta$, with k being the wavenumber ($k = 2\pi/\lambda$), and β is the gradual phase shift excitation between antennas.

Phase shifters are based on thermo-optic or electro-optic effects. Doped silicon can be used as a thermo-optic phase shifter due to its strong thermo-optic coefficient.

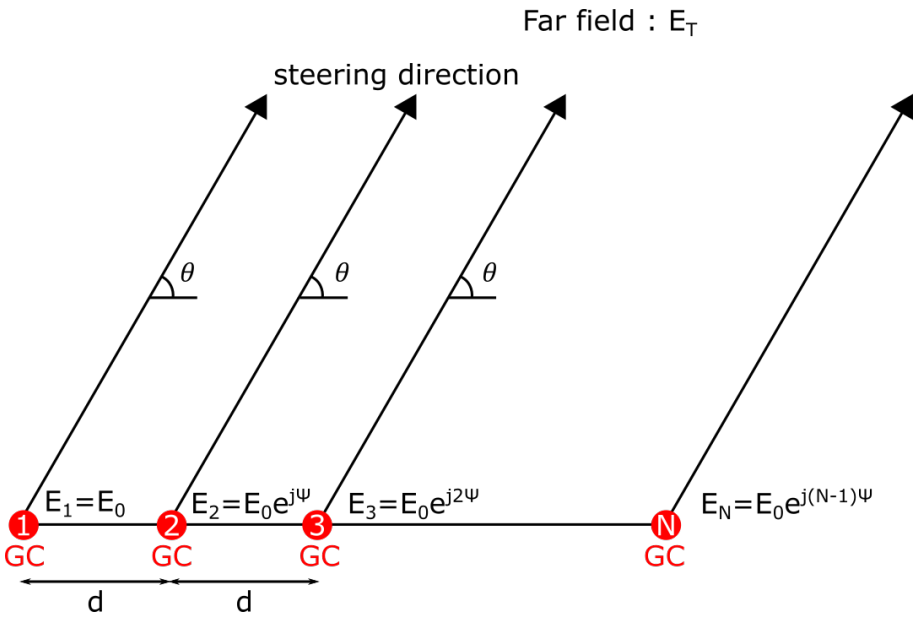

Figure 2.11: Schematic of a 1D Linear Uniform OPA.

The far field emission, $E_T(\theta)$ of this 1D OPA is the product of the antenna radiation pattern also called element factor, $E(\theta)$ (emission pattern of a single antenna) and the array factor, $AF(\Psi)$ (effect of arraying the antennas) :

$$E_T(\theta) = E(\theta).AF(\Psi) = E(\theta).\frac{\sin(N\Psi/2)}{\sin(\Psi/2)} \tag{2.15}$$

$$E_T(\theta) = E(\theta).\frac{\sin(\frac{N}{2}(kdcos(\theta)+\beta)}{\sin(\frac{1}{2}(kdcos(\theta)+\beta)} \tag{2.16}$$

The emission pattern $E_T(\theta,\beta)$ reaches a maximum when the denominator approaches zero :

$$\sin\left(\frac{\pi d}{\lambda}\cos(\theta)+\frac{\beta}{2}\right) = 0 \tag{2.17}$$

which corresponds to

$$\theta = \cos^{-1}\left(\frac{\lambda}{2\pi d}(-\beta \pm 2\pi m)\right) \tag{2.18}$$

where m is an integer. For angles θ satisfying Eq. (2.18), the maximum of radiation originates from constructive interferences between individual antennas emissions. Because m is an integer, Eq. (2.18) has several solutions resulting in grating lobes in the OPA radiation pattern as it will be explained later.

The Fig. 2.12 illustrates the simulated OPA normalized radiation pattern for several values of β, a channel count $N = 32$ and channel spacing $d = \lambda/2 = 775$ nm. Beam steering is achieved by tuning the gradual phase shift excitation β between antennas.

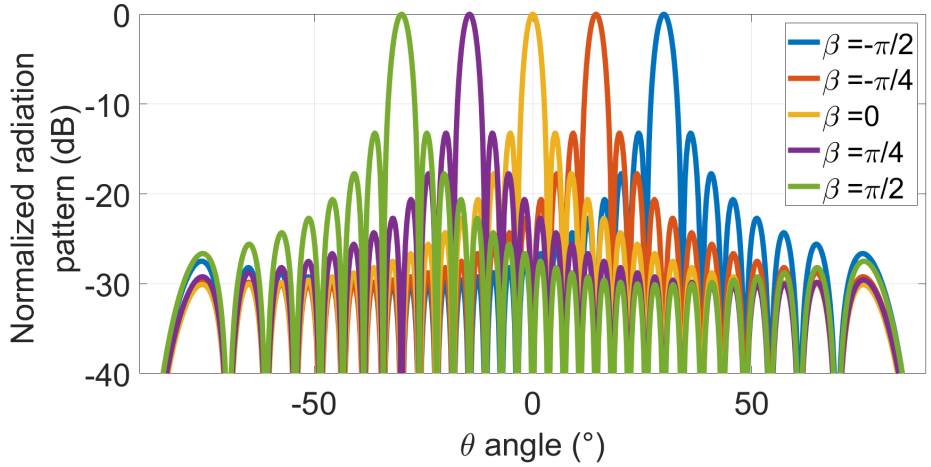

Figure 2.12: Simulated OPA radiation pattern for several values of β, $N = 32$ and $d = \lambda/2 = 775$ nm.

Wavelength scanning in OPA

Owing to the control and integration complexity of 2D OPA, vertical scanning is often achieved with wavelength tuning. The grating equation expresses the change in the vertical angle of emission Φ as a function of the grating period, Λ, the free-space wavelength, λ_0, the effective index of the guided mode of the coupler region, $n_{eff,gc}$, and the refractive index of air, n_{air} [50] as :

$$sin(\Phi) = \frac{\Lambda n_{eff,gc} - \lambda_0}{n_{air}\Lambda} \tag{2.19}$$

Typical wavelength tuning efficiency is comprised between 0.1 and 0.3 °/nm [51]. Hence, tuning range of 100nm is required to cover long-range automotive FoV of 30°.

In what follows, the OPA metrics such as angular resolution, FoV, control complexity and power consumption are derived.

Angular resolution

The angular resolution of an OPA is often expressed as the full-width at half-maximum (FWHM) beam width. The angular resolution $\Delta\theta$ in degrees is given

by [52]:

$$\Delta\theta[^\circ] \approx \frac{50\lambda}{Nd}, \tag{2.20}$$

where λ is the wavelength, N is the channel count, d is channel spacing.

The angular resolution can be improved by increasing the channel count N at the cost of increased control electronic complexity, power consumption and footprint. The Fig. 2.13 shows the 'simulated OPA normalized radiation profile at several channel count N for $\beta = 0°$ and $d = \lambda/2$, considering an operating wavelength of $\lambda = 1550nm$.

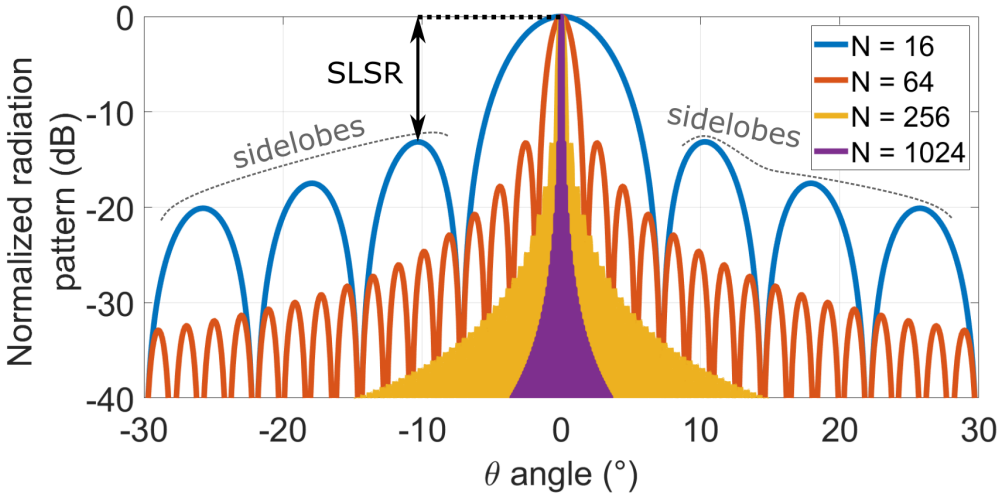

Figure 2.13: Simulated angular resolution for several channel count N, $\beta = 0°$ and $d = \lambda/2$. SLSR: Side Lobe Suppression Ratio.

Field of View and Grating Lobes (GLs)

Grating lobes are the result of the OPA periodicity. If the channel spacing $d > \lambda/2$, the main lobe is replicated at other angles with similar amplitude as the main lobe. This creates aliasing since the main lobe cannot be distinguished from grating lobes thus limiting the FoV. The Fig. 2.14 shows the schematics and the simulated normalized radiation patterns for an OPA with a channel spacing a) $d = \lambda/2$ and b) $d = 3\lambda/2$. The channel count is $N = 32$ in both cases.

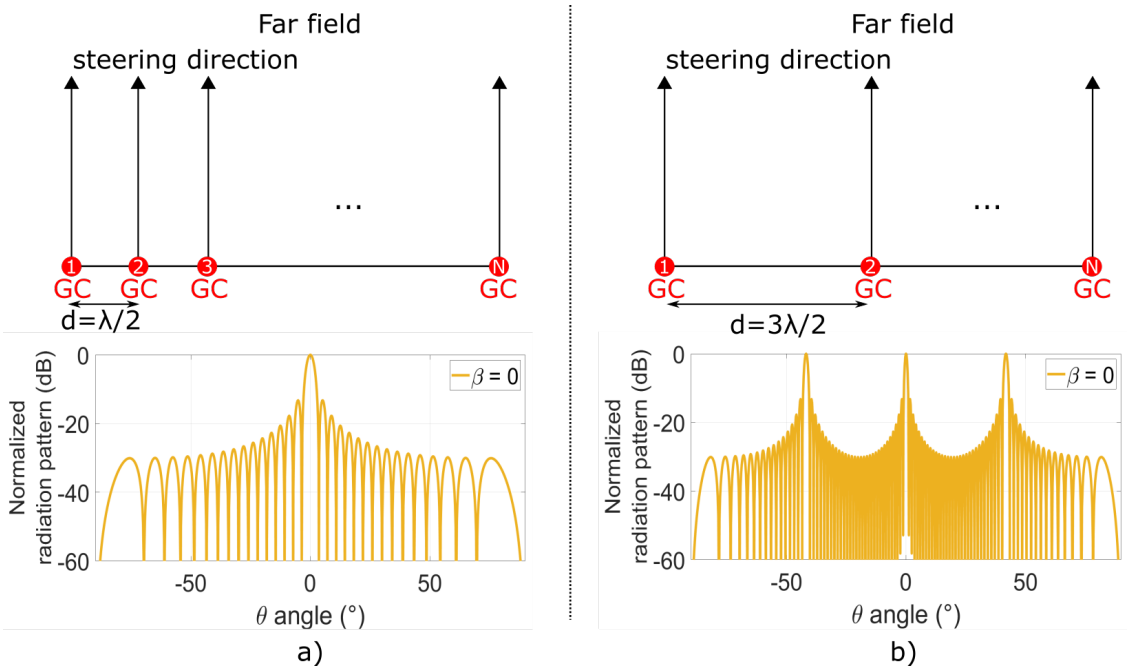

Figure 2.14: Schematics and simulated normalized radiation patterns for an OPA with a channel spacing a) $d = \lambda/2$ and b) $d = 3\lambda/2$. The channel count is $N = 32$ in both plots. GC: grating coupler.

The Fig. 2.14 a) and b) shows that increasing the channel spacing d beyond $\lambda/2$ results in unwanted grating lobes.

Several solutions have been proposed to solve the $d < \lambda/2$ challenge such as non-uniform spacing between emitters, suppressing the inter-channel crosstalk [53].

The FoV of an OPA is given by [54]:

$$FoV = 2\sin^{-1}\left(\frac{\lambda}{2d}\right) \tag{2.21}$$

To achieve full 180° FoV (±90° steering range), the channel spacing d must satisfy:

$$d = \frac{\lambda}{2} \tag{2.22}$$

The table below gives the FoV for an uniformly spaced OPA operating at $\lambda = 1550nm$ for different channel spacing d.

Channel spacing d (μm)	**FoV (°)**
0,775 μm ($\lambda/2$)	180
1.55 μm (λ)	60
3.1 μm (2λ)	29
9.3 μm (6λ)	9.5
15.5 μm (10λ)	5.73
31 μm (20λ)	2.87

This table shows that closely spaced antennas ($d \leq \lambda$) are necessary to achieve wide FoV. As explain in the next part, increasing d also brings unwanted grating lobes in the radiation pattern.

Transmitted power

In the OPA radiation pattern, the transmitted (Tx) power of interest is the power carried by the main lobe. Sidelobes and grating lobes must be minimized as they reduce the optical power available in the main lobe. The Tx power is a function of the optical power emitted at each antenna, $P_{1antenna}$, the individual antenna gain (ratio between the power radiated in the main lobe and the power radiated by a reference antenna), α, and the channel spacing, d. In [43], the power in the mainlobe is computed by integrating the Poynting vector over a surface $dA = R^2 \cos(\theta) d\theta d\phi$. This main lobe power P_{main} (in W) can be expressed as:

$$P_{main} = P_{1antenna} \frac{2.78\lambda}{2\pi d} \alpha \tag{2.23}$$

where the optical power available at each antenna in dBm is given by:

$$P_{1antenna}[dBm] = P_{in} - IL_{SN} = P_{in} - log_2(N).IL_{coupler}, \tag{2.24}$$

where P_{in} is the optical power available at the OPA input (in dBm), IL_{SN} and $IL_{coupler}$ are the splitting network and individual 3 dB coupler insertion losses, respectively.

Crosstalk and Side Lobe Suppression Ratio (SLSR)

Sidelobes are the result of the diffraction effect of the finite OPA size (sinc-like function). By controlling the radiated power of each element through windowing techniques (circular or Gaussian), side lobes can be mitigated. The Side Lobe Suppression Ratio (SLSR) is defined as the ratio of the first side lobe power to the main lobe power, as shown in Fig. 2.13. For a linear uniform OPA where each antenna radiates with equal power, the SLSR is given by [43]:

$$SLSR(dB) = 10log_{10}\Big(\Big|N \sin(\frac{3\pi}{2N})\Big|^2\Big) \tag{2.25}$$

For $N > 20$, the SLSR converges towards -13.5 dB. Using a Gaussian distribution, the SLSR can be decreased to -30 dB as shown in [55].

Power consumption

OPA requires one phase shifter per antenna.Therefore, the electrical power consumption scales as $\mathcal{O}(N)$ plus the power consumption of N SOA (one SOA per channel). Power consumption of thermo-optic phase shifters has been reduced to < 1 mW/π per element in [56]. The lowest phase shifter power consumption of 0.45 nW/π has been demonstrated in [57] using electro-optic effect.

OPA trade-off

Fig. 2.15 illustrates the trade-off related to the antenna pitch and the array size :

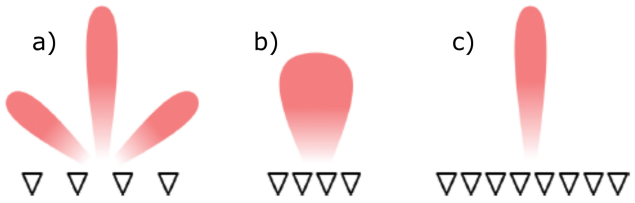

Figure 2.15: OPA tradeoff taken from [58].

In Fig. 2.15 a), widely spaced antennas produce unwanted grating lobes. In Fig. 2.15 b), densely spaced antennas suppress grating lobes (see Eq. (2.18)), but small arrays yield to poor resolution (large beam width). In Fig. 2.15 c), a large array of densely spaced emitters brings narrow beam without grating lobes in the radiation pattern.

To summarize the main OPA challenges, reducing the antenna spacing d and increasing the number of antennas N:

- improves the angular resolution
- improves the FoV
- increases the complexity and power consumption

State of the art OPA

The Table 2.2 shows a summary of state of the art OPA demonstrations up to date. The performance metrics are reported in this table.

Phase shifters performances have been improved over the last years to ensure low power consumption and high speed of operation. In [59], thermo-optic effect is replaced by electro-optic effect reducing the individual phase shifter power consumption at least by a factor 1000.

Due to the complexity of integrating a 2D OPA matrix, wavelength tuning is generally adopted to ensure vertical scanning. However, it requires complex control of tunable lasers with wide tuning range (typically 100 nm) and high output power.

The minimum channel spacing d is constantly evolving towards sub-wavelength values to ensure grating lobe suppression over the FoV. Non-uniform channel spacing is also used to suppress grating lobes and avoid crosstalk between closely spaced waveguides, at the cost of increase side lobe levels [60]. Channel count N up to 8192 have been demonstrated in [59] enabling 0.01° angular resolution.

OPA enables a high level of integration, with recent demonstrations of thousands of elements sitting on a cm^2 chip [59].

Year	Phase shifter	1D or 2D	Channel count N	Min channel spacing d	Angular resolution (°)	Field of View (°)	Power consumption	Switching speed	Chip size	SLSR	Ref
2009	Thermo-optic	2D	16	2 μm	2.7 x 2.5	2.3 x 14	8 mW/π	NA	NA	NA	[61]
2011	Thermo-optic	2D	16	3.5 μm	0.6x1.6	20x14	215 mW/π	NA	4 mm long	10dB	[62]
2011	Thermo-optic	1D	12	3.1 μm (non-unif.)	1.7	31.9	12 mW/π	100 kHz	12.5 mm long	<7dB	[63]
2013	Thermo-optic	2D	4096 (64x64)	9 μm	NA	12 x 12	8.5 mW/π	NA	576 μm x 576 μm	NA	[64]
2015	PIN phase modulator	2D	16 (4x4)	50 μm	<0.5 x 0.5	1.8 x 1.8	NA	200 MHz	<1 mm^2	NA	[65]
2016	Thermo-optic	2D	128	5.4 μm	0.14 x 0.14	80 x 17	80 mW/π	NA	NA	8.8 dB	[60]
2018	Thermo-optic	1D	1024	2 μm	0.03	45	54 mW/π	∼10-100 kHz	5.7 mm x 6.4 mm	>9 dB	[52]
2019	Thermo-optic	2D	128	5.6 μm (non-unif.)	0.8 x 0.8	16 x 16	10.6 mW/π	NA	2.08 mm^2	12 dB	[53]
2019	Thermo-optic	2D	120	1.3 μm	NA	>40 x 3.3	11 mW/π	NA	14 mm x 6 mm	7dB	[66]
2020	Thermo-optic	2D	512	1.3 μm	0.15 x 0.08	70 x 6	1.7 mW/π	∼150 kHz	8 mm x 15 mm	7.5 dB	[67]
2020	Electro-optic	2D	8192	1 μm	0.01 x 0.039	100 x 17	∼2μW (static)	∼33kHz	28 mm x 25 mm	10dB	[59]

Table 2.2: State of the art OPA demonstrations. (NA: not available).

2.7.3 Focal plane switch array (FPSA)

The working principle of a Focal Plane Switch Array (FPSA) is described in Fig. 2.16. An array of optical antennas is placed in the focal plane of a convex lens. An electrically controlled switch matrix directs the input optical signal towards each antenna. The light emitted from the selected antenna is then collimated by the lens of focal length, f. The antennas can be arranged in a 1D or 2D array and each position corresponds to a scanning direction. Therefore, by switching between emitters sequentially, using Mach-Zehnder interferometer (MZI) -based switches, the beam is steered across the FoV. In principle, the control of a FPSA is simpler compared to OPA since one emitter is turned on at a time.

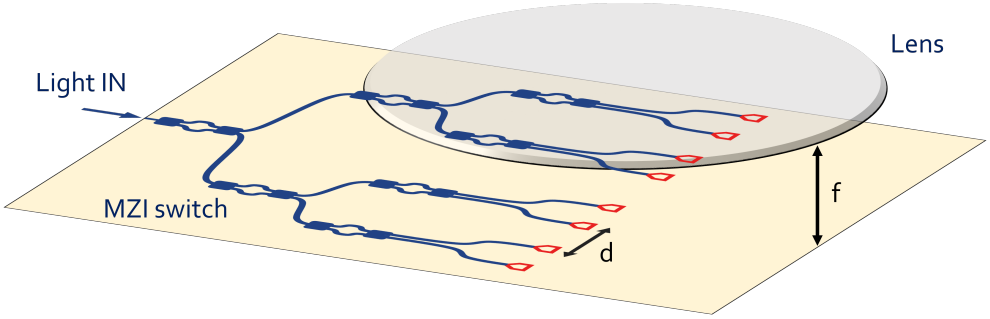

Figure 2.16: Schematic of a 8-emitter FPSA.

Angular resolution and Field of View

In a FPSA system, the angular resolution $\Delta\theta$ and FoV are expressed by [68]:

$$\Delta\theta = tan^{-1}\left(\frac{d}{f}\right) \quad \text{and} \quad FoV = 2tan^{-1}\left(\frac{L}{2f}\right) \tag{2.26}$$

where f is the lens focal length, d is the spacing between consecutive antennas and L is the array length given by :

$$L = (N-1)d \tag{2.27}$$

where N is the channel count in one direction.

Thus, high resolution is obtained when d is minimized. Large array size L offers large Field-of-View. However, optimizing resolution and FoV brings to a trade-off in the choice of the focal length f. The best operating point depends on the application.

A resolution of $\Delta\theta = 0.1°$ is often specified for automotive application. It corresponds to a beam diameter of 35 cm at a distance of 200 m. A simulation with 1024 emitters spaced by 20 μm is shown in Fig. 2.17. To satisfy this resolution a focal length larger than 10 mm is needed, limiting the FoV to 80°.

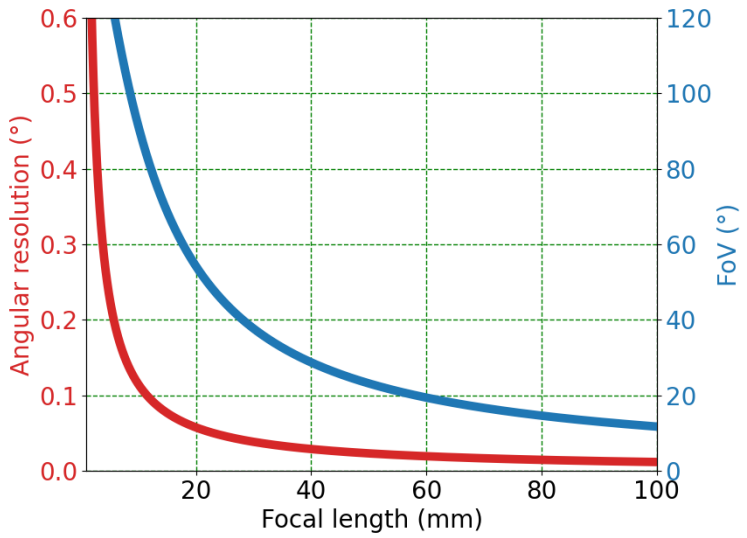

Figure 2.17: Simulation of angular resolution and FoV of a 1024-emitter 1D FPSA with d=20μm, as a function of focal length.

Grating divergence

Grating emission can be approximated as a Gaussian beam with waist diameter w_0 equals to half its mode field diameter (MFD) as shown in Fig. 2.18. Grating divergence θ_{div} is inversely proportional to the MFD through [69]:

$$\frac{\theta_{div}}{2} = \frac{2\lambda}{\pi.n_{SiO2}.MFD}, \tag{2.28}$$

where n_{SiO2} is the index in the SiO2.

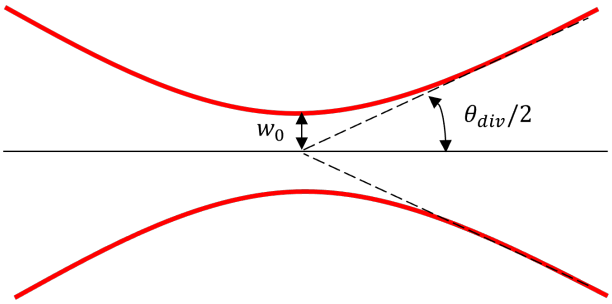

Figure 2.18: Gaussian beam approximation.

Typical MFD of 10 μm corresponds to a Grating divergence θ_{div} of 3.8° at 1550 nm.

The grating divergence also impacts the lens diameter. Indeed, to include all the rays emitted by the antennas, the lens diameter D is given by [68]:

$$D = L + 2f\tan(\theta_{div}) \tag{2.29}$$

Power consumption

In terms of power consumption, the power scales as $\mathcal{O}(log_2(N))$ since we only bias the active MZI switch path. The SOA power consumption should also be added:

$$P_{cons} = log_2(N).P_{1PS} + P_{1SOA} \tag{2.30}$$

where P_{1PS} is the average power consumption of one phase shifter.

Similarly to OPA, the optimization of the phase shifters is essential to ensure low power consumption and high scanning speed.

Transmitted power

The transmitted power, P_{TX} (in dBm), of the FPSA is determined by the switch matrix insertion loss. It is given by:

$$P_{TX} = P_{in} - log_2(N).IL_{1switch} \tag{2.31}$$

where P_{in} is the optical power available at the FPSA input (in dBm), $IL_{1switch}$ is the insertion loss associated to one switch cell (in dB).

Crosstalk

Finally, the crosstalk, Xtalk (in dB), is determined by the extinction ratio for the switch cells. We define it as the difference between the optical power transmitted in the active path i, P_i (in dBm), and the sum of unwanted optical powers transmitted over the j non-activated paths, P_k (in dBm) as :

$$Xtalk = P_i - \sum_{k \neq i, k=1}^{j} P_k \tag{2.32}$$

State of the art FPSA

The Table 2.3 summarizes the main advances in state of the art FPSA. FPSA demonstrations using optical switches based on MEMS, thermally tuned Mach-Zehnder Interferometer (MZI) or microring resonator have been reported.

In the MEMS approach, the OFF and ON switching states consist in bringing together two waveguides to ensure an efficient optical coupling over a short propagation length. MEMS benefit from the low power consumption (μW) and almost zero insertion loss in the OFF state [70].

In [71], a 20 x 20 emitter array based on MEMS switching is demonstrated with 20° x 20° FoV and 0.08° x 0.086° angular resolution. More recently in [72], the same group demonstrated the largest integrated 2D MEMS based FPSA with 16,384 antennas (128 x 128 array) fabricated on a 10 x 11 mm^2 silicon photonic chip. The measured FoV is 70° x 70° with 0.6° x 0.6° angular resolution, and the scanner can operate at 1 MHz switching speed.

For thermally tuned switches, cascaded MZI with phase shifters positioned on each arm can be used to direct the light towards one the interferometer output.

Microring resonator can also be actively tuned to couple the incoming light to their drop port or through port [73].

In [74], a switch based on cascaded Mach-Zehnder Interferometers (MZI) addresses the columns of a 4 x 4 emitter array. Microring resonators with angular gratings on their sidewalls enable the row selection and the coupling to free space. The 2D array is placed in the focal plane of a metalens. A 12.4° x 26.8° FoV is measured with <100 mW electrical power consumption to control the array.

Phase-change materials (PCMs) based optical switches have also been reported in [75][76] with fast switching operation (typically <400 ns). PCMs such as Ge–Sb–Te (GST) rely on the strong refractive index contrast upon phase transition between amorphous and crystalline states. However, this transition usually comes with high optical losses [76], which have been overcome by using other PCMs such as Ge–Sb–Se–Te (GSST) [77]. Although PCMs presents its own advantages for building optical switches, in the following the focus will rather be on the above mentioned implementations.

Finally, FPSA scanning systems have been demonstrated on several integration platforms, and using different optics to optimize the beam scanning performances. In [78], a 4 x 4 emitter array is fed by a 1 x 16 switch fabricated on a silicon nitride platform. The measured scanning rate is 37 kHz. In [79], a 1 x 16 switch is coupled to a slab waveguide, where it is diffracted. An aplanatic lens made from patterned amorphous silicon then refocuses the beam to a 1D surface grating coupler. Beam steering over a 38.8° x 12° FoV is achieved by channel switching and wavelength tuning. However, the vertical FoV of 12° requires wide tuning of the tunable laser, increasing the complexity of the laser tuning [80]. In [81], a 4 x 4 FPSA is fabricated using standard Planar Lightwave Circuit (PLC) technology. The 16 emitters are surface coupled to a 4 x 4 fiber array that is packaged with a lens to provide collimation. The measured FoV is 38.8° x 12°.

Year	Switch principle	1D/2D	Channel count N	Angular resolution	Field of View	Switch consumption (no SOA)	Switching speed	Chip size	Ref
2018	Thermo-optic MZI	2D	16 (Tx)	NA	38.8x12	NA	NA	NA	[79]
2019	Rings	1D	20 (Tx)	NA	6	NA	3MHz	7mmx12mm	[68]
2021	Thermo-optic MZI + rings	2D	16 (Tx)	0.9	12.4x26.8	83mW	NA	0.9mmx0.6mm	[74]
2019	Thermo-optic MZI	2D	16 (Tx)	0.06	2.16x4.29	NA	37kHz	few mm^2	[78]
2019	Thermo-optic MZI	2D	1024 (Tx)	0.11	160 x ?	NA	NA	NA	[82]
2020	Thermo-optic MZI	2D	16 (Tx)	NA	1.05x1.05	NA	NA	NA	[81]
2021	Thermo-optic MZI	2D	16 (Tx) 512 (Rx)	NA	1.5x0.9	160mW (Tx) ; 120mW (Rx)	100kHz	6mmx3mm	[83]
2020	MEMS (with SiPh)	2D MEMS	400 (20x20)	0.08x0.086	32x32	NA	2.5MHz	3.8mmx3.8mm	[71]
2022	MEMS (with SiPh)	2D MEMS	16384 (128x128)	0.05x0.049	70x70	NA	500kHz	7mmx7mm	[72]

Table 2.3: State of the art FPSA demonstrations. NA: not available; SiPh: Silicon Photonics

2.7.4 1D OPA vs 1D FPSA comparison

In this section, we consider a real case scenario where both OPA and FPSA scanning systems should cover a FoV of 30° and an angular resolution of 0.1°. We provide a quantitative comparison between OPA and FPSA in terms of geometry (antenna spacing d and channel count N), electrical power consumption, transmitted optical power and crosstalk level.

The Table 2.4 summarizes the keys formulas for OPA and FPSA and their specifications.

	OPA	FPSA	Spec
Field of View FoV (°)	$\frac{360}{\pi} sin^{-1}\left(\frac{\lambda}{2d}\right)$	$\frac{360}{\pi} tan^{-1}\left(\frac{(N-1)d}{2f}\right)$	30°
Angular resolution $\Delta\theta$ (°)	$\frac{50\lambda}{Nd.cos(\theta)}$	$\frac{180}{\pi} tan^{-1}\left(\frac{d}{f}\right)$	0.1°
Static power consumption (W)	$N(P_{1PS} + P_{1SOA})$	$log_2(N).P_{1PS} + P_{1SOA}$	-
Transmitted power (W or dBm)	Main lobe power : $P_{1antenna}\frac{2.78\lambda}{2\pi d}\alpha$	$P_{in} - log_2(N).IL_{1switch}$	$100mW$
Crosstalk (dB)	$SLSR = \lvert Nsin(\frac{3\pi}{2N})\rvert^2$	MZI extinction + SOA as shutter ($< -50dB$ expected)	$< -25dB$

Table 2.4: Summary table of the key formulas for OPA and FPSA and the specifications.

The Fig. 2.19 shows the two scanning architectures. The wavelength of operation is 1550 nm. In both implementations, Semiconductor Optical Amplifiers (SOAs) were inserted before the TX to ensure sufficient optical power to detect targets at 200 m with 10% reflectivity. The SOA is assumed to produce a 10 dB gain and is not saturated by the input optical power. For the OPA, all SOAs should be switched ON at once, while for FPSA, only the SOA in the active path is switched ON, to save power consumption. Another advantage of single SOA operation for FPSA is that other SOAs that are switched OFF act as shutter and filter the leakage signals contributing to crosstalk. In [84], SOAs used as shutter have shown more than -50 dB isolation level. We considered thermo-optic phase shifters for both OPA and FPSA. Therefore, the switching speed is comparable in both techniques.

In terms of average power consumption, individual doped Si thermo-optic phase shifter consumes 12 mW/π and an individual SOA consumes 200 mW.

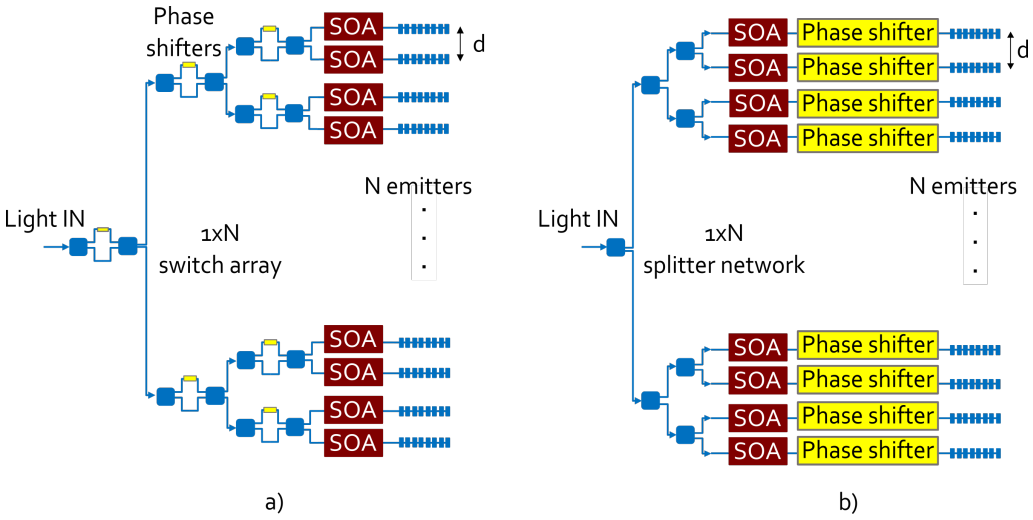

Figure 2.19: Comparison between a) FPSA and b) OPA implementations.

Channel spacing d

For the OPA, the minimum channel spacing d is 3 μm in order to cover a 30° field-of-view using Eq. (2.21). Beyond this angular range, unwanted grating lobes are produced. For FPSA, the minimum channel spacing d is determined by the angular resolution of 0.1° and the lens focal length f. The size of the grating coupler and therefore the channel spacing d between emitters is also related to the MFD of the grating. Here we will consider a grating MFD of 10 μm and a channel spacing d of 50 μm, which results in a focal f of 2.86 cm.

Channel count N

For OPA, the channel count N determines the angular resolution as described by Eq. (2.20). Therefore, angular resolution below 0.1° can be obtained with at least N=259 channels. This corresponds to a 1x8 splitter network. For FPSA, the channel count N determines the FoV using Eq. (2.26). At least 308 channels are needed to ensure a 30° field-of-view. This corresponds to 9 stages of MZI switches.

Footprint

The resulting channel spacing d and channel count N set the beam scanning chip length occupied by the antennas. The OPA offers high level of integration with a 772 μm-long 1D array of antennas. The FPSA 1D antenna array is 15352 μm-long in this example. Nevertheless, OPA requires more electrical pads than FPSA, owing to the number of phase shifters to control. Hence, in terms of chip footprint, both optical and electrical I/Os should be considered.

Static power consumption

For the OPA, the computed power consumption depends on the SOAs and the thermo-optic phase shifters. The OPA consumes 54.9 W on average, all these elements being active simultaneously. The FPSA only consumes 0.3 W on average as only one path is active at a time.

TX power

For the OPA, the power in the main lobe depends on the splitter network insertion loss and the power lost in the sidelobes. As described by Eq. (2.24), it is dependent on the individual antenna gain. For FPSA, it is reasonable to consider less than 0.5 dB insertion per switch cell [74]. It corresponds to a total switch array loss of 4.5 dB in our scenario. The 10 dB gain SOA can compensate for on-chip losses and provide 100 mW optical power at the TX. This point will be further developed in next chapter.

Crosstalk

In terms of crosstalk, OPA suffers from unwanted reflections from the sidelobes. For a linear uniform OPA, the SLSR is -13.46 dB. By using OPA with Gaussian distribution, the SLSR can be reduced down to -30 dB [55]. FPSA with SOA at each emitter is expected to reach crosstalk levels below -70 dB, considering MZI extinction ratio of -20 dB and a switched off SOA isolation of -50 dB.

The Table 2.5 summarizes the computed parameters to achieve the specifications given in Table 2.4 for the OPA and FPSA implementations.

	OPA	FPSA
Channel count N	259	308
Channel spacing d (μm)	3	50
Focal length f (cm)	-	2.86
Static power consumption (W) (P_{1PS}=12 mW; P_{1SOA}=200 mW)	54.9	0.3
Crosstalk (dB)	-30	-70

Table 2.5: Table of the computed parameters for the comparison between 1D OPA and 1D FPSA described in Table 2.4.

In conclusion, both OPA and FPSA can achieve the specified performances with their respective pros and cons. Large OPAs with sub-wavelength channel spacing offer very high level of integration, high resolution and wide FoV, at the cost of control complexity and power consumption. FPSA requires a simple convex lens to

transmit collimated beams towards the target. This technique also offers high level of integration and is very promising for power consumption and crosstalk reduction.

In chapter 4, we will report on the design and characterization of a 4-emitter FPSA circuit made from a single fully integrated circuit. Our switch array is based on cascaded MZI with thermo-optic phase shifters.

The integration of LIDAR systems on chip is essential for compactness, low power consumption, robustness and cost considerations. The integration of III-V lasers and semiconductor optical amplifiers (SOA) would enable the co-integration of the LIDAR transmitter and receiver on the same chip, suppressing the interface coupling losses compared to discrete element assembly and offering wafer-scale CMOS manufacturing and testing. The use of low loss Si/SiNx passive components with Germanium (Ge) waveguide-PD featuring high responsivity, compactness and ultra-high speed would be a key advantage.

2.8 Towards integration of LIDAR systems

2.8.1 Silicon photonics for FMCW LIDAR

The technological advances of microelectronics has enabled the mass-fabrication of nm-size component features with high reliability. Leveraging this technology, silicon photonics is gradually taking hold in foundries with the aim of guiding, modulating, emitting and detecting light on a single chip [85]. The co-integration of the LIDAR transmitter and receiver components is essential to the extensive parallelism demanded in next generations sensing applications. It reduces the assembly steps and related optical and electrical packaging losses.

The high index contrast between Si/SiNx and SiO2 enables a strong light confinement in the waveguides. Passive integrated components such as waveguides, splitters/combiners, multiplexers, grating and edge couplers have been developped to efficiently route, filter and couple the light. For example, very low loss waveguides (few dB/m) have been reported in [86].

Silicon electro-optic modulators (EOM), leveraging the plasma dispersion effect [87], are capable of high speed (>50 GHz) encoding of the information into the optical signal. IQ modulators can be used to produce LIDAR linear frequency chirp as it will be discussed later [88].

The photodetector converts an optical signal into an electrical signal using the photoelectric effect. When photons with a certain energy are impinging on a material, they can be absorbed and generate electron hole pairs. These carriers are collected, producing a photocurrent. High speed and high responsivity integrated Ge waveguide-photodiodes have been demonstrated in [89]. Balanced photodetectors have been used for improving the SNR by eliminating any common fluctuations from the two mixed signals [90].

Finally the laser produces a spatially and temporally coherent light based on the stimulated emission effect. Silicon is not a good candidate to build lasers due to its indirect bandgap, while III-V materials have direct bandgap and high gain, enabling the access to efficient lasers in the O and C bands. However, the combination of III-V material with silicon is challenging. The next section describes the main III-V/Si integration approaches.

2.8.2 III-V on Si integration

Combining the III-V material with Si can be done in several ways [91] as shown in Fig. 2.20:

a) photonic package assembly

b) flip chip of processed III-V lasers

c) micro-transfer printing

d) hetero-epitaxial growth

e) heterogeneous integration of III-V dies or wafers on the SOI wafer through bonding

Photonic package assembly can be used for coupling III-V packaged lasers with a silicon photonics chip as shown in Fig. 2.20 a). This technique requires precise aligment procedure with dedicated optics as illustrated by the laser micropackage (LaMP) developped by Luxtera [92]. However, this approach is limited by the alignment steps and coupling losses due to the multiple interfaces. Multi-laser integration also becomes complicated.

The second solution is to flip chip processed laser chips on the silicon photonics wafer as described in Fig. 2.20 b). This approach has been used in [93] where vertical alignment of the lasers is ensured by pedestals and recess patterned in the silicon photonic wafer. Spot size converter (SSC) are needed for high coupling efficiency at the interface between the laser and the waveguide.

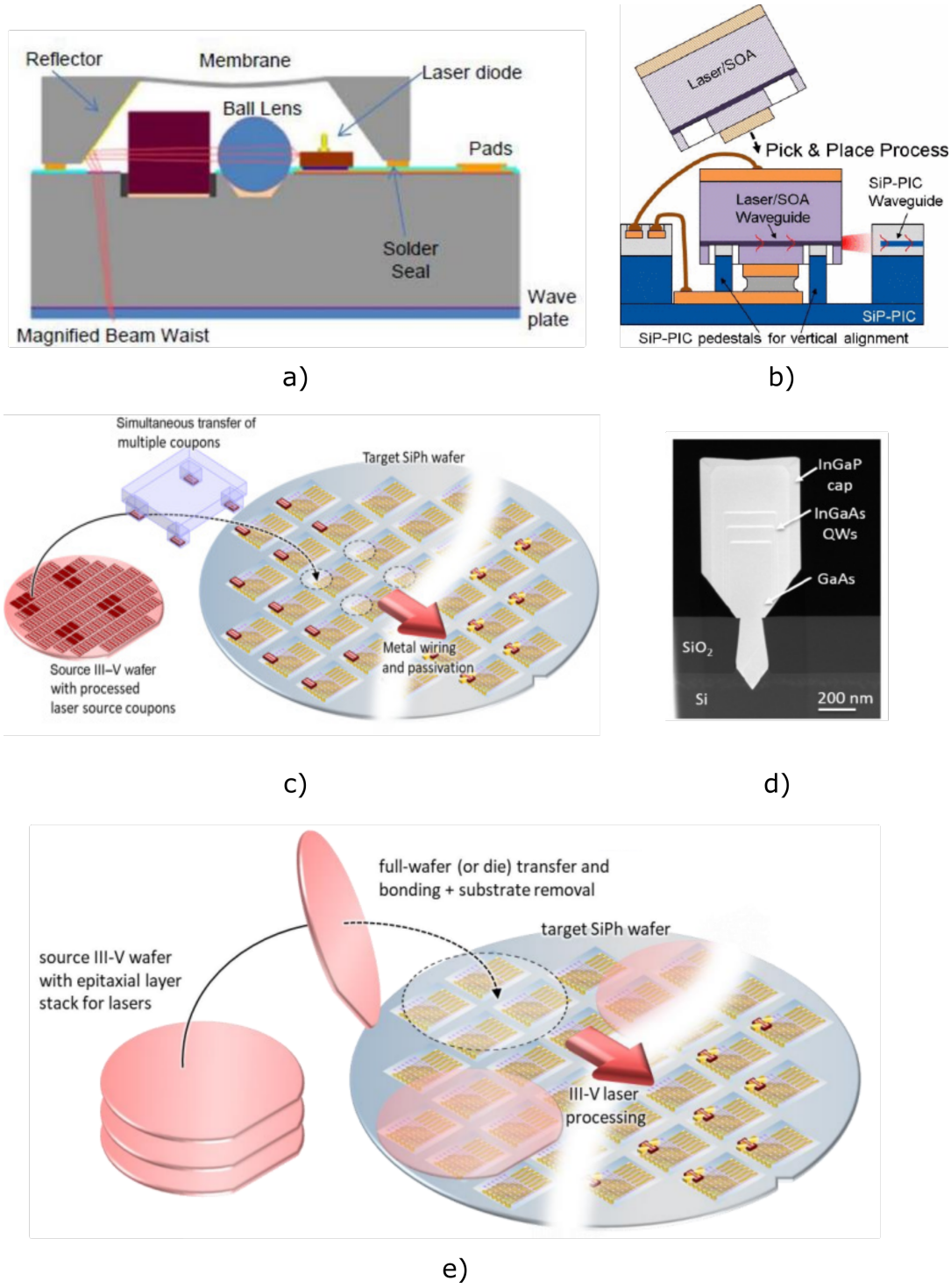

Figure 2.20: III-V material integration with silicon photonics wafer using a) photonic package assembly [92] b) flip chip bonding of processed III-V dies [93], c) micro-transfer printing [94], d) Hetero-epitaxial growth [95] and e) III-V/Si wafer or die bonding.

Micro-transfer printing uses III-V gain dies that are pre-processed on the III-V wafer and simultaneously transferred to the silicon photonics wafer using a stamp, as shown in Fig. 2.20 c). More details on this approach can be found in [96]. Micro-transfer printed SOA with small signal gain $>$ 15 dB and saturation power $>$ 10

mW have been demonstrated in the C band [97]. Widely tunable laser have also been reported in [98].

Hetero-epitaxial growth consists of selective III-V material growth on the silicon wafer using chemical vapor deposition (CVD) methods, as described in Fig. 2.20 d). This technique promises high level of integration but faces challenges due to the lattice and thermal expansion coefficient mismatches between the two materials. The resulting dislocations are a strong limitation for the laser performances [99].

Another heterogeneous integration of the III-V material consists of bonding III-V dies or wafers on the silicon photonic wafer as shown in Fig. 2.20 e). Molecular bonding, adhesive bonding or metallic bonding can be used. The III-V lasers and amplifiers are processed after the bonding step, enabling wafer scale processing and high level of integration. This approach has been pioneered by UCSB [100], and CEA-Leti, IMEC and III-V lab [101]. Relying on early integration work, Scintil Photonics is developping III-V/Si photonic circuit using its own integration process called 'Backside on Box' which is detailed hereafter.

The Scintil Photonics process flow starts with a Silicon On Insulator (SOI) with a buried oxide (BOX) thickness varying within less than 5 nm.

1) **Silicon photonics processing**
   The top Si layer is etched for defining the Si waveguides and other optical elements such as modulators, multiplexers, and demultiplexers. Waveguide photodiodes can be formed by using epitaxial growth of Ge, and SiNx can be added to form low-loss passive devices. A SiO2 encapsulation is then applied to the silicon photonics wafer, and metal levels are processed.

2) **Transfer to silicon handle**
   The silicon photonics wafer is then flip-chip bonded onto a silicon handle. and the original silicon substrate is removed, leaving the thin buried oxide (BOX) layer on top.

3) **III-V/Si molecular bonding**
   The III-V material-stack is molecular bonded on the backside of a Si photonic base wafer i.e. onto the BOX layer. The bonding step does not require any precise alignment.

4) **III-V material patterning**
   Finally, the III-V material is patterned at the wafer level to define the lasers and amplifiers. Electrical contacts are then deposited to drive active components. At the end of the manufacturing flow, a chemical mechanical planarization step enables a flat top surface, making the integration of flip chip electronic possible for package.

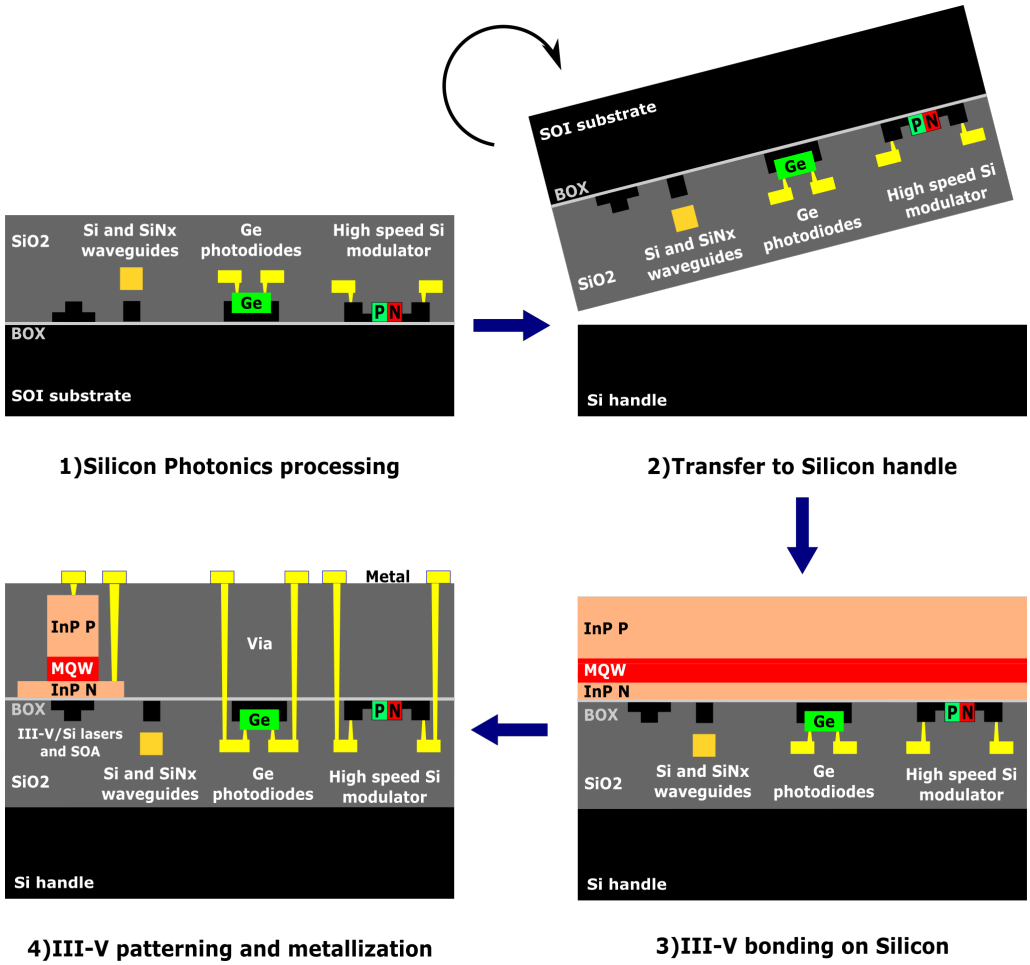

Figure 2.21: Scintil 'Backside on Box' fabrication process [102].

III-V/ Si DFB laser with 20 mW output power per laser end and 20 kHz Lorentzian linewidth has been demonstrated on this platform [103] showing its potential for integrating LIDAR sensors. The integration of III-V material with low loss Si/SiNx passive components and high sensitivity Ge photodiodes is a key advantage for detecting long-range targets with high precision.

2.8.3 State of the art FMCW LIDAR

In this section, an overview of state-of-the-art FMCW LIDAR is given. The Table 2.6 summarizes the main FMCW LIDAR demonstrations up to date. These works include different levels of integration from fibered systems to chip-scale LIDAR. The framework of this thesis is also given.

In [104], a fibered FMCW LIDAR was built from off-the-shelf fiber optic telecommunication components. It was used in a NASA space exploration program. Range and velocity (Doppler) measurements were performed on a target at a distance of 250 m.

In [105], the FMCW LIDAR system is composed of an external laser that feeds a Photonic Integrated Circuit (PIC) composed of 8-transmitter and 8-receiver switching networks. Each emitter is coupled to a fiber with a collimator and a circulator

to redirect the Rx beam towards the Rx switch. Speed and range measurements were reported for a target at a distance of 60 m.

In [106], a chip scale FMCW LIDAR circuit including a SGDBR laser and III-V balanced photodetection was built on an InP-based platform. The authors reported on the individual component performances of the circuit.

In [107], the integration of the emitter and receiver of FMCW LIDAR on the same Silicon photonic chip is demonstrated.

In [83], the frequency modulation of the source is performed by a fibered laser associated to an IQ modulator. A fiber amplifier is used as a booster to compensate for the losses of the IQ modulator. The 16 transmitters switch and the 512 receiver pixels are integrated on a Silicon photonic chip.

In [29], two LIDAR circuits were implemented with edge coupled lasers to the photonic chip. Though the laser integration process requires precise alignment of the laser with the PIC, detection of targets up to 75 m.

	Integrated materials	Footprint	Beam scanning	Power consumption	Operating range	Ref
Fiber assembly	No chip	Bulky	Rotating fibered telescopes	NA	250 m	[104]
Semi-integrated	Si ; SiN; Ge	Cigarette box size	Fibered FPSA	NA	60 m	[105]
SOI wo III-V	Si ; SiN; Ge	Cigarette box size	FPSA or OPA	NA	75 m	[83][59]
SOI and III-V chips	Si ; SiN; Ge	Cigarette box size	No beam scanning	NA	75 m	[29]
Bulk Si with III-V	III-V ; Si ; SiN ; Ge	Cigarette box size	OPA	NA	~20 m	[108]
Full III-V	III-V only	Cigarette box size	No beam scanning	NA	NA	[106]
SOI with III-V	III-V ; Si ; SiN ; Ge	Cigarette box size	FPSA	<10 W	200 m	Framework of this thesis

Table 2.6: Summary table of state of the art FMCW LIDAR demonstrations. wo : without.

Leveraging the III-V/Si integration platform, this work focuses on the realization of a compact and low power consumption FMCW LIDAR for long-range detection.

2.9 Chapter conclusion

In this chapter, a state-of-the-art on LIDAR solutions has been presented. We have shown the interest of FMCW LIDAR approach relatively to AMCW and DToF LIDARs, in the context of automotive applications. The FMCW LIDAR architecture is promising for high precision 3D sensing applications. In addition to the target distance, it provides velocity estimation, immunity to background lights and high sensitivity, making it suitable for long-range detection. Then LIDAR metrics have been introduced to quantify the performances of each LIDAR system. We also presented the different illumination families. Solid-state beam scanning approaches are preferred over bulk mechanical scanners due to their lower power consumption, footprint, probability of failure, and cost. Based on a detailed comparison between two promising solid-state beam scanning techniques, OPA and FPSA, we selected the FPSA principle for its reduced power consumption, crosstalk and complexity. Finally, we discussed the chip-scale integration of FMCW LIDAR systems in order to improve the footprint, the weight, the cost and the power consumption. Scintil Photonics integration platform, called 'Backside on Box', combines various materials (III-V; Ge; Si/SiNx) on the same chip. The integration of III-V material on Si is a differentiating factor that enables the fabrication of state of the art components and circuits.

Based on this state-of-the-art, the objective of this work is to investigate the feasibility and the challenges related to FMCW LIDAR components and circuits through three steps: modeling, layout and characterization of the fabricated chips. The next chapter consists in modeling the FMCW LIDAR system. We will start from the specifications defined in Table 2.1 and derive the corresponding photonic components specifications while identifying the system limitations.

Chapter 3

FMCW LIDAR model

In this chapter, the working principle of FMCW LIDAR is detailed. We developed a model to derive the link budget and signal-to-noise ratio (SNR) of the system. This model connects the expected LIDAR system performances described in chapter 2 and photonic component specifications.

3.1 Overview of the FMCW LIDAR system

A FMCW LIDAR can be decomposed into several building blocks as shown on Fig. 3.1:

1. the source
2. the illumination and collection module
3. the coherent receiver
4. the electronics for control and the digital signal processing block

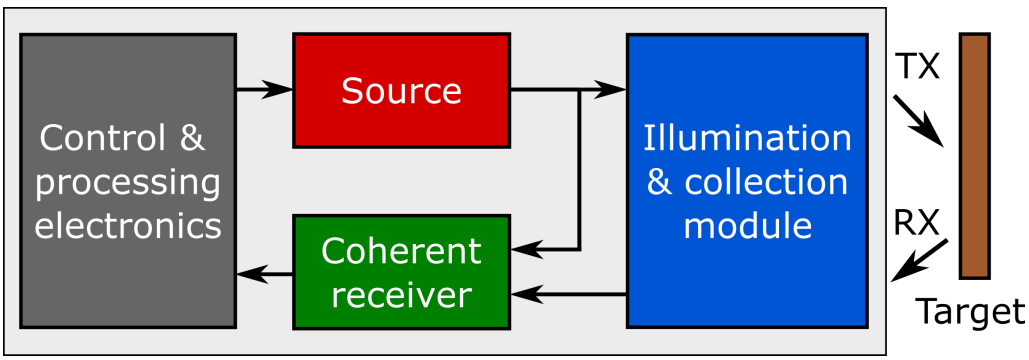

Figure 3.1: Schematic of the FMCW building blocks.

The role of the source is to produce a laser signal that is modulated in frequency.

The illumination module steers the laser beam towards certain directions in space. The goal of this unit is to cover the largest Field-of-View (FoV) with fine resolution, in a short time period that is given by the frame rate (FR).

The coherent receiver demodulates the received signal (RX) with a reference signal (LO).

The electronic unit role is to control and process the electrical signals at the interface of the photonic circuit. The beat signal produced by the coherent receiver is processed to recover the range and the speed of the target.

From a system point of view, each building block is responsible for losses and/or contributes to noise. In this section, a noise model and a power budget is built to quantify the SNR of a FMCW LIDAR circuit. This model serves as a bridge between LIDAR system performances and component specifications. The case of long-range automotive FMCW LIDAR is discussed while the model can be adapted to industrial, medical or consumer FMCW LIDAR.

In the next section, we focus on the theory of the coherent receiver.

3.2 Pre-requisite on coherent detection

Coherent receivers are made of two subsystems : an optical mixer and balanced photodiodes. The optical mixer can be realized with a simple 3 dB coupler or by using an optical 90° hybrid. We use general field expressions without considering any laser phase noise for the local oscillator (LO) and received (RX) signals given by :

$$E_{LO}(t) = E_{LO}^0 \exp(j(\omega_{LO}t + \Phi_{LO})) \tag{3.1}$$

$$E_{RX}(t) = E_{RX}^0 \exp(j(\omega_{RX}t + \Phi_{RX})), \tag{3.2}$$

with ω_{LO}, Φ_{LO} and E_{LO}^0 (respectively ω_{RX}, Φ_{RX} and E_{RX}^0) being the pulsation, initial phase and amplitude of the local oscillator field (respectively of the received field).

3.2.1 With 3 dB coupler

The simplest way to perform coherent mixing between the local oscillator (LO) and reflected (RX) signals, is to use a 3 dB coupler with a pair of balanced photodetectors as shown on Fig. 3.2.

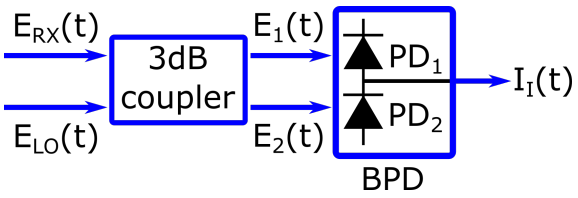

Figure 3.2: Coherent receiver using 3 dB coupler. BPD: balanced photodiodes.

An ideal 3 dB coupler (balanced, symmetric and lossless) can be described in terms of transfer matrix [109] as:

$$\begin{bmatrix} E_1(t) \\ E_2(t) \end{bmatrix} = \frac{1}{\sqrt{2}} \begin{bmatrix} 1 & j \\ j & 1 \end{bmatrix} \begin{bmatrix} E_{RX}(t) \\ E_{LO}(t) \end{bmatrix} \tag{3.3}$$

The produced photocurrent on photodiode 1 (PD1) is given by :

$$I_1(t) = \eta \Big| E_1(t) \Big|^2 = \frac{1}{2} \eta \Big| E_{RX}(t) + jE_{LO}(t) \Big|^2, \tag{3.4}$$

where η is the photodiode responsivity in A/W. Considering optical fields expressions Eq. (3.1) and Eq. (3.2), the produced photocurrent on PD1 can be expressed as:

$$I_1(t) = \frac{1}{2}\eta P_{RX} + \frac{1}{2}\eta P_{LO} + \eta\sqrt{P_{RX}P_{LO}}\cos((\omega_{LO} - \omega_{RX})t + \Phi_{LO} - \Phi_{RX}) \tag{3.5}$$

Note that the third term averages to zero in the case of incoherent waves, meaning no interference is produced. Coherent detection provides strong isolation to background light as only signals that are coherent with the LO wave can produce the interference signal (third term in Eq. (3.5)). In FMCW LIDAR, the LO is usually a beam split of the TX signal, which ensures the interference effect.

Same derivations for PD2 yield to:

$$I_2(t) = \eta \Big| E_2(t) \Big|^2 = \frac{1}{2} \eta \Big| jE_{RX}(t) + E_{LO}(t) \Big|^2 \tag{3.6}$$

$$I_2(t) = \frac{1}{2}\eta P_{RX} + \frac{1}{2}\eta P_{LO} - \eta\sqrt{P_{RX}P_{LO}}\cos((\omega_{LO} - \omega_{RX})t + \Phi_{LO} - \Phi_{RX}) \tag{3.7}$$

The balanced configuration outputs a current I_I given by:

$$I_I(t) = I_1(t) - I_2(t) = 2\eta\sqrt{P_{RX}P_{LO}}\cos((\omega_{LO} - \omega_{RX})t + \Phi_{LO} - \Phi_{RX}) \tag{3.8}$$

Therefore, the use a of 3 dB coupler provides the in phase component of the photocurrent $I_I(t)$.

3.2.2 With 90 degree hybrid

The 90° optical hybrid, also called IQ demodulator, is another type of coherent mixer having 2 inputs and 4 outputs, as shown on Fig. 3.3. It is widely used in coherent communications to demodulate complex modulation formats.

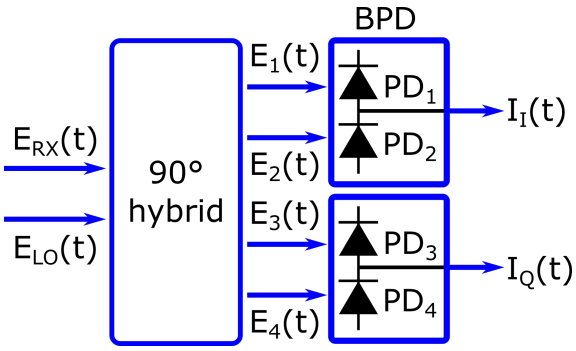

Figure 3.3: Coherent receiver using a 90° optical hybrid. BPD: balanced photodiodes.

In FMCW LIDAR, the two 90° hybrid inputs are the reflected (RX) and local oscillator (LO) signals. The four outputs are the beat signals between RX and 90° shifted version of the LO as described by this transfer matrix [109]:

$$\begin{bmatrix} E_1(t) \\ E_2(t) \\ E_3(t) \\ E_4(t) \end{bmatrix} = \frac{1}{\sqrt{2}} \begin{bmatrix} E_{RX}(t) + E_{LO}(t) \\ E_{RX}(t) - E_{LO}(t) \\ E_{RX}(t) + jE_{LO}(t) \\ E_{RX}(t) - jE_{LO}(t) \end{bmatrix} \tag{3.9}$$

Two pairs of balanced photodetectors enable to recover the in-phase (I) and quadrature (Q) components of the photocurrent that are given by:

$$I_I(t) = I_1 - I_2 = 2\eta\sqrt{P_{RX}P_{LO}}\cos((\omega_{LO} - \omega_{RX})t + \Phi_{LO} - \Phi_{RX}) \tag{3.10}$$

$$I_Q(t) = I_3 - I_4 = 2\eta\sqrt{P_{RX}P_{LO}}\sin((\omega_{LO} - \omega_{RX})t + \Phi_{LO} - \Phi_{RX}) \tag{3.11}$$

Therefore, the 90° hybrid provides the in phase $I_I(t)$ and quadrature $I_Q(t)$ components of the photocurrent. It enables to recover both intensity and phase information between the two interfering signals.

The use of 90° hybrid is beneficial over a simple 3 dB coupler. Indeed, IQ demodulation can solve the complex conjugate ambiguity [110]. Indeed, in FMCW LIDAR, the depth information is extracted from the Fourier transform of the inference signal between LO and RX signals. On the one hand, the use of a 3 dB coupler only provides a real beat signal with frequency $+f_b$ so its Fourier transform has a Hermitian symmetry with two frequency peaks at $+f_b$ and $-f_b$. As a consequence, a target that is approaching or moving away cannot be distinguished, resulting in an artefact on the image. On the other hand, the use of a 90° hybrid allows to reconstruct the complex beat signal from the I and Q components. The Fourier transform of this complex beat signal would result in a single peak at $+f_b$, removing the complex conjugate artifact.

The efficiency of a 90° optical hybrid is quantified by its insertion loss (IL), common-mode rejection ratio (CMRR), imbalance and phase error.

The 90° optical hybrid insertion loss IL is defined by:

$$IL[dB] = 10\log_{10}\left(\frac{\Sigma_i P_{out,i}}{P_{in}}\right) \tag{3.12}$$

where P_{in} is the input power in one arm of the hybrid and and $P_{out,i}$ is the optical power of the ith output.

The common mode rejection ratio (CMRR) is defined for the in-phase (I) and quadrature (Q) arms as:

$$CMRR_I[dB] = 20\log_{10}\left(\left|\frac{P_1 - P_2}{P_1 + P_2}\right|\right) \tag{3.13}$$

$$CMRR_Q[dB] = 20\log_{10}\left(\left|\frac{P_3 - P_4}{P_3 + P_4}\right|\right) \tag{3.14}$$

The CMRR is computed for a field applied to a single input port. Therefore, we denote as $(CMRR_I, CMRR_Q)_{RX}$ for input signal in the RX port and $(CMRR_I, CMRR_Q)_{LO}$ for input signal in the LO port.

The imbalance is defined as :

$$Im_I = 10\log_{10}\left(\frac{P_1}{P_2}\right) \tag{3.15}$$

and

$$Im_Q = 10\log_{10}\left(\frac{P_3}{P_4}\right) \tag{3.16}$$

We denote as $(ImI, ImQ)_{RX}$ for input signal in the RX port and $(Im_I, Im_Q)_{LO}$ for input signal in the LO port.

The phase error is defined as the error from the expected 90° phase shift [111][112] between :

- $E_{RX} + E_{LO}$ and $E_{RX} - jE_{LO}$
- $E_{RX} - E_{LO}$ and $E_{RX} + jE_{LO}$

In the next chapter, we will report on the measured performance metrics of a fabricated silicon nitride 90° hybrid. We will compare our results to state of the art 90° hybrid demonstrations and with the Integrated Coherent Transmitter-Receiver Optical Subassembly (IC-TROSA) [113] specifications.

3.2.3 Balanced photodetection

A balanced photodetector is composed of two photodiodes connected in series. Under the same illumination, if the photodiodes are identical, the produced photocurrents are equal and the balanced photodetector outputs zero signal. Subtracting the two signals suppresses the noise fluctuations associated to the laser relative intensity noise (RIN) and DC noise terms [90].

Here, we consider the coherent receiver formed by the 90° and the balanced photodiodes in Fig. 3.3. In the presence of laser relative intensity noise (RIN), the photocurrents produced in PD 1 and PD2 are expressed as:

$$I_1 = \frac{1}{2}\eta\Big(P_{LO}+P_{RX}+RIN(t)\Big)+\eta\sqrt{P_{LO}P_{RX}}\cos\Big[(\omega_{LO}-\omega_{RX})t+\Phi_{LO}-\Phi_{RX}\Big] \quad (3.17)$$

$$I_2 = \frac{1}{2}\eta\Big(P_{LO}+P_{RX}+RIN(t)\Big)-\eta\sqrt{P_{LO}P_{RX}}\cos\Big[(\omega_{LO}-\omega_{RX})t+\Phi_{LO}-\Phi_{RX}\Big]\Big) \quad (3.18)$$

Balanced photodetection results in a photocurrent I_I equals to the difference between I_1 and I_2:

$$I_I = I_1 - I_2 = 2\eta\sqrt{P_{LO}P_{RX}}\cos\Big[(\omega_{LO}-\omega_{RX})t+\Phi_{LO}-\Phi_{RX}\Big] \quad (3.19)$$

Therefore, the DC terms and the laser RIN are suppressed with perfectly balanced photodetection.

In balanced photodetection, the common mode rejection ratio (CMRR) expressed in dB, quantifies how weak the difference I_I of the two photocurrents is under equal illumination of the two photodiodes [114]:

$$CMRR = \frac{|I_I|}{|I_1|+|I_2|} \quad (3.20)$$

In [115], more than 20 dB suppression is measured using balanced photodetector.

In the next chapter, we will show measurements of Ge based balanced photodetectors.

3.3 FMCW LIDAR waveforms

In this section, we apply the general background on coherent receivers to the FMCW LIDAR system. We focus on linear frequency modulated waveforms, also called chirps, starting from a frequency f_0 to a frequency f_1 within a modulation period T. The frequency excursion B is defined as $|f_1 - f_0|$ and the chirp rate s is defined as B/T. We will present both sawtooth and triangular frequency modulation.

3.3.1 Sawtooth FMCW waveform

When applying a sawtooth frequency chirp to the laser, the angular frequency $\omega_{LO}(t)$ of the local oscillator is given by :

$$\omega_{LO}(t) = 2\pi st + \omega_0 = \frac{2\pi B}{T}t + \omega_0 \quad (3.21)$$

Fig. 3.4 a) and b) show a representation of a sawtooth linear frequency chirp in time domain and in the Fourier domain respectively.

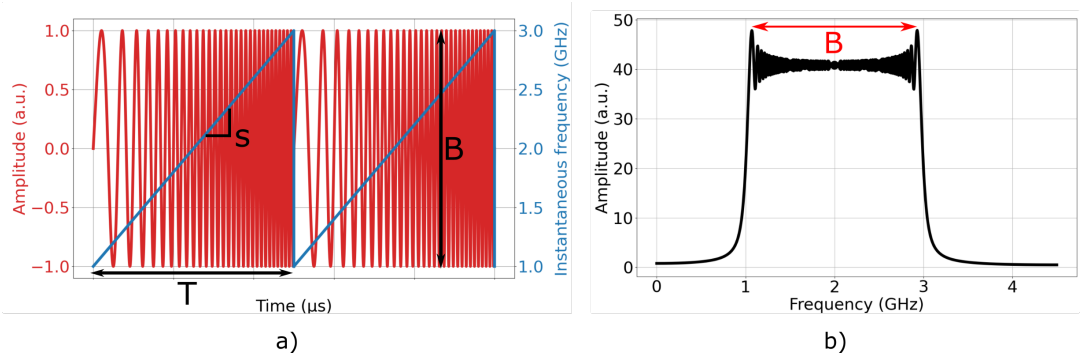

Figure 3.4: Representation of a sawtooth linear frequency chirp a) in time domain and b) in the Fourier domain.

The phase component of the local oscillator $\Phi_{LO}(t)$ is given by:

$$\Phi_{LO}(t) = \int_0^t \omega_{LO}(t)dt = \frac{1}{2}2\pi st^2 + \omega_0 t + \Phi_0 \tag{3.22}$$

where Φ_0 is the initial phase.

The electric field of the linearly chirped local oscillator signal E_{LO} can be expressed by :

$$E_{LO}(t) = E_{LO}^0 \cos(\Phi_{LO}(t)) \tag{3.23}$$

By defining the amplitude of the RX signal as E_{RX}^0, the electric field of the received signal E_{RX} is given by :

$$E_{RX}(t) = E_{RX}^0 \cos(\Phi_{RX}(t,\tau)) \tag{3.24}$$

where the round trip delay τ is considered in the RX signal phase $\Phi_{RX}(t)$ expressed as:

$$\Phi_{RX}(t,\tau) = \Phi_{LO}(t-\tau) = \frac{1}{2}2\pi s(t-\tau)^2 + \omega_0(t-\tau) + \Phi_0 \tag{3.25}$$

For simplicity, we considered a coherent receiver with a 3 dB coupler and balanced photodetectors as described in Section 3.2.1. When these two waves interfere on the coherent receiver, the resulting beat signal is expressed by Eq. (3.8). For sawtooth frequency chirps, injecting Eq. (3.25) into Eq. (3.8), the beat signal is given by :

$$I_b(t,\tau) = 2\eta\sqrt{P_{RX}P_{LO}}\cos(2\pi s\tau t + \omega_0\tau - \frac{2\pi s\tau^2}{2}) \tag{3.26}$$

Similarly, for a 90° optical hybrid, we would have two beat signals $I_{b,I}(t,\tau)$ an $I_{b,Q}(t,\tau)$ corresponding to the in-phase and quadrature components.

The beat signal frequency f_R is given by:

$$f_R = s\tau = s\frac{2R}{c} \tag{3.27}$$

where τ is the round trip delay to the target, R is the target range and c is the speed of light in vacuum. Therefore, the signal produced from coherent detection

of the LO and RX signals, has its frequency proportional to the target range. A Fourier transform is applied to the temporal signal $I_b(t, \tau)$. The beat frequency f_R is then estimated from the spectrum of I_b and the target range is obtained using Eq. (3.27). This principle is summarized in Fig. 3.5.

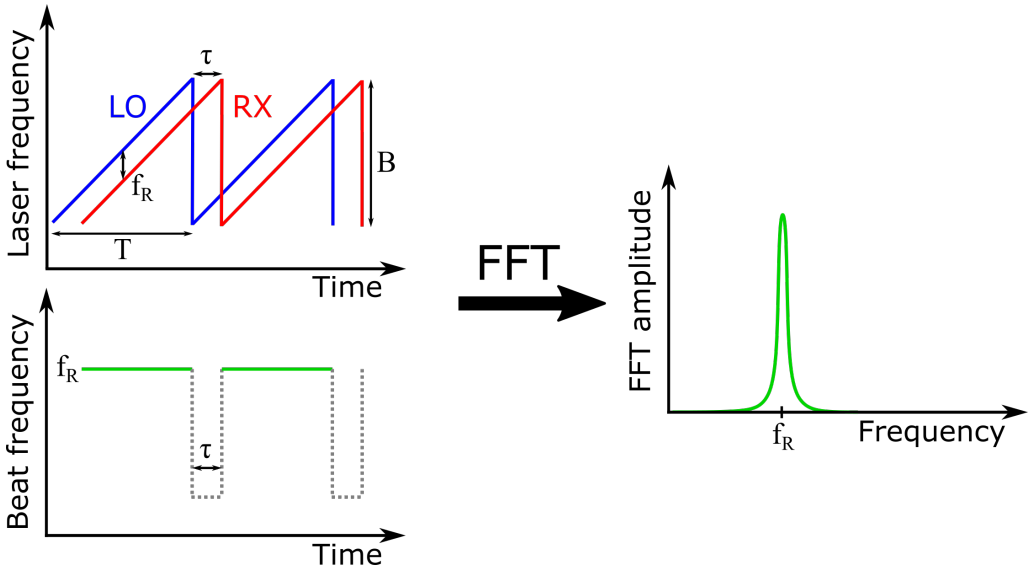

Figure 3.5: FMCW LIDAR principle using sawtooth waveform. FFT: fast Fourier transform.

To avoid any target ambiguity, one modulation ramp is transmitted and received during the measurement period T, i.e. the measurement period T should be larger than the maximum round-trip delay to the target τ_{max} [90]. T is usually taken larger than $5\tau_{max}$ to limit the apparition of spurious signals generated during ramp transitions.

If two objects in the same line of sight are separated by a distance ΔR, corresponding to a round trip delay interval $\Delta\tau$, the difference in their beat frequencies Δf_R is:

$$\Delta f_R = s\Delta\tau = s\frac{2\Delta R}{c} \tag{3.28}$$

In the frequency domain (see Section 3.9.1), two frequency components are resolved if :

$$\Delta f_R > \frac{1}{T} \tag{3.29}$$

where T is the measurement period. This leads to :

$$s\frac{2\Delta R}{c} > \frac{1}{T} \tag{3.30}$$

$$\Delta R > \frac{c}{2B} \tag{3.31}$$

Therefore the range resolutionΔR can be improved by increasing the laser frequency excursion B. To reach 10 cm range resolution, a frequency excursion B of 1.5 GHz is needed.

Now, if we consider that the target is moving with respect to the LIDAR as shown on Fig. 3.6, the generated Doppler frequency shift f_d is given by :

$$f_d = \frac{2v_r}{\lambda} \tag{3.32}$$

where v_r is the radial velocity of the target and λ is the laser wavelength.

The Doppler frequency is added to the beat frequency f_R, producing a new beat frequency f_b given by:

$$f_b = f_R + f_d = s\frac{2R}{c} + \frac{2v_r}{\lambda} \tag{3.33}$$

Therefore, the Doppler shift adds an error to the range estimation, making sawtooth waveforms only suitable for static targets detection.

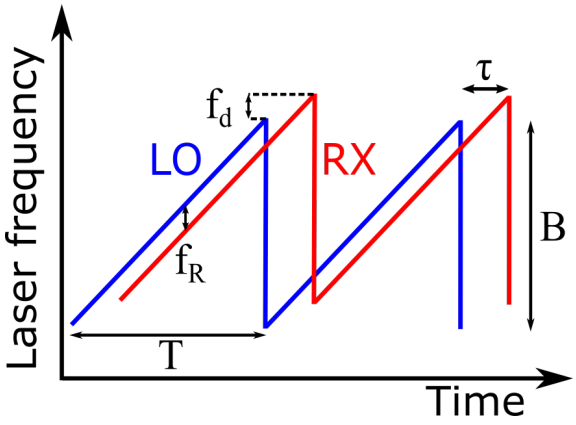

Figure 3.6: FMCW LIDAR principle using sawtooth waveform in the presence of Doppler effect.

In order to measure the target range and radial velocity with a FMCW LIDAR, triangular modulation can be used.

3.3.2 Triangular FMCW waveform

The principle of triangular modulated FMCW LIDAR is shown in Fig. 3.7.

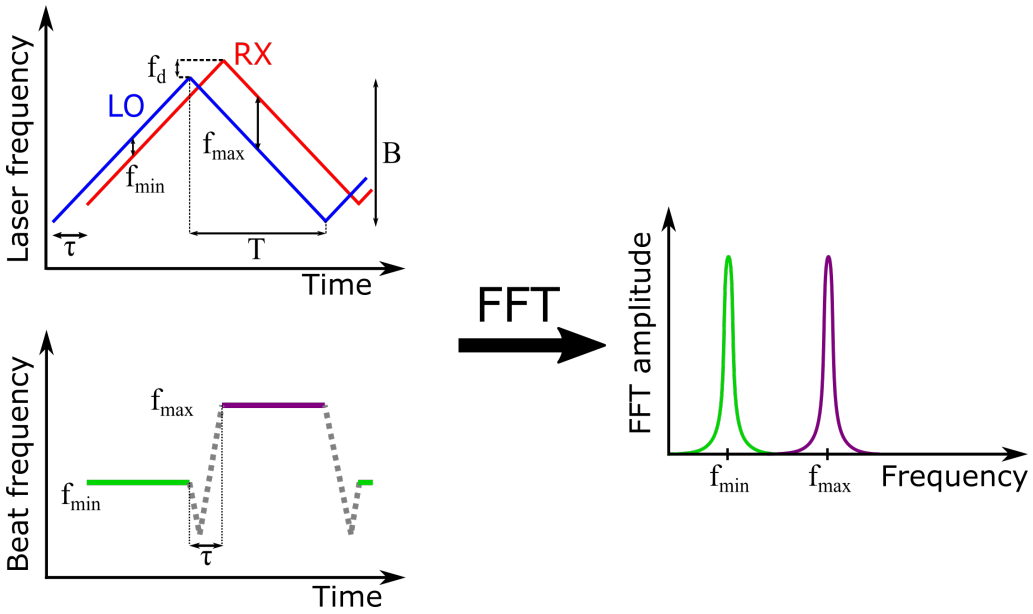

Figure 3.7: FMCW LIDAR principle using triangular waveform. FFT: fast Fourier transform.

For triangular waveforms, the produced beat signal is composed of two intermediate frequencies f_{min} and f_{max}, depending on the rising or falling frequency ramps, that are given by [25]:

$$f_{min} = \frac{2sR}{c} - \frac{2v_r}{\lambda} = f_R - f_d \tag{3.34}$$

$$f_{max} = \frac{2sR}{c} + \frac{2v_r}{\lambda} = f_R + f_d \tag{3.35}$$

where f_R is the beat frequency associated to the range (see Eq. (3.27)) and f_d is the Doppler frequency shift (see Eq. (3.32)).

A Fourier transform is applied to the beat signal for each ramp period T. The beat frequencies f_{min} and f_{max} are then estimated in the frequency domain. The target range R and radial velocity v_r are retrieved from the two beat frequencies using the following equations :

$$R = \frac{c}{4s}(f_{max} + f_{min}) \tag{3.36}$$

$$v_r = \frac{\lambda}{4}(f_{max} - f_{min}) \tag{3.37}$$

Note that a positive radial velocity v_r corresponds to a approaching target (positive Doppler shift).

3.4 Electrical bandwidth

Once the beat photocurrent I_b is produced, a transimpedance amplifier (TIA) is used to amplify and convert the photocurrent into a voltage V_{out} as shown in Fig. 3.8.

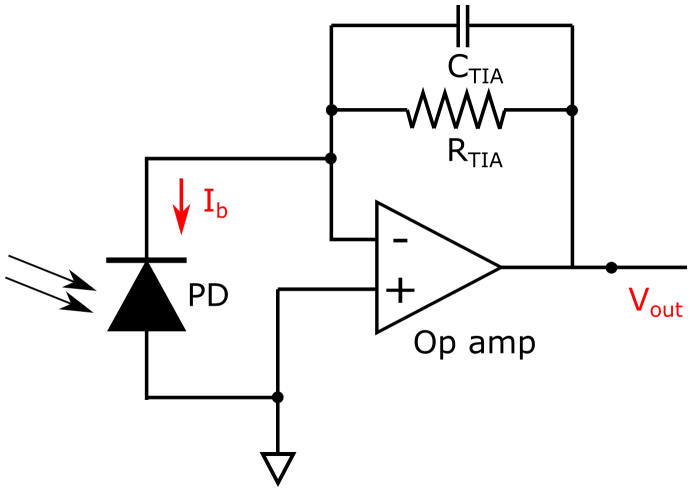

Figure 3.8: Schematic of a simple transimpedance amplifier (TIA) circuit connected to a photodiode (PD) under illumination. Op amp: operational amplifier.

The TIA inverting input has a very high impedance so that the photocurrent flows through the feedback circuit. The transfer function of this component is given by the RC circuit in the feedback loop:

$$\frac{V_{out}}{I_b} = -\frac{R_{TIA}}{1 + j\omega R_{TIA} C_{TIA}} \tag{3.38}$$

Therefore, for frequencies below the cutoff frequency $f_c = \frac{1}{2\pi R_{TIA} C_{TIA}}$, V_{out} can be approximated by:

$$V_{out} \sim -R_{TIA} I_b, \tag{3.39}$$

where R_{TIA} is the transimpedance gain in Ω.

Then, an analog to digital converter (ADC) samples and digitizes the signal. Finally, the digital signal processor (DSP) applies a fast Fourier transform (FFT) to the digital signal in order to extract the beat frequency.

The TIA electrical bandwidth BW_{elec} and the ADC sampling frequency F_s therefore needs to be set according to the operating range R_{max} and velocity v_{rmax} to be detected. The ADC sampling frequency F_s should be larger than twice BW_{elec} to satisfy the Nyquist-Shannon criterion. These lower bounds for BW_{elec} and F_s are given by:

$$BW_{elec} \geq \frac{s2R_{max}}{c} + \frac{2v_{rmax}}{\lambda} \tag{3.40}$$

$$F_s \geq 2BW_{elec} = \frac{s4R_{max}}{c} + \frac{4v_{rmax}}{\lambda} \tag{3.41}$$

As the range and velocity extractions are based on the beat signal intermediate frequency (IF), the required TIA electrical bandwidth BW_{elec} and the ADC sampling frequency F_s are below 1 GHz for long range automotive LIDAR.

In Fig 3.9, we compare two linear frequency chirps. The two chirps produce the same range resolution ΔR as described by Eq. (3.31), as the frequency excursion B

is the same. Nevertheless, for the same target maximum range R_{max} and velocity v_{rmax}, chirp A requires a higher BW_{elec} and F_s as the slope is steeper than for chirp B. In terms of scanning speed using, chirp A has the advantage of requiring half the measurement time of chirp B.

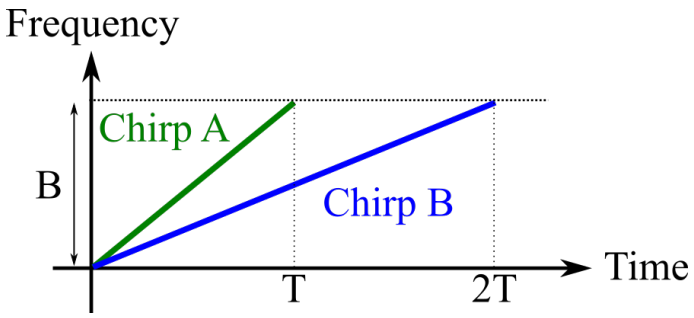

Figure 3.9: Chirp resolution comparison.

3.5 Model description

In this section, we provide a model for deriving the FMCW LIDAR system link budget and signal-to-noise ratio (SNR).

The Table 3.1 summarizes the inputs and outputs of our model.

Inputs	Outputs
Components specifications : laser, passives, photodiodes, electronics	SNR and power budget
Environmental conditions	LIDAR performances

Table 3.1: Summarize of our model inputs and outputs.

For this model, we considered an elementary tile composed of a single TX and single RX. Adding a scanning unit would result in more insertion losses in the TX path. We detail the different elements of Table 3.1 hereafter.

3.6 Free space loss

Once the light gets out of the FMCW LIDAR chip, it undergoes an important free space attenuation L_{fs} that can be approximated by the one-way LIDAR equation [10].

$$L_{fs} = \frac{P_{RX}}{P_{TX}} = e^{-2\alpha R}\rho\frac{\pi\left(\frac{D_{RX}}{2}\right)^2}{\left(\frac{4\pi R^2}{2}\right)}cos(\phi)\eta_{atm}\eta_{coupling} \tag{3.42}$$

where :
- α is the air attenuation factor which typical values are given in Table 3.2.
- R is the target distance to the LIDAR.
- ρ is the target reflectivity. A typical specified value is 10%.
- D_{RX} is the receiver aperture diameter as we considered a circular aperture.
- ϕ is the incident angle on the target.
- η_{atm} is the atmospheric loss coefficient which can be ignored ($\eta_{atm} = 1$) for automotive LIDAR.
- $\eta_{coupling}$ is the light coupling loss from the photonic circuit to free space and vice-versa.

Environmental conditions	α **[neper/km]**	α **[dB/km]**
Clear weather	0.1e-3	0.43
Haze	1e-3	4.3
Fog	10e-3	43

Table 3.2: Table of air attenuation factor values from [38]

The effect of speckle noise is not included in our model. Speckle originates from random interference effects after reflection on diffusive targets. In FMCW LIDAR, the speckle noise usually affects the reflected signal intensity and phase [116].

In addition, the heterodyne efficiency η_{het} could be added in Eq. (3.42) to describe the mismatch in phase and amplitude between the local oscillator (LO) signal and the received signal (RX) signal. As presented in [117][118], the heterodyne efficiency η_{het} is a complex entity which depends on several parameters such as the target distance and aberrations in optical components. Thus, in the following, we assume that the heterodyne efficiency is equal to unity while this factor can be modified according to each LIDAR system.

The free space loss can be divided into three different loss contributions:

a) propagation in air : $e^{-2\alpha R}\frac{\pi\left(\frac{D_{RX}}{2}\right)^2}{\left(\frac{4\pi R^2}{2}\right)}\eta_{atm}$

b) reflection on the target : $\rho.\cos(\phi)$

c) coupling efficiency : $\eta_{coupling}$

The Fig. 3.10 a) gives an example of automotive LIDAR environment specifications, where a clear weather scenario is considered. The coupling efficiency $\eta_{coupling}$ is assumed to be -6 dB (-3 dB for each TX and RX couplers). The resulting loss contributions are summarized Fig. 3.10 b) where total free space L_{fs} is -111.2 dB.

Parameter	Value
Air attenuation factor α	0.43 dB/km
Target range R	200 m
Receiver aperture diameter D_{RX}	1 cm
Atmospheric loss coefficient η_{atm}	1
Target reflectivity ρ	10%
Incidence angle ϕ	0°
Coupling efficiency $\eta_{coupling}$	-6dB

a)

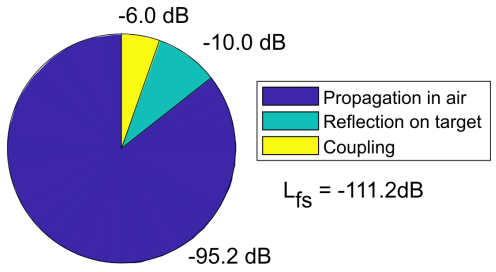

b)

Figure 3.10: a) Example of automotive LIDAR environment specifications and b) contributions to the free space loss.

The major contribution comes from the air propagation term and more specifically the ratio D_{RX}^2/R^2.

3.7 Attenuation due to polarization

During the free space propagation, the polarization can rotate depending on the target surface. As the LIDAR TX and RX couplers are polarization sensitive, the Malus law states that the intensity attenuation is proportional the $\cos^2\beta$, where β is the angle between the two states of polarization (SOP), as shown on Fig. 3.11.

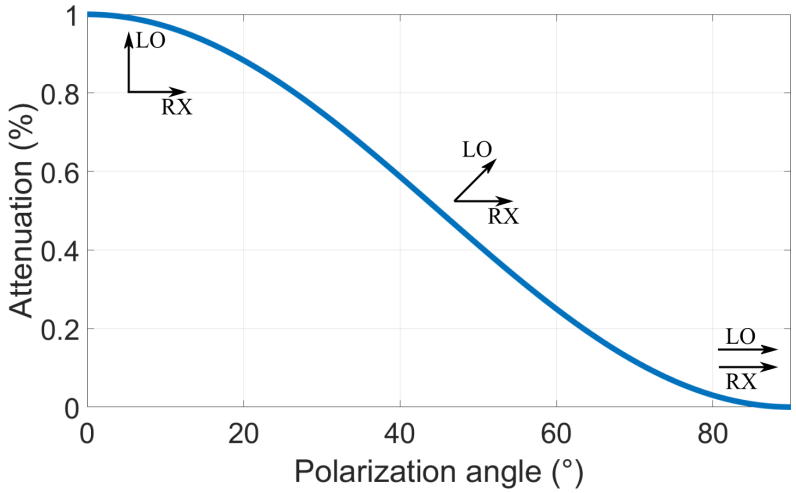

Figure 3.11: Attenuation due to polarization.

Polarization diversity coherent receiver [119] can be implemented to perform polarization mapping of the environment. Fig. 3.12 shows a schematic of a polarization diverse coherent receiver, where the coherent receiver is duplicated to detect the two orthogonal polarizations [109]. Such scheme provides additional information on the target at the cost of increased complexity. For example, in [31], targets are classified based on their material polarization signature using this type of receiver.

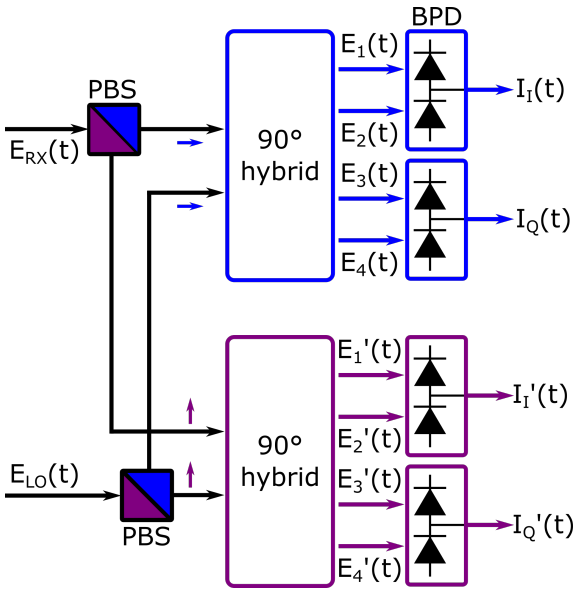

Figure 3.12: Polarization diverse coherent receiver. PBS: polarization beam splitter.

In our model, we considered a single polarization coherent receiver and the LO and RX states of polarization (SOP) are considered parallel.

3.8 Laser chirp nonlinearity

Any nonlinear distortion in the laser frequency chirp impacts the measurement accuracy of FMCW LIDARs [120]. Indeed, nonlinearities broaden the detected spectrum and can create additional peaks in the detected spectrum due to intermodulation distortions. This effect results in the apparition of ghost targets, creating false alarms as shown in Section 3.8.

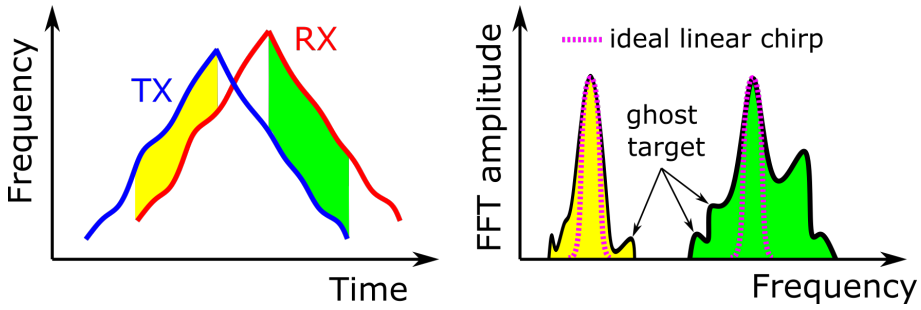

Figure 3.13: Illustration of nonlinear distortion on the beat signal.

Producing highly linear FMCW waveforms is challenging. This can be either achieved through direct laser modulation or by using an external modulator with a fixed laser frequency. For semiconductor lasers, direct modulation is based on the modulation of the laser injection current. However, the relationship between optical frequency and injection current is nonlinear. The laser frequency modulation is based on thermal and free-carrier plasma dispersion effects depending on the modulation frequency [121]. At low modulation frequencies (below 100 kHz), increasing the injection current increases the refractive index and the cavity length due to thermal heating of the junction, reducing the optical frequency (wavelength is increased

: red shift). At high modulation frequencies (above 1 MHz), increasing the injection current decreases the refractive index due to free-carrier plasma dispersion effect, increasing the optical frequency (wavelength is increased : blue shift). Usually, a nonlinear distortion, defined as the standard deviation of the optical frequency after removal of a linear fit, below 0.1% is desired [122].

We further discuss this point in next chapter with the measurement of a silicon IQ modulator with a monolithically integrated III-V/Si semiconductor optical amplifier (SOA) to quantify chirp linearity. In this model, the LIDAR source produces an ideal linear frequency chirp, while nonlinear distortion could be added in the future as demonstrated in [123].

3.9 FMCW LIDAR link budget and noise study

In this section, we derive a noise model for the typical FMCW shown in Fig. 3.14. The system noise sources are expressed in terms of their noise spectral density with unit A^2/Hz.

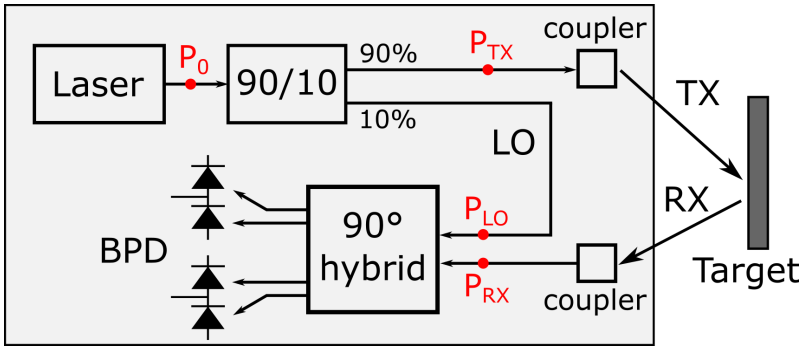

Figure 3.14: Schematic of the FMCW LIDAR tile. 90/10: 90%-10% splitter; BPD: balanced photodiodes.

The corresponding link budget using the free space loss scenario of Fig. 3.10 is given in Table 3.3.

Power	Value [dBm]	Value [mW]
P_0	13.5	22.4
P_{TX}	13	20
P_{LO}	3.5	2.2
P_{RX}	-98.2	1.5e-10

Table 3.3: Link budget of the FMCW LIDAR system.

3.9.1 FMCW LIDAR signal

The FMCW LIDAR signal, without considering any laser phase noise and using balanced photodetection with 3 dB coupler is given by Eq. (3.26).

This beat signal is digitized and a range estimation is performed in the frequency domain using a Fourier Transform of this signal. As LIDAR measurements are

performed at over each finite ramp period T, a window function $w(t)$ is applied to the produced photocurrent $I_b(t)$ [124]. We considered a rectangular window function defined as :

$$w(t) = rect(t) = \begin{cases} 1 & \text{if } |t| < \frac{T}{2} \\ 0 & \text{otherwise} \end{cases} \tag{3.43}$$

Therefore, the windowed photocurrent $I_{bw}(t)$ is given by:

$$I_{bw}(t) = I_b(t)w(t) \tag{3.44}$$

In the frequency domain, this product of functions appears as a convolution product between the two Fourier transforms. From [90], the baseband photocurrent spectrum $S^0_{bw}(f)$ (without considering any laser phase noise) can expressed by:

$$S^0_{bw}(f) = 4\eta^2 P_{LO} P_{RX} T.sinc^2\Big(\frac{T\omega}{2}\Big) \tag{3.45}$$

Eq. (3.45) shows that time domain windowing leads to a broadening of the baseband photocurrent spectrum (which would be a perfect Dirac distribution without windowing), leading to the expression of the resolution given in Eq. (3.31).

3.9.2 Shot noise and receiver sensitivity

The shot noise consists of fluctuations in the detected photocurrent due to the random photon arrival on the detector. The power spectral density of the shot noise σ^2_{shot} generated at the receiver is given by :

$$\sigma^2_{shot} = 2q\eta P_{LO} + 2q\eta P_{RX} + 2qI_d \sim 2q\eta P_{LO} \tag{3.46}$$

where q is the charge of an electron, I_d is the photodiode dark current. The shot noise produced by the LO is dominant as $P_{LO} >> P_{RX}, I_d/\eta$.

The receiver is in the fundamental quantum-limited regime when it reaches the shot noise limited operation. In this case, the SNR over a measurement time window T is proportional to the received optical power P_{RX} and is given by:

$$SNR = \frac{i_s^2}{\sigma^2_{shot}} \tag{3.47}$$

where the windowed photocurrent spectrum is given by:

$$i_s^2 = 4\eta^2 P_{LO} P_{RX} T \tag{3.48}$$

using Eq. (3.48) and Eq. (3.46), the shot noise limited SNR becomes independent of P_{LO}:

$$SNR = \frac{2\eta P_{RX} T}{q} \propto N \tag{3.49}$$

where N is the number of received photons over the measurement period T. Under shot noise elimited operation, the FMCW LIDAR is said to be single-photon sensitive as it is proportional to the number of photons [10].

The receiver sensitivity, i.e. the minimum power P_{RX} (or minimum number of received photons N) to satisfy a threshold SNR_{th} ensuring proper range and velocity estimation is given by:

$$P_{RX} \geq \frac{qSNR_{th}}{2\eta T} \tag{3.50}$$

To satisfy $SNR_{th} = 20$ (13 dB) and by considering a photodiode responsivity η of 1 A/W and a measurement period T of 10 μs, the received power P_{RX} should be higher than 0.16 pW (-98 dBm). Under the scenario described in Fig. 3.10, the minimum transmitted power P_{TX} should be 18 dBm. Reaching this amount of TX power is challenging when using integrated III-V/Si lasers as shown in the Table 3.3 where typical laser output power is 13.5 dBm, corresponding to a transmitted power P_{TX} of 13 dBm. We therefore propose to integrate a booster semiconductor optical amplifier (SOA) to amplify the transmitted signal, as shown in Fig. 3.15.

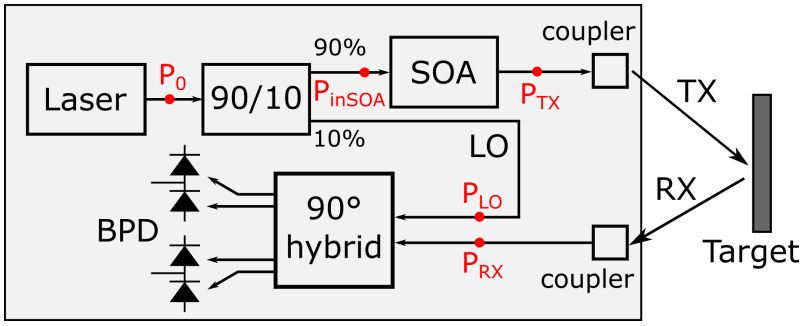

Figure 3.15: FMCW LIDAR architectures with a booster semiconductor optical amplifier (SOA) added at the TX. 90/10: 90%-10% splitter; BPD: balanced photodiodes.

The corresponding link budget using the free space loss example of Fig. 3.10 and considering a SOA gain of 10 dB, is given in Table 3.4.

Power	Value [dBm]	Value [mW]
P_0	13.5	22.4
P_{inSOA}	13	20
P_{TX}	23	199.5
P_{LO}	3.5	2.2
P_{RX}	-88.2	1.5e-9

Table 3.4: Link budget of the FMCW LIDAR system using a booster SOA.

Nevertheless, even if SOA can provide a gain larger than 20 dB [125], it also adds noise due to amplified spontaneous emission (ASE), degrading the SNR. We further discuss this point hereafter.

3.9.3 SOA noise

The noise in a semiconductor optical amplifier (SOA) is related to Amplified Spontaneous Emission (ASE). The SOA input signal interacts with the ASE noise during propagation along the amplifier structure. This interaction generates 3 categories of

noise : the shot noise σ^2_{shot}, the signal-spontaneous beat noise σ^2_{s-sp}, the spontaneous-spontaneous beat noise σ^2_{sp-sp} [126][127].

The shot noise power spectral density σ^2_{shot} of Eq. (3.46) is modified in the presence of SOA and is given by:

$$\sigma^2_{shot} = 2q\eta P_{RX}(G) + 2q\eta P_{LO} + 2q\eta P_{ASE} + 2qI_{dark} \tag{3.51}$$

where $P_{RX}(G)$ is the received power in the presence of a booster SOA in the TX path, and P_{ASE} is the amplified spontaneous emission (ASE) noise power at the receiver (i.e. impacted by the free space attenuation) given by:

$$P_{ASE} = 2h\nu n_{sp} B_0 (G-1) L_{fs} \tag{3.52}$$

where we considered an optical filter with bandwidth B_0 at the receiver, G is the SOA gain, n_{sp} is the population inversion factor, and L_{fs} is the free space loss defined by Eq. (3.42).

For a two-level system, n_{sp} is given by:

$$n_{sp} \propto \frac{N_2}{N_2 - N_1} \tag{3.53}$$

where N_1 and N_2 are the carrier density at the ground and excited states respectively. The population inversion factor is always greater than 1 with a theoretical limit corresponding to complete carrier inversion when $N_1 = 0$ i.e. $n_{sp} = 1$.

As for Eq. (3.46), the received power P_{RX} and the dark current term are negligible compared to P_{LO}. The ASE term is also negligible compared to the LO term [126], yielding to the same expression as Eq. (3.46) :

$$\sigma^2_{shot} \sim 2q\eta P_{LO} \tag{3.54}$$

Nevertheless, the dominant noise added by SOA originates from the beating between the amplified signal and the ASE, also known as signal-spontaneous beat noise. The signal-spontaneous beat noise power spectral density σ^2_{s-sp} is composed of LO-ASE and RX-ASE beat noises and is given by [128] :

$$\sigma^2_{s-sp} = \sigma^2_{LO-sp} + \sigma^2_{RX-sp} = 4q\eta n_{sp}(G-1)P_{LO}L_{fs} + 4q\eta n_{sp}(G-1)P_{RX}(G)L_{fs} \tag{3.55}$$

As the LO-ASE beat noise is the dominant term, the Eq. (3.55) reduces to:

$$\sigma^2_{s-sp} \sim \sigma^2_{LO-sp} = 4q\eta P_{LO} n_{sp}(G-1)L_{fs} \tag{3.56}$$

From Eq. (3.56), it can be seen that LO-ASE beat noise is strongly decreased by free space attenuation L_{fs}, the SOA being implemented in the LIDAR transmitter path and not on the LO path (see Fig. 3.15).

Finally the spontaneous-spontaneous beat noise power spectral density σ^2_{sp-sp} is given by [128]:

$$\sigma^2_{sp-sp} = 4q^2 B_0 n^2_{sp}(G-1)^2 L^2_{fs}, \tag{3.57}$$

where B_0 is the optical filter bandwidth used before photodetection.

The spontaneous-spontaneous beat noise is eliminated by the narrow band optical filter with bandwidth B_0 placed at the receiver.

Noise figure

The Noise Figure (NF) quantifies the noise added by the SOA. Assuming that the major contribution to the noise figure (NF) comes from the beating between amplified signal and ASE. and is expressed as [129][126]:

$$NF \sim 10log_{10}\Big(\frac{P_{ASE}}{Gh\nu B_0 L_{fs}}\Big) \sim 10log_{10}(2n_{sp}) \tag{3.58}$$

Therefore, for an ideal amplifier with total population inversion $n_{sp} = 1$ the NF theoretical limit of 3 dB is retrieved [126].

3.9.4 Thermal noise

Thermal noise is responsible for variations in the photocurrent due to thermal agitation of electrons in conductor materials. The thermal noise spectral density $\sigma^2_{thermal}$ is given by :

$$\sigma^2_{thermal} = \frac{4kT_{amb}}{R} \tag{3.59}$$

where k is the Boltzmann constant, T_{amb} is the ambient temperature and R is the photodiode load resistor, when no transimpedance amplifier (TIA) is considered.

3.9.5 NEP noise for PD with TIA

If a TIA is considered after photodetection, the Noise Equivalent Power (NEP) of the optical receiver (PD+TIA) can be defined, which integrates thermal noise and additive noise from TIA active circuitry. It corresponds to the PD minimum detectable input power (i.e. the optical power producing a signal to noise ratio of 1 in a 1 Hz bandwidth).

The NEP of the TIA σ^2_{NEP} is given by:

$$\sigma^2_{NEP} = NEP^2.\eta^2 \tag{3.60}$$

where the NEP is expressed in $W/\sqrt{Hz}$

3.9.6 Quantization noise

The quantization noise is the result of the converting analog values into discrete digital values. The ADC quantization noise spectral density $\sigma^2_{quantization}$ is given by [43]:

$$\sigma^2_{quantization} = \Big(\frac{V_{ADC}}{R_{TIA}}\Big)^2 \frac{1}{12(2^N-1)^2 BW_{ADC}} \tag{3.61}$$

where N is the ADC effective number of bits (ENOB), V_{ADC} is the input voltage range of the ADC and BW_{ADC} is the ADC bandwidth.

3.9.7 Relative intensity noise (RIN)

The laser relative intensity noise (RIN) describes the optical output power stability of a laser. The RIN is expressed by:

$$RIN = \frac{\left\langle \Delta P(t) \right\rangle^2}{P_0^2} \tag{3.62}$$

where $\Delta P(t)$ is the optical power fluctuations and P_0 is the average detected optical power. The RIN can be easily measured by connecting the laser output on a photodetector and analyze the photocurrent spectrum on an electrical spectrum analyzer. The unit of RIN is Hz^{-1} or dBc/$\sqrt{Hz}$ in relative. The RIN power spectral density σ^2_{RIN} is given by :

$$\sigma^2_{RIN} = \eta^2(P^2_{LO} + P^2_{RX})RIN \sim \eta^2 P^2_{LO} RIN, \tag{3.63}$$

as $P_{LO} >> P_{RX}$.

In our model, we consider ideal balanced photodiodes, which suppresses the RIN contribution as described in Section 3.2.3.

3.9.8 Phase noise

Laser produces coherent light waves. At a given time, spatial coherence ensures that all the points of the laser field located in a plane perpendicular to the propagation direction have the same phase. Laser beams are narrow and directive due to spatial coherence. At a given location, temporal coherence means that each emitted waves are in phase at any times. Temporal coherence is related to the purity of the laser spectrum [10].

As FMCW LIDAR relies on coherent detection, the temporal coherence is essential to ensure interferences between the LO and the RX signals over the operating range. Temporal coherence is quantified in terms of coherence time τ_c, which corresponds to the propagation delay over which the temporal coherence of the signal is ensured. Equivalently, the coherence length L_c corresponds to the propagation distance over which the temporal coherence is ensured.

In practice, laser sources are not perfectly monochromatic as they exhibit phase noise due to spontaneous emission and external fluctuations, so the temporal coherence is not infinite. The laser phase noise is usually quantified by the full-width at half maximum (FWHM) of the laser spectrum, also known as the laser linewidth $\Delta\nu$.

Assuming a Lorentzian laser lineshape, the laser coherence length L_c is inversely proportional to the laser linewidth $\Delta\nu$ and is defined as:

$$L_c = c\tau_c = \frac{c}{\pi\Delta\nu} \tag{3.64}$$

where c is the speed of light in vacuum.

The Table 3.5 summarized the coherence length values for several laser linewidth. Typical off the shelf DFB lasers have 1 MHz linewidth, corresponding to 95 m coherence length. Note that for FMCW LIDAR, as the round-trip distance to the target matters, the laser must be coherent within twice the coherence length $2L_c$.

Linewidth $\Delta\nu$	Coherence length L_c
5 MHz	19 m
1 MHz	95 m
500 kHz	190 m
100 kHz	950 m
1 kHz	95 km

Table 3.5: Table of coherence length values L_c for several laser linewidths $\Delta\nu$.

In the next section we describe the laser phase noise model that we implemented and verify its validity with Monte Carlo simulations.

3.10 Laser phase noise model

The laser electric field in the presence of phase noise can be expressed by :

$$E(t) = \cos(\omega(t)t + \Phi_n(t)) \tag{3.65}$$

where $\Phi_n(t)$ is a zero-mean stationary random Gaussian process.

Laser spontaneous emission produces a white laser frequency noise spectrum $S_{\dot{\Phi}_n}(\omega)$ equals to the laser linewidth $\Delta\omega = 2\pi\Delta\nu$ [130].

The baseband spectrum of the laser electric field $S_e^0(\omega)$ is expected to have a Lorentzian shape with FWHM equals to the laser linewidth $\Delta\omega$ in the presence of white frequency noise, which is given by [131][90]:

$$S_e^0(\omega) = \frac{\Delta\omega}{(\frac{\Delta\omega}{2})^2 + \omega^2} \tag{3.66}$$

To check the validity of the laser phase noise model, we verified, through Monte Carlo simulations using Matlab, the Lorentzian broadening by averaging the laser spectrum over multiple iterations. At each iteration, a frequency noise sample is picked within zero-mean Gaussian distribution of variance $\sigma^2 = \Delta\nu/(2\pi)$ corresponding to a white frequency noise [90]. The frequency noise sample is integrated over time to retrieve the laser phase noise. Using the computations in [90], we computed the laser field autocorrelation with the cosine of the phase noise. For a wide-sense stationary random process $x(t)$, the autocorrelation function of $x(t)$, $R_x(u)$ is defined as:

$$R_x(u) = E\left\{x(t)x(t-u)\right\}, \tag{3.67}$$

where $E\{.\}$ is the statistical expectation. For an ergodic random process, averaging over time can replace expectation as:

$$R_x(u) =< x(t)x(t-u) >_t \tag{3.68}$$

where $< . >_t$ stands for averaging over time.

The laser baseband spectrum is obtained by taking the Fourier transform of the autocorrelation and averaging of the spectrum if realized over multiple iterations. Fig. 3.16 shows Monte Carlo simulations of the 1 MHz linewidth laser spectrum for

a) 10 and b) 1000 iterations for averaging, showing the convergence to a Lorentzian shape with FWHM equals to the laser linewidth $\Delta\nu$. This confirms our model based on the Lorentzian broadening starting with a white laser frequency noise.

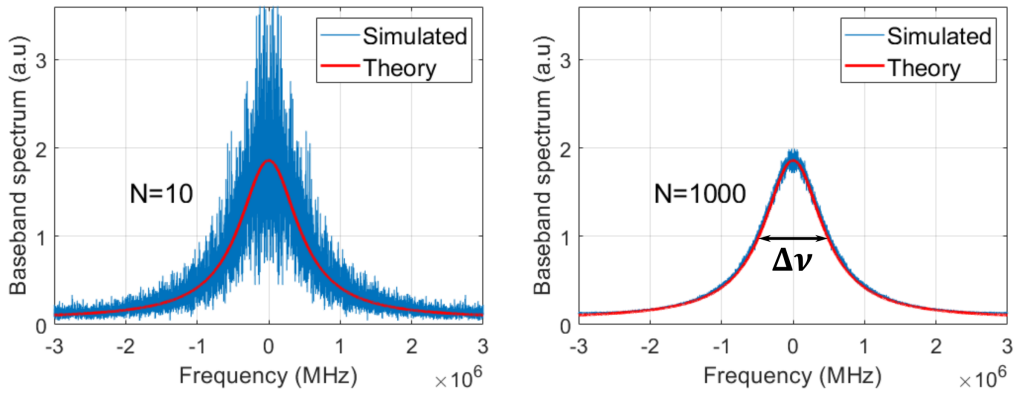

Figure 3.16: Monte Carlo simulations to validate the Lorentzian shape of the phase noise considering a laser white frequency noise model with N=10 and N=1000 iterations for averaging, and a laser linewidth $\Delta\nu$ of 1 MHz.

This model can be adapted to any form of laser phase noise. In [132], it is shown that the presence of 1/f noise broadens the laser spectrum into a Gaussian lineshape. Therefore, a Voigt lineshape could be considered as in [133], to account for the combined white frequency noise Lorentzian lineshape and 1/f noise Gaussian lineshape. In [134], the same derivation is applied to the measured colored frequency noise of a DBR laser.

In our model, we used a white frequency noise which gives a first good approximation to evaluate the impact of phase noise on the laser spectrum. In the next section, we describe the effect of the laser phase noise on the LIDAR photocurrent.

3.11 Impact of phase noise on the photocurrent

In the presence of laser phase noise, the chirped LO and RX electric fields are given by :

$$E_{LO}(t) = \cos(\Phi_{LO}(t) + \Phi_n(t)) \tag{3.69}$$

$$E_{RX}(t,\tau) = \cos(\Phi_{RX}(t,\tau) + \Phi_n(t-\tau)) \tag{3.70}$$

where $\Phi_n(t)$ is a phase noise contribution, $\Phi_{LO}(t)$ and $\Phi_{RX}(t) = \Phi_{LO}(t-\tau)$ given by Eq. (3.22) and Eq. (3.25) respectively.

The resulting photocurrent $I_b(t,\tau)$ detected at the output of the FMCW LIDAR photodiode is given by:

$$I_b(t,\tau) \propto \cos(\Phi_{LO}(t) - \Phi_{LO}(t-\tau) + \Delta\Phi_n(t,\tau)) \tag{3.71}$$

where $\Delta\Phi_n(t,\tau) = \Phi_n(t) - \Phi_n(t-\tau)$.

It is shown in [90] that the photocurrent baseband spectrum $S_i^0(\omega)$ over an measurement period T is given by:

$$S_i^0(\omega) = 4\eta^2 P_{RX} P_{LO} \left[T sinc^2\left(\frac{T\omega}{2}\right) e^{-\frac{2\tau}{\tau_c}} + \frac{\tau_c}{1+(\frac{\omega\tau_c}{2})^2} \cdot \left(1 - e^{-\frac{2\tau}{\tau_c}} \left[\cos(\omega\tau) + \frac{2}{\omega\tau_c}\sin(\omega\tau)\right]\right)\right] \tag{3.72}$$

The first term of Eq. (3.72) corresponds to the beat signal tone. The cardinal sine function is the result of the finite observation time T. The second term of Eq. (3.72) is the Lorentzian lineshape arising from the laser phase noise.

In the coherent regime where $\tau << \tau_c$, the first term of Eq. (3.72) is dominant and a clear beat tone is detected with a phase noise attenuation term $e^{-\frac{2\tau}{\tau_c}}$ almost equal to 1.

For targets located beyond the coherence length i.e. $\tau >> \tau_c$, the local oscillator (LO) signal and the received (RX) signal are strongly uncorrelated. The exponential in the first term of Eq. (3.72) converges to zero, while the second term converges to the Lorentzian function with FWHM equals to $2\Delta\nu$ i.e. twice the laser linewidth.

Fig. 3.17 illustrates the simulated spectra of the detected current for different single-trip target ranges (i.e. different values of τ) considering a laser linewidth of 1 MHz, corresponding to a laser coherence length of 95m (47.5 m round-trip) and an observation time T of 10 μs. The ratio τ/τ_c ranges from 0.8 at 20m to 4.2 at 100m.

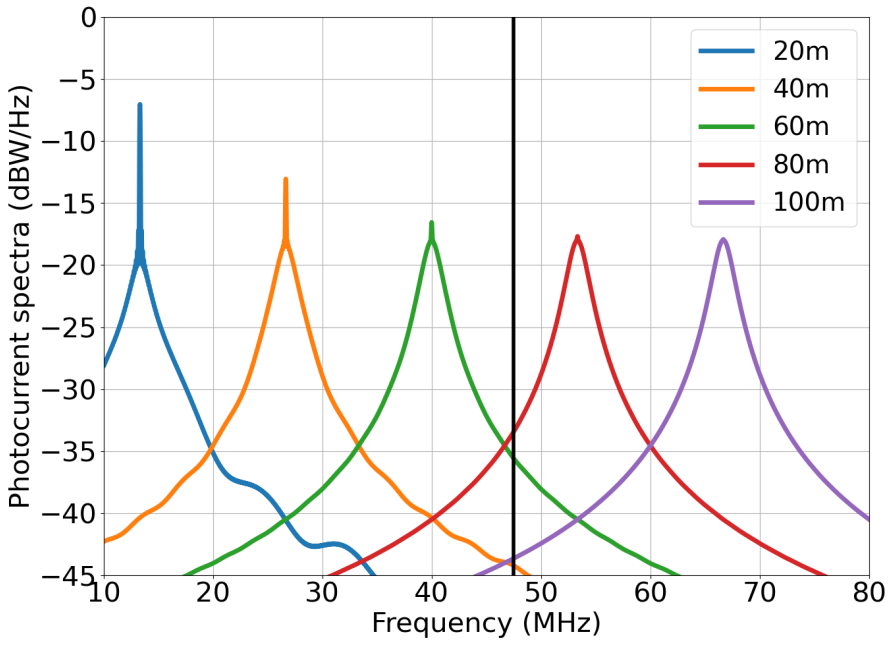

Figure 3.17: Simulation of FMCW LIDAR photodetected current spectra for different target ranges, considering a laser linewidth of 1 MHz, corresponding to a laser coherence length of 95m (47.5 m single-trip, 95 m round-trip).

From Fig. 3.17, targets located within the laser coherence length have a cardinal sine profile corresponding to the first term of Eq. (3.72). For targets that are lo-

cated beyond the laser coherence length, the photocurrent spectrum broadens and decreases in intensity to a Lorentzian profile corresponding to the second term of Eq. (3.72).

3.12 Signal-to-noise ratio (SNR)

In this section, we perform SNR simulations for the FMCW LIDAR architecture comprising a booster SOA as shown in Fig. 3.15. We considered a single TX and RX LIDAR system without scanning module. The scanning module would add insertion loss to the system, reducing the TX power.

The Table 3.6 summarizes the signal an noise formulas for SNR computations at the beat frequency.

Parameter	Power spectral density	Units
Windowed signal s^2	$4\eta^2.P_{RX}.P_{LO}.T.e^{-\frac{2\tau}{\tau_c}}$	A^2/Hz
Shot noise σ^2_{shot}	$2q.\eta.P_{LO}$	A^2/Hz
Phase noise σ^2_{phase}	$\eta^2 P_{LO} P_{RX} \tau_c \left[1 - e^{-\frac{2\tau}{\tau_c}} \left(1 + \frac{2\tau}{\tau_c}\right)\right]$	A^2/Hz
Thermal noise $\sigma^2_{thermal}$	$\frac{4kT_{amb}}{R_{TIA}}$	A^2/Hz
ADC noise $\sigma^2_{quantization}$	$\left(\frac{V_{ADC}}{R}\right)^2 \frac{1}{12(2^N-1)^2 BW_{ADC}}$	A^2/Hz
NEP σ^2_{NEP}	$NEP^2.\eta^2$	A^2/Hz
SOA noise σ^2_{s-sp}	$4q\eta P_{LO} n_{sp}(G-1)L_{fs}$	A^2/Hz

Table 3.6: Summary of formulas for SNR computation at the beat frequency.

Therefore, the Signal to Noise Ratio (SNR) of the FMCW LIDAR system can be expressed as :

$$SNR_{dB} = 10\log_{10}\left(\frac{s^2}{\sigma^2_{phase} + \sigma^2_{shot} + \sigma^2_{thermal/NEP} + \sigma^2_{quantization} + \sigma^2_{s-sp}}\right) \quad (3.73)$$

Note that, in Eq. (3.73), the photodected RIN has not been considered due to balanced photodetection. It has been shown in [43] that thermal/NEP noise contributions in Eq. (3.73) can be neglected by adjusting TIA design with large TIA gain. Moreover, when TIA gain is large, the ENOB of ADC can be chosen so that the ADC quantization noise is negligible [43]. As a consequence, for the following link budget analysis, we will focus on shot noise, SOA noise and laser phase noise contributions in the SNR.

As a comparison, when the LIDAR system does not comprise a SOA and when the laser phase noise is negligible, the shot noise limited operation can be reached for sufficient LO power P_{LO}. The shot noise limited SNR is given by Eq. (3.49).

For detecting far targets (200m), high transmitted power P_{TX} is needed due to important free space losses making the use of SOA necessary. As the ASE noise is attenuated by the free space loss term L_{fs}, the LO-ASE beat noise at the receiver is strongly reduced and the system remains limited by the LO shot noise.

In the following part, we perform simulations on the system SNR comprising a booster SOA to ensure the received signal amplitude is above the detector threshold. We discuss the impact of laser linewidth $\Delta\nu$, measurement period T, receiver aperture D_{rx} and environmental conditions on the SNR.

3.12.1 SNR against linewidth $\Delta\nu$

As discussed in Section 3.11, the laser linewidth has an impact on the photodetected spectrum.

The Fig. 3.18 shows simulations of the SNR against laser linewidth for different target range obtained and using the parameters summarized in Table 3.7.

Parameter	Value	Units
Measurement period T	10	μs
Target reflectivity ρ	10%	-
Photodiode responsivity η	1	A/W
SOA gain G	10	dB
SOA inversion factor n_{sp}	1	-
Air attenuation factor α	0.43	dB/km
Coupling loss η_{loss}	6	dB
Receiver aperture D_{rx}	1	cm
Laser output power P_0	13.5	dBm

Table 3.7: Summary of parameters for SNR simulation against linewidth.

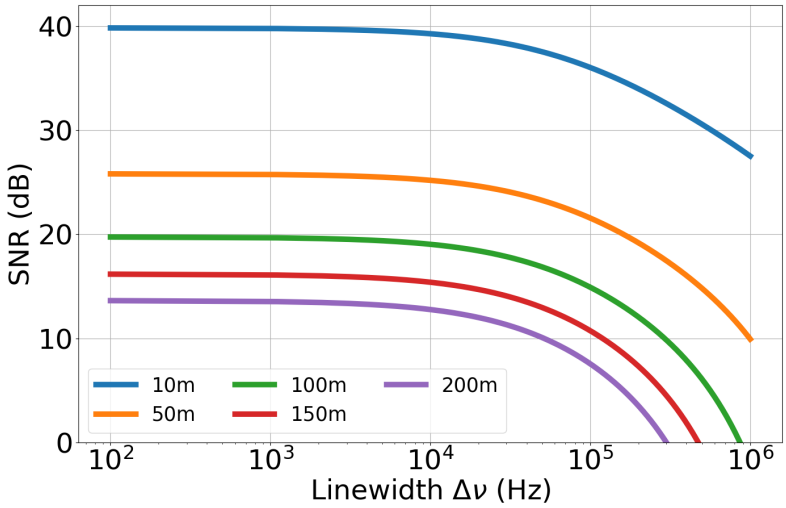

Figure 3.18: SNR against laser linewidth for several target ranges.

From Fig. 3.18, we observe that the laser linewidth is critical for the SNR beyond a certain value, typically between 100 kHz. The observed plateau correspond to a zone where the shot noise is dominant over phase noise. Below this value, lowering the linewidth does not improve the SNR.

We therefore specify a laser linewidth lower than 100 kHz to avoid phase noise limitations on the SNR.

3.12.2 SNR against measurement period T

From Eq. (3.49), the SNR is proportionnal to the measurement period T. The Fig. 3.19 shows the impact of the measurement period T on the SNR using a laser linewidth of 100 kHz and the parameters in Table 3.7.

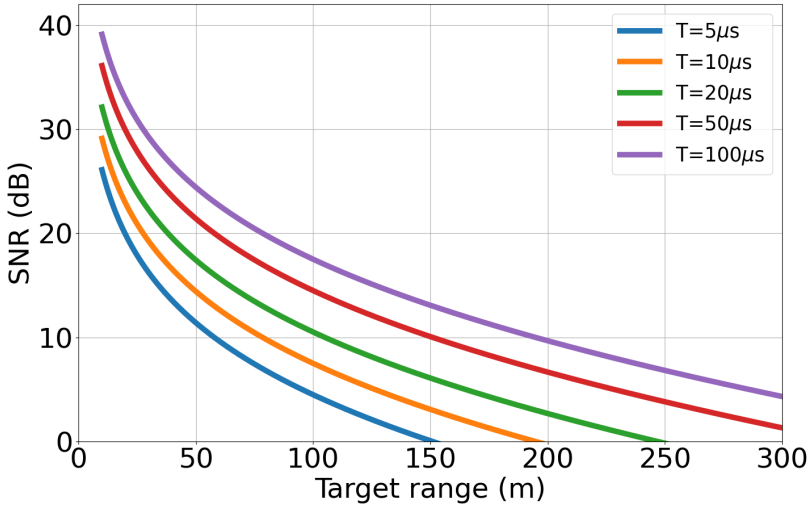

Figure 3.19: SNR against target range for several measurement periods T.

As shown in Fig. 3.19, the measurement period T has an important impact on the SNR. Increasing T is beneficial in terms of SNR, but in parallel, the scanning rate of the system should be fast. This trade-off between scanning rate and operating range (minimum SNR), can be solved by using multiplexing techniques. However, time domain multiplexing (TDM) that makes use of one tile which acquires different points of the FoV at different time slots, is a killer for the SNR. It is therefore desirable to complement TDM with Space Division Multiplexing (SDM), i.e. using multiple elementary tiles working simultaneously, each addressing different points in the FoV. Wavelength Division Multiplexing (WDM) could also be considered, by simultaneously sending different wavelengths to adress the different points of the FoV. However, these parallelism techniques comes with higher footprint. Again, tight integration is very precious in order to avoid bulky solutions.

To assess the performances of a single FMCW LIDAR tile first, we did not consider parallelism in our model. Hence, we specify a measurement period T around 10 μs. Such measurement period corresponds to the measurement time for adressing one point in the FoV plus the time to switch to the next point. Hence, 100,000 points are measured in one second. This corresponds to 0.95%-1.35% of an automotive FoV as described in Section 2.3.4.

3.12.3 SNR against receiver aperture D_{rx}

As shown by Eq. (3.49), the SNR is proportional to the received power P_{RX}. The LIDAR equation presented in Section 3.6 shows that minimizing the free space losses is essential for the link budget. Hence, large receiver aperture diameter D_{rx} are highly desired.

Fig. 3.20 shows the impact of the receiver aperture diameter D_{rx} on the SNR for a 100 kHz laser linewidth and a 10 μs measurement period.

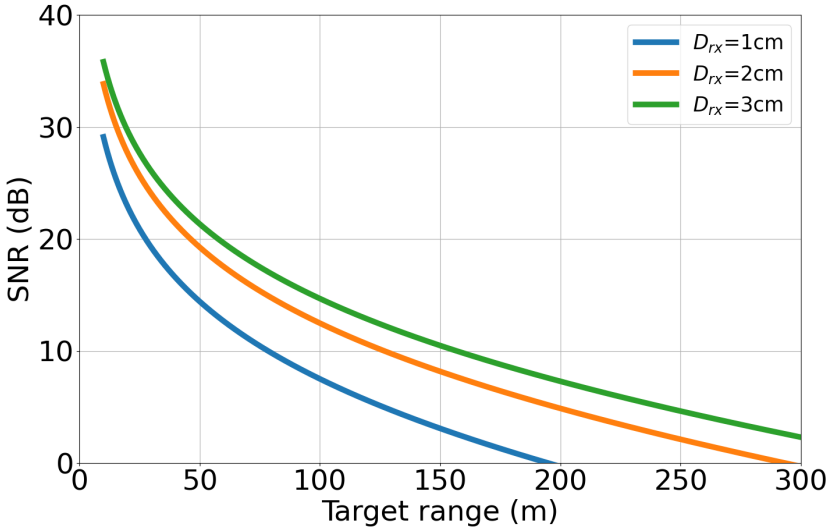

Figure 3.20: SNR against target range for several receiver apertures D_{rx}.

The optical design of the scanning unit must ensure a high collection efficiency of the RX signal by the grating coupler.

3.12.4 SNR against environment alpha and target reflectivity

Fig. 3.21 shows the impact of a) the environmental conditions using the air attenuation coefficients α from Table 3.2 and b) target reflectivities ρ on the SNR for a 100 kHz laser linewidth and a 10 μs measurement period.

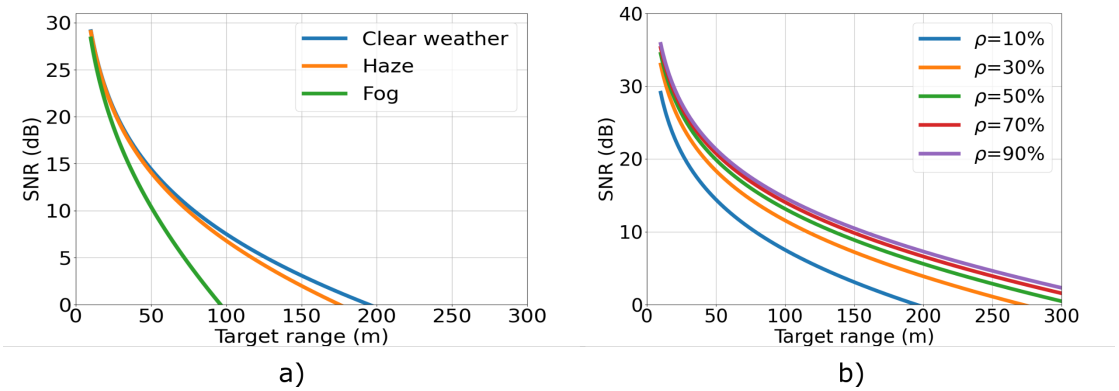

Figure 3.21: SNR against target range for several a) environmental conditions and b) target reflectivities ρ.

We observe in Fig. 3.21 a) that the SNR drops very fast under fog conditions, as the exponential term of Eq. (3.42) goes to zero. From, Fig. 3.21 b), we notice that targets with high reflectivity can improve the SNR and therefore the LIDAR operating range. The reflectivity ρ depends on the car coating and color. For instance, dark painting colors can be detrimental due to their absorption of NIR wavelengths. In [135], the reflectivities of white, grey and black rectangular targets were measured for emission wavelengths within the 400-2400 nm range and for an incident angle ϕ of 10°. At 1550 nm, the measured reflectivities of the white, grey and black targets were 90%, 50% and 5% respectively.

3.13 Target detection beyond the laser coherence length

Due to the laser phase noise, FMCW LIDAR systems are usually restricted to detection range below the laser coherence length. From the Fig. 3.17, we have seen that the photocurrent spectrum peak degrades for long range targets due to laser phase noise. The spectrum goes from a narrow cardinal sine function to a broad Lorentzian. Therefore, the use of the same frequency estimation algorithm for the two regimes is not efficient [136]. Embedded digital signal processing (DSP) is a promising approach to extend LIDAR detection range beyond L_c. In [43][136], a Lorentzian least squares estimation (LLSE) algorithm is used to estimate target range beyond the laser coherence length. In this section we did not consider the other noise sources than phase noise, in order to validate only the proof of concept.

In this section, we also use a LLSE algorithm and test its functionality using Monte Carlo simulations to evaluate the range and velocity precision beyond the laser coherence length.

Based on the laser phase noise description given in Section 3.10, a numerical model based on Monte Carlo simulations was build to generate and process realistic FMCW LIDAR signals. The block diagram describing our model is given in Fig. 3.22.

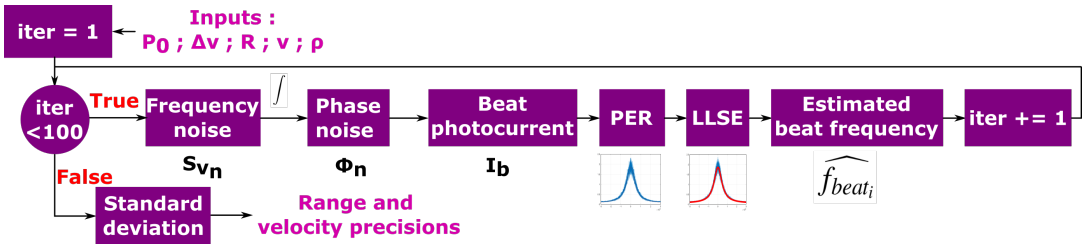

Figure 3.22: Monte Carlo model building blocks. PER: periodogram; LLSE: Lorentzian least squares estimation; iter: iteration.

The laser phase noise is again modeled as a flat frequency noise with power spectrum density $S_{\nu_n}(f)$ depending on the laser linewidth $\Delta\nu$ and is expressed as:

$$S_{\nu_n}(f) \equiv \frac{\Delta\nu}{2\pi} \tag{3.74}$$

The frequency noise samples are integrated in time to express laser phase noise contributions Φ_n as:

$$\Phi_n = \int_t 2\pi\Delta\nu dt \tag{3.75}$$

Then we computed the photodetected beat current, I_b, with beat frequency f_b as:

$$I_b \equiv cos(2\pi f_b t + \Phi_n(t) - \Phi_n(t-\tau)) \tag{3.76}$$

As we used a triangular waveform for frequency modulation, the beat frequency f_b equals f_{min} or f_{max} depending on the rising or falling ramp period.

Then, the periodogram (PER) of I_b is evaluated over the measurement period T. A Lorentzian least squares estimation (LLSE) algorithm is used to fit the PER of I_b and estimates f_{min} and f_{max} to derive R and v_r.

First, we verified the shape of the photocurrent PER in the coherent and incoherent regimes, using a linewidth of 1 MHz and running 100 Monte Carlo iterations. This linewidth corresponds to a laser coherence length of 95 m (47.5 m target range to account for round-trip). The simulations are performed on static targets at 20 m (coherent regime) and 200 m (incoherent regime) as shown on Fig. 3.23. The fitting function corresponds to the Eq. (3.72). The vertical line at a frequency f_c corresponds to the limit between coherent and incoherent regimes. As expected from Eq. (3.72), in the coherent regime, a cardinal sine function corresponding to the beat tone is obtained, while in the incoherent regime, the PER broadens to a Lorentzian shape. The Lorentzian has a FWHM equals to $2\Delta\nu$, i.e. twice the laser linewidth (2 MHz) confirming Eq. (3.72).

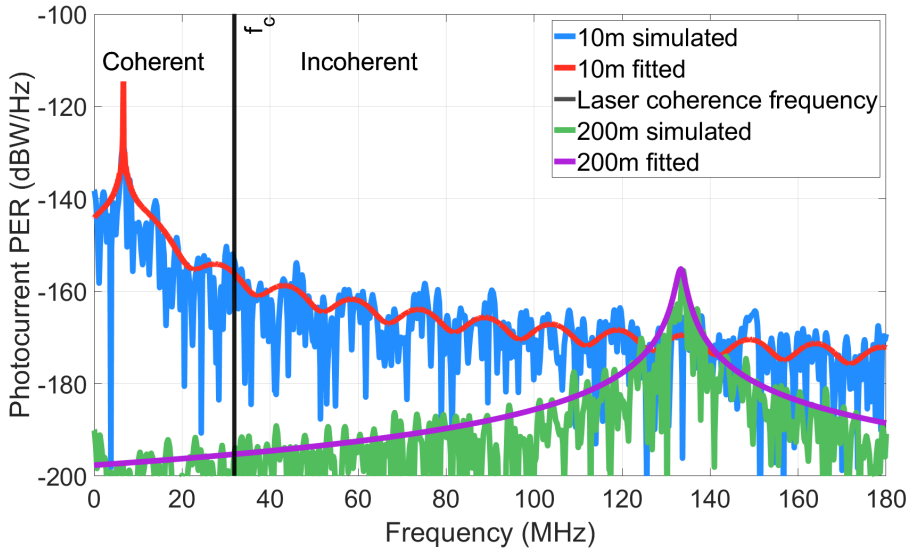

Figure 3.23: PER for coherent and incoherent regimes based on 100 Monte Carlo simulations, 1 MHz laser linewidth.

In the following, we only consider moving targets located beyond the laser coherence length L_c and we apply a Lorentzian least squares estimation (LLSE) algorithm to find f_{min} and f_{max}. The range and velocity are extracted using Eq. (3.34) and Eq. (3.35), and the range and velocity precisions are computed by taking the standard deviation of the 100 estimated ranges and velocities.

The Table 3.8 details the system specifications that we used in these simulations.

Parameter	**Value**
LIDAR transmitted power P_{TX}	10 mW
Laser linewidth $\Delta\nu$	1-10 MHz
Measurement period T	10 μs
Frequency excursion B	1 GHz
Attenuation coefficient in air α	0.43 dB/km
Target range R	up to 200 m
Target velocity v_r	60 km/h
Target reflectivity ρ	10%
Receiver aperture size D_{RX}	1 cm^2
Detector responsivity η	1 A/W
Estimation algorithm	LLSE

Table 3.8: System specifications.

We performed a sweep on the laser linewidth between 1 MHz and 10 MHz and computed the range and velocity precision over 100 Monte Carlo iterations, for target ranges between 57 m and 201 m.

The Fig. 3.24 shows the simulated range precision as a function of target range and laser linewidth.

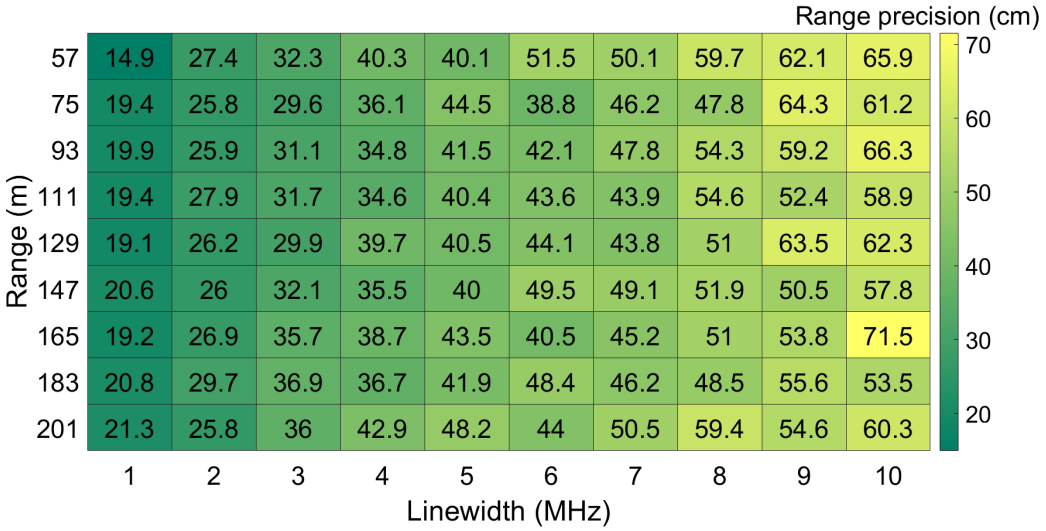

Figure 3.24: Range precision as a function of target range and laser linewidth and for a target velocity $v_r = 60$ km/h= 16.7 m/s.

From Fig. 3.24, we observe that the lower the linewidth, the higher the coherence length and the better the precision. This originates from the SNR degradation due to laser phase noise. As the signal is less attenuated for low laser linewidth, the frequency estimation algorithm is more efficient. A relative range precision of less than 1.2% is obtained over the whole span.

The Fig. 3.25 shows the velocity precision as a function of target range and laser linewidth.

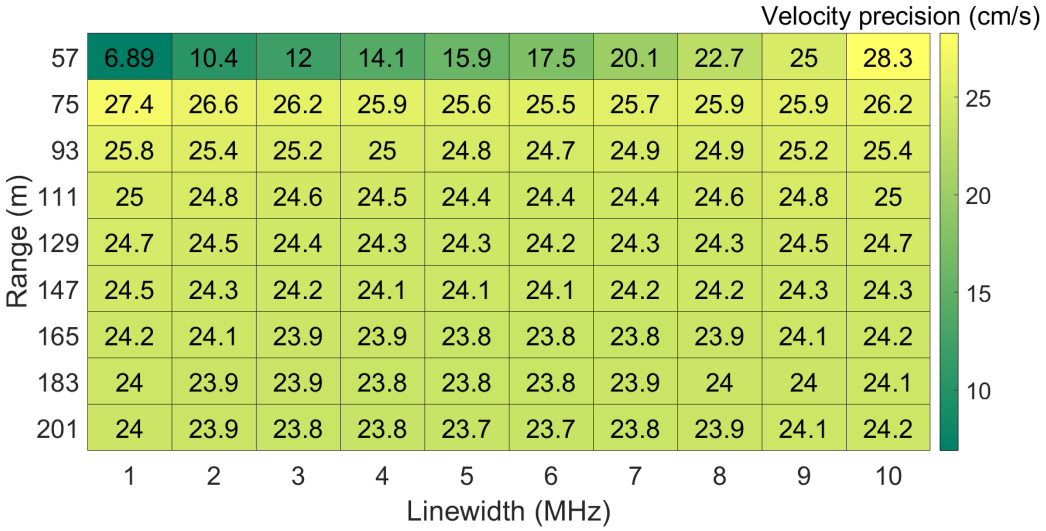

Figure 3.25: Velocity precision as a function of target range and laser linewidth and for a target velocity $v_r = 60$ km/h= 16.7 m/s.

The same observation applies to velocity precision as the two frequency peaks at f_{min} and f_{max} are less attenuated for low linewidth lasers. According to Fig. 3.25, a relative velocity precision of less than 1.7% is obtained over the whole span.

In both Fig. 3.24 and Fig. 3.25, we observed increasing precision values at small

target ranges and 10 MHz laser linewidth. As the fit is defined between 0 and half the ADC sampling frequency ($F_s/2$), at small ranges, the beat frequency f_{min} is approaching zero and the fitting is less efficient. Note that the fit could be performed over positive and negative frequencies using the 90° optical hybrid to avoid artefacts.

In conclusion, these simulations confirm that the detection of targets located beyond the laser coherence length is possible and with good range and velocity precisions. These simulations were performed under a realistic automotive FMCW LIDAR scenario. In addition, this algorithm can be adapted to any form of laser phase noise such as pseudo Voigt function or with prior-characterization of the laser phase noise. These results were presented at Optique Dijon (SFO) 2021 conference. Nevertheless, the efficiency of this technique needs to be evaluated in the context of multiple target detection, since the presence of close Lorentzian functions in detected spectrum may cause the LLSE not to identify the different Lorentzian functions with a good accuracy.

3.14 Chapter Conclusion

In this chapter, we presented the theory behind FMCW LIDAR that makes use of coherent detection. We described the range and velocity extraction using triangular waveforms and the impact on the electronic circuits bandwidth. Based on this knowledge, a model of a FMCW LIDAR tile was built. By computing the link budget, we proposed to add a booster SOA at the transmitter to reach targets at hundreds of meters. Based on the laser phase noise model, the influence of the laser linewidth on the detected signal may also be detrimental. We simulated the LIDAR SNR for several linewidths $\Delta\nu$, measurement periods T, receiver aperture diameters D_{RX}, environmental conditions and target reflectivities ρ. Additionally, we have implemented a digital signal processing technique to extend the range of the LIDAR beyond the laser coherence length for a single target detection but this technique needs to be developed and tested for multiple target detection. Finally, we are able to set LIDAR component specifications for automotive application. The Table 3.9 summarizes the silicon photonics component specifications to build the FMCW LIDAR tile discussed in this chapter. The 90° hybrid specifications are based on OIF Integrated Coherent Transmitter-Receiver Optical Subassembly (IC-TROSA) [113] standard and [137]. Note that the aim of the IC-TROSA standard is to specify the features and properties of current and future coherent communication systems.

Property	Value	Units
Laser		
Wavelength	1550	nm
Output optical power	10	dBm
Lorentzian linewidth	<100	kHz
Frequency excursion B	1.5	GHz
Measurement period T	10	μs
Chirp linearity RMS	< 0.1%	-
Wavelength tuning range	C band : 1530-1565	nm
Amplification : SOA		
Gain	10	dB
Noise Figure	<8	dB
Saturation power	>10	dBm
Coherent combiner: 90° optical hybrid		
Insertion loss	<0.5	dB
CMRR	30	dB
Imbalance	<0.5	dB
Phase error	-7.5 to +7.5	°
Detector: balanced photodiodes		
Bandwidth	1	GHz
Responsivity η	1	A/W
CMRR	>20	dB
Scanning unit: Focal Plane Switch Array		
Number of antennas N	1200×300	-
FPSA insertion loss	<10	dB
FPSA power consumption	<5	W
Scanning speed	1	MHz
Crosstalk	-20	dB
Electronics: TIA, ADC and DSP		
TIA Bandwidth BW_{elec}	1	GHz
ADC sampling rate F_s	2	GHz
DSP	Max estimation and LLSE	-

Table 3.9: Table of SiPh component specifications for an automotive FMCW LIDAR.

These component specifications will be used in the next chapter, where we describe the layout and characterization of FMCW LIDAR components and circuits based on the Scintil Photonics technology in silicon photonics.

Chapter 4

Realization of a silicon photonic FMCW LIDAR

In this section we present the realization and characterization of a FMCW LIDAR tile. The circuit is fabricated using the Scintil Photonics process enabling the integration of III-V material on silicon. We compare our measurement results with the silicon photonic component specifications given in Chapter 3.

4.1 Layout and characterization overview

The elaboration of our chips includes several steps as shown in Fig. 4.1. We describe these different steps hereafter. During my thesis, I have been involved in the layout and the characterization steps.

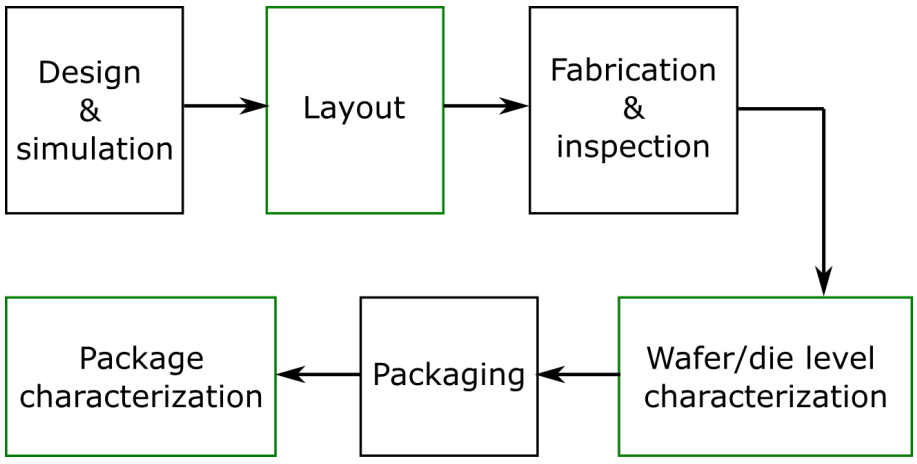

Figure 4.1: Steps for the elaboration of the demonstrators.

The first step is design and simulation, that makes use of photonic simulation softwares such as Lumerical to understand how light propagates and interacts with complex elements built from different materials in order to implement a given optical function.

The layout consists of drawing geometric surfaces into a graphic design system (GDS) file in order to produce the lithography masks for fabrication. In our case we interfaced KLayout with Matlab or Python to generate this file. Each geometric

shape is defined by a layer and can be grouped into a set of other polygons to build a component or a circuit. A layer corresponds to a process step, such as the N doping of silicon material, or a metal patterning.

While many types of geometric shapes can be designed, some design rules should be respected. Once the GDS file is ready, any violation to these rules will be detected by the design rule checking (DRC). The final layout file includes all the layers making it possible the mask fabrication. Fig. 4.2 shows an example of layout comprising two components made of four different layers.

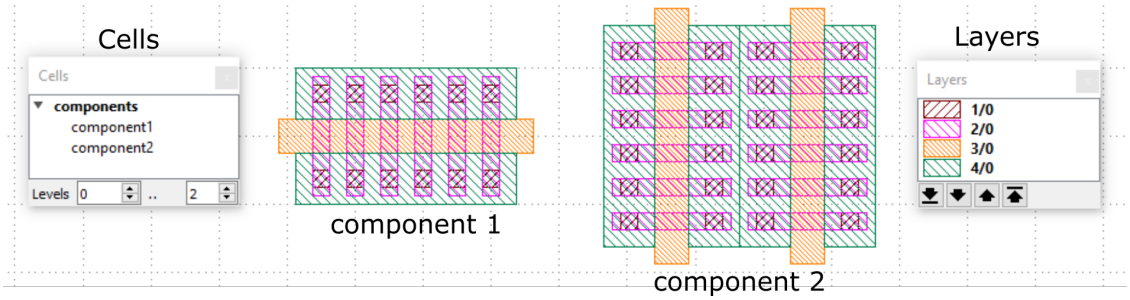

Figure 4.2: Example of a layout consisting in two components made of 4 different layers.

In the fabrication and inspection process, all the steps defined in the GDS file are executed on the wafer by the foundry. Each step is monitored using inspection tools. This step is very challenging, since small differences between fabrication and simulation can degrade the component performances.

Once the silicon photonic wafer is fabricated, the components and circuits are characterized at the wafer/die level.

The Fig. 4.3 shows the general measurement setup used for the wafer/die level measurements.

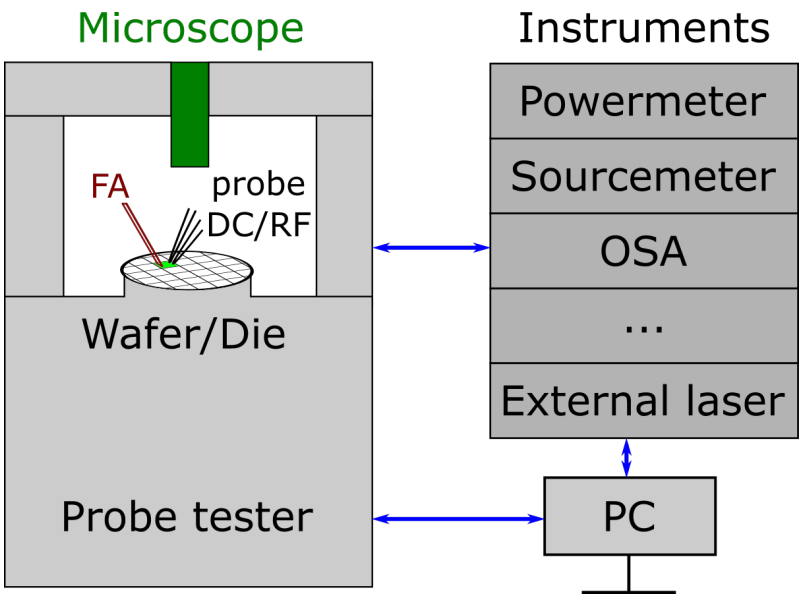

Figure 4.3: Schematic of wafer level characterization setup. FA: fiber array.

The wafer is loaded into a probe tester to perform statistical testing. A top-view microscope is used for observation and alignment procedures. The probe tester is sitting on an air pillow to isolate from vibrations. The chuck can also be controlled in temperature to assess the performances of our components under several operating temperatures. A set of instruments is used to generate and monitor the light beam that is coupled in and out the chip. Such instruments include an external tunable laser, an Optical Spectrum Analyzer (OSA), sourcemeters and powermeters. Discrete components such as fibered splitters/combiners and polarization controllers may also be used in our measurements. A personal computer (PC) is connected to these instruments and to the probe tester to control the wafer displacement and alignment, and to gather the measured data.

We can divide the characterization step into optical, electrical and electro-optic measurements. Optical measurements concern passive devices. The optical coupling is managed with optical fibers that are organized in arrays with well defined fiber spacing (controlled with few μm precision). The fiber array (FA) is brought at a height position Z = +20 μm on top of surface grating couplers to ensure high coupling efficiency between the fiber and the photonic element on the wafer. The X and Y positions can be adjusted manually or automatically using self alignment procedures. Electrical measurements are performed using DC/RF probes in contact with pads on the wafer. Electro-optical measurements use both electrical and optical signals. This includes laser, optical amplifier, modulator or photodiode measurements.

Wafer level testing is possible as the chuck can move from one die to another without moving the fiber array and the DC probes. Statistical wafer testing is very interesting as correlation can be made with some fabrication steps and known good dies can be sent for packaging. The Fig. 4.4 shows a picture of the automatic probe tester with a wafer, two DC probes and a fiber array.

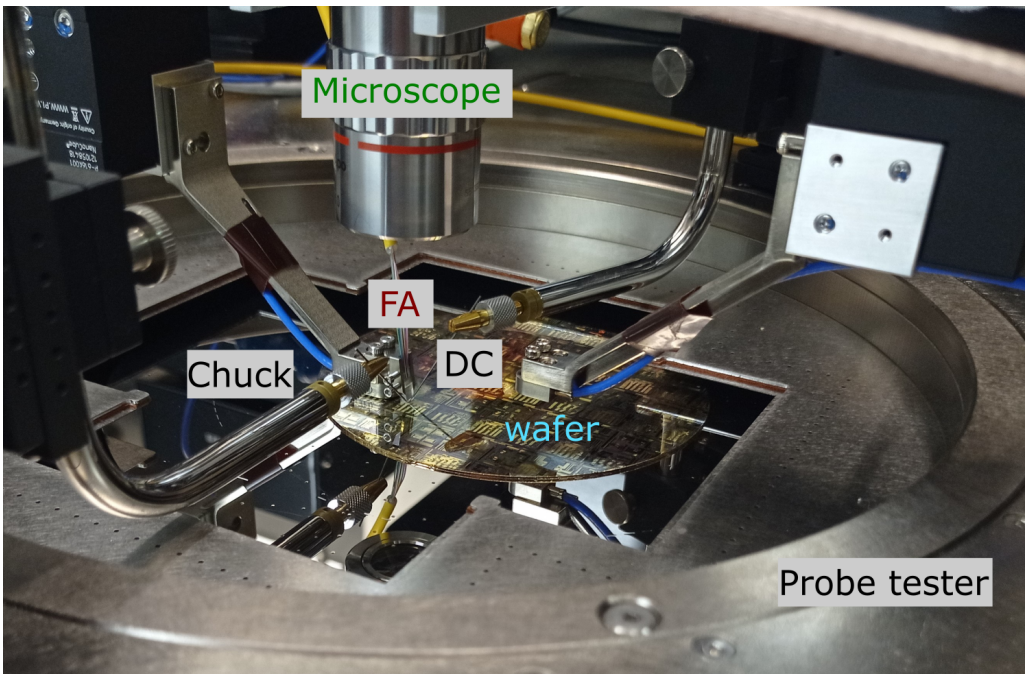

Figure 4.4: Picture of the automatic probe tester with a fiber array (FA) and two DC probes.

In some measurements where a large number of elecrical I/Os is needed, multi-probes can be employed with a significant room save.

Leveraging this environment, we describe hereafter the design and characterization of our components and circuits enabling the realization of a fully integrated FMCW LIDAR tile.

The Table 4.1 shows an overview of the FMCW LIDAR building blocks that have been investigated.

LIDAR blocks	Name	Tested components	Package or wafer/die
Coherent RX and SOA	FMCW LIDAR tile	GC; MMI; 90° hybrid; PD; SOA	wafer/die
Source and modulator	Tunable laser	microrings resonators; GC	package
	DBR laser	GC; DBR laser	wafer/die
	IQ modulator with SOA	SOA; IQ modulator; GC	package
Scanning module	4-emitter FPSA	thermo-optic phase shifter; GC	wafer/die

Table 4.1: Overview of the FMCW LIDAR building blocks. GC: grating coupler; MMI: MultiMode Interference coupler; PD: photodiode; SOA: semiconductor optical amplifier; DBR: Distributed Bragg Grating.

4.2 FMCW LIDAR circuit overview

The Fig. 4.5 shows the designed and fabricated FMCW LIDAR circuit. It consists of a transmitter (TX) and a receiver (RX) tiles, made up from a single fully integrated circuit integrating Si, SiN, Ge and III-V layers. An external laser is coupled to the circuit through a SiN surface grating coupler (GC in). In the TX path, a III-V/Si booster SOA was placed to ensure a high transmitted power. A SiN 1x2 MultiMode Interferometer (MMI) splits the laser signal into a first part that serves as a local oscillator (LO) and a second part directed to a SiN GC (GC TX out). The echo signal being reflected on a target is coupled back to the RX unit through a SiN GC (GC RX in). A preamplifier SOA, not shown in Fig. 4.5, could also be added in the RX path. The RX signal is then mixed with the LO on coherent receiver that comprises 2x2 SiN MMI, SiN crossings and a pair of Ge balanced PDs. The circuit dimensions are 0.8 mm x 4 mm.

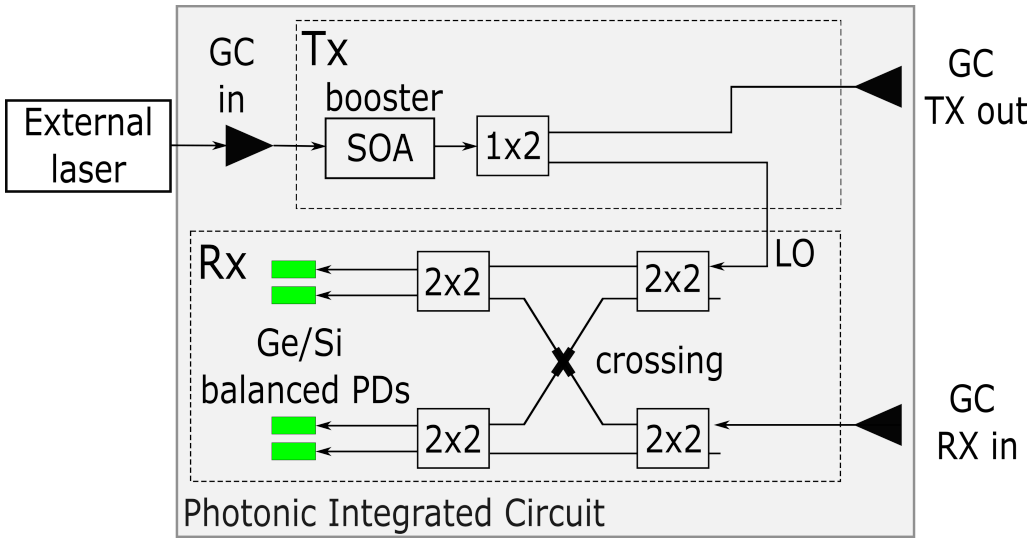

Figure 4.5: Schematic of the FMCW LIDAR core circuit architecture with III-V/Si booster SOA, SiN 2x2 MMI coupler and Ge photodiodes.

We present the characterization results of each building block of this circuit hereafter. This work was presented at the 2022 European Conference on Optical Communication (ECOC) in Bassel, Switzerland. To our knowledge, this is the first demonstration of monolithic integration with III-V/Si SOAs, Ge waveguide-PDs, Si active and Silicon Nitride (SiN) passive devices.

4.3 Grating couplers

Light coupling from the chip to an optical fiber (and vice-versa) can be performed with edge couplers or surface grating couplers (GC). During my thesis, I have mainly manipulated surface grating couplers. Such component makes use of diffraction gratings to create constructive light interferences at a certain angle corresponding to the fiber direction, as illustrated in Fig. 4.6.

Two rays interfere constructively at an angle θ if their phase difference is a multiple integer m of 2π. This angle is given by [138]:

$$\sin(\theta) = \frac{n_{eff} - \frac{m\lambda}{p}}{n_{SiO_2}}, \tag{4.1}$$

where n_{eff} is the effective index of the grating, p is the diffraction period, λ is the wavelength and n_{SiO2} is the index of the SiO2 cladding.

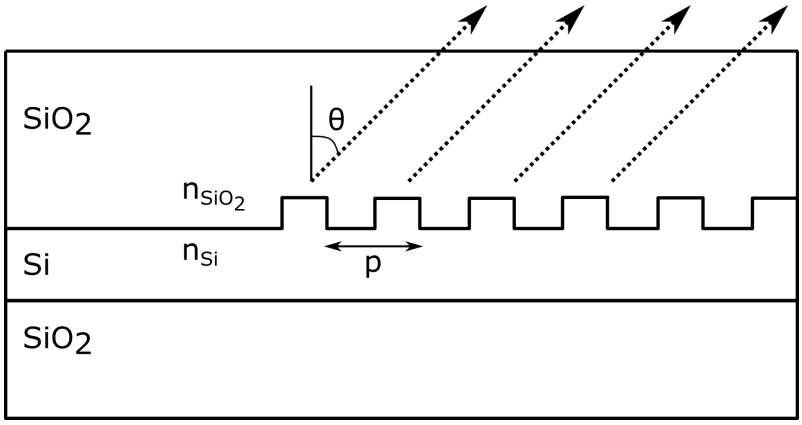

Figure 4.6: Schematic of a grating coupler.

Grating couplers are polarization dependent components. Hence, in all our measurements, we use a fiber polarization controller to align the input light polarization with the grating coupler.

To characterize the grating coupler from our circuit, we performed wafer level measurements of shunt grating coupler over 10 dies. A shunt grating coupler test structure is composed of two grating couplers connected by a short SiN waveguide. By dividing by two the measured transmission loss and neglecting the propagation loss induced by the short waveguide, the insertion loss of one grating coupler is obtained. The Fig. 4.7 shows the measured transmission spectrum of one SiN grating coupler within the 1500-1600 nm wavelength span, using a resolution of 10 pm.

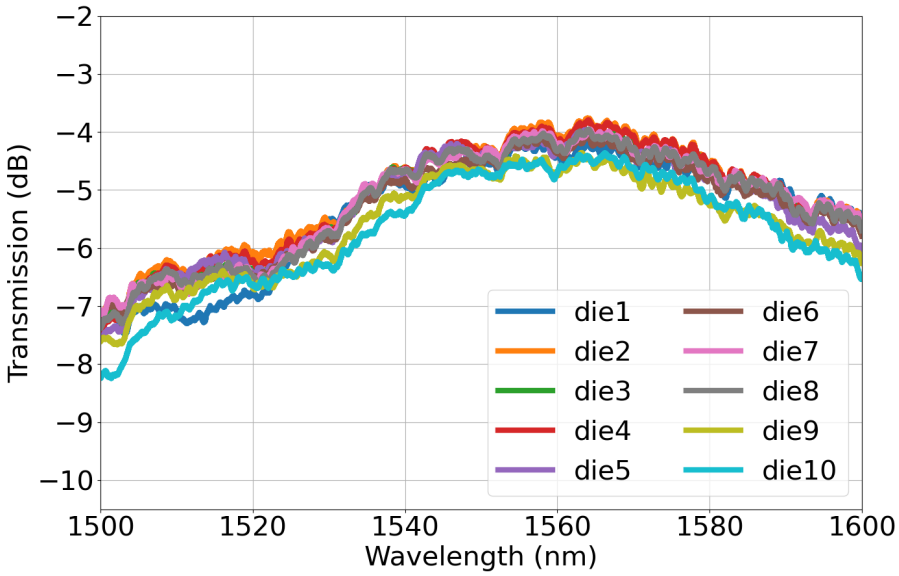

Figure 4.7: Measured transmission response of one SiN grating coupler over 10 dies.

The measured transmission spectra in Fig. 4.7 are very consistent over the tested dies. Fig. 4.8 a) and b) shows the statistical normalized distribution of the peak wavelength and insertion loss respectively, for one SiN grating coupler. The mean peak wavelength over the measured dies is 1564 nm. The mean insertion loss at this peak wavelength among the measured dies is 4 dB.

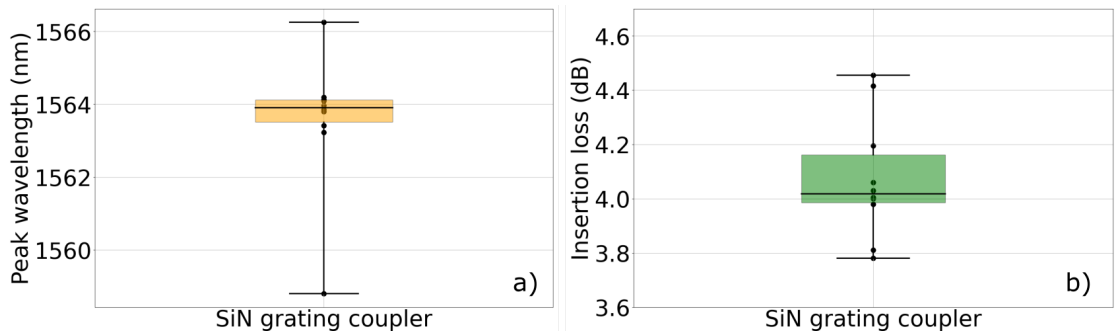

Figure 4.8: Wafer level characterization of SiN grating couplers on 10 dies showing a) the peak wavelength and b) the insertion loss at the average peak wavelength.

4.4 MMI

In our FMCW LIDAR tile, the MMI is used to split the signal into the LO and TX signals but is also in the coherent receiver. This MMI has been designed so that the light is equally splitted at the output, i.e. 50% of the light is directed to the bar output and 50% goes to the cross output.

The Fig. 4.9 shows the measured insertion loss of the SiN 2x2 MMI for the bar and cross outputs. The solid line corresponds to the average insertion loss (IL) and the width of the shadow region corresponds to twice the standard deviation over the 10 tested dies.

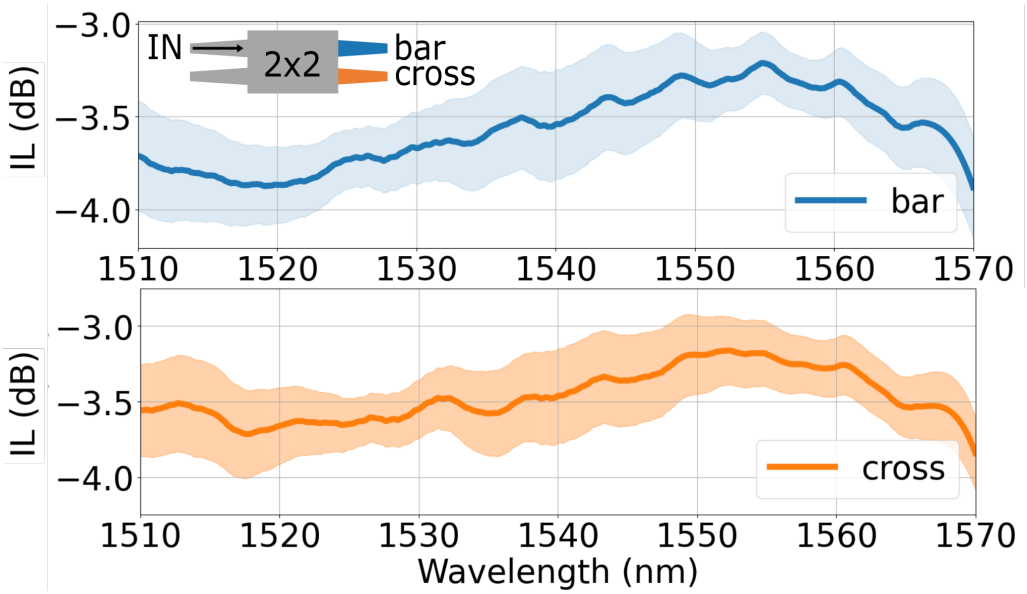

Figure 4.9: Measured transmission of a 2x2 SiN MMI. IL: insertion loss.

From Fig. 4.9, we observe that the SiN 2x2 MMI is well balanced between bar and cross outputs over the measured wavelength span. At the peak wavelength of the grating coupler (1564 nm), the mean insertion loss is 3.5 dB for both bar and cross outputs.

As discussed in chapter 3, the 2x2 MMI can be used as a mixer in the coherent receiver, but the 90° optical hybrid offers additional benefits.

4.5 90° optical hybrid

We first measured the 90° hybrid insertion loss, imbalance and CMRR using the test structure shown in Fig. 4.10. The 90° hybrid is composed of four connected SiN 2x2 MMI. Then, the phase error is extracted using another dedicated test structure.

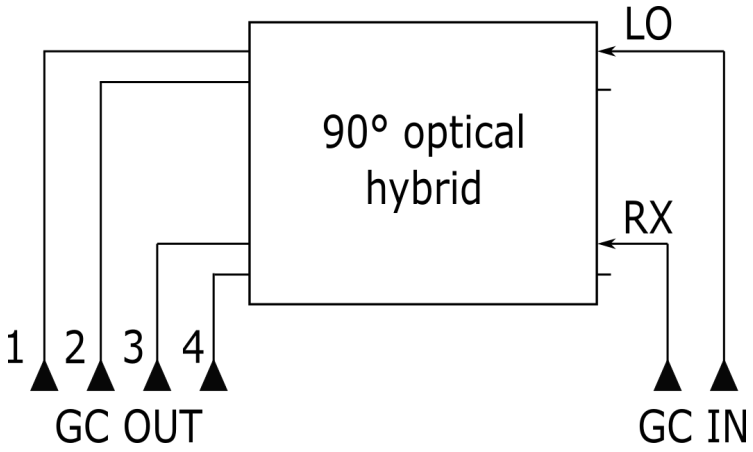

Figure 4.10: Test structure for measuring the 90° hybrid insertion loss, imbalance and CMRR.

4.5.1 Insertion loss

The hybrid insertion loss IL has been defined in Eq. (3.12). The Fig. 4.11 shows the measured statistical insertion loss of the SiN 90° hybrid measured with both RX and LO input ports, at the grating coupler peak wavelength (1564 nm).

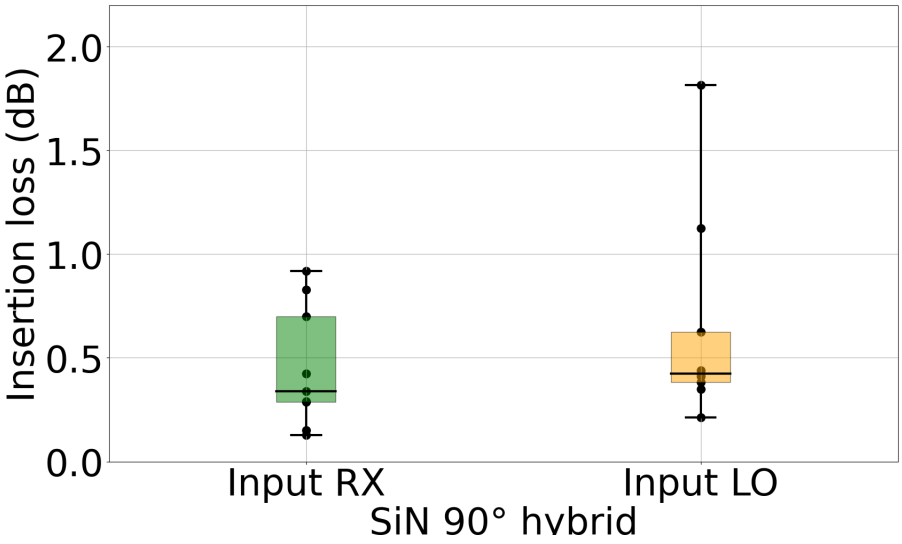

Figure 4.11: Measured insertion loss of the SiN 90° hybrid over 10 dies.

The measured insertion loss is very consistent over the measured dies. Indeed, the mean values for the IL are 0.45 dB and 0.64 dB when using the RX and LO ports as the inputs, respectively. Nevertheless, when the light is coupled to the LO input, one die presented high insertion loss that is responsible for the extreme value of 1.8 dB in Fig. 4.11. When discarding this non-functional die (i.e. considering 9 good dies out of 10), the mean value of the IL drops to 0.5 dB using the LO port as the input.

4.5.2 Imbalance

The imbalance has been defined in Eq. (3.15) and Eq. (3.16) for the I and Q paths, respectively. For each measurement, only one input port (either RX or LO) is fed by the external laser while the other is not used. The four output signals (see Fig. 4.10) are measured and the four imbalance configurations (Imb I input RX, Imb Q input RX, Imb I input LO, Imb Q input LO) are computed.

The Fig. 4.12 shows the measured imbalance of the SiN 90° hybrid over 10 dies, at the peak wavelength of the SiN grating coupler (1564 nm).

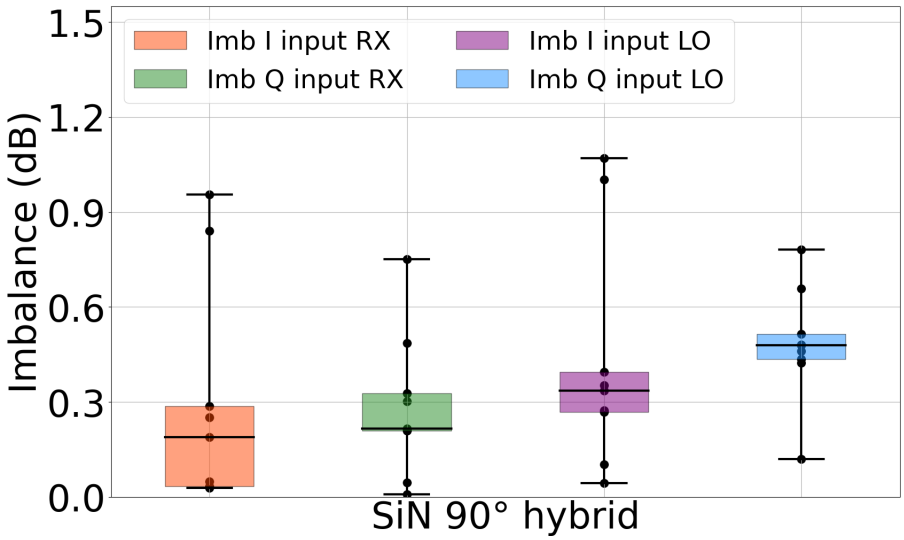

Figure 4.12: Measured imbalance of the SiN 90° hybrid at 1564 nm and over 10 dies.

From Fig. 4.12, the mean imbalance over the four measurements is 0.4 dB. When using the LO input port, the average quadrature imbalance Im_Q (in blue) is slightly higher than the others. This could come from small MMI imbalance in the propagation path. For the in-phase imbalances Im_I measured with both RX and LO ports (orange and purple), the upper values does not originate from the same non-functional die than for the insertion loss measurement.

4.5.3 CMRR

The common mode rejection ratio (CMRR) has been defined for the in-phase (I) and quadrature (Q) arms in Eq. (3.13) and Eq. (3.14).

The Fig. 4.13 shows the CMRR at the peak wavelength determined in Fig. 4.8 of the SiN 90° hybrid measured with both RX and LO input ports.

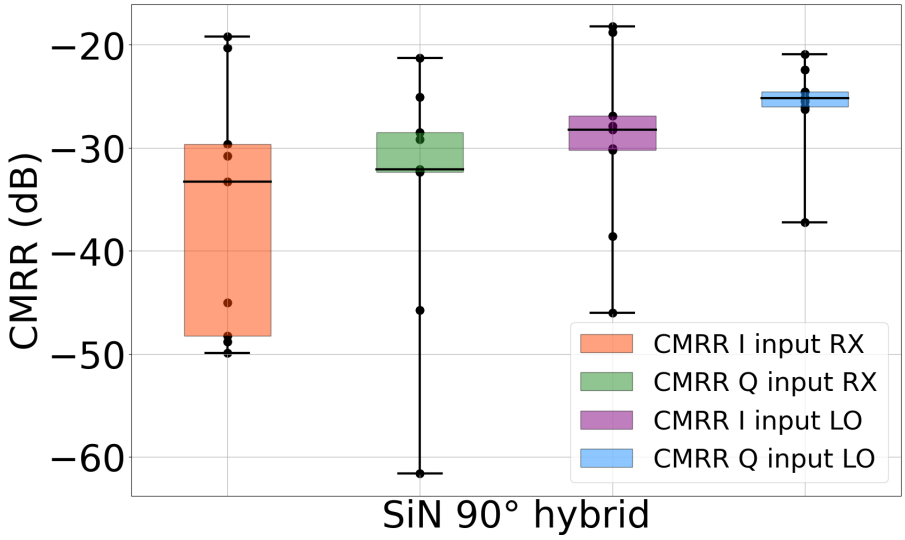

Figure 4.13: Measured CMRR of the SiN 90° hybrid at 1564 nm and over 10 dies.

The mean CMRR over the four measurements is -31 dB but the we observed a large dispersion bewteen the tested dies resulting in a standard deviation of 10 dB.

4.5.4 Phase errors

We used the test structure shown in Fig. 4.14 to evaluate the hybrid phase errors. A delay line interferometer (DLI) was placed before the 90° hybrid, where one arm has an extra length ΔL. The Free Spectral Range (FSR) of the DLI is 8.3 nm and is assumed constant over the observed wavelength region. We expect the four output spectra to follow sinusoids with phase shifts of 0°, 90°, 180° and 270°. The same principle is used in [111].

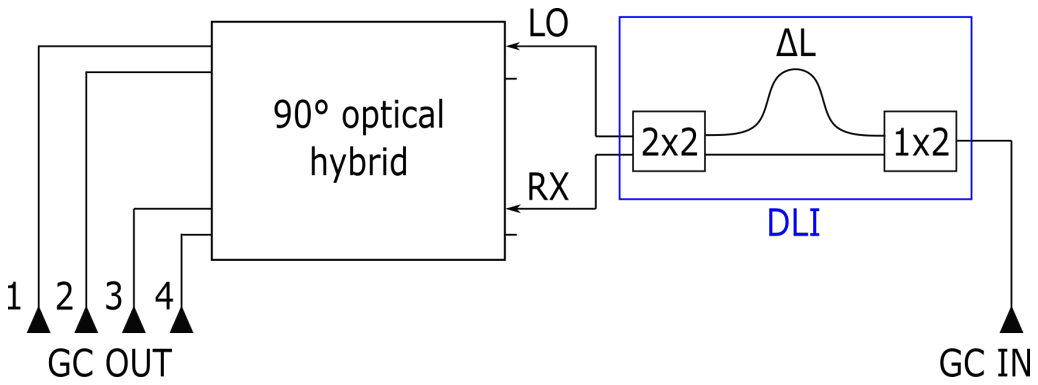

Figure 4.14: Test structure for measuring the 90° hybrid phase error. DLI: delay line interferometer.

The phase error is defined as the error from the expected 90° phase shift between :

- $E_1 = E_{RX} + E_{LO}$ and $E_4 = E_{RX} - jE_{LO}$
- $E_2 = E_{RX} - E_{LO}$ and $E_3 = E_{RX} + jE_{LO}$

Assuming constant FSR over the observed wavelength span, the phase errors are expressed by:

$$\delta\phi_{E1-E4} = 90° - \frac{360° \times \Delta\lambda_{E1-E4}(nm)}{FSR(nm)} \tag{4.2}$$

$$\delta\phi_{E2-E3} = 90° - \frac{360° \times \Delta\lambda_{E2-E3}(nm)}{FSR(nm)} \tag{4.3}$$

The Fig. 4.15 shows the measured transmission at the the four outputs using the test structure shown in Fig. 4.14. As expected, the transmission spectra have sinusoidal shapes (converted into dB scale) with period equals to the FSR. We fitted the measured curves using a non-linear least squares algorithm in order to extract the position of each gap in the transmission spectra from which $\Delta\lambda_{E1-E4}$ and $\Delta\lambda_{E2-E3}$ can be deduced.

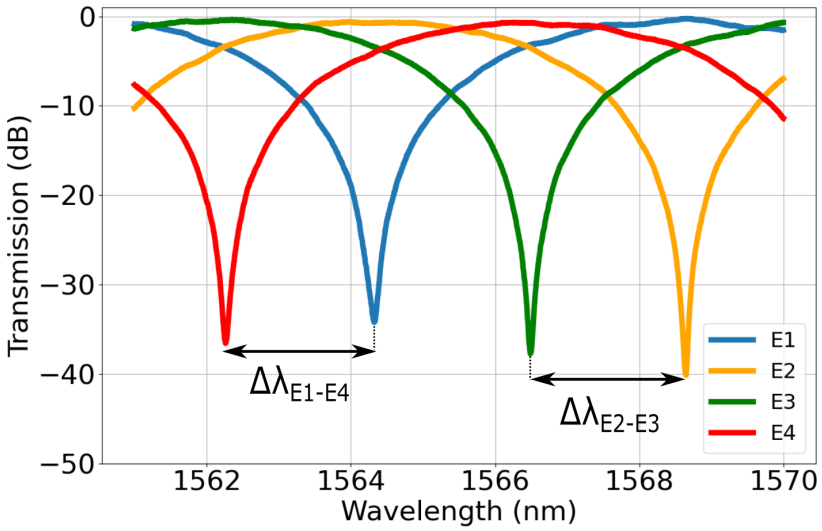

Figure 4.15: Spectral response of the four hybrid outputs using the error test structure.

The statistical measured phase errors over 10 dies for E1-E4 and E2-E3 are shown in Fig. 4.16 a) and b), respectively. The whole phase error is comprised between -5.7° and 0.6° which is in good agreement with the IC-TROSA specifications of -7.5° to 7.5°.

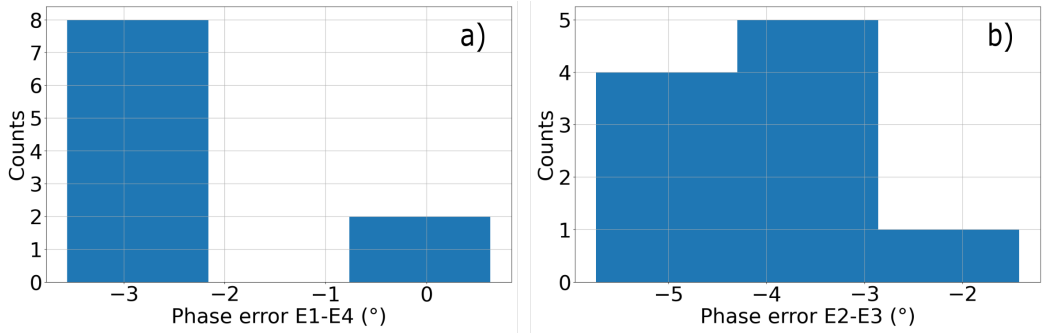

Figure 4.16: Histogram of a) E1-E4 and b) E2-E3 phase errors.

4.5.5 90° hybrid summary

In Table 4.2, we compare the performances of our 90° hybrid with the Integrated Coherent Transmitter-Receiver Optical Subassembly (IC-TROSA) specifications and a state-of-the-art demonstration of the 90° hybrid in a silicon photonics platform [137].

Property	IC-TROSA specifications	[137]	This work (mean value)
IL	<0.5 dB	<0.5 dB	0.5 dB
CMRR	30 dB	31 dB	31 dB
Imbalance	<0.5 dB	<0.25 dB	0.4 dB
Phase error	-7.5° to +7.5°	-1° to 0°	-5.7° to 0.6°

Table 4.2: Comparative table summarizing the performances of our 90° hybrid with IC-TROSA specifications and a reference publication [137].

As shown on Table 4.2, all the IC-TROSA specifications are fulfilled by our 90° optical hybrid. Nevertheless, note that the IC-TROSA standard specifies the features and properties of current and future coherent communication systems and not specifically for FMCW LIDAR. To our knowledge, no FMCW LIDAR standard is available yet.

Compared to [137], our measurement results are very promising for building a high performance coherent receiver.

4.6 Photodiodes

4.6.1 Ge photodiode

A photodiode is a transducer that converts an optical signal into an electrical signal using the photoelectric effect. When photons with a certain energy are impinging on the photodiode, they can be absorbed and generate electron hole pairs. These carriers are collected and the produced photocurrent is measured. More precisely, absorption occurs when the emitted photon energy is larger than the detector material energy bandgap. Thus, the material choice is crucial in order to measure an optical signal with specific energy or wavelength. A photon is absorbed if its energy is higher than the material energy bandgap E_g :

$$E_{ph} = h\nu_{ph} > E_g \leftrightarrow \lambda_{ph} < \frac{1.24\mu m}{E_g(eV)} \tag{4.4}$$

Direct bandgap materials are more likely to absorb photons since only photon energy is required to create the electron hole pair. For indirect bandgap semiconductors, photons and phonons (lattice vibration) interaction is required. Thus, direct bandgap semiconductors typically offer higher absorption, and therefore require smaller absorption volume leading to higher speed. The Table 4.3 shows the absorption coefficient against wavelength for a set a photodetector materials.

Around 1550 nm, Ge and III-V photodiodes are good candidates. Ge has an indirect bandgap but the energy difference between its direct and indirect band gap is very small, enabling absorption of photons. In addition, Ge is CMOS compatible material. Hence, photodiodes can be fabricated along with Si and SiNx waveguides.

Material	Bandgap	Typical wavelengths of operation
InGaAs	Direct	1310-1550 nm
GaAs (AlGaAs)	Direct	800-900 nm
Si	Indirect	800-900 nm
Ge	Indirect	1310-1550 nm

Table 4.3: Materials used as photodiodes with their bandgap and typical wavelengths of operation.

The measured Ge photodiodes are based on vertical PIN diodes [139]. A microscope image of two vertical PIN Ge photodiodes in balanced configuration is shown in Fig. 4.17.

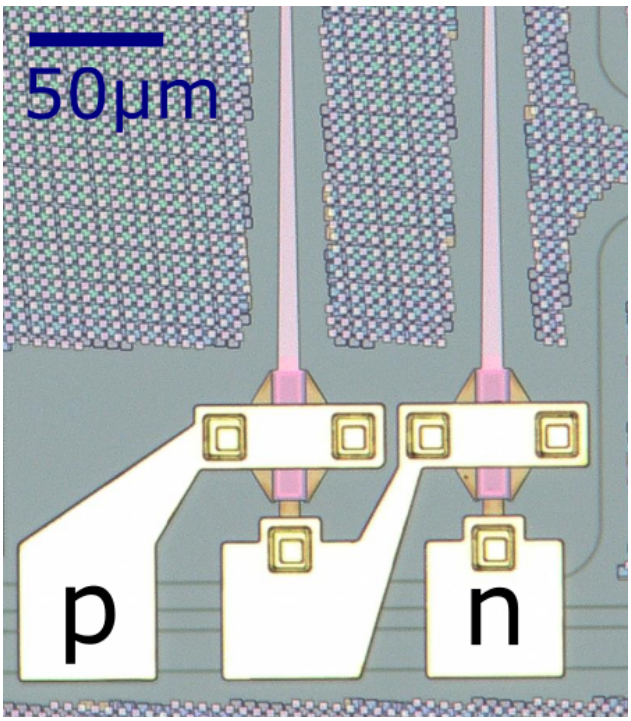

Figure 4.17: Optical microscope view of two vertical PIN Ge photodiodes in balanced configuration. P and N contacts are also indicated.

The photocurrent at the output of the Ge PD was measured for different input optical powers, laser wavelengths and reverse biases. An external laser was coupled to a grating coupler (GC) being connected to the Ge PD. To compute the responsivity, the Ge PD input power was obtained by correcting the laser output power with the loss from the GC. The Fig. 4.18 shows the Ge photodiode responsitivity R against the laser wavelength and for several reverse biases.

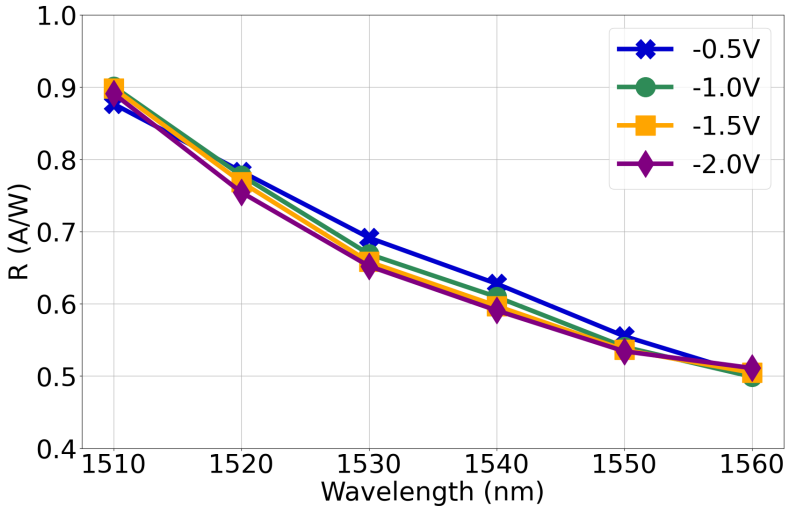

Figure 4.18: Ge photodiode responsivity as a function of wavelength for several reverse bias.

The photodiode is 50 μm-long. We measured responsivities up to 0.9 A/W at 1510 nm wavelength.

The Fig. 4.19 shows the measured IV curve of the Ge photodiode. At -0.1 V and -2 V bias, the PD dark current is 8 nA and 290 nA respectively. Note that the photodiode bandwidth increases with more reverse bias. For automotive FMCW LIDAR, the maximum beat frequency is few hundreds of MHz. Hence, the PD can be biased at low reverse voltage to prioritize a low dark current over bandwidth. The bandwidth of this photodiode was not measured. Nevertheless, from the design, the simulated bandwidth is several tenth of GHz.

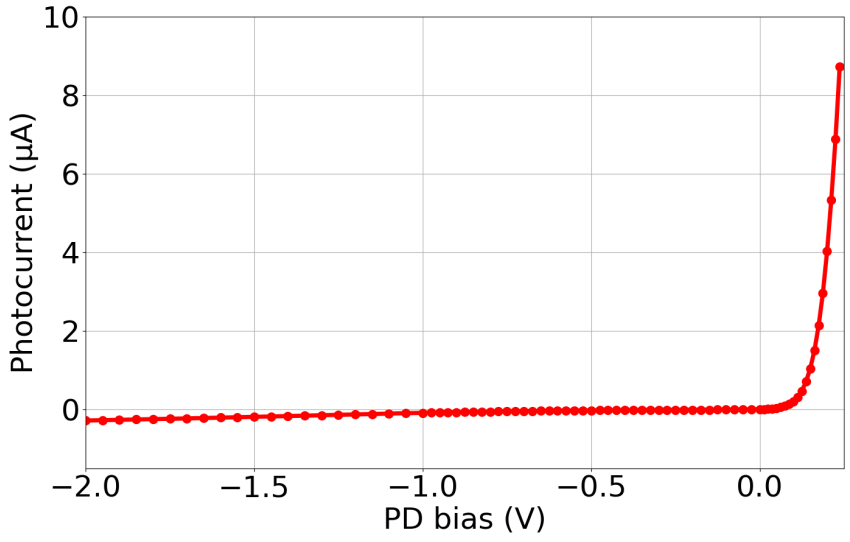

Figure 4.19: Measured I-V curve of the Ge photodiode.

Balanced configuration

We measured the photocurrents (I_1 and I_2) at the output of the two photodiodes

(PD1 and PD2) in the balanced configuration, for several photodiode input optical powers. We computed the CMRR using Eq. (3.20).

The Fig. 4.20 shows the measured CMRR at 1510 nm wavelength for several values of the PD bias.

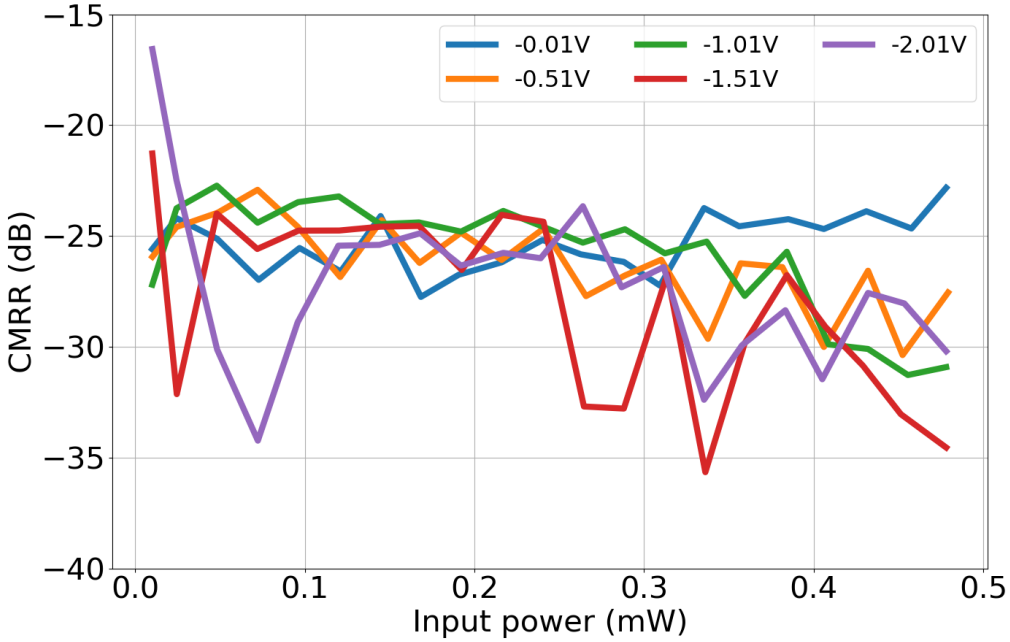

Figure 4.20: Measured CMRR of the Ge balanced photodiodes at 1510 nm wavelength for several PD biases.

The CMRR does not vary significantly with the applied PD bias. The measured balanced PD CMRR is around -25 dB. In future works, we plan to integrate a TIA after the BPDs. The CMRR obtained with TIA will be computed and compared with the CMRR measured here.

We also plan to measure the response of the Ge photodiode at several temperatures to quantify the change in dark current and responsivity as discussed in [140].

4.6.2 III-V photodiodes

We also characterized III-V/Si photodiodes but the electrical contacts between the Tungsten DC probes and the thin metal layer deposited on the pads was very unstable. We tested another type of DC probes made of Beryllium Copper (BeCu) which is more efficient on gold pads, but we did not manage to improve the contact. The Fig. 4.21 shows a microscope view of the fabricated III-V/Si balanced photodiodes.

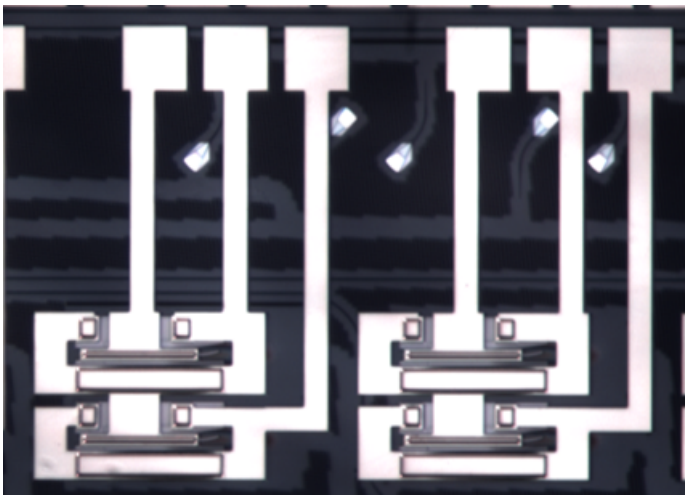

Figure 4.21: Microscope image of the fabricated III-V/Si balanced photodiodes.

4.7 The semiconductor optical amplifier

4.7.1 SOA gain

The fabricated SOA is 800 μm long and consists of a III-V active region without any mirror compared to a laser. The SOA gain was measured using the dedicated on-chip test structure of Fig. 4.22. A tunable laser (TL) with a polarization controller (PC) is coupled to the SiN "GC in" of the test structure. We measured the transmission loss of the "reference" path ("GC in" to "GC out1") and the "amplified" path ("GC in" to "GC out2") comprising exactly the same components of the "reference" path, but with an SOA prior to the output GC. We varied the SOA input power between -20 dBm and -2 dBm by changing the tunable laser output power. The OSA resolution bandwidth is 0.1 nm corresponding to 12.5 GHz at 1550 nm wavelength.

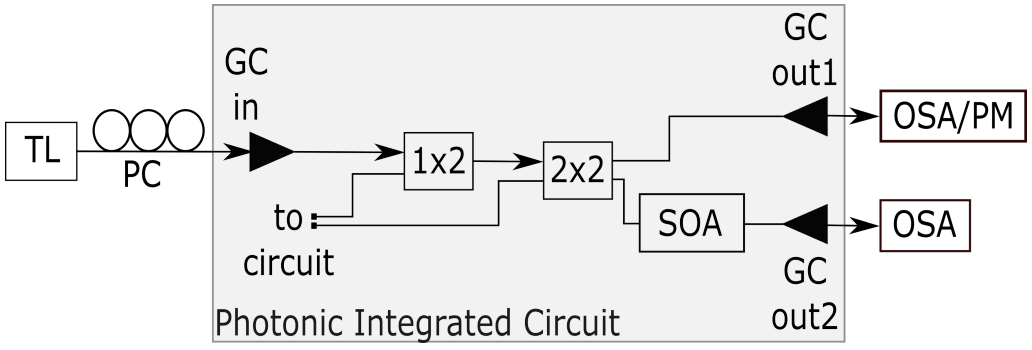

Figure 4.22: Dedicated test structure for the measurement of SOA gain. OSA: Optical Spectrum Analyzer, PM: Power meter.

The Fig. 4.23 shows the measured transmission loss of the "reference" path over the 1510-1570 nm spectral range at several chip temperatures using the power meter. As expected, negligible temperature dependence is observed as the "reference" path comprises SiN passive components with temperature dependency <10 pm/°C.

Temperature variations strongly can affect the VI characteristic of semiconductor diodes, as it modifies the carrier concentration at the junction and therefore the

current flowing through the diode [141]. For the SOA, the gain G and the noise figure NF can be affected by these temperature variations as shown in [142].

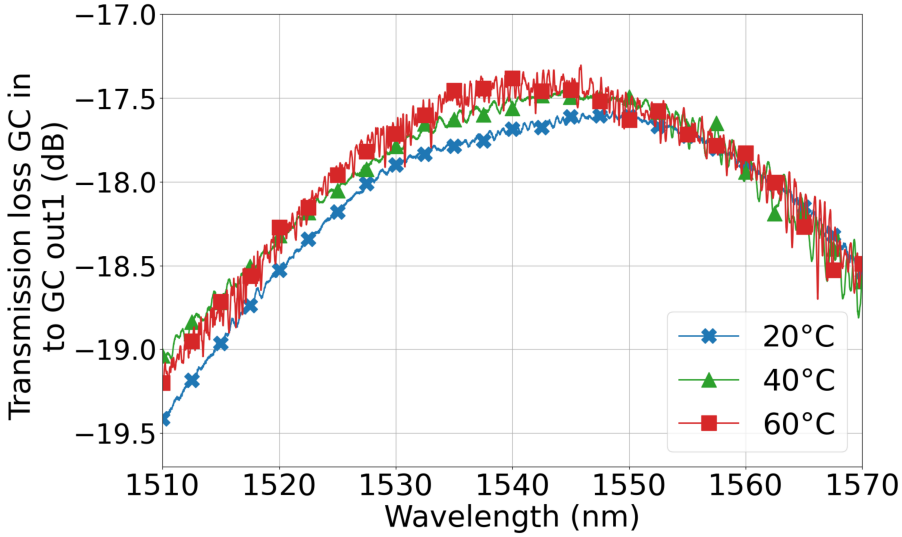

Figure 4.23: Measured transmission loss of the "reference path" from ("GC in" to "GC out1") at several chip temperatures.

The SOA voltage against current curves (VI curves) at the three temperatures are shown on Fig. 4.24, indicating that its power consumption for a 120 mA driving current is $\sim$ 220 mW. From Fig. 4.24, the measured VI characteristics are stable within the measured temperature range.

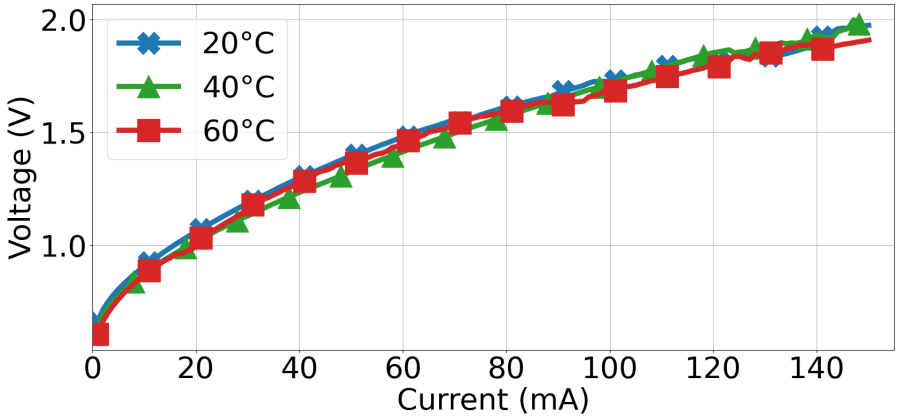

Figure 4.24: SOA VI curves at 20°C, 40°C and 60°C.

We then measured both the "reference" and "amplified" paths using the Optical Spectrum Analyzer (OSA). The SOA gain is extracted by measuring the power at the TL wavelength with and without the SOA. The Fig. 4.25 shows the measured gain against chip temperature at several wavelengths and SOA currents. Two SOA input optical power configurations were tested:
1) To investigate the SOA behaviour as a booster, we set the TL output power so that the input power of the integrated SOA reaches -2 dBm (Fig. 4.25 top). At 20°C

and 120 mA driving current, the SOA gain can be > 10 dB from 1510 to 1550 nm. The gain decreases gradually as the chip temperature increases, down to ∼ 5 dB at 60 °C. Above 80°C, the SOA shows no amplification at the measured wavelengths. 2) To assess the SOA behaviour as a preamplifier, we set the TL output power so that the input power of the integrated SOA reaches -20 dBm (Fig. 4.25 bottom). At 20 °C and 120 mA driving current, the SOA gain can be > 15 dB from 1510 to 1550 nm. The gain decreases gradually as the chip temperature increases, down to ∼ 5 dB at 60 °C.

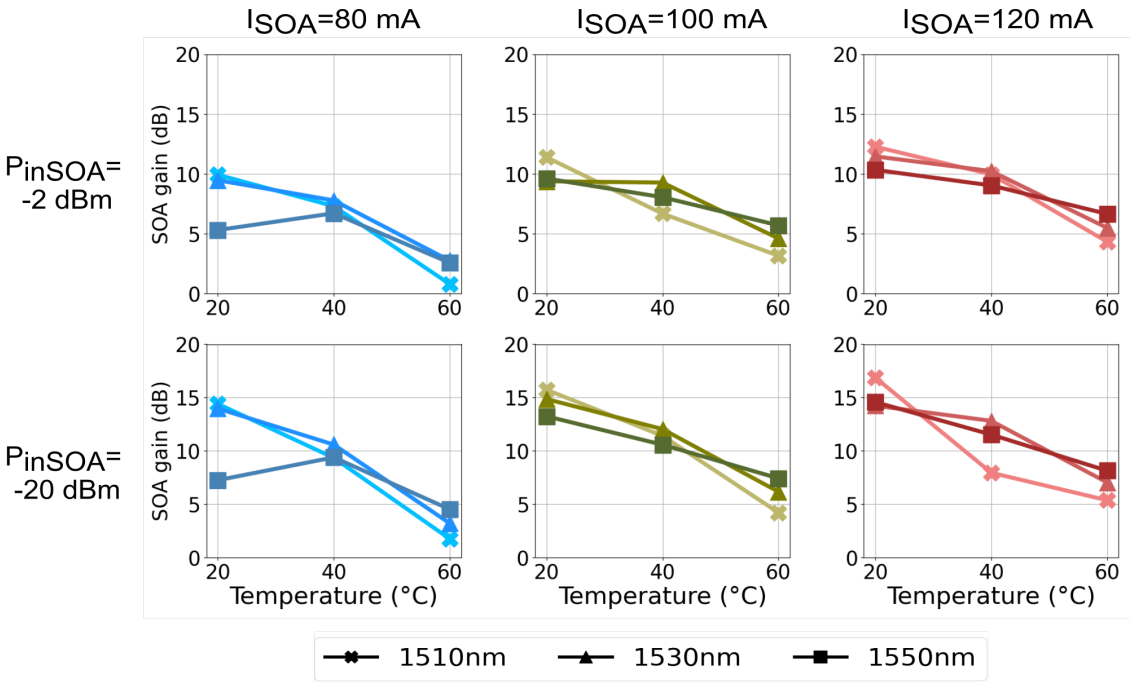

Figure 4.25: SOA gain against chip temperature at 1510, 1530 and 1550 nm for 80 mA, 100 mA and 120 mA SOA currents. The SOA input power is set to -2 dBm (top) and -20 dBm (bottom).

4.7.2 SOA noise figure

The noise figure (NF) was also extracted to quantify the amount of noise added by the SOA. The NF is expressed by Eq. (3.58).

P_{ASE} is extracted from the amplified spectrum at that is measured at the SOA output. An interpolation of the noise floor at the peak wavelength gives a good estimate for P_{ASE} as shown in Fig. 4.26.

In order to provide the on-chip noise figure, we measured and subtract the losses before and after the SOA to get the power at the input and output of the SOA.

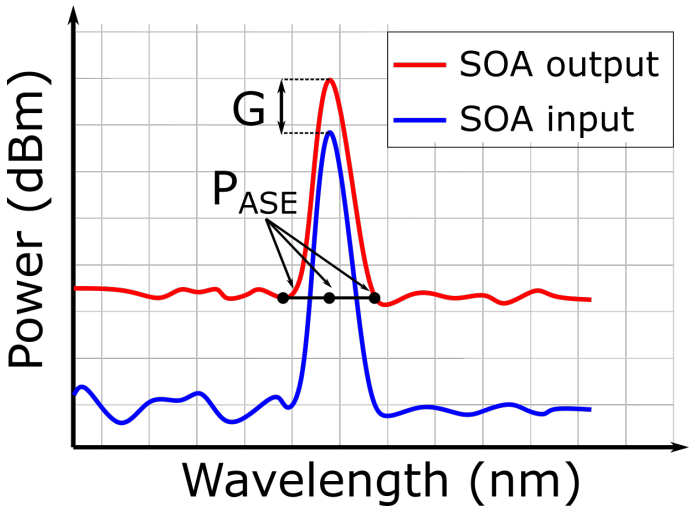

Figure 4.26: Measurement of P_{ASE} and G for noise figure extraction.

The Table 4.4 summarizes the measured gain (G) and noise figure (NF) for -2 dBm and -20 dBm SOA input powers, for a 1510 nm wavelength, a 120 mA SOA current and at 20°C.

SOA input power (dBm)	Gain (dB) at 1510 nm, SOA current = 120 mA	Noise figure (dB) at 1510 nm, SOA current = 120 mA
-2	12	13
-20	17	13

Table 4.4: Summary table of the SOA gain and noise figure measured for -2 dBm and -20 dBm SOA input powers, at λ=1510 nm and with a SOA current of 120 mA. The temperature is 20 °C.

In our measurements, the SOA input power was limited by the maximum output optical power provided by the instruments and also due to the grating coupler losses. In future works, we would try to increase the SOA input power even closer to the saturation of the amplifier and compute the gain and the noise figure. Close to the saturation, we expect a decrease of the gain and an increase of the noise figure [143].

To conclude, we presented a fully integrated silicon photonic circuit that monolithically integrates III-V/Si SOA, Ge waveguide-PD and Si/SiN passive and active components. The 90° optical hybrid meets the specifications given in Table 3.9, with average values for the insertion loss of 0.5 dB, CMRR of 31 dB, imbalance of 0.4 dB and phase error between -5.7° and 0.6°. The measured Ge waveguide-PD responsivity of 0.9 A/W compares well with the specification of 1 A/W, and the measured CMRR meets the 20 dB requirement. The photodiode bandwidth was not measured but we expect several tenth of GHz from simulation, which is much larger than the specified value. Finally, we measured a SOA gain >10 dB at 20°C. Nevertheless, the measured SOA noise figure of 13 dB is high compared to the 8 dB specification, and the SOA saturates at 0 dBm input optical power which is lower than the 10 dBm specification. This will be further investigated in future works.

4.8 Low linewidth tunable laser

The use of tunable laser sources for FMCW LIDAR applications is relevant for several reasons. First, the wavelength tunability of such lasers can be useful for Wavelength Division Multiplexing (WDM). Indeed, FMCW signals at different wavelengths can be transmitted to adress different points of the FoV. In addition, as described by Eq. (2.19), most 2D OPA scanners use wavelength tuning and diffraction gratings to steer the optical beam along the vertical axis. Tunability over 40 nm with a Side Mode Suppression Ratio (SMSR) of 35 dB was demonstrated in [144] [145]. More recently, 60 nm tuning range with more than 46 dB SMSR have been shown [146]. The second advantage, as with have seen during the SNR study in Chapter 3, Section 3.12.1, laser phase noise should be reduced to about 100 kHz to make it negligible the laser phase noise impact on FMCW LIDAR system performances for target range <200 m. In [146], a hybrid integrated tunable laser is made of a Reflective Semiconductor Optical Amplifier (RSOA) coupled to an external cavity built from two ring resonators. The measured Lorentzian linewidth is <80 kHz across the entire C band. The same tunable laser structure but using heterogeneous integration is studied in [147]. A loop mirror is used instead of a reflective surface on one side of the SOA and a 2 kHz Lorentzian linewidth is demonstrated. Extending the laser external cavity by adding rings and cm-long spirals made of low loss SiN material, increases the total quality factor, offering sub-kHz linewidths as demonstrated in [148][147].

4.8.1 The tunable laser structure

Our tunable laser structure is described in Fig. 4.27. The active III-V waveguide is a 800 μm long Semiconductor Optical Amplifier (SOA). The active layers include InGaAlAs quantum wells (QW). The tuning section is composed of two cascaded ring resonators made in silicon. The current injection in thermo-optic phase shifters heats the waveguide which results in a phase shift $\Delta\phi$ [149]:

$$\Delta\phi = \frac{2\pi}{\lambda}\Big(\frac{dn_{eff}}{dT}\Big)\Delta T L, \tag{4.5}$$

where λ is the wavelength, dn_{eff}/dT is the thermo-optic coefficient of the silicon waveguide, L is the thermo-optic phase shifter length and ΔT is the change of temperature given by:

$$\Delta T = \frac{P_{cons}}{C_p \rho_m L S}, \tag{4.6}$$

where P_{cons} is the power consumption of the heater, C_p is the heat capacity of the waveguide, ρ_m is the waveguide material density, and S is the cross-sectional area of the waveguide. To quantify the efficiency of the thermo-optic phase shifter, the power consumption of the heater to achieve a π phase shift P_π is expressed as :

$$P_\pi = \frac{\lambda}{2}\Big(\frac{dT}{dn_{eff}}\Big) C_p \rho_m S \tag{4.7}$$

The cavity modes can be selected based on Vernier effect i.e. by aligning the two ring resonances to one of the cavity mode wavelength. Ring 1 and ring 2 have a

Free Spectral Range (FSR) of 2.63 nm and 2.79 nm respectively that are given by:

$$FSR_i = \frac{\lambda^2}{2\pi R_i n_g} \tag{4.8}$$

with R_i being the radius of ring i and n_g the group index of the two rings. The FSR of the whole filter based on the Vernier effect [150] is:

$$FSR_{Vernier} = \frac{FSR_1 FSR_2}{|FSR_1 - FSR_1|} \tag{4.9}$$

In our design $FSR_{Vernier}$ = 45.9 nm. Both rings have a bend radius of 20 μm. Ring 1 and ring 2 have a physical length of 238.9 μm and 225.7 μm respectively. We measured a Full Width at Half Maximum (FWHM) of 0.19 nm for both rings at 1540 nm which results in a loaded quality factor Q = 7700 [151]. The power coupling coefficients for through and drop ports are both equal to 0.2. The rings are made tunable using heaters implemented in a N-type doped Si waveguide, allowing resonance shift. Changing the voltage on each heater enable to tune the ring resonance over several FSRs. Resonators with high quality factor provide phase noise reduction by decreasing the number of spontaneously emitted photons. For a III-V/SiN resonator the quality factor is given by [80]:

$$Q^{-1} = \Gamma Q_{III-V}^{-1} + (1-\Gamma) Q_{Si/SiN}^{-1} \tag{4.10}$$

where Γ is the confinement factor in the III-V material, Q_{III-V} is the quality factor of the III-V section dominated by absorption and $Q_{Si/SiN}$ is the quality factor of the passive silicon and silicon nitride section. Making $Q_{Si/SiN} >> Q_{III-V}$ enables to reach very low laser linewidth. One advantage of this tunable laser is that both sections can be optimized separately. The SiN spiral is 2 cm-long and SiN surface grating couplers enable to couple light from the photonic chip to a fiber. The inputs/outputs associated with grating couplers are labelled with numbers from 2 to 5.

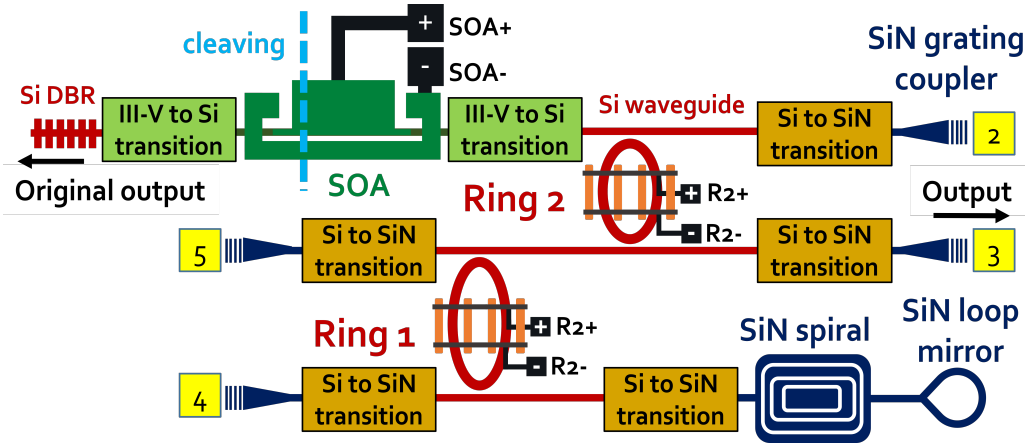

Figure 4.27: Schematic of the tunable laser.

Due to Distributed Bragg Grating (DBR) fabrication issues, we were not able to measure the original output of the tunable laser. Therefore, we cleaved the left facet of the SOA to produce a mirror with a reflection coefficient $R_{cleaved}$ given by the

Fresnel equation [152]. Assuming a normal incidence of the beam at the III-V/air interface, the Fresnel equation is given by :

$$R_{cleaved} = \left(\frac{n_{III-V} - n_{air}}{n_{III-V} + n_{air}}\right)^2, \tag{4.11}$$

where $n_{III-V} = 3.23$ is the effective index of the optical mode in the III-V material at 1550 nm, and $n_{air} = 1$ the refractive index of air. It results in a mirror reflection coefficient $R_{cleaved} = 28\%$.

We measured the output 3 for the laser output in order to keep the SiN spiral in the light path while having maximum power. The new optical path is composed of two drops (ring 2 and ring 1), the SiN spiral with the loop mirror, the drop of ring 1 again and the through of ring 2. Due to this modification, the measured output power is lower than expected and we observed some back reflections in the cavity. Finally, the absence of phase tuning section has an impact on the varying peak intensity at different wavelengths.

The tunable laser was packaged using a fiber array. It was mounted on a Thermoelectric Cooler (TEC) as shown in Fig. 4.28.

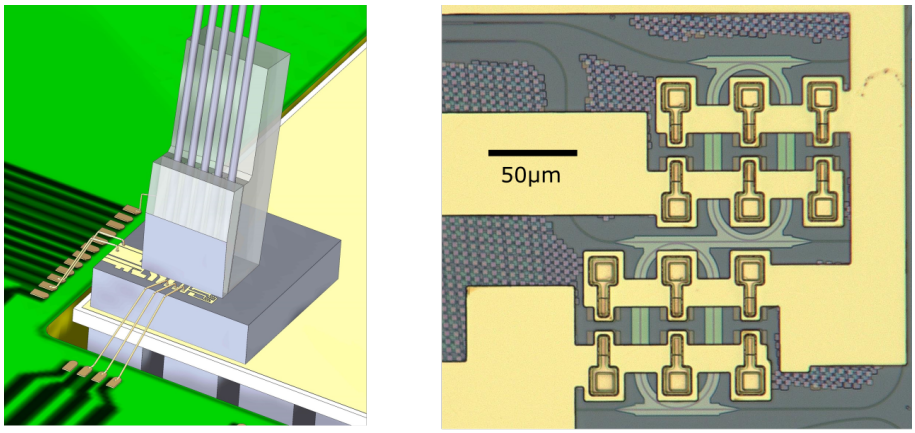

Figure 4.28: a) 3D view of the packaged tunable laser using vertical fiber coupling and b) microscope image of the ring resonators.

4.8.2 Grating coupler measurement

The grating coupler insertion loss was evaluated by measuring the losses between 3 and 5 and neglecting the coupling loss of the through ports of ring 1 and ring 2 out of resonance. This assumption is verified by simulation of ring 1 and ring 2 through port transmissions, as shown in Fig. 4.29.

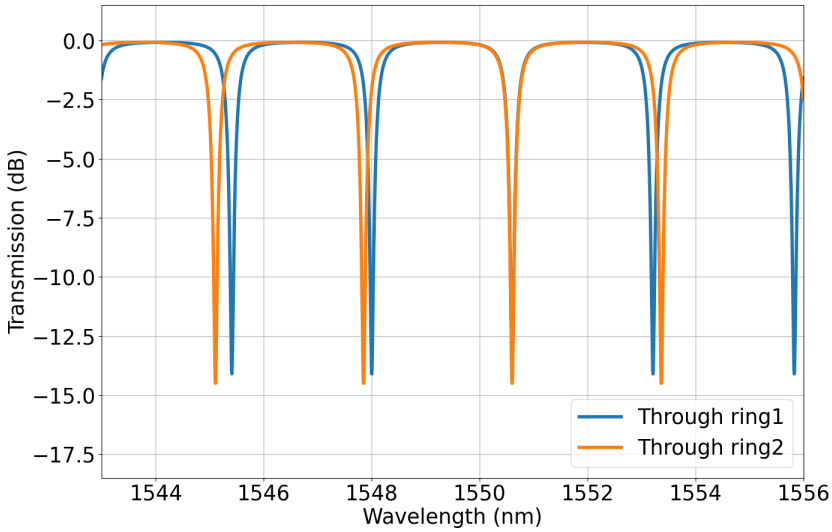

Figure 4.29: Through port transmissions of ring 1 and ring 2.

The setup is composed of an external laser source with a polarization controller before entering in 3, and a powermeter after the output 5. In order to obtain a precise estimation of the grating coupler insertion loss, a voltage sweep on one ring heater was applied and the spectrum for each voltage was recorded as shown in Fig. 4.30 a). The applied voltage ranges from 0.1 V to 4.5 V with 0.2 V steps that are represented by the different colors. Therefore, the envelope can be approximated as the insertion loss of the two grating couplers. The insertion loss of one grating coupler with a cubic interpolation is shown in Fig. 4.30 b). We estimate the insertion loss per grating coupler to be 7.3dB at 1550nm.

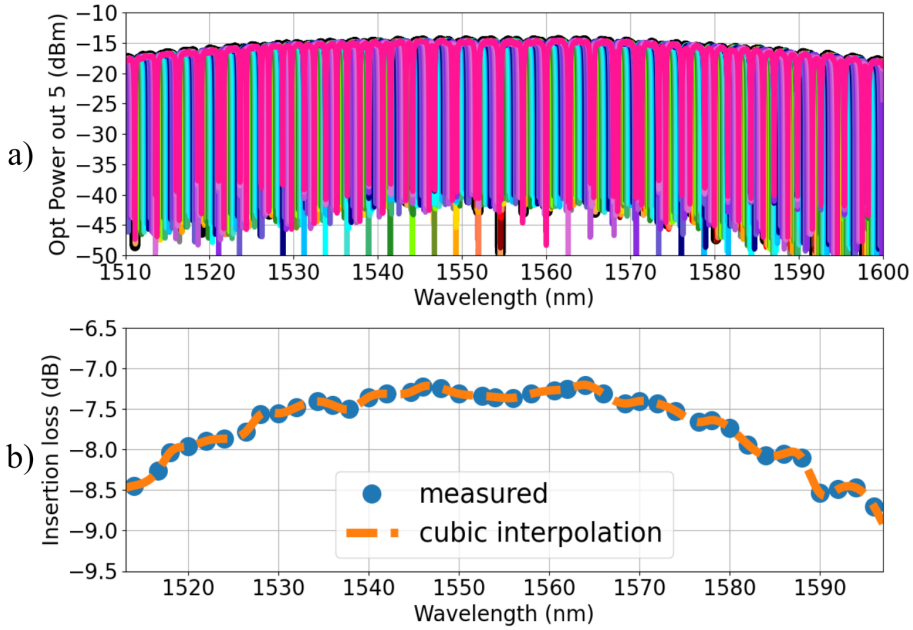

Figure 4.30: a) Transmission between 3 and 5. Light path includes two grating couplers, through port of ring 2 and through port of ring 1. The superposed spectra correspond to a voltage sweep on ring 1 b) Insertion loss of one grating coupler based on cubic interpolation of the measured envelope in a).

4.8.3 Ring filter characterization

The individual drop responses of ring 1 and ring 2 was measured as shown in Fig. 4.31 a) and b). For ring 1, light was coupled in port 4 and measured in port 5 for several ring 1 voltages. For ring 2, light was coupled in port 3 and measured in port 2 for several ring 2 voltages. In the vicinity of 1550 nm, we measured FSR of 2.63 nm and 2.79 nm for ring 1 and ring 2 respectively. Note that the grating coupler losses are not removed in Fig. 4.31 a) and b).

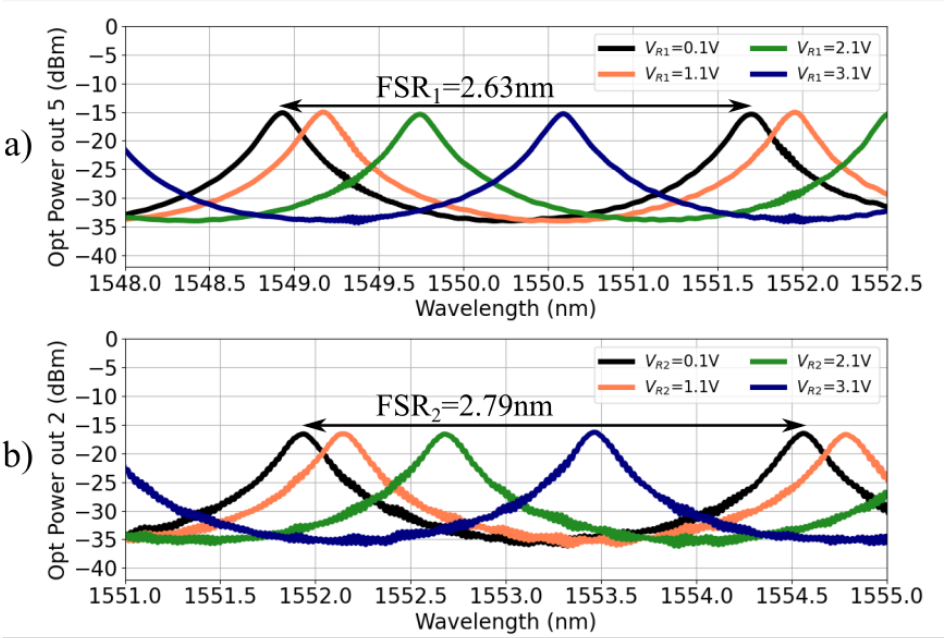

Figure 4.31: Drop port measurements of a) ring 1 for several ring 1 voltages and b) ring 2 for several ring 2 voltages.

Based on these individual ring measurements, the filter response corresponding to the drop of "ring 1 + ring 2" combination was computed as shown in Fig. 4.32.

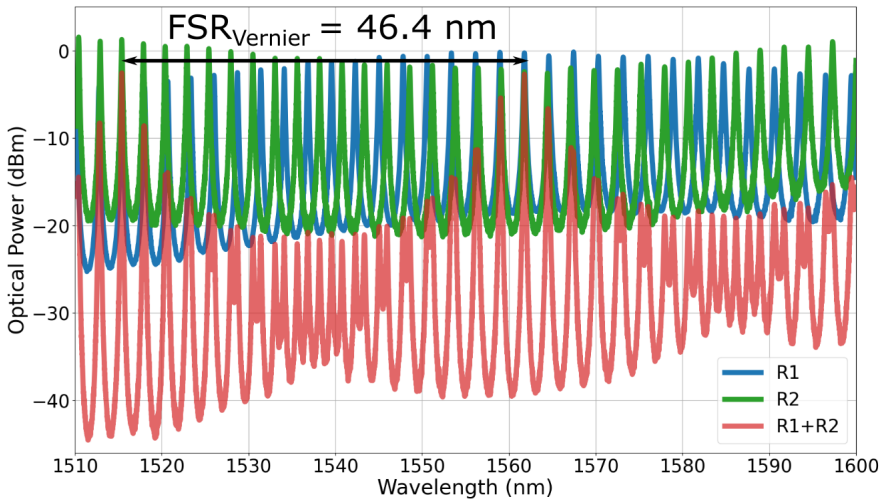

Figure 4.32: Individual measurement response of ring 1 (blue) in out 5, ring 2 (green) in out 2 and computed filter response ring 1 + ring 2 (red).

The extracted Vernier FSR is 46.4 nm which matches the theoretical value of 45.9 nm computed in Eq. (4.9).

In addition, we characterized the whole filter (drop ring 1 + drop ring 2) by entering with the external laser in 4, exiting in 5, connecting a fiber between 5 to 3 and then exiting in 2. The measured spectra are shown in Fig. 4.33 a) and b), for a voltage sweep applied to ring 1 and ring 2 respectively.

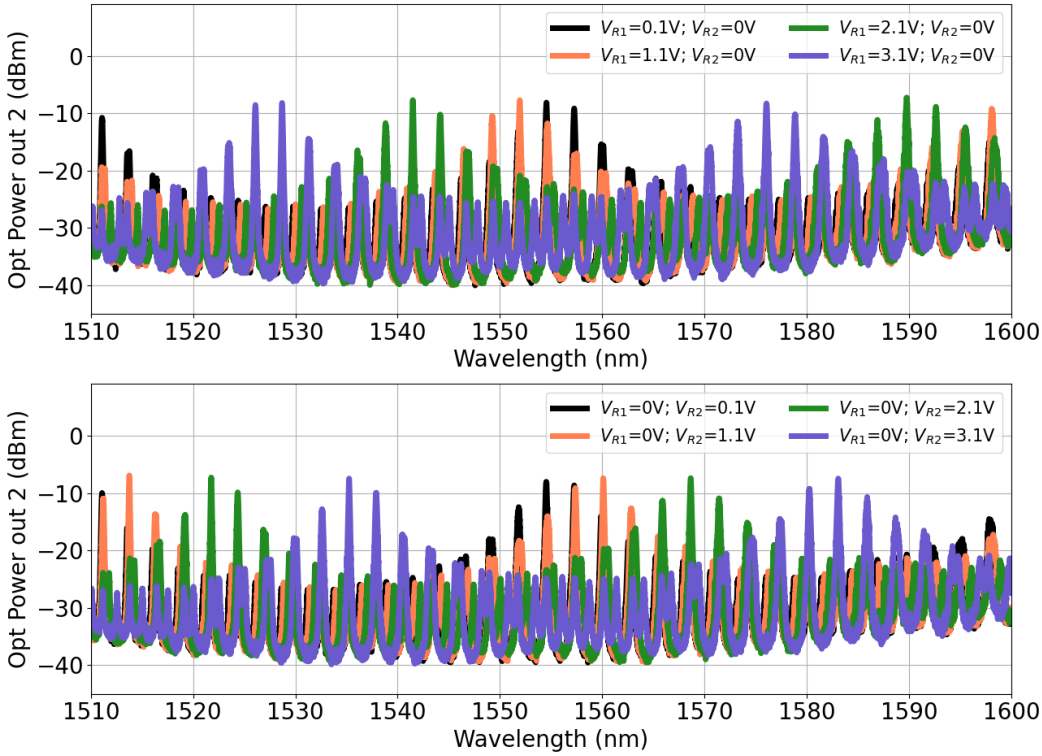

Figure 4.33: Measurement of the filter response on output 3 with a) a voltage sweep on ring 1 and b) a voltage sweep on ring 2.

As shown in Fig. 4.33 a) and b), the Vernier effect enables wide tunability over the measured wavelength range. The measured Vernier FSR is 46.6 nm which matches the theoretical value of 45.9 nm and the computed value of 46.4 nm from single ring measurements. The extinction relative to neighbor peaks could be improved in future designs by increasing the quality factors of the rings.

The electrical power consumption of ring 1 and ring 2 is shown in Fig. 4.34. As expected from thermo-optic effect, a linear relationship is obtained between the wavelength tuning and the electrical power consumption of the heater. The power to achieve one FSR is 54 mW and 56 mW for ring 1 and ring 2, respectively.

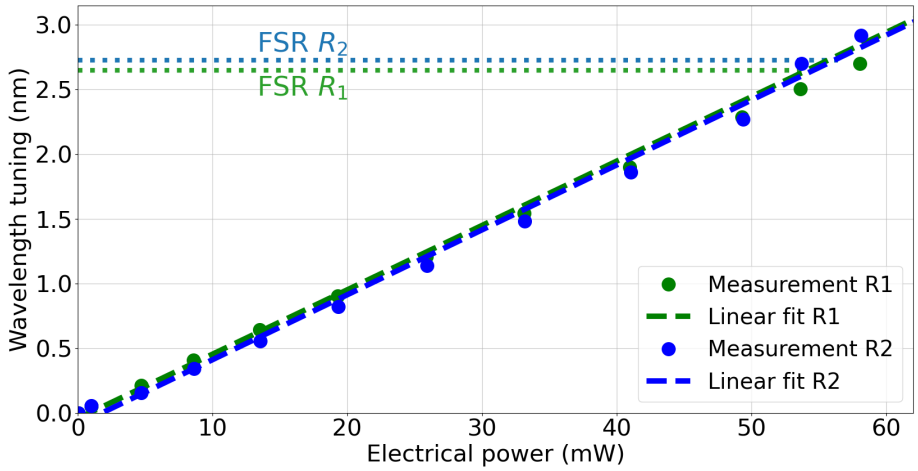

Figure 4.34: Ring heaters electrical power consumption.

4.8.4 Tunability measurement

We measured the laser tuning range by sweeping ring 1 and ring 2 voltages. As shown in Fig. 4.35, the laser can be tuned over the entire C band (1530-1565 nm) with Side-Mode-Suppression-Ratio (SMSR) larger than 35 dB. On the Optical Spectrum Analyzer (OSA), the stacked spectra were taken with a 30 pm resolution and a Video BandWidth (VBW) of 1 kHz.

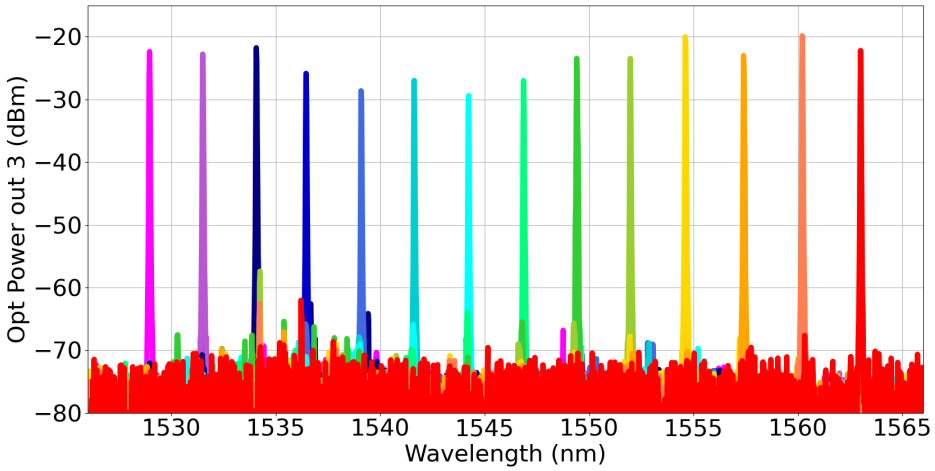

Figure 4.35: Superposition of spectra measured at the output 3 by tuning the wavelength across the C band (1530 nm-1565 nm) SMSR greater than 35 dB.

The variation of peak intensity across the C band between -19.5 dBm and -29.4 dBm can be solved by adding a phase tuning section in the laser cavity in order to precisely align the position of the cavity modes with the ring filter.

4.8.5 Linewidth measurement

The linewidth measurement setup is described on Fig. 4.36. Our tunable laser was driven using a low noise current source (ILX LightWave LDX-3620) on a battery. Due to internal losses, the optical power at the laser output was only -17dBm. We first placed an isolator to mitigate back reflections into the laser cavity with >40dB isolation and 1dB insertion loss. Then, an Erbium-Doped Fiber Amplifier (EDFA) (Keopsys CEFA-C) with up to 30dB gain was used after the isolator. As shown [153], adding an EDFA after the laser has negligible impact on the laser linewidth. A tunable filter (Alnair Labs CVF-200CL) was used to filter the spectral lines around the main laser peak. 10% of the signal was used for monitoring the laser monomodicity on an Optical Spectrum Analyzer (Advantest Q8384), while the remaining 90% was sent to the interferometer for linewidth measurement. The linewidth measurement setup is based on a Delayed Self Heterodyne Interferometer (DSHI) [154] [155], where one arm of the interferometer is delayed so that the two interfering signals are uncorrelated. As we expected the laser linewidth to be around 100kHz (corresponding to 955m coherence length), we used a 12km fiber delay line ensuring that the two arms of the interferometer are decorrelated. On the other arm, a polarization controller was placed to match the polarization states of both arms, and an Acousto-Optic Modulator (AOM) modulates the signal at 100 MHz.

The beating between both signals is produced on a InGaAs photodiode (Discovery Semiconductor Lab Buddy) and sent to an Electrical Spectrum Analyzer (Rohde and Schwarz FSU). The EDFA gain was increased until enough power reaches the photodiode.

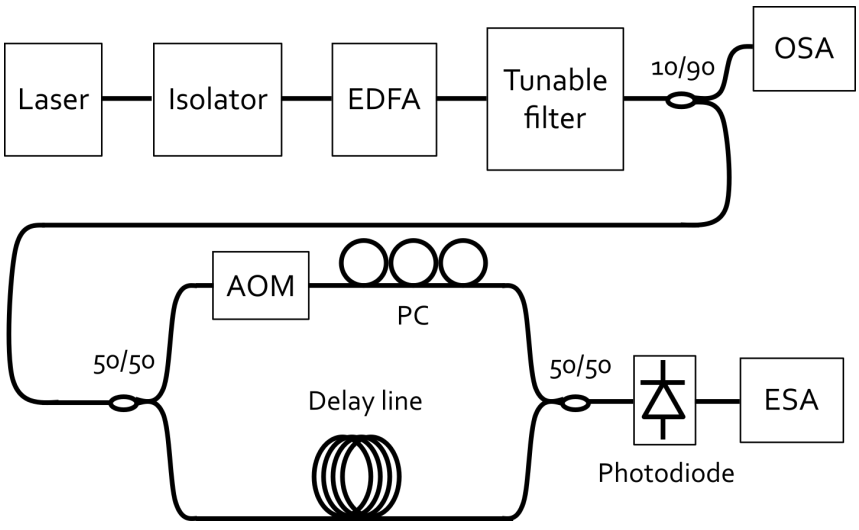

Figure 4.36: Linewidth measurement setup based on the Delayed Self Heterodyne Interferometer technique. EDFA: Erbium- Doped Fiber Amplifier; PC: Polarization Controller; AOM: Acousto-Optic Modulator; ESA: Electrical Spectrum Analyzer.

The beat signal can be expressed as a function of the FM noise spectrum $S_F(f)$ by [148]:

$$S(f) = \mathcal{F}\Big[\exp\big(-4\int_0^\infty S_F(f)\frac{sin^2(\pi f\tau)}{f^2}(1-\cos(2\pi f\tau_d))df\big)\Big] \tag{4.12}$$

where $\mathcal{F}$ denotes the Fourier transform and τ_d is the delay time.

The Lorentzian linewidth is related to the Full-Width-Half- Maximum (FWHM) of the Power Spectral Density observed at the ESA.

The measured laser output power was -17 dBm. Adding 1 dB of loss due to the isolator, the EDFA input power was -18 dBm. We biased the EDFA at 200 mA and measured an optical power after the EDFA of 15 dBm resulting in a gain of 33 dB.

4.8.6 Results and discussion

To check the validity of our linewidth measurement setup, we connected a reference DFB laser (Alcatel 1905 LMI) and used a 12 km delay line. The spectrum measured at the Electrical Spectrum Analyzer (ESA) is shown in Fig. 4.37.

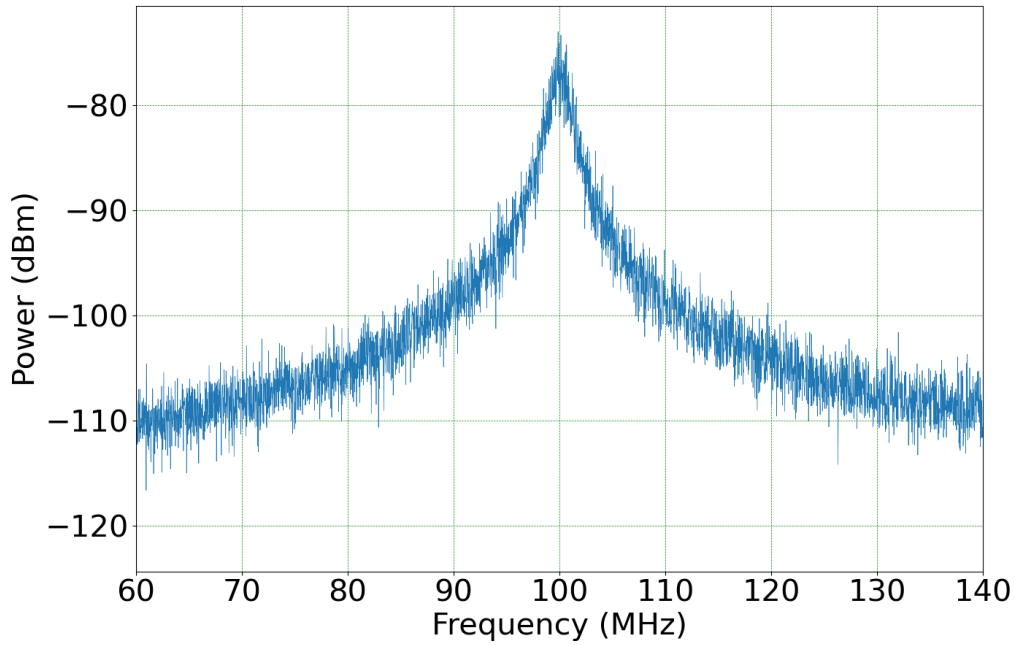

Figure 4.37: Linewidth measurement of a reference DFB laser (Alcatel 1905 LMI).

We measured a -3 dB linewidth of 0.9 MHz that agrees the fabricant specification of 1 MHz. This ensures that the two arms of the interferometer are decorrelated after 12 km of fiber delay.

Then, we connected our tunable laser to the linewidth measurement setup. The measured ESA spectrum for a tunable laser bias current of 82 mA and the TEC Temperature of 29°C is shown in Fig. 4.38. A pseudo-Voigt fit is applied to the measured data to account for technical noise (Gaussian contribution) and intrinsic laser phase noise (Lorentzian contribution) [156]. The fitted Lorentzian linewidth is 184 kHz while the Gaussian linewidth is 177 kHz.

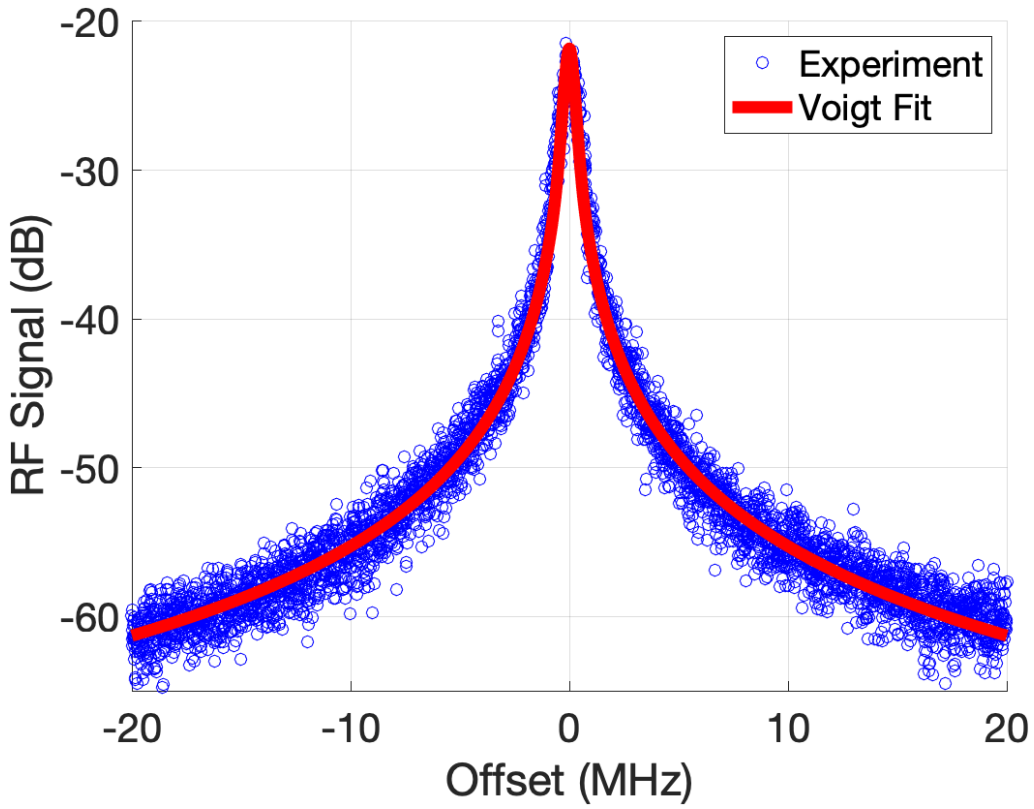

Figure 4.38: Linewidth measurement of the tunable laser fitted with pseudo-Voigt function.

The Lorentzian linewidth could even be reduced by increasing the quality factor of the cavity. To do so, the losses inside the passive region must be reduced while longer cavities can be designed [154].

During our measurements, we observed that the tunable laser is extremely sensitive to temperature variations. Any fluctuations in the SOA applied current or TEC temperature can misalign the cavity modes with the ring filter, and degrade the laser spectral response. For a given SOA bias current, we varied the TEC temperature and we observed at the OSA that laser peak was moving at 0.07 nm/°C, as shown in Fig. 4.39.

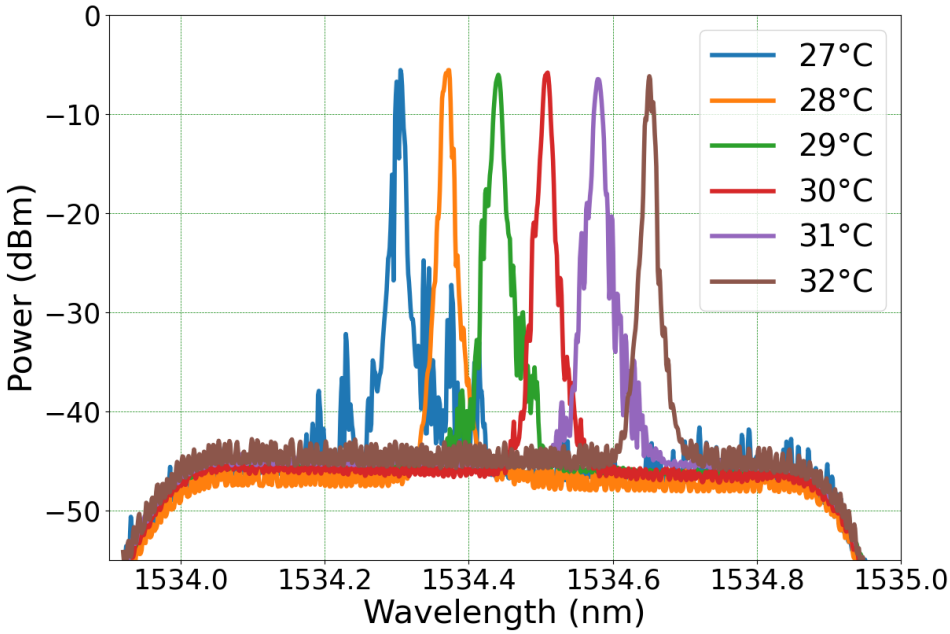

Figure 4.39: Spectra measured at the OSA for several TEC temperatures and at 82 mA SOA current.

From Fig. 4.39, the optical spectra are polluted by peaks with lower intensity around the main ray. This could originate from self injection into the laser cavity due to internal reflections at the grating couplers interface for instance.

As a conclusion, we reported on a III-V on silicon backside processed fully integrated tunable laser. We reported on wavelength tuning over the C band with >35 dB SMSR. Measurements based on DSHI technique show 184 kHz Lorentzian linewidth. The measured value does not meet the linewidth specification of 100 kHz given in Table 3.9. In future tunable laser implementations, we will mitigate internal reflection and use the dedicated output laser port for linewidth measurements.

4.9 DBR laser

Another option that was evaluated for the FMCW LIDAR source was the Distributed Feedback (DFB) laser. A DFB laser uses a Bragg grating along the active region to provide the optical feedback. A phase shift is usually created in the center of the periodic grating, ensuring single mode laser operation. Moreover, DFB lasers can produce frequency chirps with large frequency excursion by modulating the injection current [105][122]. However, due to the same grating fabrication issue as the tunable laser, the DFB laser gratings were not resolved properly. In the next fabrication run, we had the opportunity to replace this initial DFB laser into a Distributed Bragg Grating (DBR) laser. Our DBR laser is formed by an active III-V laser active region that is sandwiched between a 60% reflectivity broad band (BB) silicon loop mirror and a 60% reflectivity narrow band (NB) Bragg mirror defined in the silicon nitride (SiN), as shown in Fig. 4.40. On the side of the BB Si loop mirror, we use a SiN grating coupler “GC 1” to couple the light outside from the chip. On

the NB DBR mirror side, the light is directed towards the rest of the circuit. The measurements presented hereafter make use of "GC 1" as the output.

The measurement setup is shown in Fig. 4.40. We used a 10%/90% tap at the "GC 1" output in order to simultaneously measure the optical flux at the powermeter and the spectrum at the OSA.

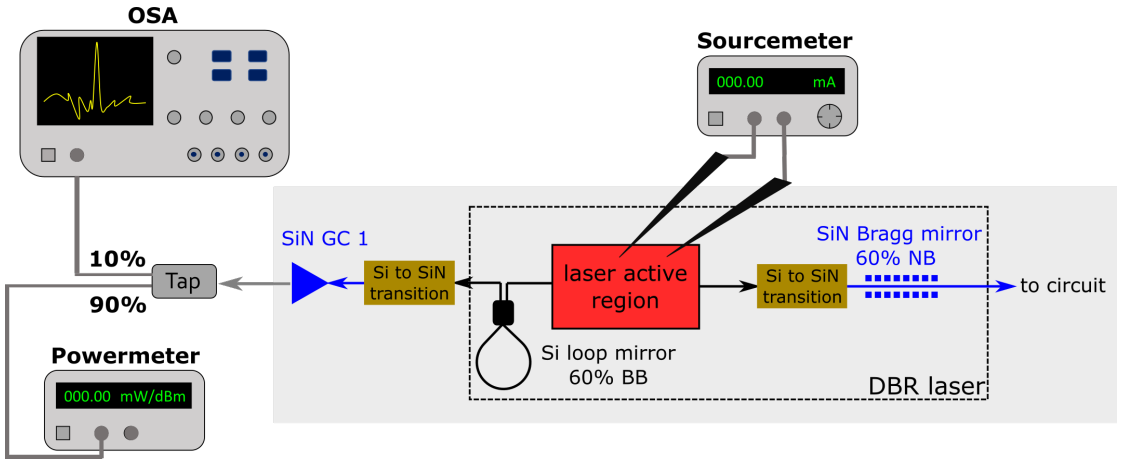

Figure 4.40: DBR laser measurement setup.

A microscope image of the fabricated DBR is shown in Fig. 4.41 with the two electrical pads for the cathode and the anode. The metal layers are designed with large width (several hundreds of μm) to withstand several hundreds of mA of injection current. The DBR laser is 800 μm long.

Figure 4.41: Microscope image of the fabricated III-V/Si DBR laser.

Prior to the laser characterization, the insertion loss of one SiN GC was measured on a dedicated shunt test structure as shown in Fig. 4.42. Over the 7 measured dies, the peak wavelength is 1570 nm and the average insertion loss of one grating coupler is 6 dB at this wavelength.

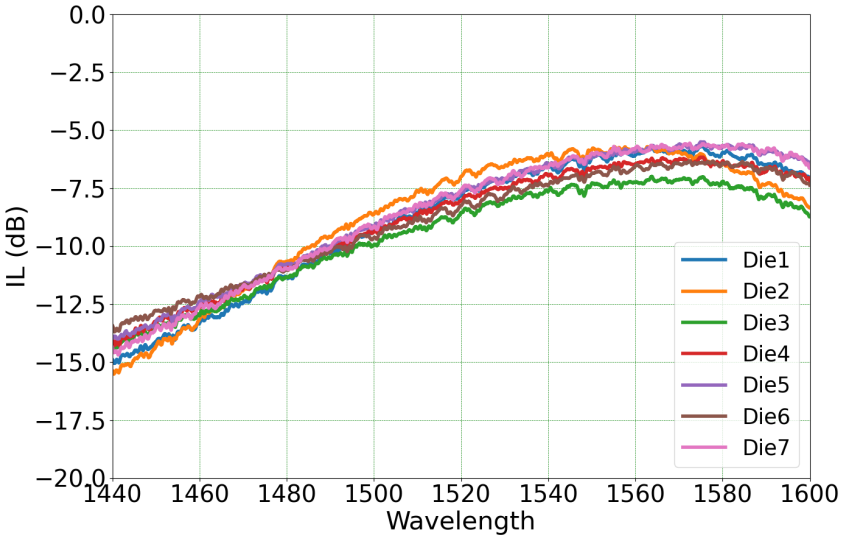

Figure 4.42: Insertion loss (IL) of one SiN GC over 7 dies.

The light-current-voltage (LIV) curves of the DBR lasers over 7 dies are shown in Fig. 4.43. The flux is measured on the powermeter after a 90% tap and the sourcemeter measures the voltage under the applied laser current. First, we identified die 5 as a non functional die due to its zero measured flux and flattened IV characteristic. The measured laser threshold current is around 37 mA except for die 7 where the threshold is 50 mA and the measured flux is three times lower than for the other dies. The LI curves show some fluctuations when the injection current increases. This is typical when the laser mode hopes, i.e. when the laser suddenly switches to another mode. Considering die 2 and an injection current of 150 mA, the laser approximately consumes 200 mW.

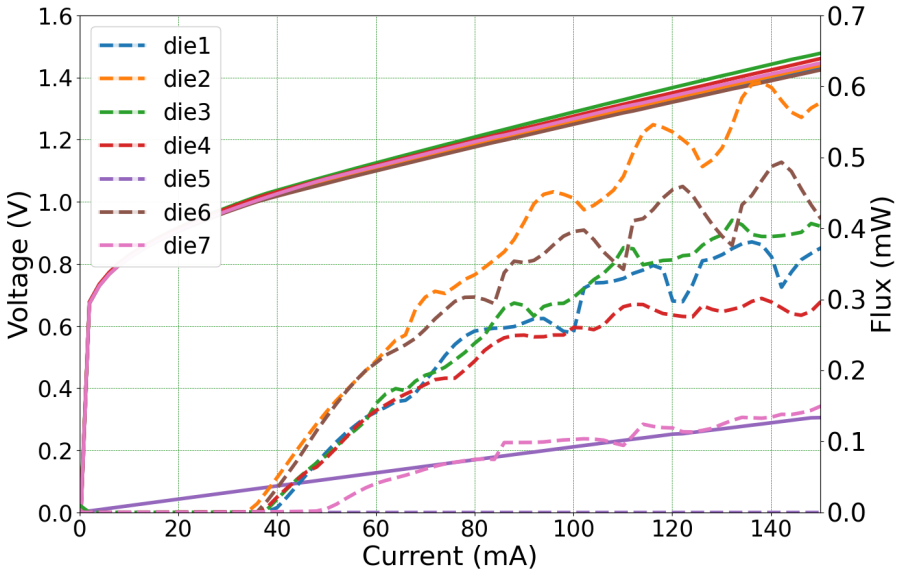

Figure 4.43: LIV curve of the DBR laser measured at “GC 1” over 7 dies.

The spectra of the DBR laser in die 6 under several laser currents for a wide and narrow wavelength span are shown in Fig. 4.44 a) and b) respectively. For the wide span (1510-1570 nm), the OSA resolution is 0.1 nm while for the narrow span

(1542.6-1543.8 nm) the OSA resolution is 4 pm. To recover the on chip optical power (in the Si waveguide), we should add 17dB because of the 10% tap and the 7 dB of GC loss around 1543 nm. The resulting on chip power at the laser output is around -1 dBm (0.8 mW). From Fig. 4.44 b), we measured a Side Mode Suppression Ratio (SMSR) > 40 dB.

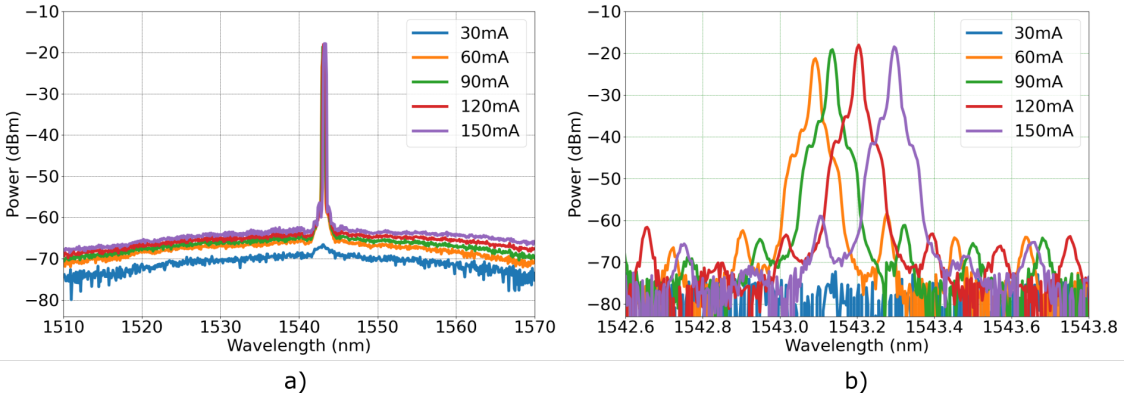

Figure 4.44: Measured a) wide wavelength span spectrum and b) narrow wavelength span spectrum for the DBR laser in die 6.

On the other dies, the spectrum was highly multimode especially when increasing the laser injection current. The superimposed spectra for a DBR laser current of 150 mA are shown in Fig. 4.45.

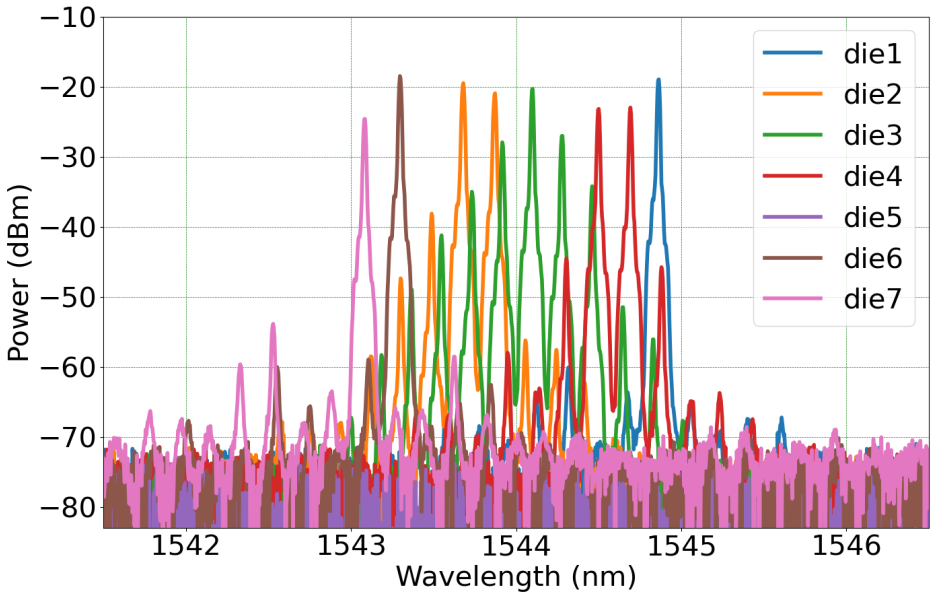

Figure 4.45: Measured spectra at 150 mA of the DBR laser over the 7 dies.

We did not perform direct frequency chirp measurement on either the DBR and tunable laser. Nevertheless, in the following section, we present indirect frequency chirp linearity measurement using an external laser coupled to a integrated IQ modulator made in silicon.

4.10 Frequency chirp with IQ modulator

In addition to the low linewidth requirement, the FMCW LIDAR source should also have high chirp linearity. In this section, we present our work on a Silicon IQ modulator with a monolithically integrated III-V/Si semiconductor optical amplifier (SOA) to demonstrate highly linear chirp generation. This work has been submitted as an article to Photonics Technology Letters journal.

Nonlinear distortion of the frequency chirp broadens the detected signal spectrum, degrading the SNR and resolution [120]. Chirping the FMCW LIDAR signal can be either achieved through direct laser modulation or by using an external modulator with a fixed laser frequency. Direct modulation suffers from the nonlinear relationship between optical frequency and injection current. To mitigate non-linearities, resampling methods [157], iterative learning pre-distortion of the driving signal [158], optical phase locked loop (OPLL) [159], or engineering of the laser structure [122] can be used. However, these chirp linearization methods may add latency, complexity, and cost to the system. Another drawback of direct laser modulation is a degradation of the laser linewidth due to the unwanted intensity modulation [160]. External modulation is therefore preferable for solving the narrow linewidth and chirp linearity challenges independently. The low linewidth tunable laser described in Section 4.8 could be combined with IQ modulator to produce high linear frequency chirps at several wavelengths. External modulation also offers flexibility in the transmitted signal as shown in [161], where a fibered IQ modulator generates two independent linear frequency chirps in the lower and upper side bands (LSB and USB) for simultaneous measurement of the target range and radial velocity, reducing the time allocated to each pixel. Nevertheless, IQ modulation comes with high loss as the modulation is made at the carrier suppression point. In [88], a fibered FMCW LIDAR comprising an IQ modulator followed by an Erbium doped fiber amplifier (EDFA) has been reported but the chirp linearity was not measured.

Our PIC is composed of a Si based high speed IQ modulator and a III-V/Si SOA fabricated on the same platform. The IQ modulator consists of two nested Mach-Zehnder Modulators (MZM I and MZM Q) that are DC biased at the minimum transmission point. A phase shift of $\pi/2$ is inserted between the two MZMs. Light is coupled in and out of the chip by a fiber array aligned to surface Grating Couplers (GCs) defined in the Si. The PIC is mounted on a thermoelectric cooler (TEC) to ensure stable temperature operation. An electronic control board, including RF drivers was developed to command the PIC. The motherboard is fed by a 12 V power supply. The Fig. 4.46 shows a picture of the fabricated package.

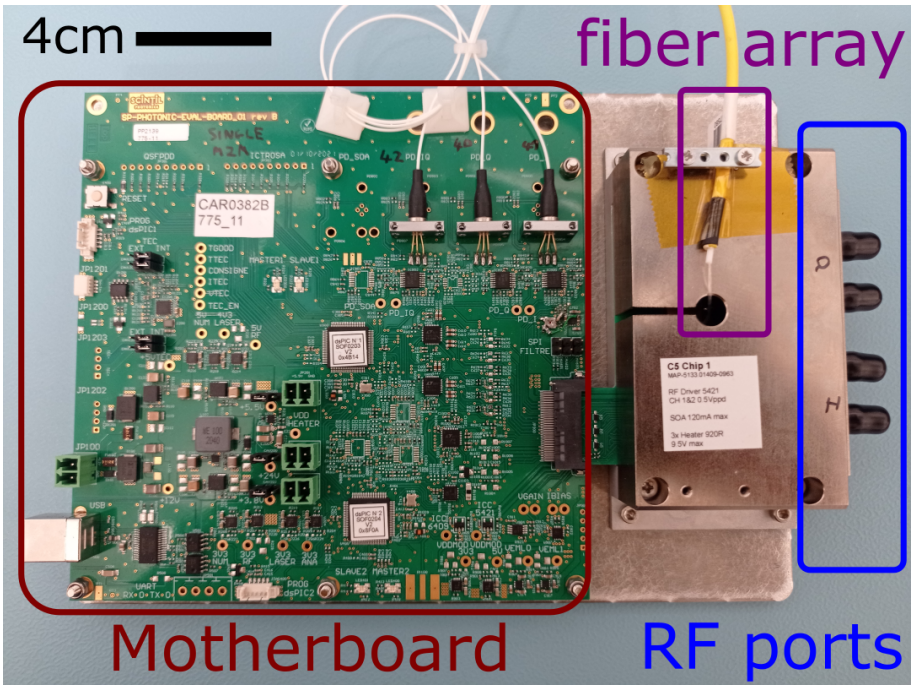

Figure 4.46: Picture of the PIC package with its motherboard.

The schematic on Fig. 4.47 shows the working principle for FMCW LIDAR frequency synthesis in our circuit. An external laser having an optical power $P_{las} = 13$ dBm and an optical frequency $f_{las} = 195.9$ THz (corresponding to a wavelength of 1530 nm) feeds the on-chip IQ modulator and SOA. To produce the frequency chirp, a complex RF modulating signal $u(t)$ is applied to the IQ modulator as:

$$u(t) = u_I(t) + ju_Q(t) \tag{4.13}$$

where $u_I(t)$ and $u_Q(t)$ are the RF chirped signals applied to MZM I and MZM Q respectively. To produce the $u_I(t)$ and $u_Q(t)$ signals, we used a 24 GHz RADAR phase-locked loop (PLL) composed of a phase detector, a low pass filter and a voltage controlled oscillator (VCO) [162].

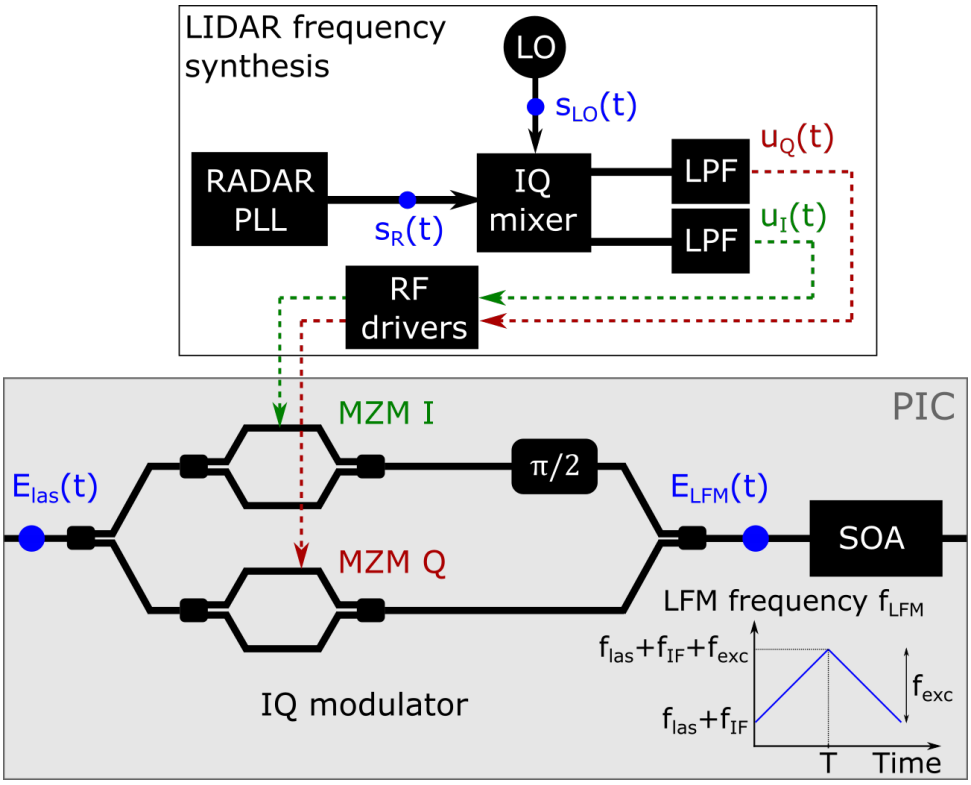

Figure 4.47: Schematic of our FMCW LIDAR frequency synthesis scheme. The I and Q RF signals generation are applied to the PIC composed of an IQ modulator and III-V/Si SOA.

We performed triangular modulation composed of symmetric up- and down-ramps with period duration T of 154 μs. The calculations are done for the signal under an up-ramp, while the same derivation applies to a down-ramp. Over an up-ramp period T, the PLL provides a RF output signal s_R(t) given by:

$$s_R(t) \propto \cos\left(2\pi f_R t + \frac{\pi f_{exc}}{T} t^2\right), \tag{4.14}$$

where s_R(t) describes an up linear frequency chirp starting at f_R = 24 GHz with frequency excursion f_{exc}.

A local oscillator (LO) sine-wave s_{LO}(t) (f_{LO} = 21.2 GHz) is generated as:

$$s_{LO}(t) \propto \cos\left(2\pi f_{LO} t\right), \tag{4.15}$$

s_R(t) and s_{LO}(t) are then mixed within the IQ mixer followed by Low Pass Filters (LPFs) to produce the $u_I(t)$ and $u_Q(t)$ signals [88]:

$$u_I(t) = \alpha_{RF} \cos\left(2\pi f_{IF} t + \frac{\pi f_{exc}}{T} t^2\right) \tag{4.16}$$

$$u_Q(t) = \alpha_{RF} \sin\left(2\pi f_{IF} t + \frac{\pi f_{exc}}{T} t^2\right), \tag{4.17}$$

where f_{IF} = f_R-f_{LO} = 2.8 GHz and α_{RF} is the amplitude of the RF signal.

The two RF signals are applied to the I and Q ports of the modulator to produce a Linear Frequency Modulation (LFM) with optical field, E_{LFM}(t) by:

$$E_{LFM}(t) = E_{las}(t).exp\Big[j(2\pi f_{IF}t + \frac{\pi f_{exc}}{T}t^2\Big], \tag{4.18}$$

where E_{las}(t) is the external l laser field. The time domain evolution of the LFM frequency f_{LFM}(t) is described on the insert of Fig. 4.47. In our measurement, we produced a frequency excursion f_{exc} of 1.5 GHz.

The chirped signal is then amplified by a SOA biased at 120 mA to produce a measured optical gain of G_{SOA} = 10 dB.

The Fig. 4.48 describes the chirp linearity measurement setup. It is based on delayed self-heterodyne interferometry (DSHI), where one arm of the interferometer is delayed so that the beat signal produced by the two interfering signals can be processed to assess the frequency chirp linearity [158]. We used a L = 2 m fiber delay line corresponding to a delay time τ = 9.8 ns in the first arm. In the other arm, a polarization controller was placed to match the polarization states of both arms.

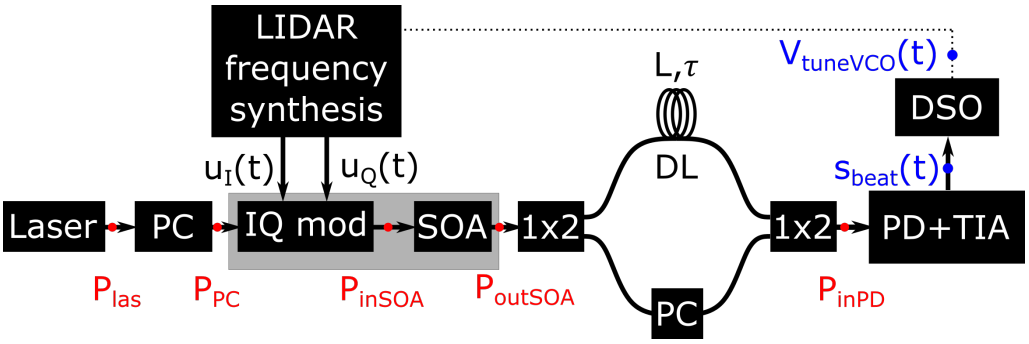

Figure 4.48: Measurement setup to evaluate the chirp linearity from the IQ modulator. PC: polarization controller; SOA: semiconductor optical amplifier; DL: delay line; PD: photodiode; TIA: transimpedance amplifier; DSO: digital storage oscilloscope.

The computed optical power budget of the measurement setup is described in Table I considering ideal splitters and lossless polarization controllers. The IQ modulator insertion loss IL_{IQ} is computed from:

$$IL_{IQ} = 4.SL^2.EL.\Big(\frac{\pi}{2V_\pi}\Big)^2.\alpha_{RF}^2 \tag{4.19}$$

where we note SL the splitter loss, EL the MZM excess loss, V_π is the voltage to achieve π phase shift, and α_{RF} is the amplitude of the RF signals. A V_π of 6.5 V was measured on each MZM with a delivered amplitude α_{RF} of 2 V. The MZMs are 3 mm-long, and we measured a propagation loss due to the doped silicon of 2 dB/mm, resulting in a MZM excess loss EL of 6 dB. Considering ideal splitters (SL = 0.5), the IQ modulator insertion loss is estimated around 18 dB.

Labels	Optical powers	Units
P_{las}	13	dBm
P_{PC}	13	dBm
P_{inSOA}	-5	dBm
P_{outSOA}	5	dBm
P_{inPD}	2	dBm

Table 4.5: Computed optical power budget of the chirp linearity measurement setup.

The beat signal s_{beat}(t) is produced from the recombination of the two arms on an external photodiode. A transimpedance amplifier (TIA) with gain G_{TIA} = 10 V/A amplifies the photocurrent and converts it into a voltage. The beat signal is expressed by:

$$s_{beat}(t) \propto \eta.P_{inPD}.G_{TIA}.\cos(2\pi f_{beat}(t).t) \tag{4.20}$$

where η is the photodiode responsivity (1 A/W), P_{inPD} is the optical power at the photodiode input and f_{beat}(t) = f_{beat}(t) - f_{beat}(t-τ) is the beat signal frequency. For $\tau << T$, the beat frequency can be approximated by its 1st order Taylor series expansion, i.e. $f_{beat}(t) \sim f'_{LFM}(t).\tau$. In our experiment, τ/T=1/15306 << 1, which validates this approximation.

The beat signal phase Φ_{beat}(t) can then be extracted using a Hilbert transform (HT) over the ramp period T [157][158]:

$$\Phi_{beat}(t) = 2\pi\tau \int_T f'_{LFM}(t)dt = 2\pi\tau f_{LFM}(t) \tag{4.21}$$

The instantaneous frequency f_{LFM}(t) is then obtained through:

$$f_{LFM}(t) = \frac{\Phi_{beat}(t)}{2\pi\tau} \tag{4.22}$$

The Fig. 4.49(a) and (b) show the VCO command signal $V_{tuneVCO}$(t) and the resulting time domain beat signal $s_{beat}(t)$ respectively, observed on a digital storage oscilloscope (DSO).

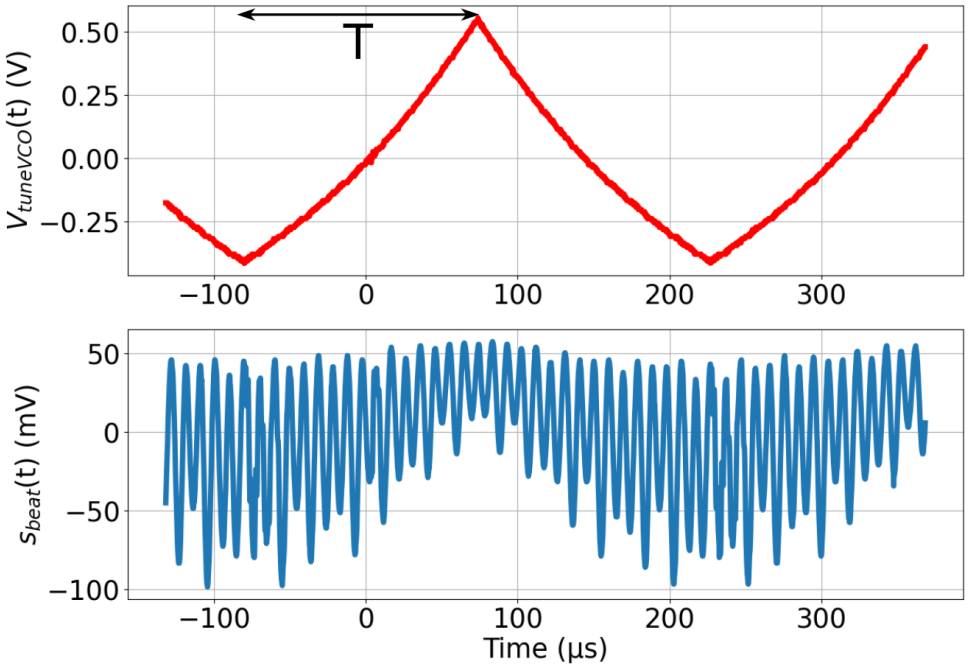

Figure 4.49: Measured a) VCO command signal, $V_{tuneVCO}$(t) and b) time domain beat signal, s_{beat}(t) on the DSO.

The $V_{tuneVCO}$(t) curvature in Fig. 4.49(a) originates from the VCO nonlinearity compensation, ensuring linear frequency chirps at the PLL output. We focus on the up-ramp of the frequency modulation for evaluating the linearity. Fig. 4.50(a) shows the instantaneous frequency retrieved from (9) and taken over 5%-95% of the up-ramp period T. The measured frequency excursion f_{exc} over this segment is 1.38 GHz. The frequency chirp nonlinearity, as plotted on Fig. 4.50(b), is evaluated as the difference between the measured instantaneous optical frequency data and their best linear fit [159]. The superimposed curves on Fig. 4.50(b) correspond to 30 up-ramp periods. The standard deviation of the mean of these 30 curves is 24.3 MHz, which corresponds to 1.8% nonlinear distortion for a 1.38 GHz frequency excursion. From Fig. 4.50(b), we noticed that the initial and final portion of the up-ramp are responsible for high nonlinearities. In these regions, the optical frequency undergoes sharp transitions. By considering 20%-80% of the chirp period T, the nonlinear distortion reduces to 0.4%. Iterative learning pre-distortion algorithms [158] could be used to reach a nonlinear distortion below 0.1% for automotive applications, as detailed in Table 3.9 .

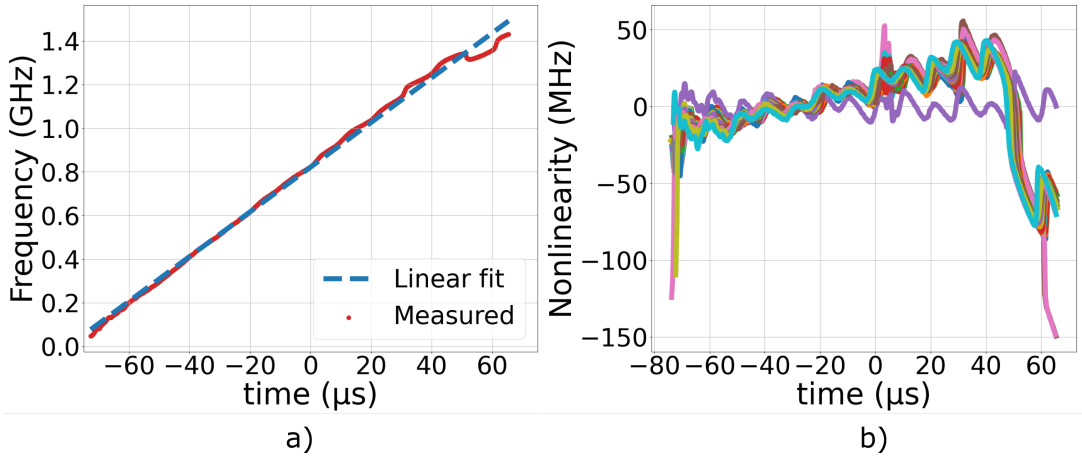

Figure 4.50: a) Retrieved instantaneous frequency profile over 5%-95% of the up-ramp period T. b) Chirp nonlinearity obtained by subtracting the instantaneous frequency profile with a linear fit.

FMCW LIDAR ranging measurements can be used as an alternative method for evaluating chirp nonlinearity, since the dependency between the beat frequency and the fiber length is linear for an applied linear frequency chirp. We performed these measurements for several fiber delay lengths (from 2-18 m). For each fiber delay line, the polarization controller in the interferometer was adjusted to match the polarization state of the two arms. An estimate of the beat signal frequency is given by the maximum peak frequency of the Fast Fourier Transform (FFT) applied to the beat signal over 5%-95% of the period T. The measured spectra for each fiber length are superimposed on Fig. 4.51.

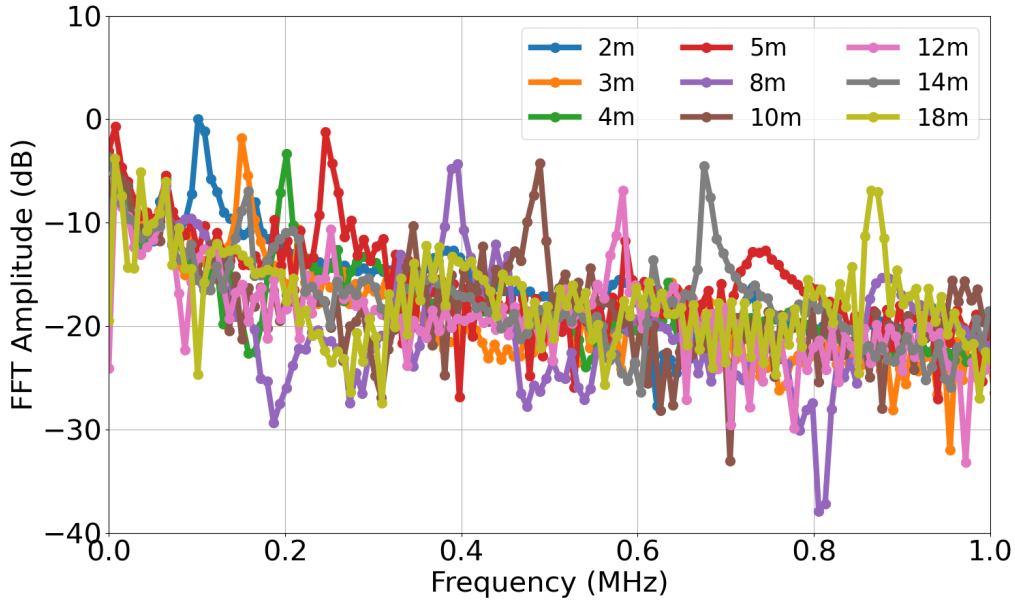

Figure 4.51: Measured FFT spectra for several fiber lengths.

In Fig. 4.52, the measured beat frequencies are plotted against fiber length. We obtained a high linear coefficient of determination (R^2=0.999), confirming the chirp linearity measurement results. We measured the slope γ of the data plotted in

Fig. 4.52, the frequency excursion f_{exc} can be obtained as:

$$f_{exc} = \gamma \frac{c}{n_g} T_{90\%} \tag{4.23}$$

where c is the speed of light in vacuum, n_g is the group index in the single mode fiber (1.4675 at 1550 nm) and $T_{90\%}$ corresponds to the 5%-95% portion of the up-ramp period T, $T_{90\%} = 138$ μs.

We measured a fitted slope γ of 48.2 kHz/m corresponding to a frequency excursion f_{exc} of 1.36 GHz that matches the 1.38 GHz frequency excursion measured previously. This translates into a range resolution of 11 cm [158].

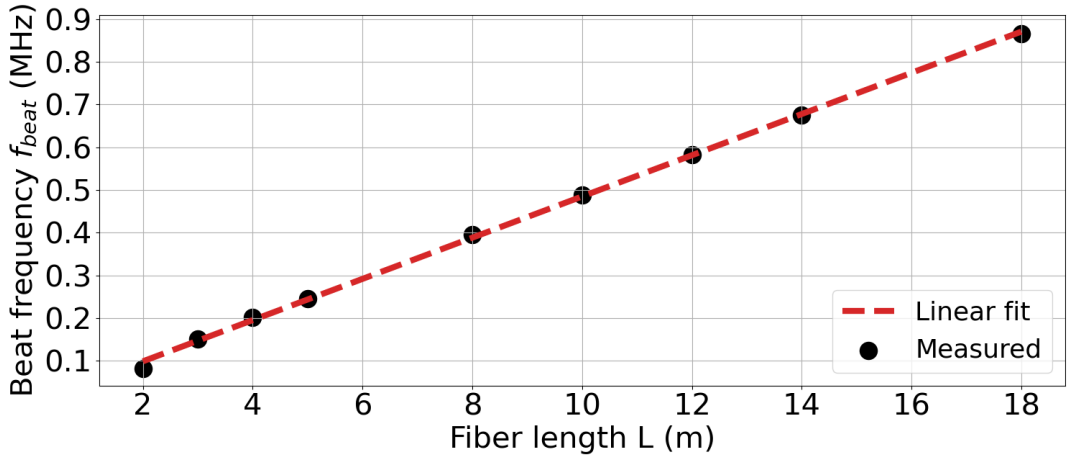

Figure 4.52: Beat frequency against fiber length showing high linear dependency (R^2=0.999).

In conclusion, we perform laser frequency chirping with a silicon photonic circuit integrating on the same chip a silicon IQ modulator and a III-V/Si SOA. The linearity of the generated chirp was measured and showed nonlinear distortion as low as 1.8% over 5% to 95% of the chirp period. These results were confirmed through range measurements with several fiber delay lines (2 to 18 m) with good resolution. In the future, this PIC will be integrated with the coherent receiver to allow long range FMCW LIDAR operation. Shorter modulation periods will be evaluated in order to satisfy the FMCW LIDAR scanning speed.

4.11 Beam scanning unit

As shown in chapter 2, quantifying the power consumption and the scanning speed of the beam steering unit is essential as it may differ between techniques. Our circuit has been fabricated on our integration platform that makes use of Si, SiN, Ge for building switches and monitoring photodiodes. As this circuit was part of a multi project wafer (MPW) run, we did not integrate III-V material. Therefore, the light is coupled into the circuit using an external laser and no optical amplification is used. Through DC characterization, the circuit power consumption is extracted. AC characterization is then described for obtaining the scanning speed of our circuit. In order to evaluate the switch functionality, we designed a 4-emitter focal plane switch array (FPSA).

In this section, we present this fully integrated circuit structure and its characterization.

4.11.1 The structure

The circuit is shown in Fig. 4.53. It is composed of three switches based on Mach-Zehnder interferometers (MZI) with thermo-optic phase shifters on one arm. By tuning each phase shifter, the input optical power can be directed towards the left (L) or right path (R) of the switch output.

An external laser feeds the circuit through a SiN grating coupler ("GC in"). The light enters the switch 1 (S1) and is directed towards the second stage of switches composed of switch 2 and switch 3. Depending on the voltage applied to switch 1, the light can either be directed to S2 or S3. In between S1 and S2, a 10%/90% power tap was placed to monitor the signal intensity either on an integrated Ge photodiode or to a grating coupler for external measurement. If the light is coupled to S3, using the same principle, the light can be either directed towards GC A, GC B or GC C emitters. If light is directed to S2, either GC D, GC E or GC F can be used as emitters. The emitters are equally spaced by a distance d of 127 μm, to match standard fiber array pitch. Not shown on Fig. 4.53, we also placed taps in the opposite arms where no monitoring PD was placed, in order to compensate for losses and balance the circuit.

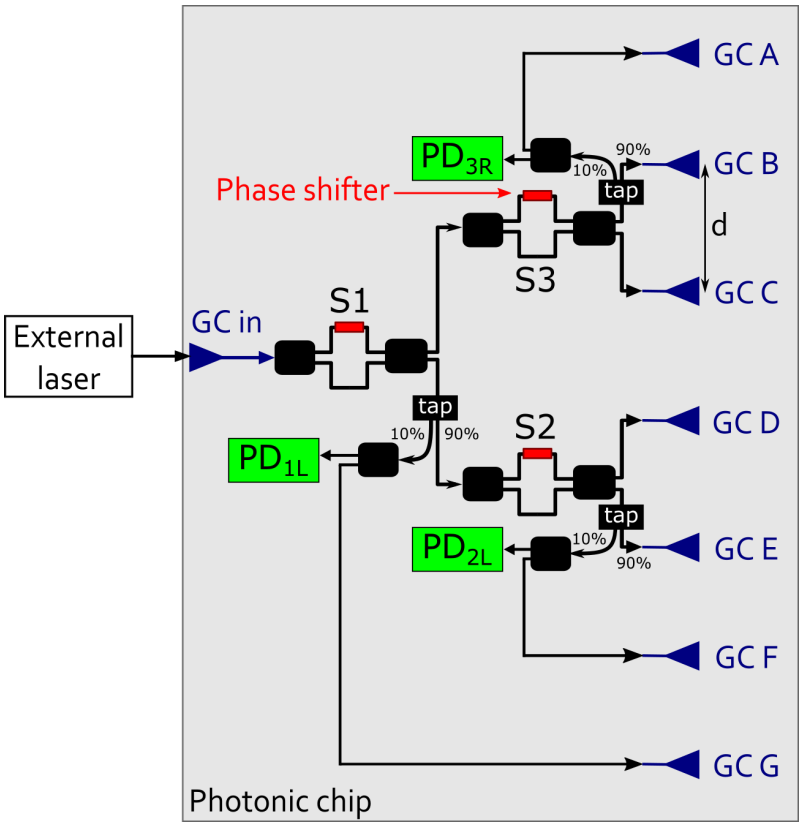

Figure 4.53: Schematic of the 4-emitter focal plane switch array circuit. GC: grating coupler; S1: switch 1; S2: switch 2; S3: switch 3; PD: photodiode; tap: 10%/90% tap.

We present the characterization of this circuit that enables to select one of the four switch outputs as the emitter. The idea of this work is to evaluate the switch performances using a small scale array.

A microscope view of the fabricated FPSA circuit is shown in Fig. 4.54. The chip dimensions are 1 mm x 1.5 mm.

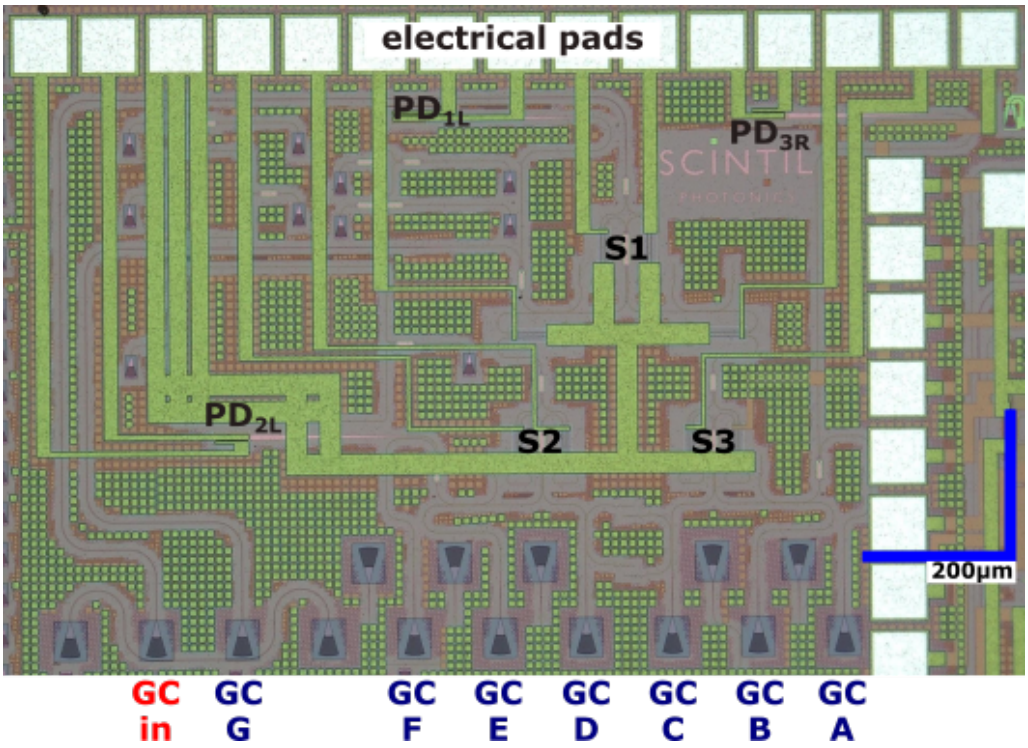

Figure 4.54: Microscope view of the fabricated 4-emitter FPSA circuit. GC: grating coupler; PD: photodiode; S: switch.

4.11.2 Characterization overview

First, we performed electrical measurements to characterize the three thermo-optic phase shifters in terms of resistance and power consumption. Then, we connected the input grating coupler "GC in" to an external laser and we performed electro-optical measurements to extract the insertion loss of an individual switch. We identified the switch heater combinations for commuting power between the steering circuit's outputs. In addition, the optical crosstalk corresponding to the optical power measured at the undesired outputs was obtained. We also did AC characterization of the thermo-optic phase shifter to extract the response time of the switch. Rise and fall time measurements are reported. Finally, we checked electrical and optical power stability over time.

4.11.3 Grating coupler measurement

We first characterized the SiN grating coupler using a dedicated shunt test structure. An external laser emitting at 1550 nm is coupled to the circuit through a SiN grating coupler. The spectral response is shown in Fig. 4.55, with -4.3 dB insertion loss at 1568 nm.

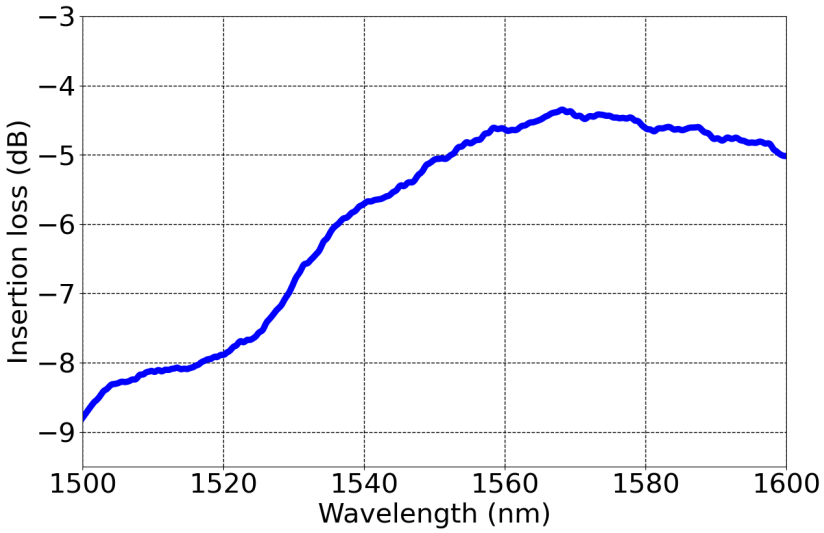

Figure 4.55: Measured transmission of one SiN grating coupler.

4.11.4 Heater characterization

We swept the voltage applied to each p-doped Silicon heater between 0 and 12 V and measured the current on a sourcemeter. The measured current-voltage (I-V) characteristics of the three heaters are shown in Fig. 4.56. The three electrical characteristics are very consistent. The corresponding resistance is around 1.44 kΩ.

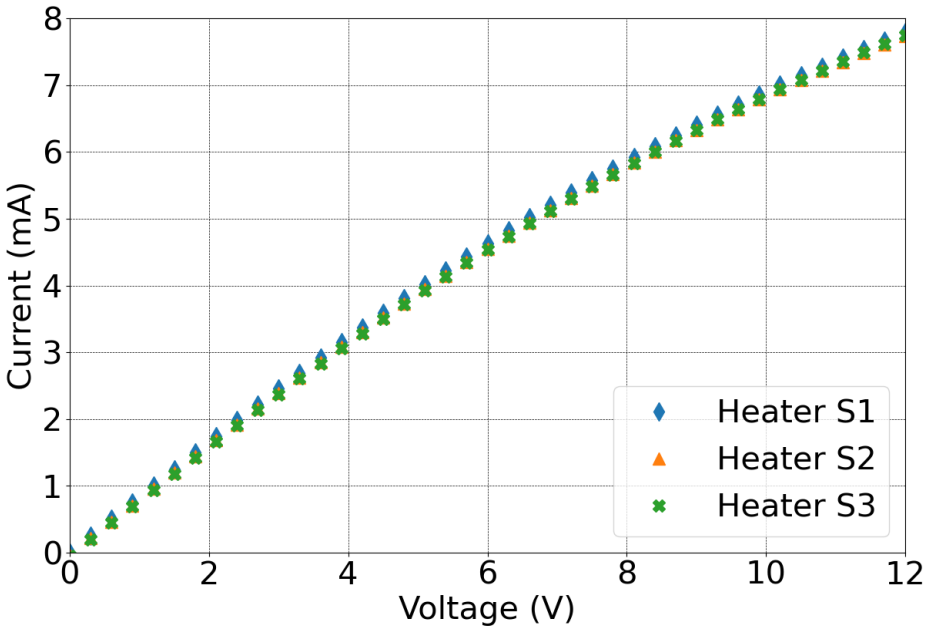

Figure 4.56: Measured IV curves of the three of thermo-optic phase shifters.

4.11.5 Switch insertion loss

In order to extract the insertion loss of one switch, we connected an external laser emitting at 1568 nm wavelength and with 10 dBm output power, to the input grating coupler "GC in". We focus on the insertion loss of the switch 1 for simplicity but we also performed the same measurements for S2 and S3. Hence, for S1, we connected the monitoring output grating coupler "GC G" to a powermeter and we swept the voltage applied on the heater 1. The measured output power against the heater electrical power of heater 1 is shown in Fig. 4.57.

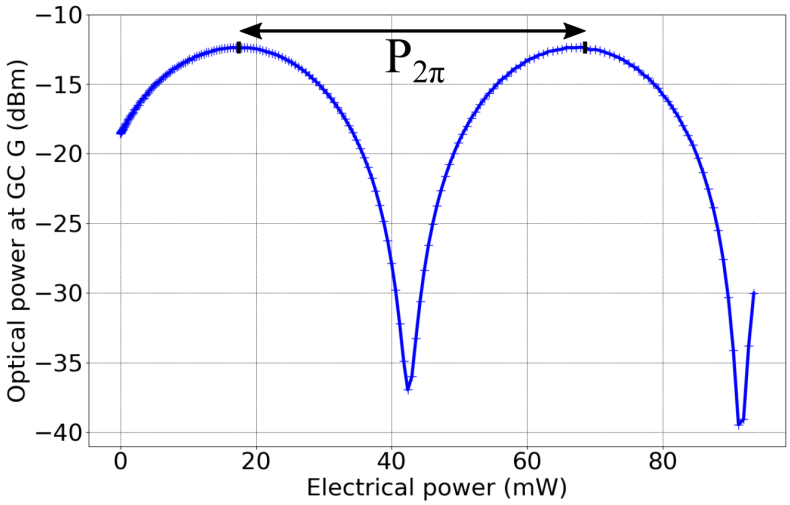

Figure 4.57: Measured optical power at the output of switch 1 "GC G" against the electrical power of heater 1. $P_{2\pi}$ is the required heater electrical power to produce a 2π phase shift.

We measured a maximum received optical power of -12.3 dBm for heater electrical powers Pb1 = 17.5 mW and Pb2 = 68 mW, corresponding to applied voltage bias Vb1 = 4.6 V and Vb2 = 9.9 V respectively. These two bias points correspond to states where the light is commuted towards switch 2. In order to quantify the insertion loss X of S1, we computed the link budget as shown in Fig. 4.58 a) and b).

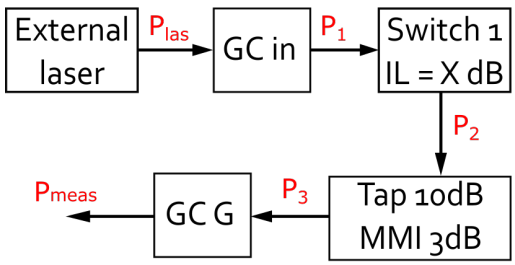

a)

Parameter	Value	Unit
P_{las}	10	dBm
IL GC in	4.3	dB
P_1	5.7	dBm
IL switch 1	X	dB
P_2	5.7 - X	dBm
IL tap and MMI	13	dB
P_3	- 7.3 - X	dBm
IL GC G	4.3	dB
P_{meas}	- 11.6 - X = - 12.3	dBm

b)

Figure 4.58: a) Link budget to compute the IL of switch 1 and b) table of corresponding powers and IL.

From Fig. 4.58 b), the insertion loss X of the switch 1 is only 0.6 dB to direct the

light towards S2. This measured value is comparable to the 0.5 dB N-doped silicon MZI switch insertion loss reported in [163].

4.11.6 Heater electrical power consumption

To quantify the heater electrical power consumption, we usually measure the required power to achieve a π phase shift (P_π) or a 2π phase shift ($P_{2\pi}$). From Fig. 4.57, we measured a switch 1 heater electrical power to produce a 2π phase shift, $P_{2\pi}$ of 50 mW (corresponding to a P_π of 25 mW). In this section we verify that the power consumption of the switch 2 heater is comparable to this value by monitoring the output signal on an integrated Ge photodiode. Again, the external laser emitting at 1568 nm and 10 dBm output power is connected to "GC in" (Fig. 4.53) and we bias heater 1 at the maximum transmission point obtained in Fig. 4.57 to direct the light towards S2. Then, we swept the voltage applied to heater 2 between 0 and 12 V and we monitored the output optical power on the PD_{2L} Ge integrated photodiode. Fig. 4.59 a) shows the photocurrent measured at the output of PD_{2L} as a function of electrical power consumed by the switch 2 heater. Fig. 4.59 b) shows the electric power consumed by this heater versus the produced phase shift.

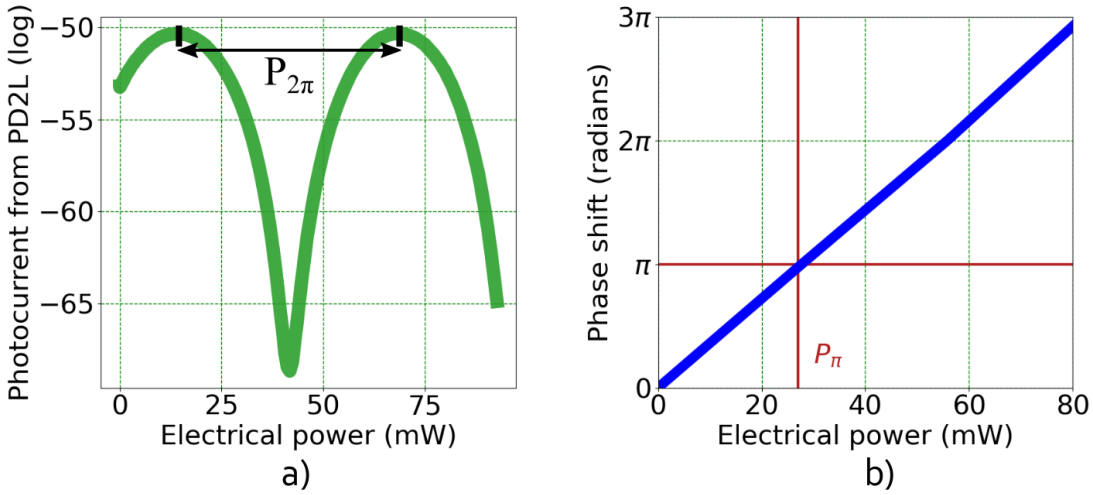

Figure 4.59: a) Measured photocurrent at the output of the internal photodiode PD_{2L} (in log scale) and b) produced phase shift as a function of electrical power consumed by the switch 2 heater.

Even though the photocurrent amplitude is small (in the μA range) due to the 10% tap, it is possible to retrieve the P_π. From Fig. 4.59 b), to achieve π phase shift with heater 2, a P_π of 27 mW electrical power is required. This value is consistent with the P_π of 25 mW measured for the heater of switch 1.

4.11.7 Crosstalk

We also performed crosstalk measurements. Our methodology was to bias each switch heater so that maximum power is obtained on each of the four FPSA outputs consecutively. The optical power of the four outputs is measured with the

powermeter. The results are summarized in Table 4.6 where the expected outputs have been highlighted in green.

	Outputs			
	B	C	D	E
Power (dBm)	-1.65	-15.7	-17.5	-16.6
	-23	-1.44	-17.9	-15.4
	-21.6	-24.1	-2.04	-26.4
	-30.8	-23.4	-16.5	-1.4

Table 4.6: Measured crosstalk on the four emitter FPSA circuit.

The measured power at the undesired outputs is -20.7 dBm on average, which is 18 dB lower than the measured power in the expected output. In futur designs, crosstalk can be improved by acting on the extinction ratio of the MZI to reach -25 dB to -30 dB.

4.11.8 Power stability

To assess the power stability of the heater, we measured the heater 1 electrical power evolution over 10 minutes as shown in Fig. 4.60. Over this time period, the electrical power is very stable with 0.002% maximum deviation from the mean value.

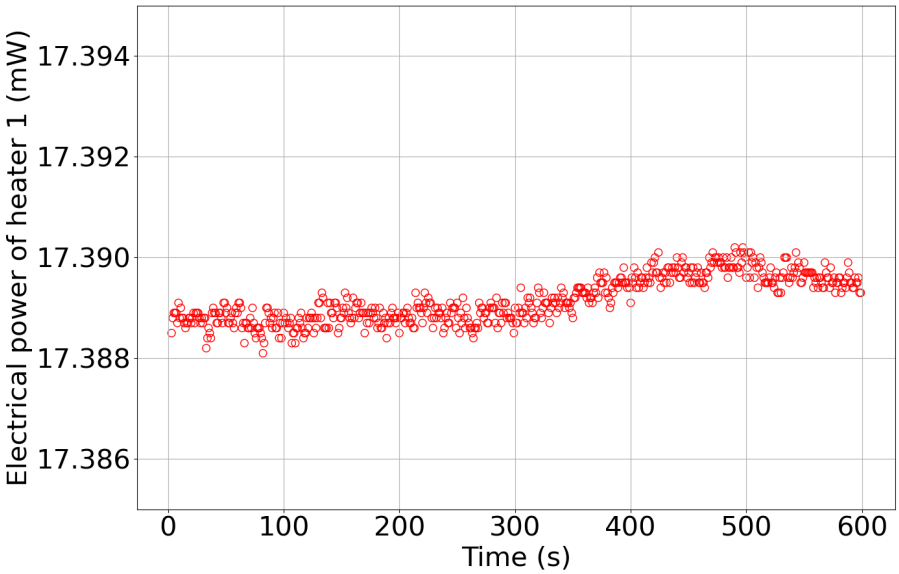

Figure 4.60: Evolution of heater 1 electrical power consumption over a 10 minute time period.

In a real system, an automatic control loop could be used to set the exact electrical power to the heater by monitoring the optical outputs of the switch.

4.11.9 AC characterization

Finally, we performed AC characterization to quantify the switch temporal response. The AC measurement setup is shown in Fig. 4.61.

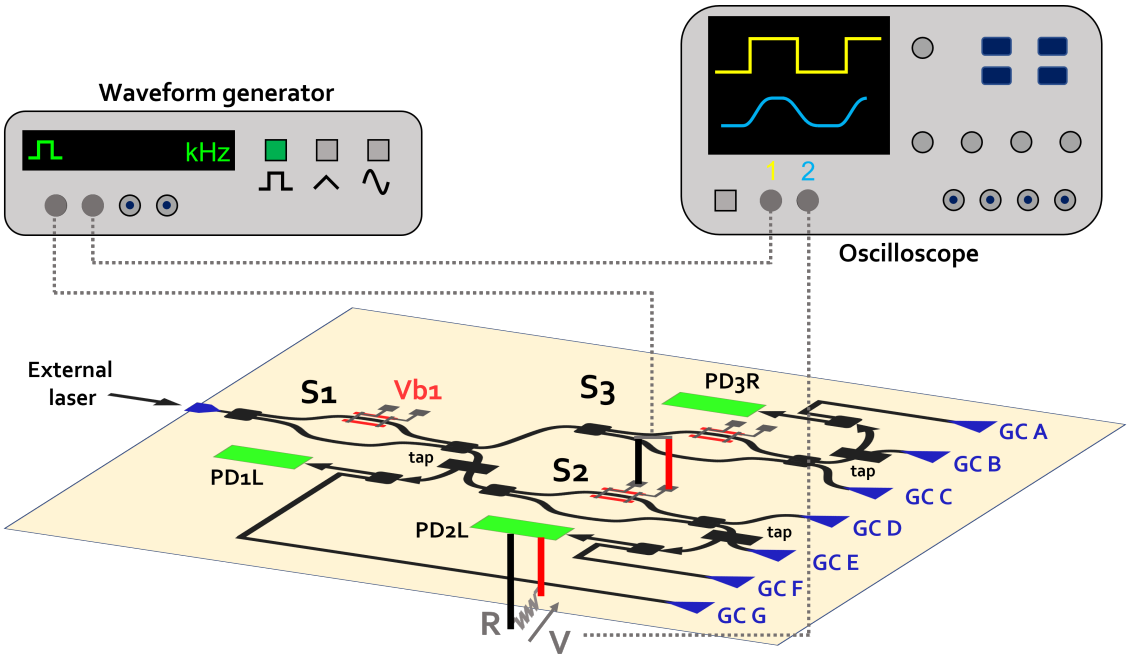

Figure 4.61: AC measurement setup to assess the switch 2 temporal response.

We focused on switch 2 for this part. We bias heater 1 at Vb1 = 4.6 V to direct the light towards S2 with maximum transmission. A waveform generator operating in square mode is connected to heater 2. The voltage step waveform is applied between the voltages producing the maximum and minimum of transmission of the switch (4 to 7.5 V for switch 2). The optical signal is sensed by an on-chip Ge photodiode. The photocurrent is then converted into a voltage by mean of a resistance. This signal is observed on the oscilloscope to measure the rise and fall times of the switch.

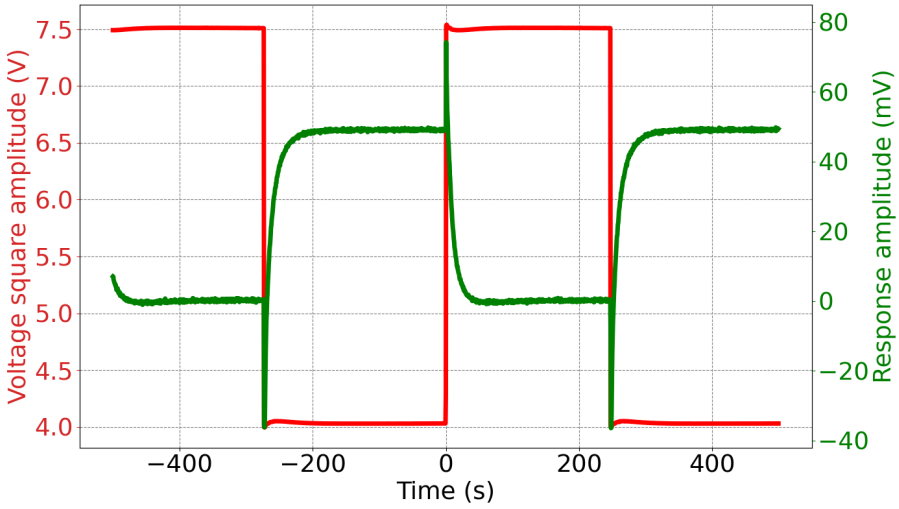

Figure 4.62: Measured temporal square voltage input waveform and output voltage response.

From Fig. 4.62, we observed overshoot at the voltage square waveform transitions. Overshoot occurs as the photodiode load resistance of 900 kΩ was not matched

with the oscilloscope impedance of 1 MΩ, resulting in reflections of the EM wave. In the response signal measurement, these reflections add to the measured voltage. In future works, overshoot will be suppressed by using proper terminations. To determine the rise and fall times of our switch, we fitted the response signal with the response of a first order system.

A rise time measurement of switch 2 is shown in Fig. 4.63. The rise and fall times correspond to the time duration within 10% to 90% of the final value. From Fig. 4.63 a rise time of 26 μs was measured.

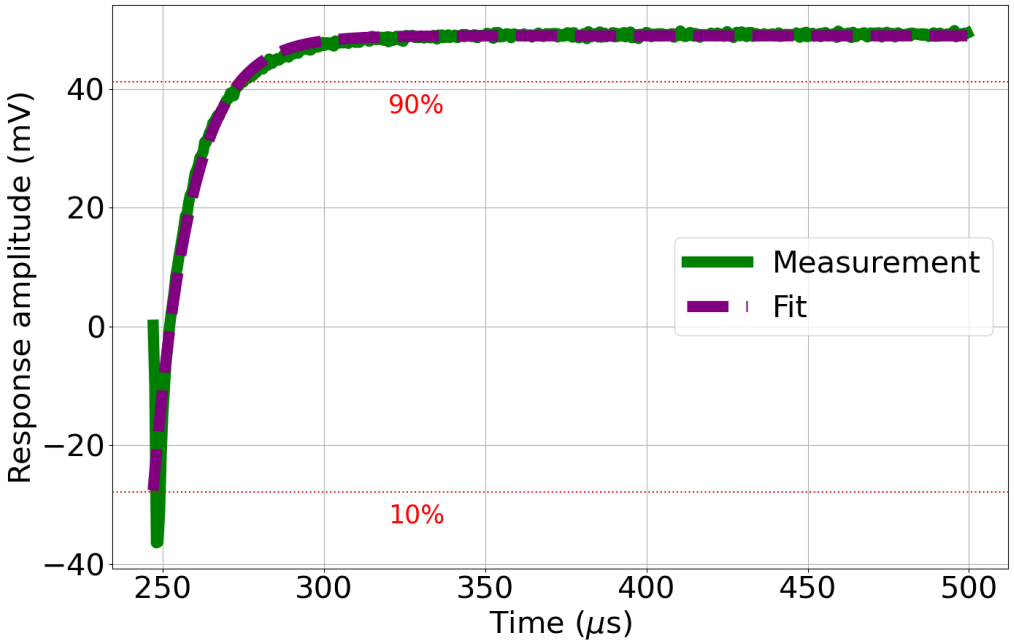

Figure 4.63: Measurement of the response measurement of switch 2 showing 26 μs rise time.

Rise and fall times for the 3 switches were measured and the values were comprised within 16-33 μs limiting the scanning rate to 62.5 kHz. While these values indicate slower operation than the automotive specification of < 10 μs, future approaches will be studied to decrease it. For instance, switches based on electro-optic free-carrier plasma dispersion effect could solve the speed limitation of the thermo-optic effect.

To summarize, we demonstrated and characterized an elementary tile of a FPSA circuit composed of 4 emitters. DC tests show 27 mW heater electrical power consumption for achieving π phase shift. As a comparison, in [164], two thermo-optic phase shifters made in TiN and N++ doped silicon were fabricated and characterized with P_π equal to 21.4 mW and 22.8 mW respectively. The measured crosstalk is lower than -15 dB across all the outputs. The electrical power consumed by the heater is stable after 10 minutes, and future developments would ensure stability for continuous operation. Finally, AC tests show tens of μs switch temporal response. This could be improved in order to reach automotive LIDAR scanning rate. Compared to the set of specifications given in Table 3.9, this 4-emitter circuit is a first step towards large scale FPSA. From our individual switch measurement, if we consider a FPSA of 1200 emitters corresponding to 11 cascaded MZI switch stages,

the total insertion loss and power consumption would be 6.6 dB and 300 mW, respectively. By adding a SOA (consuming 200 mW on average) at each emitter, the static power consumption is only 500 mW.

4.12 Chapter conclusion

In this chapter, we presented the structure and characterization of fully integrated FMCW LIDAR building blocks. First, a FMCW LIDAR single TX/RX comprising a III-V/Si amplifier and a coherent receiver made of a SiN 90° optical hybrid and a pair of Ge photodiodes was designed and fully characterized at the component level. The coherent receiver fulfils the specifications from the IC-TROSA standard and matches well with the state-of-the-art [137]. The key advantage of Scintil Photonics platform is to integrate this high performance coherent receiver with lasers and amplifiers based on III-V materials. The SOA provides an on-chip amplification > 10 dB in the C band and can operate at temperatures between 20-60 °C. Then, we implemented two types of integrated lasers based on DBR mirrors : a tunable laser and fixed DBR laser. We measured a 184 kHz Lorentzian linewidth for the tunable laser with a wide wavelength tunability. We also reported on the measurements of a III-V/Si DBR laser. Some fabrication defects did not enable to reach the power performance. However, we believe the laser should stay outside, temperature controlled and with an optical isolator, to feed the rest of the chip. In order to evaluate the frequency chirp linearity, we presented our results on the IQ modulator with SOA packaged circuit, demonstrating FMCW LIDAR measurements using fiber delay lines. Finally, we described the structure and characterization of a 4-emitter FPSA circuit for investigating the FMCW LIDAR beam scanning module. The switch shows low insertion loss (<0.6 dB), low power consumption (27 mW) and the crosstalk between emitters is <-15 dB. The measured switch temporal response (16-33 μs) indicates that thermo-optic effect might be a limiting factor to achieve the targeted automotive LIDAR scanning rates.

The integration of III-V material with Si, SiN and Ge is beneficial for building a chip-scale FMCW LIDAR. Indeed, integrated laser sources presenting low linewidth can be chirped with high linearity using a Si IQ modulator. A III-V/Si booster SOA can compensate the modulator losses, ensuring a high transmitted signal power. Finally, an on-chip coherent receiver made of SiN 90° hybrid and Ge balanced photodiodes is used to detect the target range and radial velocity with high precision.

Chapter 5

Conclusion and perspectives

5.1 Conclusion

The aim of this work was to evaluate the feasibility and the challenges related to the integration of FMCW LIDAR components and circuits on a III-V/Si photonic chip. The first objective of this work was to identify the FMCW LIDAR architecture and establish the system level specifications in the context of automotive application. The second step consisted in deriving the photonic component specifications. The final objective was the realization of the FMCW LIDAR components and circuits based on Scintil Photonics III-V/Si integration platform and characterize their performances.

We started by identifying the potential of FMCW LIDAR for automotive applications compared to its counterparts, and we have defined the main performance metrics for the considered scenario. Considering the illumination unit, we have highlighted the benefits of integrated beam scanning compared to commercial mechanical scanners. Based on a detailed comparison between Optical Phased Array (OPA) and Focal Plane Switch Array (FPSA), we selected the FPSA architecture for its reduced power consumption, crosstalk and complexity. We presented an overview of the FMCW LIDAR integration approaches with the aim of improving the footprint, the weight and the power consumption. Scintil Photonics integration platform has the unique advantage of integrating III-V material with Ge, Si and SiNx to build high performance components and circuits. Based on automotive LIDAR specifications, we concluded that integration of FMCW LIDAR is necessary to answer this demand for high level of parallelism. Afterwards, we provided a numerical model to understand the FMCW LIDAR system performances and limitations. This model showed the critical importance of laser linewidth on FMCW LIDAR performances. A digital processing technique has been proposed to extend the detection range of the FMCW LIDAR system beyond the coherence length of the laser source. An overall link budget has been evaluated, showing the need to integrate a booster SOA for detecting targets at hundreds of meters. We also analyzed the different noise contributions in the system through SNR simulations under several conditions, and proposed a set of silicon photonics component specifications. A FMCW LIDAR circuit architecture was identified and the layout was drawn based on the III-V/Si elementary components (MMI, GC, SOA, 90° hybrid, PD, ring resonators, heaters, DBR gratings, etc...). A single TX/RX FMCW LIDAR tile comprising a booster

amplifier and a coherent receiver was described and fully characterized. To our knowledge, this is the first monolithic integration of III-V/Si SOAs, Ge waveguide-PDs, Si active and Silicon Nitride (SiN) passive devices on a photonic integrated circuit (PIC). The coherent receiver meets the IC-TROSA standard specifications and the SOA provides on-chip amplification in the C band in a temperature range between 20-60 °C. The FMCW LIDAR source was also investigated with measurements of a 184 kHz Lorentzian linewidth tunable laser and high chirp linearity using a silicon IQ modulator followed by a SOA. We also explored a DBR integrated laser source and reported on its characterization. Finally, a 4-emitter FPSA beam scanning unit was realized to assess the performances of thermo-optic based MZI switches. We concluded on the power consumption and crosstalk benefits of this approach. We also highlighted the limitation in terms of scanning rate, which could be overcome using the electro-optic effect.

Therefore, the main conclusions of this work can be summarized as follows :

- The integration of the FMCW LIDAR components and circuits on a silicon photonics chip is possible using the unique III-V/Si integration platform developped by Scintil Photonics. The integration offers many improvements over bulk systems in terms of power consumption, footprint, coupling losses and risk of mechanical failure.
- The FMCW LIDAR source is a critical building block, as the laser phase noise and the chirp nonlinearities should be minimized. Laser linewidth <100 kHz will enable the detection of targets at 200 m and IQ modulators can be used to produce high linearity frequency ramps.
- The on-chip gain provided by the semiconductor optical amplifier (SOA) enables to meet the FMCW LIDAR power budget.
- The coherent detection is a centerpiece of the FMCW LIDAR system, enabling high sensitivity, reduced receiver bandwidth and immunity to background noise.
- Digital signal processing techniques could be used to alleviate the constraints on component/system specifications. For example, an estimation algorithm can be used to realize power spectrum density detection in the measured spectrum, to detect target beyond the laser coherence length, reducing the constraint on laser linewidth specification. Additional work needs to be carried on to evaluate the possibility of multiple target detection.
- Focal Plane Switch Array (FPSA) is a promising solid-state beam scanning technique for high resolution and wide field-of-view imaging.
- High level of repeatability between components will be essential to the mass deployment of integrated FMCW LIDAR. Wafer level characterization offers statistical representation of the fabricated elements. The component drift due to temperature should also be monitored.

Some perspectives have also been identified to complete this work. First, the investigation of the optical coupling interface between the scanning unit and free space

is essential to transmit collimated beams and ensure a high receiver aperture. This is one of the main challenge before running free space FMCW LIDAR measurements with our single TX/RX tile. For this circuit, we could also implement the detection algorithm and verify the ability to detect close targets by extracting their range and velocity. The second proposed area of improvements concerns the components performance optimization to reach higher SNR levels. Indeed, low noise figure SOA are highly desirable. PIN photodiodes could be replaced by avalanche photodiodes (APD) to provide additional gain at the receiver, but the additional noise should not be limiting. The investigation of multiplexing techniques will also be essential to meet the requirements of next-generation automotive LIDAR. Other integrated laser structures such as comb lasers could be interesting for future FMCW LIDAR systems.

In parallel, the FMCW LIDAR system model could be strengthen by integrating each component specifications (such as the phase errors of the 90°, the chirp non-linearity etc...) to evaluate more precisely the impact of each specification on the SNR and the accuracy of the estimated target distance and speed.

Concerning the digital processing technique, it would be interesting to evaluate if the detection algorithm can detect multiple targets and how efficiently. We could also adapt it to identify ghost targets.

Lastly, the integration of new materials such as Lithium Niobate (LiNbO3) or Barium Titanate (BTO) with silicon (Si) to boost the performances of current modulators, shows the great versatility of this platform. This could pave the way to a wide range of applications where integration will replace bulky solutions.

Bibliography

[1] National Highway Traffic Safety Administration (NHTSA) Releases 2019 Crash Fatality Data. URL: https://www.nhtsa.gov/press-releases/nhtsa-releases-2019-crash-fatality-data.

[2] Hafeez Cholakkal, Simone Mentasti, Mattia Bersani, Stefano Arrigoni, Matteo Matteucci, and Federico Cheli. "LiDAR - Stereo Camera Fusion for Accurate Depth Estimation". In: Nov. 2020, pp. 1–6.

[3] Giugudeanu Calin and Valentin Obac Roda. "Real-time disparity map extraction in a dual head stereo vision system". In: *Latin American Applied Research* 37 (2007), pp. 21–24.

[4] E. Grosso and M. Tistarelli. "Active/dynamic stereo vision". In: *IEEE Transactions on Pattern Analysis and Machine Intelligence* 17.9 (1995), pp. 868–879. DOI: 10.1109/34.406652.

[5] John Minkoff. "Signals, noise, and active sensors - Radar, sonar, laser radar". In: *NASA STI/Recon Technical Report A* 93 (Jan. 1992), p. 17900.

[6] Society of Automotive Engineers (SAE). URL: https://www.sae.org/.

[7] Yole Market and Technology Report. *LiDAR for Automotive and Industrial Applications 2021*.

[8] IDTechEx LIDAR Markets and Forecasts. URL: https://www.idtechex.com/.

[9] Graham T Reed and Andrew P Knights. *Silicon photonics: an introduction*. John Wiley & Sons, 2004.

[10] Paul McManamon. *LiDAR Technologies and Systems*. July 2019. DOI: 10.1117/3.2518254.

[11] Milad Gholipour Vazimali, Orges Furxhi, Yousef Alahmadi, and Ronald Driggers. "Comparison of illumination sources for imaging systems for different applications". In: *Laser Radar Technology and Applications XXIV*. Vol. 11005. International Society for Optics and Photonics. SPIE, 2019, pp. 265–272. DOI: 10.1117/12.2519208.

[12] Fan-Yi Lin and Jia-Ming Liu. "Chaotic lidar". In: *IEEE Journal of Selected Topics in Quantum Electronics* 10.5 (2004), pp. 991–997. DOI: 10.1109/JSTQE.2004.835296.

[13] H.L. Ho, Jun-Da Chen, Ching-An Yang, Chia-Chi Liu, Cheng-Ting Lee, Yu-Hsiang Lai, and Fan-Yi Lin. "High-speed 3D imaging using a chaos lidar system". In: *The European Physical Journal Special Topics* 231 (2022), pp. 435–441.

[14] Chih-Hao Cheng, Chih-Ying Chen, Jun-Da Chen, Da-Kung Pan, Kai-Ting Ting, and Fan-Yi Lin. "3D pulsed chaos lidar system." In: *Optics express* 26 9 (2018), pp. 12230–12241.

[15] Matteo Perenzoni, Daniele Perenzoni, and David Stoppa. "6.5 A 64x64-pixel digital silicon photomultiplier direct ToF sensor with 100Mphotons/s/pixel background rejection and imaging/altimeter mode with 0.14% precision up to 6km for spacecraft navigation and landing". In: *2016 IEEE International Solid-State Circuits Conference (ISSCC)*. 2016, pp. 118–119. DOI: 10.1109/ISSCC.2016.7417935.

[16] Preethi Padmanabhan, Chao Zhang, and Edoardo Charbon. "Modeling and Analysis of a Direct Time-of-Flight Sensor Architecture for LiDAR Applications". In: *Sensors* 19.24 (2019). ISSN: 1424-8220. DOI: 10.3390/s19245464.

[17] Feiyang Sun, Yue Xu, Zhong Wu, and Jun Zhang. "A Simple Analytic Modeling Method for SPAD Timing Jitter Prediction". In: *IEEE Journal of the Electron Devices Society* 7 (2019), pp. 261–267. DOI: 10.1109/JEDS.2019.2895151.

[18] Miles Hansard, Seungkyu Lee, Ouk Choi, and Radu Horaud. *Time of Flight Cameras: Principles, Methods, and Applications*. SpringerBriefs in Computer Science. Springer, 2012, p. 95. DOI: 10.1007/978-1-4471-4658-2.

[19] Santiago Royo and Maria Ballesta-Garcia. "An Overview of Lidar Imaging Systems for Autonomous Vehicles". In: *Applied Sciences* 9.19 (2019). ISSN: 2076-3417.

[20] Sony DepthSensing solutions. URL: https://www.sony-depthsensing.com/technology/.

[21] Terabee. URL: https://www.terabee.com/.

[22] PMD Technologies. URL: https://pmdtec.com/.

[23] Mesa Imaging. URL: www.mesa-imaging.ch.

[24] Matteo Perenzoni and David Stoppa. "Figures of Merit for Indirect Time-of-Flight 3D Cameras: Definition and Experimental Evaluation". In: *Remote Sensing* 3.11 (2011), pp. 2461–2472. ISSN: 2072-4292. DOI: 10.3390/rs3112461.

[25] Jesse Zheng. *Optical Frequency-Modulated Continuous-Wave (FMCW) Interferometry*. Springer Series in Optical Sciences. Springer, 2005. DOI: https://doi.org/10.1007/b100384.

[26] Behnam Behroozpour, Phillip A. M. Sandborn, Ming C. Wu, and Bernhard E. Boser. "Lidar System Architectures and Circuits". In: *IEEE Communications Magazine* 55.10 (2017), pp. 135–142. DOI: 10.1109/MCOM.2017.1700030.

[27] D. Rife and R. Boorstyn. "Single tone parameter estimation from discrete-time observations". In: *IEEE Transactions on Information Theory* 20.5 (1974), pp. 591–598. DOI: 10.1109/TIT.1974.1055282.

[28] Mikhail Ronkin and Aleksey Kalmykov. "Investigation of the time delay difference estimator for FMCW signals". In: Oct. 2017.

[29] Keyvan Sayyah, Raymond Sarkissian, Pamela Patterson, Biqin Huang, Oleg Efimov, Danny Kim, Ken Elliott, Louis Yang, and David Hammon. "Fully Integrated FMCW LiDAR Optical Engine on a Single Silicon Chip". In: *Journal of Lightwave Technology* 40.9 (2022), pp. 2763–2772. DOI: 10.1109/JLT.2022.3145711.

[30] Phillip Sandborn. "FMCW Lidar: Scaling to the Chip-Level and Improving Phase-Noise-Limited Performance". PhD thesis. EECS Department, University of California, Berkeley, 2019.

[31] E. J. Nunes-Pereira, H. Peixoto, J. Teixeira, and J. Santos. "Polarization-coded material classification in automotive LIDAR aiming at safer autonomous driving implementations". In: *Appl. Opt.* 59.8 (2020), pp. 2530–2540. DOI: 10.1364/AO.375704.

[32] Matt Traverso, Marco Mazzini, Kumar Lakshmikumar, Sanjay Sunder, Alex Kurylak, Craig Appel, Cristiana Muzio, Ravi Tummidi, Alberto Cervasio, Mary Nadeau, Weizhuo Li, Jarrett Neiman, and Mark Webster. "Integrated Silicon Photonics Transceiver Module for 100Gbit/s 20km Transmission". In: *2021 Optical Fiber Communications Conference and Exhibition (OFC)*. 2021, pp. 1–3.

[33] Denis Guilhot and Pol Ribes-Pleguezuelo. "Laser Technology in Photonic Applications for Space". In: *Instruments* 3.3 (2019). ISSN: 2410-390X. DOI: 10.3390/instruments3030050.

[34] Frank Tittel, Rafał Lewicki, Mohammad Jahjah, Briana Foxworth, Yufei Ma, L. Dong, Robert Griffin, Karol Krzempek, Przemyslaw Stefanski, and Jan Tarka. "Mid-infrared Laser Based Gas Sensor Technologies for Environmental Monitoring, Medical Diagnostics, Industrial and Security Applications". In: Jan. 2014, pp. 153–165. ISBN: 978-94-017-8571-6. DOI: 10.1007/978-94-017-8572-3_21.

[35] D. Jung, S. R. Bank, M. L. Lee, and Daniel Wasserman. "Next-generation mid-infrared sources". In: *Journal of Optics* 19 (2017).

[36] Van Nguyen, Alexei Baranov, Zeineb Loghmari, Laurent Cerutti, Jean-Baptiste Rodriguez, Julie Tournet, Gregoire Narcy, Guilhem Boissier, Gilles Patriarche, Michael Bahriz, Eric Tournié, and Roland Teissier. "Quantum cascade lasers grown on silicon". In: *Scientific Reports* 8 (May 2018). DOI: 10.1038/s41598-018-24723-2.

[37] Jacek Wojtanowski, Marek Zygmunt, Mirosława Kaszczuk, Zygmunt Mierczyk, and Michał Muzal. "Comparison of 905 nm and 1550 nm semiconductor laser rangefinders' performance deterioration due to adverse environmental conditions". In: *Opto-Electronics Review* 22 (Sept. 2014). DOI: 10.2478/s11772-014-0190-2.

[38] Isaac I. Kim, Bruce McArthur, and Eric J. Korevaar. "Comparison of laser beam propagation at 785 nm and 1550 nm in fog and haze for optical wireless communications". In: *Optical Wireless Communications III*. Ed. by Eric J. Korevaar. Vol. 4214. SPIE, 2001, pp. 26–37. URL: https://doi.org/10.1117/12.417512.

[39] Xiaochen Sun, Lingxuan Zhang, Qihao Zhang, and Wenfu Zhang. "Si Photonics for Practical LiDAR Solutions". In: *Applied Sciences* 9.20 (2019). ISSN: 2076-3417. DOI: 10.3390/app9204225.

[40] Prasad P Iyer. "Beam Steering approaches for Automotive and Consumer LIDARS". In: *Zemax Optics Talks* (Jan. 2021).

[41] Voyant Photonics. URL: https://voyantphotonics.com/.

[42] Jordi Riu. "Solid-state imaging LIDAR for close proximity navigation in the new generation of medium size satellites". In: *EPIC meeting on New Space* (Sept. 2019).

[43] Taehwan Kim. "Realization of Integrated Coherent LiDAR". PhD thesis. EECS Department, University of California, Berkeley, 2020.

[44] Velodyne Lidar. URL: https://velodynelidar.com/.

[45] Sven T. S. Holmström, Utku Baran, and Hakan Urey. "MEMS Laser Scanners: A Review". In: *Journal of Microelectromechanical Systems* 23.2 (2014), pp. 259–275. DOI: 10.1109/JMEMS.2013.2295470.

[46] M. Merli, G. Mendicino, R. Carminati, and N. Boni. "Modeling and experimental validation of hysteretic scan behavior of quasi-static piezoelectric micromirror". In: *MOEMS and Miniaturized Systems XXI*. Vol. 12013. International Society for Optics and Photonics. SPIE, 2022, 120130J. DOI: 10.1117/12.2608531.

[47] Eakkachai Pengwang, Kanty Rabenorosoa, Micky Rakotondrabe, and Nicolas Andreff. "Scanning Micromirror Platform Based on MEMS Technology for Medical Application". In: *Micromachines* 7 (Feb. 2016), p. 24. DOI: 10.3390/mi7020024.

[48] Kazuki Nakamura, Kenji Narumi, Kohei Kikuchi, and Yasuhisa Inada. "Liquid crystal-tunable optical phased array for LiDAR applications". In: ed. by Sailing He and Laurent Vivien. Vol. 11690. Society of Photo-Optical Instrumentation Engineers (SPIE) Conference Series. Mar. 2021, 116900W. DOI: 10.1117/12.2591230.

[49] C.A. Balanis. *Antenna Theory: Analysis and Design*. Wiley-interscience. Wiley Interscience, 2005. ISBN: 9788126524228. URL: https://books.google.fr/books?id=2SJ0CgAAQBAJ.

[50] Karel Van Acoleyen, Hendrik Rogier, and Roel Baets. "Two-dimensional optical phased array antenna on silicon-on-insulator". In: *Opt. Express* 18.13 (2010), pp. 13655–13660. DOI: 10.1364/OE.18.013655.

[51] Ching-Pai Hsu, Boda Li, Braulio Solano-Rivas, Amar R. Gohil, Pak Hung Chan, Andrew D. Moore, and Valentina Donzella. "A Review and Perspective on Optical Phased Array for Automotive LiDAR". In: *IEEE Journal of Selected Topics in Quantum Electronics* 27.1 (2021), pp. 1–16. DOI: 10.1109/JSTQE.2020.3022948.

[52] SungWon Chung, Hooman Abediasl, and Hossein Hashemi. "A Monolithically Integrated Large-Scale Optical Phased Array in Silicon-on-Insulator CMOS". In: *IEEE Journal of Solid-State Circuits* 53.1 (2018), pp. 275–296. DOI: 10.1109/JSSC.2017.2757009.

[53] Reza Fatemi, Aroutin Khachaturian, and Ali Hajimiri. "A Nonuniform Sparse 2-D Large-FOV Optical Phased Array With a Low-Power PWM Drive". In: *IEEE Journal of Solid-State Circuits* 54.5 (2019), pp. 1200–1215. DOI: 10.1109/JSSC.2019.2896767.

[54] Hooman Abediasl and Hossein Hashemi. "Monolithic optical phased-array transceiver in a standard SOI CMOS process". In: *Opt. Express* 23.5 (2015), pp. 6509–6519. DOI: 10.1364/OE.23.006509.

[55] Anh Hang Nguyen, Jun-Hyung Cho, Ho-Jun Bae, and Hyuk-Kee Sung. "Sidelobe Level Reduction of an Optical Phased Array Using Amplitude and Phase Modulation of Array Elements Based on Optically Injection-Locked Semiconductor Lasers". In: *Photonics* 7.1 (2020). ISSN: 2304-6732.

[56] Christopher Vincent Poulton, Matthew J. Byrd, Peter Russo, Erman Timurdogan, Murshed Khandaker, Diedrik Vermeulen, and Michael R. Watts. "Long-Range LiDAR and Free-Space Data Communication With High-Performance Optical Phased Arrays". In: *IEEE Journal of Selected Topics in Quantum Electronics* 25.5 (2019), pp. 1–8. DOI: 10.1109/JSTQE.2019.2908555.

[57] Zhaoyang Zhang, Hui Yu, Qikai Huang, Zhiyan Zhou, Bei Chen, Tingge Dai, Huiye Qiu, Yuehai Wang, and Jianyi Yang. "High-Speed and Low-Power Silicon Optical Phased Array Based on the Carrier-Depletion Mechanism". In: *IEEE Photonics Technology Letters* 34.5 (2022), pp. 271–274. DOI: 10.1109/LPT.2022.3151059.

[58] Martijn J.R. Heck. "Highly integrated optical phased arrays: photonic integrated circuits for optical beam shaping and beam steering". In: *Nanophotonics* 6.1 (2017), pp. 93–107. DOI: doi:10.1515/nanoph-2015-0152.

[59] Christopher V. Poulton, Matthew J. Byrd, Benjamin Moss, Erman Timurdogan, Ron Millman, and Michael R. Watts. "8192-Element Optical Phased Array with 100° Steering Range and Flip-Chip CMOS". In: *Conference on Lasers and Electro-Optics*. 2020, JTh4A.3. DOI: 10.1364/CLEO_AT.2020.JTh4A.3.

[60] David N. Hutchison, Jie Sun, Jonathan K. Doylend, Ranjeet Kumar, John Heck, Woosung Kim, Christopher T. Phare, Avi Feshali, and Haisheng Rong. "High-resolution aliasing-free optical beam steering". In: *Optica* 3.8 (2016), pp. 887–890. DOI: 10.1364/OPTICA.3.000887.

[61] Karel Van Acoleyen, Wim Bogaerts, Jana Jágerská, Nicolas Le Thomas, Romuald Houdré, and Roel Baets. "Off-chip beam steering with a one-dimensional optical phased array on silicon-on-insulator". In: *Opt. Lett.* 34.9 (2009), pp. 1477–1479. DOI: 10.1364/OL.34.001477.

[62] J. K. Doylend, M. J. R. Heck, J. T. Bovington, J. D. Peters, L. A. Coldren, and J. E. Bowers. "Two-dimensional free-space beam steering with an optical phased array on silicon-on-insulator". In: *Opt. Express* 19.22 (2011), pp. 21595–21604. DOI: 10.1364/OE.19.021595.

[63] David Kwong, Amir Hosseini, Yang Zhang, and Ray Chen. "1 x 12 Unequally spaced waveguide array for actively tuned optical phased array on a silicon nanomembrane". In: *Applied Physics Letters* 99 (2011), pp. 051104–051104. DOI: 10.1063/1.3619847.

[64] Jie Sun, Erman Timurdogan, Ami Yaacobi, Ehsan hosseini, and M.R. Watts. "Large-scale nanophotonic phased array". In: *Nature* 493 (2013), pp. 195–9. DOI: 10.1038/nature11727.

[65] Firooz Aflatouni, Behrooz Abiri, Angad Rekhi, and Ali Hajimiri. "Nanophotonic coherent imager". In: *Opt. Express* 23.4 (2015), pp. 5117–5125. DOI: 10.1364/OE.23.005117.

[66] Yu Zhang, Yi-Chun Ling, Kaiqi Zhang, Cale Gentry, David Sadighi, Greg Whaley, James Colosimo, Paul Suni, and S. J. Ben Yoo. "Sub-wavelength-pitch silicon-photonic optical phased array for large field-of-regard coherent optical beam steering". In: *Opt. Express* 27.3 (2019), pp. 1929–1940. DOI: 10.1364/OE.27.001929.

[67] Steven A. Miller, You-Chia Chang, Christopher T. Phare, Min Chul Shin, Moshe Zadka, Samantha P. Roberts, Brian Stern, Xingchen Ji, Aseema Mohanty, Oscar A. Jimenez Gordillo, Utsav D. Dave, and Michal Lipson. "Large-scale optical phased array using a low-power multi-pass silicon photonic platform". In: *Optica* 7.1 (2020), pp. 3–6. DOI: 10.1364/OPTICA.7.000003.

[68] Daisuke Inoue, Tadashi Ichikawa, Akari Kawasaki, and Tatsuya Yamashita. "Demonstration of a new optical scanner using silicon photonics integrated circuit". In: *Opt. Express* 27.3 (2019), pp. 2499–2508. DOI: 10.1364/OE.27.002499.

[69] Rüdiger Paschotta. *Field guide to lasers*. Vol. 12. SPIE press Bellingham, WA, 2008.

[70] Ming C. Wu, Tae Joon Seok, Kyungmok Kwon, Johannes Henriksson, and Jianheng Luo. "Large Scale Silicon Photonics Switches Based on MEMS Technology". In: *Optical Fiber Communication Conference (OFC) 2019*. 2019, Th1E.1. DOI: 10.1364/OFC.2019.Th1E.1.

[71] Xiaosheng Zhang, Kyungmok Kwon, Johannes Henriksson, Jianheng Luo, and Ming C. Wu. "A 20x20 Focal Plane Switch Array for Optical Beam Steering". In: *Conference on Lasers and Electro-Optics*. Optica Publishing Group, 2020, SM1O.3.

[72] Xiaosheng et al. Zhang. "A large-scale microelectromechanical-systems-based silicon photonics LiDAR". In: *Nature* 603 (Mar. 2022), pp. 253–258. DOI: 10.1038/s41586-022-04415-8.

[73] W. Bogaerts, P. De Heyn, T. Van Vaerenbergh, K. De Vos, S. Kumar Selvaraja, T. Claes, P. Dumon, P. Bienstman, D. Van Thourhout, and R. Baets. "Silicon microring resonators". In: *Laser and Photonics Reviews* 6.1 (2012), pp. 47–73. DOI: https://doi.org/10.1002/lpor.201100017.

[74] You-Chia Chang, Min Chul Shin, Christopher T. Phare, Steven A. Miller, Euijae Shim, and Michal Lipson. "2D beam steerer based on metalens on silicon photonics". In: *Opt. Express* 29.2 (2021), pp. 854–864. DOI: 10.1364/OE.409711.

[75] Miquel Rudé, Josselin Pello, Robert E. Simpson, Johann Osmond, Gunther Roelkens, Jos van der Tol, and Valerio Pruneri. "Optical switching at 1.55 μm in silicon racetrack resonators using phase change materials". In: *Applied Physics Letters* 103 (2013), p. 141119.

[76] Takumi Moriyama, Daiki Tanaka, Paridhi Jain, Hitoshi Kawashima, Masashi Kuwahara, Xiaomin Wang, and Hiroyuki Tsuda. "Ultra-compact, self-holding asymmetric Mach-Zehnder interferometer switch using Ge2Sb2Te5 phase-change material". In: *IEICE Electron. Express* 11 (2014), p. 20140538.

[77] Yifei Zhang, Jeffrey Chou, Junying Li, Huashan Li, Qingyang Du, Anupama Yadav, Si Zhou, Mikhail Shalaginov, Zhuoran Fang, Huikai Zhong, Christopher Roberts, Paul Robinson, Bridget Bohlin, Carlos Rios Ocampo, Hongtao Lin, Myungkoo Kang, Tian Gu, Jamie Warner, Vladimir Liberman, and Juejun Hu. "Broadband transparent optical phase change materials for high-performance nonvolatile photonics". In: *Nature Communications* 10 (Sept. 2019), pp. 1–9. DOI: 10.1038/s41467-019-12196-4.

[78] Chao Li, Xianyi Cao, Kan Wu, Xinwan Li, and Jianping Chen. "Lens-based integrated 2D beam-steering device with defocusing approach and broadband pulse operation for Lidar application". In: *Opt. Express* 27.23 (2019), pp. 32970–32983.

[79] Josué J. López, Scott A. Skirlo, Dave Kharas, Jamison Sloan, Jeffrey Herd, Paul Juodawlkis, Marin Soljačić, and Cheryl Sorace-Agaskar. "Planar-lens Enabled Beam Steering for Chip-scale LIDAR". In: *Conference on Lasers and Electro-Optics*. Optica Publishing Group, 2018, SM3I.1.

[80] Minh A Tran, Duanni Huang, and John E Bowers. "Tutorial on narrow linewidth tunable semiconductor lasers using Si/III-V heterogeneous integration". In: *APL photonics* 4.11 (2019), p. 111101.

[81] Xianyi Cao, Gaofeng Qiu, Kan Wu, Minglu Cai, Chao Li, and Jianping Chen. "A Lidar System Based on Integrated Lens Assisted Two-Dimensional Beam Steering". In: *2020 Conference on Lasers and Electro-Optics (CLEO)*. 2020, pp. 1–2.

[82] Samuel Kim, Jamison Sloan, Josué J. López, Dave Kharas, Jeffrey Herd, Suraj Bramhavar, Paul Juodawlkis, George Barbastathis, Steven Johnson, Cheryl Sorace-Agaskar, and Marin Soljačić. "Luneburg Lens for Wide-Angle Chip-Scale Optical Beam Steering". In: *2019 Conference on Lasers and Electro-Optics (CLEO)*. 2019, pp. 1–2. DOI: 10.1364/CLEO_SI.2019.SF3N.7.

[83] Christopher Rogers, Alexander Y. Piggott, David J. Thomson, Robert F. Wiser, Ion E. Opris, Steven A. Fortune, Andrew J. Compston, Alexander A. Gondarenko, Fanfan Meng, Xia Chen, Graham T. Reed, and Remus Nicolaescu. "A universal 3D imaging sensor on a silicon photonics platform." In: *Nature* 590 7845 (2021), pp. 256–261.

[84] Jing Zhang, Clemens J. Krückel, Bahawal Haq, Bozena Matuskova, Johanna Rimböck, Stefan Ertl, Agnieszka Gocalinska, Emanuele Pelucchi, Brian Corbett, Joris Van Campenhout, Guy Lepage, Peter Verheyen, Dries Van Thourhout, Roel Baets, and Gunther Roelkens. "Lossless High-speed Silicon Photonic MZI switch with a Micro-Transfer-Printed III-V amplifier". In: *2022 IEEE 72nd Electronic Components and Technology Conference (ECTC)*. 2022, pp. 441–445. DOI: 10.1109/ECTC51906.2022.00077.

[85] Lukas Chrostowski and Michael Hochberg. *Silicon Photonics Design: From Devices to Systems*. Cambridge University Press, 2015.

[86] Houssein El Dirani, Laurene Youssef, Camille Petit-Etienne, Sebastien Kerdiles, Philippe Grosse, Christelle Monat, Erwine Pargon, and Corrado Sciancalepore. "Ultralow-loss tightly confining Si3N4 waveguides and high-Q microresonators". In: *Opt. Express* 27.21 (2019), pp. 30726–30740. DOI: 10.1364/OE.27.030726.

[87] R. Soref and B. Bennett. "Electrooptical effects in silicon". In: *IEEE Journal of Quantum Electronics* 23.1 (1987), pp. 123–129. DOI: 10.1109/JQE.1987.1073206.

[88] S. Gao and R. Hui. "Frequency-modulated continuous-wave lidar using I/Q modulator for simplified heterodyne detection". In: *Opt. Lett.* 37.11 (2012), pp. 2022–2024. DOI: 10.1364/OL.37.002022.

[89] Laurent Vivien, Andreas Polzer, Delphine Marris-Morini, Johann Osmond, Jean Michel Hartmann, Paul Crozat, Eric Cassan, Christophe Kopp, Horst Zimmermann, and Jean Marc Fédéli. "Zero-bias 40Gbit/s germanium waveguide photodetector on silicon". In: *Opt. Express* 20.2 (2012), pp. 1096–1101. DOI: 10.1364/OE.20.001096.

[90] Arseny Vasilyev. "The optoelectronic swept-frequency laser and its applications in ranging, three-dimensional imaging, and coherent beam combining of chirped-seed amplifiers". PhD thesis. California Institute of Technology, 2013.

[91] Paramjeet Kaur, Andreas Boes, Guanghui Ren, Thach G Nguyen, Gunther Roelkens, and Arnan Mitchell. "Hybrid and heterogeneous photonic integration". In: *APL Photonics* 6.6 (2021), p. 061102.

[92] Michael Mack, A. Ayazi, Y. Chi, A. Dahl, Peter De Dobbelaere, Scott Denton, Steffen Gloeckner, Hon Kam-Yan, S. Hovey, Y. Liang, Gianlorenzo Masini, Attila Mekis, Mark Peterson, Thierry Pinguet, Subal Sahni, J. Schramm, M. Sharp, C. Sohn, K. Stechschulte, Peng Sun, G. Vastola, L. Verslegers, and R. Zhou. "Luxtera's Silicon Photonics Platform for Transceiver Manufacturing". In: 2014.

[93] A. Moscoso-Mártir, F. Merget, J. Mueller, J. Hauck, S. Romero-García, B. Shen, F. Lelarge, R. Brenot, A. Garreau, E. Mentovich, A. Sandomirsky, A. Badihi, D. E. Rasmussen, R. Setter, and J. Witzens. "Hybrid Silicon Photonics Flip-Chip Laser Integration with Vertical Self-Alignment". In: *Conference on Lasers and Electro-Optics Pacific Rim*. 2017. DOI: 10.1364/CLEOPR.2017.s2069.

[94] Gunther Roelkens, Jing Zhang, Grigorij Muliuk, Jeroen Goyvaerts, Bahawal Haq, Camiel Op de Beeck, Alexandros Liles, Zheng Wang, Sören Dhoore, Sulakshna Kumari, Joan Juvert, Joris Van Campenhout, Bart Kuyken, Dries Van Thourhout, Brian Corbett, Antonio Jose Trindade, Chris Bower, and Roel Baets. "III-V/Si PICs based on micro-transfer-printing". In: Jan. 2019, W4E.6. DOI: 10.1364/OFC.2019.W4E.6.

[95] Yuting Shi, Bernardette Kunert, Yannick De Koninck, Marianna Pantouvaki, Joris Van Campenhout, and Dries Van Thourhout. "Novel adiabatic coupler for III-V nano-ridge laser grown on a Si photonics platform". In: *Opt. Express* 27.26 (2019), pp. 37781–37794. DOI: 10.1364/OE.27.037781.

[96] Gunther Roelkens, Jing Zhang, Grigorij Muliuk, Jeroen Goyvaerts, Bahawal Haq, Camiel Op de Beeck, Alexandros Liles, Zheng Wang, Sören Dhoore, Sulakshna Kumari, Joan Juvert, Joris Van Campenhout, Bart Kuyken, Dries Van Thourhout, Brian Corbett, Antonio Jose Trindade, Chris Bower, and Roel Baets. "III-V/Si PICs based on micro-transfer-printing". In: Jan. 2019, W4E.6. DOI: 10.1364/OFC.2019.W4E.6.

[97] Bahawal Haq, Sulakshna Kumari, Kasper van gasse, Jing Zhang, Agnieszka Gocalinska, Emanuele Pelucchi, B. Corbett, and Gunther Roelkens. "Micro-Transfer-Printed III-V-on-Silicon C-Band Semiconductor Optical Amplifiers". In: *Laser and Photonics Reviews* 14 (June 2020). DOI: 10.1002/lpor.201900364.

[98] Jing Zhang, A. Gocalinkska, Emanuele Pelucchi, J. Campenhout, Guy Lepage, P. Verheyen, B. Corbett, and Gunther Roelkens. "III-V-on-silicon widely tunable laser realized using micro-transfer-printing". In: Jan. 2019, 91 (4 pp.)–91 (4 pp.) DOI: 10.1049/cp.2019.0825.

[99] Jae-Seong Park, Mingchu Tang, Siming Chen, and Huiyun Liu. "Heteroepitaxial Growth of III-V Semiconductors on Silicon". In: *Crystals* 10.12 (2020). ISSN: 2073-4352. DOI: 10.3390/cryst10121163.

[100] Alexander W. Fang, Hyundai Park, Oded Cohen, Richard Jones, Mario J. Paniccia, and John E. Bowers. "Electrically pumped hybrid AlGaInAs-silicon evanescent laser". In: *Opt. Express* 14.20 (2006), pp. 9203–9210. DOI: 10.1364/OE.14.009203.

[101] Guang-Hua Duan, Christophe Jany, Alban Le Liepvre, Alain Accard, Marco Lamponi, Dalila Make, Peter Kaspar, Guillaume Levaufre, Nils Girard, François Lelarge, Jean-Marc Fedeli, Antoine Descos, Badhise Ben Bakir, Sonia Messaoudene, Damien Bordel, Sylvie Menezo, Guilhem de Valicourt, Shahram Keyvaninia, Gunther Roelkens, Dries Van Thourhout, David J. Thomson, Frederic Y. Gardes, and Graham. T. Reed. "Hybrid III–V on Silicon Lasers for Photonic Integrated Circuits on Silicon". In: *IEEE Journal of Selected Topics in Quantum Electronics* 20.4 (2014), pp. 158–170. DOI: 10.1109/JSTQE.2013.2296752.

[102] SCINTIL Photonics. URL: https://www.scintil-photonics.com/.

[103] Torrey Thiessen, Sylvie Menezo, Christophe Jany, Jason C. C. Mak, and Joyce K. S. Poon. "Back-side-on-BOX heterogeneously integrated III-V-on-silicon O-band discrete-mode lasers". In: *Opt. Express* 28.26 (2020), pp. 38579–38591. DOI: 10.1364/OE.412839.

[104] Diego Pierrottet, Farzin Amzajerdian, Larry Petway, Bruce Barnes, George Lockard, and Manuel Rubio. "Linear FMCW laser radar for precision range and vector velocity measurements". In: *MRS Online Proceedings Library (OPL)* 1076 (2008).

[105] Aude Martin, Delphin Dodane, Luc Leviandier, Daniel Dolfi, Alan Naughton, Peter O'Brien, Thijs Spuessens, Roel Baets, Guy Lepage, Peter Verheyen, Peter De Heyn, Philippe Absil, Patrick Feneyrou, and Jérôme Bourderionnet. "Photonic Integrated Circuit-Based FMCW Coherent LiDAR". In: *J. Lightwave Technol.* 36.19 (2018), pp. 4640–4645.

[106] Brandon J. Isaac, Bowen Song, Sergio Pinna, Larry A. Coldren, and Jonathan Klamkin. "Indium Phosphide Photonic Integrated Circuit Transceiver for FMCW LiDAR". In: *IEEE Journal of Selected Topics in Quantum Electronics* 25.6 (2019), pp. 1–7. DOI: 10.1109/JSTQE.2019.2911420.

[107] Paul J. M. Suni, James R. Colosimo, S. J. Ben Yoo, John Edward Bowers, Larry A. Coldren, and Jonathan Klamkin. "Photonic Integrated Circuit FMCW Lidar On A Chip". In: 2018.

[108] Dongjae Shin, Hyunil Byun, Dongshik Shim, Jungho Cha, Yonghwack Shin, Changg Yun Shin, Changbum Lee, Eunkyung Lee, Bongyong Jang, Jisan Lee, Inoh Hwang, Kyunghyun Son, Yongchul Cho, Tatsuhiro Otsuka, Hyuck Choo, and Kyoungho Ha. "Bulk-Si Platform: Born for DRAM, Upgraded With On-Chip Lasers, and Transplanted to LiDAR". In: *Journal of Lightwave Technology* 40.10 (2022), pp. 3137–3148.

[109] Matthias Seimetz. *High-Order Modulation for Optical Fiber Transmission*. Vol. 143. Jan. 2009. ISBN: 9783540937708. DOI: 10.1007/978-3-540-93771-5.

[110] Oscar Carrasco-Zevallos and Joseph A. Izatt. "Complex Conjugate Removal in SS Optical Coherence Tomography". In: *Optical Coherence Tomography: Technology and Applications*. Springer International Publishing, 2015, pp. 255–276. ISBN: 978-3-319-06419-2. DOI: 10.1007/978-3-319-06419-2_9.

[111] Yohei Sakamaki, Yusuke Nasu, Toshikazu Hashimoto, Kuninori Hattori, Takashi Saida, and Hiroshi Takahashi. "Reduction of phase-difference deviation in 90° optical hybrid over wide wavelength range". In: *IEICE Electron. Express* 7 (2010), pp. 216–221.

[112] Jin Wang, Matthias Lauermann, Crispin Zawadzki, W. Brinker, Ziyang Zhang, David de Felipe, Norbert Keil, Norbert Grote, and Martin Schell. "Quantifying Direct DQPSK Receiver with Integrated Photodiode-Array by Assessing an Adapted Common-Mode Rejection Ratio". In: *Proc SPIE* 8308 (Nov. 2011). DOI: 10.1117/12.904384.

[113] IC-TROSA specifications from the Optical Internetworking Forum (OIF). URL: https://www.oiforum.com/technical-work/implementation-agreements-ias/.

[114] Yves Painchaud, Michel Poulin, Michel Morin, and Michel Têtu. "Performance of balanced detection in a coherent receiver". In: *Opt. Express* 17.5 (2009), pp. 3659–3672. DOI: 10.1364/OE.17.003659.

[115] Abhay Joshi, Don Becker, Christoph Wree, and Dan Mohr. "Coherent optical receiver system with balanced photodetection". In: *SPIE Defense and Commercial Sensing*. 2006.

[116] Esther Baumann, Jean-Daniel Deschênes, Fabrizio R. Giorgetta, William C. Swann, Ian Coddington, and Nathan R. Newbury. "Speckle phase noise in coherent laser ranging: fundamental precision limitations". In: *Opt. Lett.* 39.16 (2014), pp. 4776–4779. DOI: 10.1364/OL.39.004776.

[117] Rod G. Frehlich and Michael J. Kavaya. "Coherent laser radar performance for general atmospheric refractive turbulence". In: *Appl. Opt.* 30.36 (Dec. 1991), pp. 5325–5352. DOI: 10.1364/AO.30.005325.

[118] Diana M. Chambers. "Modeling heterodyne efficiency for coherent laser radar in the presence of aberrations". In: *Opt. Express* 1.3 (Aug. 1997), pp. 60–67. DOI: 10.1364/OE.1.000060.

[119] Honglin Ji, Xian Zhou, Chuanbowen Sun, and William Shieh. "Polarization-diversity receiver using remotely delivered local oscillator without optical polarization control". In: *Opt. Express* 28.15 (2020), pp. 22882–22890. DOI: 10.1364/OE.394371.

[120] Lijie Qiao, Dongsong Sun, Xiaofu Zhang, and Yuan Zhao. "Linearity requirement for a linear frequency modulation lidar". In: *Optical review* 6.2 (1999), pp. 160–162.

[121] Shouichi Ogita, Yuji Kotaki, Hiroshi Ishikawa, and Hiroshi Onaka. "Direct frequency modulation of semiconductor laser". In: *Electronics and Communications in Japan (Part II: Electronics)* 74.2 (1991), pp. 39–49. DOI: https://doi.org/10.1002/ecjb.4420740205.

[122] S. Ayotte, K. Bédard, M. Morin, S. Boudreau, A. Desbiens, P. Chrétien, A. Babin, F. Costin, É. Girard-Deschênes, G. Paré-Olivier, L.-P. Perron, M. Wichmann, R. Korn, E. Baumgart, O. Kern, and N. Caspers. "Narrow linewidth semiconductor DFB laser with linear frequency modulation for FMCW LiDAR". In: *Photonic Instrumentation Engineering VIII*. Vol. 11693. SPIE, 2021, 116930F. DOI: 10.1117/12.2578594.

[123] Xiaosheng Zhang. "Laser Chirp Linearization and Phase Noise Compensation for Frequency-modulated Continuous- wave LiDAR". In: 2021.

[124] Alexander Piggott. "Understanding the physics of coherent LiDAR". In: (Nov. 2020).

[125] Kasper Van Gasse, Ruijun Wang, and Gunther Roelkens. "27 dB gain III-V on silicon semiconductor optical amplifier with > 17 dBm output power". In: *Opt. Express* 27.1 (2019), pp. 293–302. DOI: 10.1364/OE.27.000293.

[126] Youssef Said, Houria Rezig, and A. Bouallegue. "Analysis of Noise Effects in Long Semiconductor Optical Amplifiers". In: *The Open Optics Journal* 2 (Oct. 2008). DOI: 10.2174/1874328500802010061.

[127] Douglas M. Baney, Philippe Gallion, and Rodney S. Tucker. "Theory and Measurement Techniques for the Noise Figure of Optical Amplifiers". In: *Optical Fiber Technology* 6.2 (2000), pp. 122–154. ISSN: 1068-5200. DOI: https://doi.org/10.1006/ofte.2000.0327.

[128] Philippe C. Becker, N. Anders Olsson, and Jay R. Simpson. "Erbium-Doped Fiber Amplifiers—Amplifier Basics". In: 1999.

[129] J-C Simon, P Doussiere, L Pophillat, and B Fernier. "Gain and noise characteristics of a 1.5 mu m near-travelling-wave semiconductor laser amplifier". In: *Electronics Letters* 7.25 (1989), pp. 434–436.

[130] C. Henry. "Theory of the linewidth of semiconductor lasers". In: *IEEE Journal of Quantum Electronics* 18.2 (1982), pp. 259–264. DOI: 10.1109/JQE.1982.1071522.

[131] Gianni Di Domenico, Stéphane Schilt, and Pierre Thomann. "Simple approach to the relation between laser frequency noise and laser line shape". In: *Appl. Opt.* 49.25 (2010), pp. 4801–4807. DOI: 10.1364/AO.49.004801.

[132] K. Kikuchi. "Effect of 1/f-type FM noise on semiconductor-laser linewidth residual in high-power limit". In: *IEEE Journal of Quantum Electronics* 25.4 (1989), pp. 684–688. DOI: 10.1109/3.17331.

[133] L.B. Mercer. "1/f frequency noise effects on self-heterodyne linewidth measurements". In: *Journal of Lightwave Technology* 9.4 (1991), pp. 485–493. DOI: 10.1109/50.76663.

[134] Behnam Behroozpour, Phillip A. M. Sandborn, Niels Quack, Tae-Joon Seok, Yasuhiro Matsui, Ming C. Wu, and Bernhard E. Boser. "Electronic-Photonic Integrated Circuit for 3D Microimaging". In: *IEEE Journal of Solid-State Circuits* 52.1 (2017), pp. 161–172. DOI: 10.1109/JSSC.2016.2621755.

[135] Michèle Colomb, Pierre Duthon, and Frédéric Bernardin. "Spectral reflectance characterization of the road environment to optimize the choice of autonomous vehicle sensors". In: *2019 IEEE Intelligent Transportation Systems Conference (ITSC)*. 2019, pp. 1085–1090. DOI: 10.1109/ITSC.2019.8917455.

[136] Taehwan Kim, Pavan Bhargava, and Vladimir Stojanovic. "Optimal Spectral Estimation and System Trade-Off in Long-Distance Frequency-Modulated Continuous-Wave Lidar". In: *2018 IEEE International Conference on Acoustics, Speech and Signal Processing (ICASSP)*. 2018, pp. 1583–1587. DOI: 10.1109/ICASSP.2018.8461653.

[137] Hang Guan, Yangjin Ma, Ruizhi Shi, Xiaoliang Zhu, Rick Younce, Yaojia Chen, Jose Roman, Noam Ophir, Yang Liu, Ran Ding, Thomas Baehr-Jones, Keren Bergman, and Michael Hochberg. "Compact and low loss 90° optical hybrid on a silicon-on-insulator platform". In: *Opt. Express* 25.23 (2017), pp. 28957–28968. DOI: 10.1364/OE.25.028957.

[138] Yun Wang. "Grating coupler design based on silicon-on-insulator". PhD thesis. University of British Columbia, 2013. DOI: http://dx.doi.org/10.14288/1.0073806.

[139] Léopold Virot, Laurent Vivien, Jean-Marc Fédéli, Yann Bogumilowicz, Jean-Michel Hartmann, Frédéric Bœuf, Paul Crozat, Delphine Marris-Morini, and Eric Cassan. "High-performance waveguide-integrated germanium PIN photodiodes for optical communication applications". In: *Photon. Res.* 1.3 (2013), pp. 140–147. DOI: 10.1364/PRJ.1.000140.

[140] M. Balbi, V. Sorianello, L. Colace, and G. Assanto. "Analysis of temperature dependence of Ge-on-Si p–i–n photodetectors". In: *Physica E: Low-dimensional Systems and Nanostructures* 41.6 (2009), pp. 1086–1089. DOI: https://doi.org/10.1016/j.physe.2008.08.015.

[141] Takahiro Numai. *Fundamentals of Semiconductor Lasers*. Springer Japan, 2015. DOI: 10.1007/978-4-431-55148-5_5.

[142] Nicolas Volet, Alexander Spott, Eric J. Stanton, Michael L. Davenport, Lin Chang, Jonathan Peters, Travis C. Briles, Igor Vurgaftman, Jerry R. Meyer, and John Edward Bowers. "Semiconductor optical amplifiers at 2.0-μm wavelength on silicon". In: *Laser & Photonics Reviews* 11 (2017).

[143] Jin-Long Xiao and Yong-Zhen Huang. "Numerical Analysis of Gain Saturation, Noise Figure, and Carrier Distribution for Quantum-Dot Semiconductor-Optical Amplifiers". In: *Quantum Electronics, IEEE Journal of* 44 (June 2008), pp. 448–455. DOI: 10.1109/JQE.2007.916683.

[144] Jared Hulme, Jonathan Doylend, and John Bowers. "Widely tunable Vernier ring laser on hybrid silicon". In: *Optics express* 21 (Aug. 2013), pp. 19718–19722. DOI: 10.1364/OE.21.019718.

[145] Jing Zhang, Yanlu Li, Sören Dhoore, Geert Morthier, and Gunther Roelkens. "Unidirectional, widely-tunable and narrow-linewidth heterogeneously integrated III-V-on-silicon laser". In: *Opt. Express* 25.6 (2017), pp. 7092–7100. DOI: 10.1364/OE.25.007092.

[146] Hang Guan, Ari Novack, Tal Galfsky, Yangjin Ma, Saeed Fathololoumi, Alexandre Horth, Tam N. Huynh, Jose Roman, Ruizhi Shi, Michael Caverley, Yang Liu, Thomas Baehr-Jones, Keren Bergman, and Michael Hochberg. "Widely-tunable, narrow-linewidth III-V/silicon hybrid external-cavity laser for coherent communication". In: *Opt. Express* 26.7 (2018), pp. 7920–7933. DOI: 10.1364/OE.26.007920.

[147] Minh Tran Anh, Duanni Huang, Joel Guo, Tin Komljenovic, Paul Morton, and John Bowers. "Ring-Resonator Based Widely-Tunable Narrow-Linewidth Si/InP Integrated Lasers". In: *IEEE Journal of Selected Topics in Quantum Electronics* PP (Aug. 2019), pp. 1–1. DOI: 10.1109/JSTQE.2019.2935274.

[148] Minh A. Tran, Duanni Huang, and John Edward Bowers. "Tutorial on narrow linewidth tunable semiconductor lasers using Si/III-V heterogeneous integration". In: *APL Photonics* (2019).

[149] Shengping Liu, Junbo Feng, ye Tian, Heng Zhao, Li Jin, Boling Ouyang, Jiguang Zhu, and Jin Guo. "Thermo-optic phase shifters based on silicon-on-insulator platform: state-of-the-art and a review". In: *Frontiers of Optoelectronics* 15 (Dec. 2022). DOI: 10.1007/s12200-022-00012-9.

[150] Christos Theodoros Santis, Scott T. Steger, Yaakov Vilenchik, Arseny Vasilyev, and Amnon Yariv. "High-coherence semiconductor lasers based on integral high-Q resonators in hybrid Si/III-V platforms". In: *Proceedings of the National Academy of Sciences* 111.8 (2014), pp. 2879–2884. DOI: 10.1073/pnas.1400184111.

[151] Wim Bogaerts, Peter Heyn, Thomas Van Vaerenbergh, Katrien Vos, Shankar Kumar Selvaraja, Tom Claes, Pieter Dumon, Peter Bienstman, Dries Thourhout, and Roel Baets. "Silicon microring resonators". In: *Laser & Photonics Reviews* 6 (Jan. 2012), pp. 47–73. DOI: 10.1002/lpor.201100017.

[152] Hans Joachim Eichler, Jürgen Eichler, and Oliver Lux. *Lasers - Basics, Advances and Applications*. Nov. 2018. ISBN: 978-3-319-99895-4. DOI: 10.1007/978-3-319-99895-4.

[153] E. Rochat and R. Dandliker. "New investigations on the effect of fiber amplifier phase noise". In: *IEEE Journal of Selected Topics in Quantum Electronics* 7.1 (2001), pp. 49–54. DOI: 10.1109/2944.924009.

[154] S.A. Havstad, Y. Xie, A.B. Sahin, Z. Pan, A.E. Willner, and B. Fischer. "Delayed self-heterodyne interferometer measurements of narrow linewidth fiber lasers". In: *Conference on Lasers and Electro-Optics (CLEO 2000). Technical Digest. Postconference Edition. TOPS Vol.39 (IEEE Cat. No.00CH37088).* 2000, pp. 310–311. DOI: 10.1109/CLEO.2000.907051.

[155] E. Rochat and R. Dandliker. "New investigations on the effect of fiber amplifier phase noise". In: *IEEE Journal of Selected Topics in Quantum Electronics* 7.1 (2001), pp. 49–54. DOI: 10.1109/2944.924009.

[156] Heming Huang. "Optical nonlinearities in quantum dot lasers for high-speed communications". 2017ENST0012. PhD thesis. 2017. URL: http://www.theses.fr/2017ENST0012.

[157] Tae-Jung Ahn, Ji Yong Lee, and Dug Young Kim. "Suppression of nonlinear frequency sweep in an optical frequency-domain reflectometer by use of Hilbert transformation". In: *Appl. Opt.* 44.35 (2005), pp. 7630–7634. DOI: 10.1364/AO.44.007630.

[158] Xiaosheng Zhang, Jazz Pouls, and Ming C. Wu. "Laser frequency sweep linearization by iterative learning pre-distortion for FMCW LiDAR". In: *Opt. Express* 27.7 (2019), pp. 9965–9974. DOI: 10.1364/OE.27.009965.

[159] Naresh Satyan, Arseny Vasilyev, George Rakuljic, Victor Leyva, and Amnon Yariv. "Precise control of broadband frequency chirps using optoelectronic feedback". In: *Opt. Express* 17.18 (2009), pp. 15991–15999. DOI: 10.1364/OE.17.015991.

[160] G.H. Duan and P. Gallion. "Drive current noise induced linewidth in tunable multielectrode lasers". In: *IEEE Photonics Technology Letters* 3.4 (1991), pp. 302–304. DOI: 10.1109/68.82093.

[161] Shuang Gao, Maurice O'Sullivan, and Rongqing Hui. "Complex-optical-field lidar system for range and vector velocity measurement". In: *Opt. Express* 20.23 (2012), pp. 25867–25875. DOI: 10.1364/OE.20.025867.

[162] S.J. Goldman. *Phase-locked Loop Engineering Handbook for Integrated Circuits*. Artech House microwave library. Artech House, 2007. ISBN: 9781596931541.

[163] Michael R. Watts, Jie Sun, Christopher DeRose, Douglas C. Trotter, Ralph W. Young, and Gregory N. Nielson. "Adiabatic thermo-optic Mach-Zehnder switch". In: *Opt. Lett.* 38.5 (2013), pp. 733–735. DOI: 10.1364/OL.38.000733.

[164] Maxime Jacques, Alireza Samani, Eslam El-Fiky, David Patel, Zhenping Xing, and David V. Plant. "Optimization of thermo-optic phase-shifter design and mitigation of thermal crosstalk on the SOI platform". In: *Opt. Express* 27.8 (2019), pp. 10456–10471. DOI: 10.1364/OE.27.010456.

List of publications

International conference

- M. Peyrou, J. Mak, T. Thiessen, K. Froberger, F. Denis-Le Coarer, Z. Yong, L. Milord, M. Marchenay, F. Mazur, Y. Le Guennec, C. Jany, J. K. S. Poon, and S. Menezo: **Fully Integrated Silicon Photonic Circuit technology with SiN passives, Ge photodetectors and III-V/Si SOAs**. *European Conference on Optical Communication*, September 2022, Bassel, Switzerland

Communications

- M. Peyrou, Y. Le Guennec, and S. Menezo: **FMCW lidar range and velocity estimation beyond the laser coherence**. *Conférence Optique Dijon, workshop LIDAR*, July 2021, Dijon, France.

- M. Peyrou: **Conception et test de composants/circuits photoniques intégrés hybrides InP/Si pour applications LIDAR**. *Webminar GDR Ondes*, March 2021.

Paper submitted to international journal and under review

- M. Peyrou, F. Enault, F. Mazur, K. Froberger, Z. Yong, T. Thiessen, J. Mak, F. Denis-Le-Coarer, M. Marchenay, L. Milord, Y. Le Guennec, F. Moysan and S. Menezo: **Laser Frequency Chirping with Silicon Photonic Circuit comprising an IQ Modulator and a III-V/Si SOA**. *Photonics Technology Letters*, submitted in October 2022.

Publications as co-author

- S. Menezo, Z. Yong, K. Froberger, T. Thiessen, J. C.C. Mak, F. Denis-le Coarer, M. Peyrou, L. Milord, J. Da Fonseca, C. Jany, P. Grosse, F. Mazur, and J. K. S. Poon: **40GBaud PAM4 silicon Mach-Zehnder modulator boosted by a heterogeneously integrated SOA with 10dB-gain**. *Optical Fiber Communication Conference (OFC) 2022*, 6-10 March 2022, San Diego, California, USA.

- P. Iovanna, A. Bigongiari, F. Cavaliere, A. Bianchi, F. Testa, S. Marconi, M. Romagnoli, V. Sorianello, A. Sgambelluri, F. Denis-Le Coarer, L. Milord, M. Peyrou, and S. Menezo: **Optical Components for Transport Network Enabling The Path to 6G**. *Journal of Lightwave Technology*, January 2022.

- T. Thiessen, J. Mak, F. Denis-Le Coarer, Z. Yong, K. Froberger, M. Marchenay, M. Peyrou, L. Milord, J. K. S. Poon, C Jany, S. Menezo: **Fully Integrated III-V-on-Silicon Multi-Port DFB Laser Comb Source for 100 GHz DWDM** . *Optical Fiber Communication Conference (OFC) 2023*, March 2023, San Diego, California, USA.